Time-Dependent
Current-Density-Functional Theory
for Metals

Pina Romaniello

Front cover: Schematic representation of the self-consistent-field calculation of the microscopic and macroscopic parts of the induced density (chapter 3) shaped into a wave.

The work described in this thesis was performed in the Theoretical Chemistry Group of the Materials Science Centre at the University of Groningen, Nijenborgh 4, 9747 AG Groningen, The Netherlands.

Pina Romaniello,

Time-Dependent Current-Density-Functional Theory for Metals,

Proefschrift Rijksuniversiteit Groningen.

RIJKSUNIVERSITEIT GRONINGEN

Time-Dependent Current-Density-Functional Theory for Metals

Proefschrift

ter verkrijging van het doctoraat in de
Wiskunde en Natuurwetenschappen
aan de Rijksuniversiteit Groningen
op gezag van de
Rector Magnificus, dr. F. Zwarts,
in het openbaar te verdedigen op
maandag 9 oktober 2006
om 16.15 uur

door

Pina Romaniello

geboren op 27 mei 1977
te Tricarico, Italië

Promotor:	Prof. dr. R. Broer
Copromotor:	Dr. ir. P. L. de Boeij

Beoordelingscommissie:	Prof. dr. E. J. Baerends
	Prof. dr. X. Gonze
	Prof. dr. R. A. de Groot

ISBN 90-367-2761-8

Alla mia famiglia

Contents

Chapter 1

Optical Properties of Crystalline Solid Systems

The linear response of a solid to an external electromagnetic field can be described in connection with two kinds of experiments: the optical absorption spectra for energies ranging from the infrared to the far vacuum ultraviolet, and the energy-loss determinations of electrons traversing solid samples. Despite the apparent disparity between the two phenomena, they are in fact closely related.

1.1 Optical properties and plasma effects

The optical properties and electron energy-loss spectra of solids[a] provide an important tool for studying elementary excitations, such as excitons, lattice vibrations, magnetic excitations, plasmons, and provide information about the energy band structures, impurity levels, localized defects. In the experiments performed to determine these properties one measures, for instance, the reflectivity, absorption, differential cross-section, from where the dielectric function and the energy-loss function can be deduced. These kinds of experiments involve external fields characterized by wavelengths that are long if compared to the interatomic distance (long-wavelength limit), and are carried out over a wide range of frequencies.

---

[a] For an exhaustive discussion of optical properties and plasma effects in solids see H. Ehrenreich, in *Proceeding of the International School of Physics "Enrico Fermi", Course XXXIV*, edited by J. Tauc (Academic Press, Inc., New York, 1966) p. 106.

From the theoretical point of view the most natural quantity to describe the elementary excitations of the system produced by photons and fast electrons is the macroscopic complex dielectric tensor $\tilde{\epsilon}(\mathbf{q},\omega)$, where $\mathbf{q}$ is the wavevector describing the propagation of the light or the momentum lost by the traversing electron, and ω is the frequency of the light or the energy lost. For isotropic systems there exist only two independent components of this tensor, the longitudinal and the transverse dielectric functions,

$$\tilde{\epsilon}_{ij}(\mathbf{q},\omega) = \tilde{\epsilon}_L(\mathbf{q},\omega)\frac{q_i q_j}{|\mathbf{q}|^2} + \tilde{\epsilon}_T(\mathbf{q},\omega)\left(\delta_{ij} - \frac{q_i q_j}{|\mathbf{q}|^2}\right). \tag{1.1}$$

The longitudinal component describes the response to longitudinal fields, which are involved in electron energy-loss experiments, where the scattering cross-section of an electron traversing a medium is proportional to $-Im\left\{\tilde{\epsilon}_L^{-1}(\mathbf{q},\omega)\right\}$. The transverse component describes the response to optical fields, which are characterized by small $q \approx \omega/c \approx 0$. In the long-wavelength limit $q \to 0$ the two quantities are equal [1, 2], thus optical and energy-loss measurements contain the same physical information.

The theoretical description of the propagation of electromagnetic fields in a solid is provided by the Maxwell equations (c.g.s. units),

$$\begin{aligned}
\nabla \times \mathbf{B} - \frac{1}{c}\frac{\partial \mathbf{E}}{\partial t} &= \frac{4\pi \mathbf{j}}{c}, && (1.2)\\
\nabla \times \mathbf{E} + \frac{1}{c}\frac{\partial \mathbf{B}}{\partial t} &= 0, && (1.3)\\
\nabla \cdot \mathbf{E} &= 4\pi\rho, && (1.4)\\
\nabla \cdot \mathbf{B} &= 0. && (1.5)
\end{aligned}$$

Here $\mathbf{E}$=$\mathbf{E}$($\mathbf{r}$,t) is the electric field and $\mathbf{B}$=$\mathbf{B}$($\mathbf{r}$,t) is the magnetic induction. In order to describe the influence of the solid on the electromagnetic field, one identifies three different kinds of sources of charge $\rho = \rho(\mathbf{r},t)$ and current $\mathbf{j} = \mathbf{j}(\mathbf{r},t)$ in the system,

$$\begin{aligned}
\rho &= \rho_{ext} + \rho_f + \rho_b,\\
\mathbf{j} &= \mathbf{j}_{ext} + \mathbf{j}_f + \mathbf{j}_b.
\end{aligned}$$

Here ρ_{ext} and $\mathbf{j}_{ext}$ are the free charge contributions describing particles brought from outside, ρ_f and $\mathbf{j}_f$ are contributions from those electrons belonging to the system, which are relatively free to move, whereas ρ_b and $\mathbf{j}_b$ are contributions from electrons that are tightly bound to the relatively immobile nuclei. We assume that both the free-charge and bound-charge contributions satisfy the continuity equation

$$\nabla \cdot \mathbf{j} + \frac{\partial \rho}{\partial t} = 0.$$

By using the above equation for the bound-charge contributions, one can define two vectors **P** and **M**, known as the polarization and the magnetization, respectively, such that

$$\rho_b = -\nabla \cdot \mathbf{P}, \tag{1.6}$$

$$\mathbf{j}_b = \frac{\partial \mathbf{P}}{\partial t} + \nabla \times \mathbf{M}. \tag{1.7}$$

Within the linear response regime the polarization and the magnetization are induced by the field, and one defines the electric and magnetic susceptibilities according to

$$\mathbf{P} = \chi_e \mathbf{E}, \tag{1.8}$$

$$\mathbf{M} = \frac{\chi_m}{1 + 4\pi\chi_m}\mathbf{B}, \tag{1.9}$$

for isotropic systems. In this regime the free current is proportional to the electric field *via* the conductivity tensor σ,

$$\mathbf{j}_f = \sigma \mathbf{E}. \tag{1.10}$$

The two Maxwell equations which contain the source terms **j** and ρ can now be rewitten as

$$\nabla \times \mathbf{H} - \frac{1}{c}\frac{\partial \mathbf{D}}{\partial t} = \frac{4\pi(\mathbf{j}_f + \mathbf{j}_{ext})}{c}, \tag{1.11}$$

$$\nabla \cdot \mathbf{D} = 4\pi(\rho_f + \rho_{ext}), \tag{1.12}$$

with

$$\mathbf{D} = (\mathbf{E} + 4\pi\mathbf{P}) = \epsilon\mathbf{E}, \tag{1.13}$$

$$\mathbf{H} = (\mathbf{B} - 4\pi\mathbf{M}) = \frac{1}{\mu}\mathbf{B}, \tag{1.14}$$

where the quantities ϵ and μ are, respectively, the permittivity and permeability of the medium,

$$\epsilon = 1 + 4\pi\chi_e$$

$$\mu = 1 + 4\pi\chi_m.$$

If we consider an isotropic medium in which the charge density is zero, and thus $\nabla \cdot \mathbf{E} = 0$, and $\mathbf{j} = \mathbf{j}_f$, then Eqs (1.2)-(1.4), (1.10), (1.11), and (1.13)-(1.14) yield a wave equation for the electric field **E**,

$$\nabla^2 \mathbf{E} = \frac{\epsilon}{c^2}\frac{\partial^2 \mathbf{E}}{\partial t^2} + \frac{4\pi\sigma}{c^2}\frac{\partial \mathbf{E}}{\partial t}, \tag{1.15}$$

where we have considered a non-magnetic material for which we can take $\mu = 1$. This equation has solutions of the following form,

$$\mathbf{E} = \mathbf{E}_0 \exp\{i(\tilde{\mathbf{K}} \cdot \mathbf{r} - \omega t)\}, \tag{1.16}$$

where ω is the frequency of the light and $\tilde{\mathbf{K}}$ is a complex valued propagation vector which satisfies the relation

$$\tilde{\mathbf{K}} \cdot \tilde{\mathbf{K}} = \frac{\epsilon\omega^2}{c^2} + \frac{4\pi i\sigma\omega}{c^2} = \tilde{\epsilon}(\omega)\frac{\omega^2}{c^2}. \tag{1.17}$$

Here we have introduced the complex dielectric function $\tilde{\epsilon}(\omega)$, given as

$$\tilde{\epsilon}(\omega) = \epsilon + \frac{i4\pi\sigma}{\omega} = \epsilon_1 + i\epsilon_2. \tag{1.18}$$

The real part of $\tilde{\mathbf{K}}$ can be identified as a wavevector, whereas the imaginary part accounts for the damping of the wave as it progresses inside the solid. The real part of the complex dielectric function measures the ability of a medium to polarize in response to an applied electric field, and thereby to cancel, partially, the field inside the material. The imaginary part is related to the rate at which energy is absorbed by the medium. Media with a negative real part are considered to be metals, in which no propagating electromagnetic waves exist. Those with a positive real part are dielectrics. In order to obtain the dielectric function from the experiments, it is convenient to introduce a complex refractive index $\widetilde{N}$, such as

$$\widetilde{\epsilon} = \widetilde{N}^2 = (n + ik)^2, \tag{1.19}$$

from where we have the two important relations

$$\epsilon_1 = n^2 - k^2, \tag{1.20}$$

$$\epsilon_2 = 2nk, \tag{1.21}$$

with ϵ_1, ϵ_2, n, and k all frequency-dependent. The quantities n and k are called the optical constants of the solid, with n the index of refraction and k the extinction coefficient. These quantities can be obtained from measurements of optical reflection measurements. Since we have two optical constants, one can measures the reflectivity at two different angles of incidence. Many measurements of optical properties of solids involve the normal incidence reflectivity R, which is related to the optical constants through the simple form

$$R = \left|\frac{1 - \widetilde{N}}{1 + \widetilde{N}}\right|^2 = \frac{(1 - n)^2 + k^2}{(1 + n)^2 + k^2}. \tag{1.22}$$

In this case we can still obtain the two optical constants provided that the reflectivity measurements are performed for all optical frequencies. This is because the two constants are related through Kramers-Kronig dispersion relation,

$$\epsilon_1(\omega) = 1 + \frac{2}{\pi}\mathcal{P}\int_0^{\infty} \omega'\epsilon_2(\omega')\frac{1}{\omega'^2 - \omega^2}d\omega'. \tag{1.23}$$

A given experiment, however, only yields values of the optical constants over a finite frequency range. This is typically handled by using some model extrapolation for the optical constants outside the measured frequency range. More accurate and more reproducible than the conventional reflection measurements are ellipsometry measurements. In this technique one obtains directly the complex dielectric function from the change in polarization of light upon reflection on the surface of a sample.

A practical tool to sketch simple pictures and rough estimates of properties of solids is the Drude model. This model assumes that the material contains immobile positive ions with relatively tightly bound electrons, known as core electrons, and an "electron gas" of classical, noninteracting valence electrons. These last carries wander freely through the solid and their motion is damped due to collisions with the ions, characterized by a relaxation time τ. Within this model the dielectric function can be expressed as

$$\epsilon(\omega) = \epsilon_{core} + \frac{4\pi i}{\omega}\frac{N\tau}{m^*(1 - i\omega\tau)}. \tag{1.24}$$

Here we have indicated with $\epsilon(\omega)$ the dielectric function $\widetilde{\epsilon}$ given in the previous expressions. In the following we will keep this notation. The second term on the right-hand side of Eq. (1.24) represents the free-carrier contribution, with τ the relaxation time associated with the scattering mechanism, m^* the effective mass of the electron, and N the total carrier density, while ϵ_{core} contains all the other possible contributions to the dielectric function. Two limiting cases of Eq. (1.24) are of interest: the low- and high-frequency response.

In the low-frequency regime ($\omega\tau \ll 1$) Eq. (1.24) becomes

$$\epsilon(\omega) \simeq \epsilon_{core} + \frac{4\pi i N\tau}{m^*\omega}. \tag{1.25}$$

Since the free-carrier contribution show now a ω^{-1}-dependence, it dominates in the low frequency limit. In this case the optical constants n and k are given as

$$n + ik \simeq \sqrt{\frac{4\pi N\tau}{m^*\omega}}\frac{(1 + i)}{\sqrt{2}}. \tag{1.26}$$

We see that in the low frequency limit $n \approx k$ and both are large. In this case the normal incidence reflectivity given in Eq. (1.22) becomes

$$R \simeq 1 - \frac{2}{n}. \tag{1.27}$$

The Drude theory shows that in the low-frequency limit a material with a large concentration of free carriers (for example a metal) is a perfect reflector.

In the high-frequency regime ($\omega\tau \gg 1$) Eq. (1.24) can be approximated as

$$\epsilon(\omega) \simeq \epsilon_{core} - \frac{4\pi N}{m^* \omega^2}. \tag{1.28}$$

As the frequency increases, the ω^{-2}-dependence of the free-carrier term makes this contribution less important and other processes will dominate. In the high-frequency regime the free-carrier contribution to the dielectric function can be neglected and the complex refraction index becomes real $\widetilde{N} \simeq \sqrt{\epsilon_{core}}$. This implies that $n > 0$ and $k = 0$, thus the material behaves like a dielectric.

The characteristic frequency at which a material changes from metallic to insulator behavior is called plasma frequency ω_p, which is defined as the frequency at which the real part of the dielectric function vanishes, $\epsilon_1(\omega_p) = 0$. The real and imaginary parts of the dielectric function, as given in Eq, (1.24), can be expressed as

$$\begin{aligned} \epsilon_1(\omega) &= \epsilon_{core} - \frac{4\pi N \tau^2}{m^*(1+\omega^2\tau^2)}, \qquad (1.29) \\ \epsilon_2(\omega) &= \frac{4\pi}{\omega} \frac{N\tau}{m^*(1+\omega^2\tau^2)}. \qquad (1.30) \end{aligned}$$

From Eq. (1.29) it becomes immediately clear that the plasma frequency has the following form,

$$\omega_p^2 = \frac{4\pi N}{m^* \epsilon_{core}} - \frac{1}{\tau^2} \simeq \frac{4\pi N}{m^* \epsilon_{core}}. \tag{1.31}$$

Here we have considered that the term $1/\tau^2$ on the right-hand side is usually small compared to the other one. The quantity ω_p described by Eq. (1.31) is known as the screened plasma frequency, since the screening of the free carries is taken into account through the core dielectric constant ϵ_{core} of the medium. One can also consider the unscreened plasma frequency by setting $\epsilon_{core} = 1$. The reflectivity is small at plasma frequency. Indeed, around this frequency, ϵ_1 is small and ϵ_2 is often small as well, as one can verify from the expression (1.30) for $\omega\tau \gg 1$. From Eqs (1.20) and (1.21) we have that at the plasma frequency $\epsilon_2(\omega_p) \simeq 2n^2$ (here we have considered $n \approx k$), thus if $\epsilon_2(\omega_p)$ is small also the optical constant n, and consequently the reflectivity

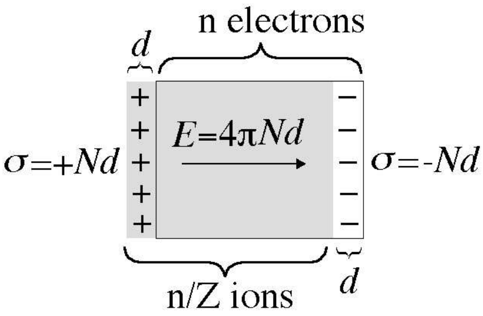

Figure 1.1: Simple model of a plasma oscillation. Here n and n/Z, with Z the atomic number, are the total numbers of electrons and of ions, respectively, in the system, and d is the displacement which is applied to the entire electron gas as a whole. The shaded region represents the electron gas system before the displacement.

R, tends to be small near ω_p. The longer the relaxation time the sharper the plasma feature in the reflectivity spectum.

The plasma frequency represents the frequency of a longitudinal collective mode of oscillation in an electron gas. The nature of this mode can be understood in term of a simple model. Imagine to rigidly displace the entire electron gas system through a distance d with respect to the fixed positive background of the ions, Fig. 1.1. This displacement establishes a surface charge $\sigma = -Nd$ on the left surface and a surface charge $\sigma = +Nd$ on the right one, with N the electron concentration. The resulting surface charge gives rise to an electric field inside the system with magnitude $E = 4\pi Nd$. This field tends to restore the electron gas system to its equilibrium position. Consequently a unit of volume $N = n/V$ (here n is the total number of electrons in the system and V is the total volume) of the electron gas will obey to the equation of motion

$$Nm\ddot{d} = -NE = -4\pi N^2 d,$$

which leads to oscillation at the plasma frequency ω_p. Many observations have been made of these plasma oscillations, afforded by the energy losses of fast electrons in penetrating thin metallic films. Perhaps the most notable is the observation of energy losses at frequencies that are multiples of ω_p, which can be understood if one assumes that the plasma oscillations in a metal can be represented by a finite set of harmonic oscillators with angular frequency ω_p. According to elementary quantum theory the energy of each oscillator must have one of the values given by the expression $(n+\frac{1}{2})\omega_p$, with n a positive integer. Pines has given the name plasmon to each quantum of plasma energy [3]. Of course, even in a free-electron metal the losses will not be in multiples of exactly ω_p, due to the dispersion of the frequency of oscillation, which is, however, slight.

1.2 Bloch functions and energy bands

In this thesis we will describe the optical properties of metallic systems within the density functional formalism. In the next two chapters we will give an overview of the fundamental theory and its further development in order to treat the linear response of extended systems to a general electromagnetic field. The essential feature of this approach is that one can describe the system by using a one-particle picture. Within this description, each electron in a solid, moving in a periodic potential $U(\mathbf{r}+\mathbf{R}) = U(\mathbf{r})$, for all Bravais lattice vectors $\mathbf{R}$, is described by a Bloch function

$$\psi_{n\mathbf{k}}(\mathbf{r}) = u_{n\mathbf{k}}(\mathbf{r}) \exp(i\mathbf{k}\cdot\mathbf{r}), \tag{1.32}$$

where $u_{n\mathbf{k}}(\mathbf{r})$ has the periodicity of the Bravais lattice. The index n appears in the Bloch function because for any $\mathbf{k}$ there are many solutions to the Schrödinger equation. This can be understood by considering that the eigenvalue problem is set in a finite volume, generally commensurate to the primitive cell, due to the use of periodic boundary conditions for the wavefunction. This leads to an infinite family of solutions with discretely spaced eigenvalues, which are labelled with the index n. These energy values are expected to vary continuously with $\mathbf{k}$. We then arrive at a description of the levels of an electron in a periodic potential in terms of a family of continuous functions $\epsilon_{n\mathbf{k}}$, each with the periodicity of the reciprocal lattice. The information contained in these functions is referred to as band structure of the solid. For each n the set of electronic levels specified by $\epsilon_{n\mathbf{k}}$ is called an energy band. The ground state of N Bloch electrons is constructed by filling all the one-electron levels with energies $\epsilon_{n\mathbf{k}} \leqslant \epsilon_F$, with ϵ_F being the Fermi level. This upper level is determined by requiring the total number of one-electron levels with $\epsilon_{n\mathbf{k}} \leqslant \epsilon_F$ to be equal to the total number of electrons. Different configurations can results by the filling of these energy levels. The valence electrons can exactly fill one or more bands, leaving others empty. If the energy difference between the top of the highest occupied band and the bottom of the lowest unoccupied band (band gap) is much bigger than k_BT (with k_B the Boltzmann constant and T near room temperature), then the crystal will have an insulating band structure. If, instead, the band gap is comparable to k_BT, the crystal will have an intrinsic semiconducting band structure. Since the number of levels for each energy band is equal to the number of primitive cells, a band gap can be expected only if the number of electrons per primitive cell is even. Even in this case, however, if the occupied and unoccupied bands overlap in energy along some directions in the Brillouin zone, then we have two partially occupied bands. In this case the crystal has a metallic band structure or, if the overlap is small with only few states involved, a semimetallic one. In the case in which each primitive cell contributes with odd numbers of electrons, the crystal has a metallic band structure. In Fig. 1.2 we have reported a schematic representation of these different configurations of the valence electrons in a solid.

Within this simple picture the elementary electronic excitations, which determine the behavior of the dielectric function, can be described, in the long-wavelength limit, by one-particle vertical transitions. There are two kinds of these transitions: interband and intraband transitions. Interband transitions occur between different (partially) occupied and unoccupied bands, and their contribution to the dielectric function can be identified as due to bound-charges. Intraband transitions occur within the same partially occupied bands, and their contribution to the dielectric function can be identified as due to free charges. This last kind of transitions is possible only in metallic band structures, which in addition to fully occupied and unoccupied bands, are characterized by partially occupied bands as well.

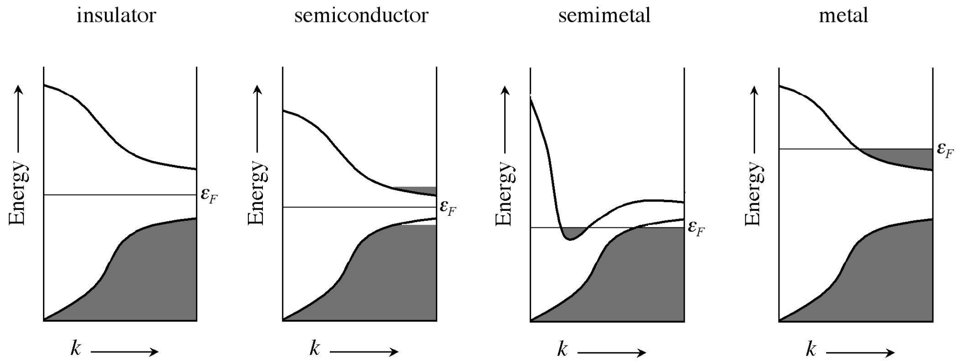

Figure 1.2: Schematic representation of the electron occupation of the energy bands around the Fermi level in an insulating band structure, a semiconducting band structure at a finite temperature with carries exited thermally, a semimetallic, and a metallic band structures.

1.3 Outline of the thesis

This thesis is the result of a research aimed to investigate, understand, and predict optical properties of extended systems by means of rigorous and efficient theoretical approaches. For these purposes we have used time-dependent current-density-functional theory. We have formulated the linear response of metals within this theory, we have included the treatment of relativistic effects by combining this formulation with the zeroth-order regular approximation, and we have derived a spin-dependent version of the method, which can allows a future treatment of magnetic response as well. This thesis is organized as follows.

In chapter 2 the key concepts in density functional theory, from the basic theorems of Hohenberg and Kohn to its extension to the time-dependent current-density-functional approach, are given.

In chapter 3 we show how the time-dependent current-density formulation for the linear response of nonmetallic systems by Kootstra *et al.* needs to be modified in order to treat metals as well. We applied our formulation to calculate the dielectric and electron energy-loss function of the noble metals copper and silver.

In chapter 4 we show how relativistic effects can be taken into account within our theoretical framework. First relativistic density functional theory based on the 4-component current as well as the Dirac-Kohn-Sham equations are described. Then we introduce the two-component zeroth-order regular approximation (ZORA) used to treat the dominant scalar and spin-orbit effects in static problems. Finally we give our derivation of the time-dependent ZORA equations.

In chapter 5 we extend our formulation of the linear response to treat the scalar relativistic effects within the ZORA formalism. We calculate the response of gold and we show that, although scalar relativistic effects shift the onset of the interband absorption from about 3.5 eV to 2.5 eV, thus justifying the yellow color of gold, spin-orbit effects are expected to be important in the intensity of the absorption.

In chapter 6 we successfully apply our method to calculate the dielectric functions and the electron energy-loss spectra (EELS) of the group VB and VIB bcc transition metals V, Nb, Ta, and Cr (in the paramagnetic phase), Mo, W, respectively.

In chapter 7 we include in our formulation the Vignale-Kohn current functional. Within this approximation the exchange-correlation kernel $f_{xc}(\mathbf{r}, \mathbf{r}', \omega)$ used in the response equations is ω-dependent, unlike within the adiabatic local density approximation used in the calculations of the previous chapters. Relaxation effects due to electron-electron scattering, which are in part responsible for the low-frequency Drude-like absorption in metals, can then be taken into account. We show that our results for the dielectric functions and EELS of the noble metals Cu, Ag, and Au are in an overall good agreement with the experiments and that the failures of ALDA are overcome.

In chapter 8 a spin-dependent version of the linear response formulation is presented. The method is successfully used to include the spin-orbit coupling within ZORA in the optical property calculations of the metals Au and W, the semiconductors ZnTe and CdTe, and the semimetal HgTe.

Chapter 2

DFT and its Progeny

To describe completely the quantum-mechanical behaviour of a stationary system of N interacting electrons it is necessary to calculate its many-electron wavefunction. In principle this may be obtained from the time-independent Schrödinger equation (in the relativistic case one has to solve the Dirac equation). However, since the motion of each electron is coupled to that of the other electrons in the system, in practice the equation is not solvable analytically and approximations are needed. This chapter is an introduction to the key concepts in the density functional formalism, from the fundamental Hohenberg-Kohn theorem for stationary systems, to its extension to treat time-dependent phenomena and transverse fields.

2.1 The main ideas behind DFT

The Schrödinger equation for a stationary system of N interacting electrons can be written, in the Born-Oppenheimer approximation, as

$$\hat{H}\Psi(\mathbf{r}_1\sigma_1, \mathbf{r}_2\sigma_2, ..., \mathbf{r}_N\sigma_N) = E\Psi(\mathbf{r}_1\sigma_1, \mathbf{r}_2\sigma_2, ..., \mathbf{r}_N\sigma_N). \tag{2.1}$$

Here E is the energy of the system, and $\Psi(\mathbf{r}_1\sigma_1, \mathbf{r}_2\sigma_2, ..., \mathbf{r}_N\sigma_N)$ is the electronic wavefunction, with $\mathbf{r}_i$ and σ_i the space and spin coordinates of the electron i. The Hamiltonian of the system is defined as

$$\hat{H} = -\frac{1}{2}\sum_i \nabla_i^2 + \frac{1}{2}\sum_{i\neq j}\frac{1}{|\mathbf{r}_i - \mathbf{r}_j|} + \sum_i v(\mathbf{r}_i). \tag{2.2}$$

We will use atomic units ($\hbar = m_e = e = 4\pi\epsilon_0 = 1$) throughout the thesis. The first term on the right-hand side of expression (2.2) is the kinetic energy operator $\hat{T}$, the second term represents the Coulomb electron-electron interaction energy operator $\hat{W}$, and the last term is the potential energy operator $\hat{V}$ of the electrons in the external potential $v(\mathbf{r})$. The Hamiltonian is parametrized by the external potential $v(\mathbf{r})$, thus the energies $E = \langle\Psi|\hat{H}_v|\Psi\rangle$ and the electronic wavefunctions Ψ, which satisfy the Schrödinger equation (2.1), can be considered functionals of this external potential. We will denote $\Psi = \Psi[v]$ and $E = E[v]$. We can now introduce the electron density $\rho(\mathbf{r})$ of the system through

$$\rho(\mathbf{r}) = \langle\Psi|\hat{\rho}(\mathbf{r})|\Psi\rangle = N\int |\Psi(\mathbf{r}\sigma_1, \mathbf{r}_2\sigma_2, ..., \mathbf{r}_N\sigma_N)|^2 d\mathbf{r}_2...d\mathbf{r}_N d\sigma_1...d\sigma_N, \tag{2.3}$$

in which the density operator $\hat{\rho}(\mathbf{r})$ is defined as

$$\hat{\rho}(\mathbf{r}) = \sum_i \delta(\mathbf{r} - \mathbf{r}_i). \tag{2.4}$$

Using this density operator, we can write the potential energy due to the external potential $\hat{V}$ as

$$V = \langle\Psi|\hat{V}|\Psi\rangle = \langle\Psi|\int \hat{\rho}(\mathbf{r})v(\mathbf{r})d\mathbf{r}|\Psi\rangle = \int \rho(\mathbf{r})v(\mathbf{r})d\mathbf{r}. \tag{2.5}$$

In the next section we will show that there is a one-to-one mapping between the external potential $v(\mathbf{r})$ and the ground-state density $\rho(\mathbf{r})$. These two quantities can now be considered to be conjugate variables in the meaning of a Legendre transform,

$$\begin{aligned} \frac{\delta E_0[v]}{\delta v(\mathbf{r})} &= \langle\frac{\delta\Psi_0[v]}{\delta v(\mathbf{r})}|\hat{H}_v|\Psi_0[v]\rangle + \langle\Psi_0[v]|\hat{H}_v|\frac{\delta\Psi_0[v]}{\delta v(\mathbf{r})}\rangle + \langle\Psi_0[v]|\frac{\delta\hat{H}_v}{\delta v(\mathbf{r})}|\Psi_0[v]\rangle \\ &= E_0[v]\frac{\delta}{\delta v(\mathbf{r})}\langle\Psi_0[v]|\Psi_0[v]\rangle + \langle\Psi_0[v]|\hat{\rho}(\mathbf{r})|\Psi_0[v]\rangle = \rho[v](\mathbf{r}), \end{aligned} \tag{2.6}$$

where we have used that the wavefunction $\Psi_0[v]$ is normalized and the ground-state eigenfunction of the Hamiltonian $\hat{H}_v$ with energy $E_0[v]$. We can use the density as basic variable by defining a Legendre transform

$$\mathcal{F}[\rho] = E_0[\rho] - \int \rho(\mathbf{r})v(\mathbf{r})d\mathbf{r} = \langle\Psi_0[v]|\hat{V} + \hat{W}|\Psi_0[v]\rangle, \tag{2.7}$$

where $v(\mathbf{r})$ must be regarded as a functional of $\rho(\mathbf{r})$. The uniqueness of this functional is garanteed by the one-to-one mapping between the external potential and the ground-state density. The functional $\mathcal{F}[\rho]$ is defined for so-called v-representable densities, i.e., ground-state densities for a Hamiltonian with external potential v [4]. By using the chain rule of differentiation and the result in Eq. (2.6), it immediately follows that

$$\frac{\delta\mathcal{F}[\rho]}{\delta\rho(\mathbf{r})} = \int \frac{\delta E_0[\rho]}{\delta v(\mathbf{r}')}\frac{\delta v(\mathbf{r}')}{\delta\rho(\mathbf{r})}d\mathbf{r}' - \int \rho(\mathbf{r}')\frac{\delta v(\mathbf{r}')}{\delta\rho(\mathbf{r})}d\mathbf{r}' - v(\mathbf{r}) = -v(\mathbf{r}). \tag{2.8}$$

2.1.1 The Hohenberg-Kohn theorems

The main objective of density functional theory [a] is to replace the many-body electronic wavefunction with the electronic ground-state density as basic quantity [5]. Whereas the many-body wavefunction is dependent on $3N$ spatial variables and N spin variables, the density is a function of only three variables and is a simpler quantity to deal with both conceptually and practically. Besides this, a deeper reason for a density functional formulation is given by Eq. (2.6). The method is in principle exact and is firmly based on two theorems derived and proved by Hohenberg and Kohn in 1964 [6]. The first theorem shows that the density ρ of a nondegenerate ground state uniquely determines the external potential $v(\mathbf{r})$ (up to an arbitrary constant) to which the many-electron system is subjected. Consequently the density determines the electronic wavefunction of the system and thus all the electronic properties of the ground state. The proof of the theorem is rather simple. First we notice that the external potential $v(\mathbf{r})$ defines a mapping $v \rightarrow \rho$, where $\rho(\mathbf{r})$ is the corresponding nondegenerate ground-state density from the Schrödinger equation. The inverse mapping $\rho \rightarrow v$ can be proved by *reductio ad absurdum.* First we show that if two potentials $v(\mathbf{r})$ and $v'(\mathbf{r})$ differ by more than a constant they will not lead to the same wavefunction Ψ. From the Schrödinger equation (2.1) we have for the two potentials,

$$\begin{aligned} \left(\hat{T}+\hat{V}+\hat{W}\right)|\Psi_0\rangle &= E_0|\Psi_0\rangle, & (2.9)\\ \left(\hat{T}+\hat{V}'+\hat{W}\right)|\Psi_0'\rangle &= E_0'|\Psi_0'\rangle. & (2.10)\end{aligned}$$

If Ψ_0 and Ψ_0' were to be the same, then by subtracting (2.10) from (2.9) one would get

$$\left(\hat{V}-\hat{V}'\right)|\Psi_0\rangle = \left(E_0-E_0'\right)|\Psi_0\rangle, \tag{2.11}$$

where $\hat{V}$ and $\hat{V}'$ appear to differ only by a constant if Ψ_0 does not vanish. However, for "reasonably well behaved" potentials, i.e., potentials which do not exhibit infinite barriers, etc., Ψ_0 cannot vanish on a set with nonzero measure by the unique continuation theorem [7]. So we obtain a contradiction with our initial assumption, and hence we can conclude that $\Psi_0 \neq \Psi_0'$. We can now prove that two potentials $v(\mathbf{r})$ and $v'(\mathbf{r})$ with corresponding Hamiltonians $\hat{H}$ and $\hat{H}'$ and nondegenerate ground-state wavefunctions Ψ_0 and Ψ_0' yield two different densities $\rho(\mathbf{r})$ and $\rho'(\mathbf{r})$. By using the

---

[a] Books on this topic are: R. G. Parr and W. Yang, *Density Functional Theory of Atoms and Molecules* (Oxford University Press, New York, 1989); R. M. Dreizler and E. K. U. Gross, *Density functional Theory: An Approach to the Quantum Many Body Problem* (Springer-Verlag, Berlin, 1990).

variational principle we have that

$$E_0 = \langle \Psi_0 | \hat{H} | \Psi_0 \rangle < \langle \Psi_0' | \hat{H} | \Psi_0' \rangle = \langle \Psi_0' | \hat{H}' + \hat{V} - \hat{V}' | \Psi_0' \rangle, \tag{2.12}$$

so that

$$E_0 < E_0' + \int \rho'(\mathbf{r})[v(\mathbf{r}) - v'(\mathbf{r})] d\mathbf{r}. \tag{2.13}$$

Similarly, interchanging primed and unprimed quantities, one finds

$$E_0' < E_0 + \int \rho(\mathbf{r})[v'(\mathbf{r}) - v(\mathbf{r})] d\mathbf{r}. \tag{2.14}$$

If $\rho(\mathbf{r})$ and $\rho'(\mathbf{r})$ were to be the same, the addition of (2.13) and (2.14) would lead to the inconsistency

$$E_0 + E_0' < E_0 + E_0', \tag{2.15}$$

and consequently we conclude that there cannot exist two different external potentials $v(\mathbf{r})$ and $v'(\mathbf{r})$ corresponding to the same density $\rho(\mathbf{r})$. This defines our mapping $\rho \rightarrow v$, and thus the one-to-one mapping $v \leftrightarrow \rho$ is constructed. We can then conclude that the mapping between v, Ψ_0, and ρ is one-to-one. The immediate result is that the total energy of a (Coulomb) many-electron system in an external static potential can be expressed in terms of the potential energy due to this external potential and of an energy functional $\mathcal{F}[\rho]$ of the ground-state density,

$$E_0[\rho] = \langle \Psi_0[\rho] | \hat{H} | \Psi_0[\rho] \rangle = \int \rho(\mathbf{r}) v(\mathbf{r}) d\mathbf{r} + \mathcal{F}[\rho], \tag{2.16}$$

with $\mathcal{F}[\rho]$ defined in Eq. (2.7). Note that this functional is defined independently of the external potential $v(\mathbf{r})$, and thus it is a universal functional of the density. This means that, if the explicit form is known, it can be used for any system. The second Hohenberg-Kohn theorem states that the exact ground-state density of a system in a particular external potential $v(\mathbf{r})$ minimizes the energy functional

$$E_0 = \min_{\rho} \left\{ \mathcal{F}[\rho] + \int \rho(\mathbf{r}) v(\mathbf{r}) d\mathbf{r} \right\}, \tag{2.17}$$

where E_0 is the ground-state energy for the system in an external potential $v(\mathbf{r})$. The proof uses the variational principle. The previous theorem assures that a trial density $\tilde{\rho}(\mathbf{r})$, such that $\tilde{\rho}(\mathbf{r}) \geqslant 0$ and $\int \tilde{\rho}(\mathbf{r}) d\mathbf{r} = N$, with N a number of electrons, determines its own potential $\tilde{v}(\mathbf{r})$, Hamiltonian $\hat{H}$, and wavefunction $\tilde{\Psi}$. This wavefunction can be taken as trial function for the problem of interest having external potential $v(\mathbf{r})$. The variational principle asserts that

$$\langle\tilde{\Psi}|\hat{H}|\tilde{\Psi}\rangle = \mathcal{F}[\tilde{\rho}] + \int \tilde{\rho}(\mathbf{r})v(\mathbf{r})d\mathbf{r} \geqslant \mathcal{F}[\rho] + \int \rho(\mathbf{r})v(\mathbf{r})d\mathbf{r}, \tag{2.18}$$

which proves the second Hohenberg-Kohn theorem. Assuming differentiability of $\{\mathcal{F}[\rho] + \int \rho(\mathbf{r})v(\mathbf{r})d\mathbf{r}\}$, this theorem requires that the ground-state density satisfies the Euler-Lagrange equations

$$0 = \frac{\delta}{\delta\rho(\mathbf{r})}\left\{\mathcal{F}[\rho] + \int \rho(\mathbf{r})v(\mathbf{r})d\mathbf{r} - \mu\left(\int \rho(\mathbf{r})d\mathbf{r} - N\right)\right\}, \tag{2.19}$$

where we have introduced the Lagrange multiplier μ to satisfy the constraint that the density integrates to the correct number of electrons. Although exact, this method requires in fact approximations to the universal functional, for which no explicit expressions in terms of the density are known.

2.1.2 The Kohn-Sham equations

A practical scheme to approximate the energy functional has been proposed by Kohn and Sham who re-introduced the orbitals in the density functional framework [8]. They introduced an auxiliary noninteracting electron system in an effective external potential $v_s(\mathbf{r})$, which reproduces the same ground-state density as in the corresponding interacting system. If $v_s(\mathbf{r})$ exists, then the first Hohenberg-Kohn theorem ensures its uniqueness. In other words the interacting density is assumed to be noninteracting-v-representable. Like for the interacting system, we can define the energy functional $E_s[v_s]$ and its Legendre transform $\mathcal{F}_s[\rho]$ along the same lines described above by putting $\hat{W}$ to zero. We obtain

$$\begin{aligned} E_s[v_s] &= \langle\Psi_s[v_s]|\hat{T} + \hat{V}_s|\Psi_s[v_s]\rangle, &(2.20)\\ \mathcal{F}_s[\rho] &= E_s[v_s] - \int \rho(\mathbf{r})v_s(\mathbf{r})d\mathbf{r} = \langle\Psi_s[v_s]|\hat{T}|\Psi_s[v_s]\rangle, &(2.21)\end{aligned}$$

with the derivatives

$$\begin{aligned} \frac{\delta E_s[v_s]}{\delta v_s(\mathbf{r})} &= \rho(\mathbf{r}), &(2.22)\\ \frac{\delta F_s[\rho]}{\delta\rho(\mathbf{r})} &= -v_s(\mathbf{r}). &(2.23)\end{aligned}$$

We can now introduce the exchange-correlation energy functional $E_{xc}[\rho]$, which relates the functionals $\mathcal{F}[\rho]$ and $\mathcal{F}_s[\rho]$ of the interacting and the corresponding noninteracting systems in the following way,

$$\mathcal{F}[\rho] = \mathcal{F}_s[\rho] + \frac{1}{2}\int \frac{\rho(\mathbf{r})\rho(\mathbf{r}')}{|\mathbf{r}-\mathbf{r}'|} d\mathbf{r} d\mathbf{r}' + E_{xc}[\rho], \tag{2.24}$$

where the second term on the right-hand side represents the classical Hartree electron-electron interaction energy. By differentiating this expression with respect to the density $\rho(\mathbf{r})$, the following relation between the external potential and the effective Kohn-Sham potential can be obtained,

$$v_s(\mathbf{r}) = v(\mathbf{r}) + \int \frac{\rho(\mathbf{r}')}{|\mathbf{r}-\mathbf{r}'|} d\mathbf{r}' + v_{xc}(\mathbf{r}), \tag{2.25}$$

where

$$v_{xc}(\mathbf{r}) = \frac{\delta E_{xc}[\rho]}{\delta\rho(\mathbf{r})}. \tag{2.26}$$

Since the state $\Psi_s[v_s]$ is the ground state for a system of noninteracting particles, it can be written as a single Slater determinant of one-electron orbitals ψ_i,

$$\Psi_s(\mathbf{r}_1\sigma_1, \mathbf{r}_2\sigma_2, ..., \mathbf{r}_N\sigma_N) = \frac{1}{\sqrt{N!}} \begin{pmatrix} \psi_1(\mathbf{r}_1\sigma_1) & \cdots & \psi_N(\mathbf{r}_1\sigma_1) \\ \vdots & \ddots & \vdots \\ \psi_1(\mathbf{r}_N\sigma_N) & \cdots & \psi_N(\mathbf{r}_N\sigma_N), \end{pmatrix}, \tag{2.27}$$

where ψ_i satisfy the self-consistent Kohn-Sham equations

$$\left(-\frac{\nabla^2}{2} + v(\mathbf{r}) + \int \frac{\rho(\mathbf{r}')}{|\mathbf{r}-\mathbf{r}'|} d\mathbf{r}' + v_{xc}(\mathbf{r})\right)\psi_i(\mathbf{r}) = \epsilon_i\psi_i(\mathbf{r}), \tag{2.28}$$

in which the ground-state density is to be obtained by occupying the N one-electron orbitals that are lowest in energy,

$$\rho(\mathbf{r}) = \sum_{i=1}^{N} |\psi_i(\mathbf{r})|^2. \tag{2.29}$$

Within the Kohn-Sham scheme one has to approximate, instead of $\mathcal{F}[\rho]$, only a small part of it, $E_{xc}[\rho]$ (and $v_{xc}[\rho]$), which contains all the many-body effects. A huge effort is put into finding approximations for the xc energy and potential that can describe with increasing accuracy the physical and chemical properties of an electronic system. The existing approximations are for example based on the uniform electron gas model (local density approximation) [8] or on the slowly varying electron gas expansion (generalized gradient approximations) [9–12]. Despite their simplicity, these approximations work very well for many properties and systems, although some problematic cases exist, which require more advanced approximations.

2.2 Time-dependent DFT

The many-electron wavefunction of a nonrelativistic many-electron system in a time-dependent external potential $v(\mathbf{r}, t)$ must satisfy the time-dependent Schrödinger equation,

$$\hat{H}(t)\Psi(\mathbf{r}_1\sigma_1, \mathbf{r}_2\sigma_2, ..., \mathbf{r}_N\sigma_N, t) = i\frac{\partial}{\partial t}\Psi(\mathbf{r}_1\sigma_1, \mathbf{r}_2\sigma_2, ..., \mathbf{r}_N\sigma_N, t), \tag{2.30}$$

where the time-dependent Hamiltonian takes the form

$$\hat{H}(t) = -\frac{1}{2}\sum_i \nabla_i^2 + \frac{1}{2}\sum_{i \neq j}\frac{1}{|\mathbf{r}_i - \mathbf{r}_j|} + \sum_i v(\mathbf{r}_i, t). \tag{2.31}$$

Analogously to the stationary case, we have the kinetic energy operator $\hat{T}$, the Coulombic electron-electron interaction energy operator $\hat{W}$, and the potential energy operator $\hat{V}(t)$ of the electrons in the time-dependent potential $v(\mathbf{r}, t)$. In 1984 Runge and Gross [13] derived the analog of the Hohenberg-Kohn theorem for time-dependent systems by establishing a one-to-one mapping between time-dependent densities and time-dependent potentials for a given initial state.

2.2.1 The Runge-Gross proof

The theorem states that the densities $\rho(\mathbf{r}, t)$ and $\rho'(\mathbf{r}, t)$, evolving from the same initial state $\Psi_0 = \Psi(t = t_0)$ under the influence of the two potentials $v(\mathbf{r}, t)$ and $v'(\mathbf{r}, t)$ (both expandable in Taylor series around the initial time $t = t_0$), are always different provided that the two potentials differ by more than a pure function of time,

$$v(\mathbf{r}, t) - v'(\mathbf{r}, t) \neq c(t). \tag{2.32}$$

In this case there is a one-to-one mapping between densities and potentials, and one can construct a time-dependent version of density functional theory. We give the essential steps of the demonstration of the theorem, by closely following Ref. [13]. We will consider the time-dependent density and current-density as

$$\begin{aligned}
\rho(\mathbf{r}, t) &= \langle\Psi(t)|\hat{\rho}(\mathbf{r})|\Psi(t)\rangle, && (2.33)\\
\mathbf{j}(\mathbf{r}, t) &= \langle\Psi(t)|\hat{\mathbf{j}}(\mathbf{r})|\Psi(t)\rangle, && (2.34)
\end{aligned}$$

in which the density operator $\hat{\rho}(\mathbf{r})$ has been given in (2.4) and the current-density operator $\hat{\mathbf{j}}(\mathbf{r})$ is defined as

$$\hat{\mathbf{j}}(\mathbf{r}) = \frac{1}{2}\sum_i^N \left\{-i\nabla, \delta(\mathbf{r} - \mathbf{r}_i)\right\}, \tag{2.35}$$

where $\{\hat{A}, \hat{B}\} = (\hat{A}\hat{B} + \hat{B}\hat{A})$ denotes the anticommutator of two operators $\hat{A}$ and $\hat{B}$. We first show that the current-densities $\mathbf{j}(\mathbf{r}, t)$ and $\mathbf{j}'(\mathbf{r}, t)$ corresponding to the two different external potentials $v(\mathbf{r}, t)$ and $v'(\mathbf{r}, t)$ must differ for $t > t_0$. To prove this we use the condition that the potentials $v(\mathbf{r}, t)$ and $v'(\mathbf{r}, t)$ can be expanded in Taylor series around t_0,

$$v(\mathbf{r}, t) = \sum_{k=0}^{\infty} \frac{1}{k!} v_k(\mathbf{r})(t - t_0)^k, \tag{2.36}$$

with a similar expression for $v'(\mathbf{r}, t)$ with coefficients $v'_k(\mathbf{r})$. Eq. (2.32) implies that there is a minimum value $k \geqslant 0$ such that

$$w_k(\mathbf{r}) = v_k(\mathbf{r}) - v'_k(\mathbf{r}) = \left.\frac{\partial^k}{\partial t^k}\left(v(\mathbf{r}, t) - v'(\mathbf{r}, t)\right)\right|_{t=t_0} \neq \mathit{constant}. \tag{2.37}$$

If now we use the quantum mechanical equation of motion for a Schrödinger operator $\hat{A}(t)$,

$$\frac{d}{dt}\langle\Psi(t)|\hat{A}(t)|\Psi(t)\rangle = \langle\Psi(t)|\frac{\partial}{\partial t}\hat{A}(t) - i[\hat{A}(t), \hat{H}(t)]|\Psi(t)\rangle, \tag{2.38}$$

for the two current-densities we obtain

$$\begin{aligned} \left.\frac{\partial}{\partial t}\left(\mathbf{j}(\mathbf{r}, t) - \mathbf{j}'(\mathbf{r}, t)\right)\right|_{t=t_0} &= -i\langle\Psi_0|[\hat{\mathbf{j}}, \hat{H}(t_0) - \hat{H}'(t_0)]|\Psi_0\rangle \\ &= -\rho_0(\mathbf{r})\nabla\left(v_{ext}(\mathbf{r}, t_0) - v'_{ext}(\mathbf{r}, t_0)\right), \end{aligned} \tag{2.39}$$

where we have considered that the two Hamiltonians $\hat{H}(t)$ and $\hat{H}'(t)$ differ only in their external potentials. Here $\rho_0(\mathbf{r}) = \rho(\mathbf{r}, t_0)$ is the initial density. One can repeatedly use the equation of motion such to arrive at [13]

$$\left.\frac{\partial^{k+1}}{\partial t^{k+1}}\left(\mathbf{j}(\mathbf{r}, t) - \mathbf{j}'(\mathbf{r}, t)\right)\right|_{t=t_0} = -\rho_0(\mathbf{r})\nabla w_k(\mathbf{r}) \neq 0. \tag{2.40}$$

We can conclude that the two current-densities will differ infinitesimally later than t_0, which proves the first part of the theorem. In the second part we extend the proof to the densities. We make use of the continuity equation,

$$\frac{\partial}{\partial t}\rho(\mathbf{r}, t) = -\nabla \cdot \mathbf{j}(\mathbf{r}, t), \tag{2.41}$$

which, after differentiating $k + 1$ times, gives for the density difference at t_0

$$\left.\frac{\partial^{k+2}}{\partial t^{k+2}}\left(\rho(\mathbf{r}, t) - \rho'(\mathbf{r}, t)\right)\right|_{t=t_0} = \nabla \cdot \left(\rho_0(\mathbf{r})\nabla w_k(\mathbf{r})\right). \tag{2.42}$$

The right-hand side of this expression can not vanish for the following arguments. We note that

$$\begin{aligned}\int \rho_0(\mathbf{r})|\nabla w_k(\mathbf{r})|^2 d\mathbf{r} &= \oint \rho_0(\mathbf{r}) w_k(\mathbf{r}) \nabla w_k(\mathbf{r}) d\mathbf{s} \\ &- \int w_k(\mathbf{r}) \nabla \cdot (\rho_0(\mathbf{r}) \nabla w_k(\mathbf{r})) d\mathbf{r}, \end{aligned} \tag{2.43}$$

where we have applied Gauss' theorem. For finite systems the surface integral will vanish, since any realistic potential (i.e., potentials due to normalizable external charge densities) falls off at least as fast as $1/r$ at $r = \infty$, while the density will decay exponentially. Thus $\nabla \cdot (\rho_0(\mathbf{r}) \nabla w_k(\mathbf{r}))$ can not vanish everywhere otherwise the left-hand side of Eq. (2.43) would be zero. This in turn would imply that $|\nabla w_k(\mathbf{r})|^2 = 0$, which is in contradiction to the assumption that $w_k(\mathbf{r})$ is not a constant. This completes the proof of the theorem for finite systems. An important observation is that the density difference in Eq. (2.42) is linear in the $w_k(\mathbf{r})$, and thus it does not vanish already at first order in $v(\mathbf{r}, t) - v'(\mathbf{r}, t)$. In particular this implies that the linear density response function is invertible for switch-on processes.

2.2.2 The time-dependent Kohn-Sham equations

One can prove that the time-dependent density $\rho(\mathbf{r}, t)$ obtained from a many-particle system with Hamiltonian $\hat{H}(t)$ and initial state Ψ_0 can be reproduced exactly in a different system evolving from a different initial state Ψ'_0 of finite momentum, under a different Hamiltonian $\hat{H}'(t)$, with different two-particle interaction and external potential, provided that the initial density and initial first derivative of the density are the same in both systems. The external potential of the second system is then uniquely determined up to a pure function of time. This theorem solves the noninteracting v-representability problem for the time-dependent case, provided we can find the appropriate initial state, although it is still unknown whether this initial state can be chosen to be the ground state for the noninteracting system [14]. It follows that, as in the stationary case, one can introduce an auxiliary system of noninteracting electrons which satisfies the time-dependent Kohn-Sham equations

$$i \frac{\partial}{\partial t} \psi_i(\mathbf{r}, t) = \left(-\frac{\nabla^2}{2} + v_s(\mathbf{r}, t) \right) \psi_i(\mathbf{r}, t), \tag{2.44}$$

and with density

$$\rho(\mathbf{r}, t) = \sum_{i=1}^{N} |\psi_i(\mathbf{r}, t)|^2, \tag{2.45}$$

which is exactly that of the interacting system. The effective potential $v_s(\mathbf{r},t)$ is uniquely determined up to a purely time-dependent function, and it can be decomposed in external, Hartree, and exchange-correlation contributions,

$$v_s(\mathbf{r},t) = v(\mathbf{r},t) + \int \frac{\rho(\mathbf{r}',t)}{|\mathbf{r}-\mathbf{r}'|} d\mathbf{r}' + v_{xc}(\mathbf{r},t). \tag{2.46}$$

The time-dependent exchange-correlation potential $v_{xc}(\mathbf{r},t)$ is not obtained as functional derivative of any action functional, but is implicitly defined by this relation. Indeed, attempts to base time-dependent density functional theory on the stationary action have led to paradoxes [15]. However, approximations for the exchange-correlation potentials can still be constructed based on exact constraints that the exchange-correlation potential has to satisfy [16]. In particular, the zero-force and zero-torque theorem, which states that the exchange-correlation potential cannot exert any net force or torque on the system, and the generalized translational invariance, which requires that a rigid translation of the current-density implies a rigid translation of the exchange-correlation potentials. Recently van Leeuwen has shown that the problems related to the formulation of TDDFT based on the action functional can be solved by using the Keldysh action functional [15]. This new kind of action functional is defined on the Keldysh contour [17], in which the physical time is parametrized by an underlying parameter τ, called pseudotime. In this case the Kohn-Sham potential can be obtained as functional derivative of the Keldysh action functional.

2.3 Time-dependent current-DFT

In the previous section we have shown that the second part of the Runge-Gross proof is valid under the conditions of a positive density $\rho_0(\mathbf{r})$ and time-dependent potentials vanishing at the boundary. The proof becomes questionable for extended system in external longitudinal electric fields. In this case the ground-state density remains finite everywhere, and we can choose two electric fields $\mathbf{E}[v](\mathbf{r},t) = \nabla v(\mathbf{r},t)$ and $\mathbf{E}'[v'](\mathbf{r},t) = \nabla v'(\mathbf{r},t)$ so that

$$\mathbf{E}[v](\mathbf{r},t) - \mathbf{E}'[v'](\mathbf{r},t) = \frac{\mathbf{c}(t)}{\rho_0(\mathbf{r})}, \tag{2.47}$$

with $\mathbf{c}(t)$ an arbitrary function of time, expandable in Taylor series around $t = t_0$. This immediately follows from Eq. (2.40) in the proof of the Runge-Gross theorem. Although the potentials themselves are not finite, this kind of fields are finite everywhere, hence physically acceptable. They will lead to nonvanishing uniform current-densities, but to constant densities, since these currents are divergence free. The first part of the Runge-Gross theorem still holds in this case, whereas the second part is not needed if one formulates a density functional theory in terms of the current-density as fundamental variable. In order to treat also magnetic fields in the time-dependent density functional framework, Ghosh and Dhara were the first to reformulate the theory in terms of the current-density [18,19]. Following the same line of the Runge-Gross proof, Ghosh and Dhara showed that the single-particle current-density uniquely determines, up to an arbitrary gauge transformation, the time-dependent scalar and vector potentials of the system, and hence the many-electron wavefunction. Recently Vignale has given an alternative formulation of the TDCDFT [20], which closely follow that one given by van Leeuwen for the TDDFT [14], and which is easier and more complete than the Ghosh-Dhara one. We give here the statement of the theorem and the essential steps of its proof, by closely following Ref. [20].

2.3.1 Mapping from current-densities to vector potentials

We consider an interacting many-particle system moving in a scalar and vector potentials $v(\mathbf{r},t)$ and $\mathbf{A}(\mathbf{r},t)$, which are analytic functions of time around t_0. The motion of the system is governed by the following Hamiltonian $\hat{H(t)}$,

$$\hat{H(t)} = \sum_i \left\{ \frac{1}{2}[-i\nabla_i + \frac{1}{c}\mathbf{A}(\mathbf{r}_i,t)]^2 + v(\mathbf{r}_i,t) \right\} + \sum_{i<j} U(\mathbf{r}_i - \mathbf{r}_j), \tag{2.48}$$

where $U(\mathbf{r}_i - \mathbf{r}_j)$ is a two-particle interaction. The density operator takes the same form as in Eq. (2.4) for the ordinary TDDFT, whereas the current-density operator is given in term of the velocity operator $\hat{v_i} = (-i\nabla_i + \mathbf{A}(\mathbf{r}_i,t)/c)$ as

$$\hat{\mathbf{j}}(\mathbf{r},t) = \frac{1}{2}\sum_i \{\hat{v_i}(t), \delta(\mathbf{r}-\mathbf{r}_i)\}. \tag{2.49}$$

If $\rho(\mathbf{r},t)$ and $\mathbf{j}(\mathbf{r},t)$ are the time-dependent density and current-density, respectively, of the system, then one can prove that the same density and current-density can be reproduced by another many-particle system evolving under a different Hamiltonian $\hat{H}'(t)$,

$$\hat{H}'(t) = \sum_i \left\{ \frac{1}{2}[-i\nabla_i + \frac{1}{c}\mathbf{A}'(\mathbf{r}_i,t)]^2 + v'(\mathbf{r}_i,t) \right\} + \sum_{i<j} U'(\mathbf{r}_i - \mathbf{r}_j), \tag{2.50}$$

from a different initial state Ψ_0' which produces the same density and current-density as Ψ_0 at $t = t_0$ in the unprimed system. The potentials $v'(\mathbf{r},t)$ and $\mathbf{A}'(\mathbf{r},t)$ are uniquely determined by $v(\mathbf{r},t)$, $\mathbf{A}(\mathbf{r},t)$, Ψ_0, and Ψ_0' up to gauge transformations of the form

$$\begin{aligned} v'(\mathbf{r},t) &\rightarrow v'(\mathbf{r},t)+\frac{\partial\Lambda(\mathbf{r},t)}{\partial t}, \\ \mathbf{A}'(\mathbf{r},t) &\rightarrow \mathbf{A}'(\mathbf{r},t)+\nabla\Lambda(\mathbf{r},t), \end{aligned} \tag{2.51}$$

with $\Lambda(\mathbf{r},t)$ a regular function of $\mathbf{r}$ and t. One can always make a gauge transformation of the form (2.51) to eliminate the scalar potential at all times. To obtain this, we choose $\Lambda(\mathbf{r},t)$ such that the scalar potential is always zero in both primed and unprimed systems, i.e., $\partial\Lambda(\mathbf{r},t)/\partial t = -v(\mathbf{r},t)$ at all times, with the initial condition $\Lambda(\mathbf{r},t_0)=0$. The current-density obeys the equation of motion

$$\begin{aligned} \frac{d\mathbf{j}(\mathbf{r},t)}{dt} &= \frac{\partial\mathbf{j}(\mathbf{r},t)}{\partial t}+i\langle[\hat{H(t)},\hat{\mathbf{j}}(\mathbf{r},t)]\rangle=\rho(\mathbf{r},t)\frac{1}{c}\frac{\partial\mathbf{A}(\mathbf{r},t)}{\partial t} \\ &- \frac{1}{c}\mathbf{j}(\mathbf{r},t)\times[\nabla\times\mathbf{A}(\mathbf{r},t)]+\mathbf{F}(\mathbf{r},t)+\nabla\cdot\sigma(\mathbf{r},t), \end{aligned} \tag{2.52}$$

with $1/c\,\partial\mathbf{A}(\mathbf{r},t)/\partial t$ and $\nabla\times\mathbf{A}(\mathbf{r},t)$ the external electric and magnetic fields, respectively. The quantities $\mathbf{F}(\mathbf{r},t)$ and $\sigma(\mathbf{r},t)$ represent the internal force density and the stress tensor, respectively, and are defined as

$$\mathbf{F}(\mathbf{r},t)=-\left\langle\sum_i\delta(\mathbf{r}-\mathbf{r}_i)\sum_{j\neq i}\nabla_{\mathbf{r}_i}U(\mathbf{r}_i-\mathbf{r}_j)\right\rangle, \tag{2.53}$$

$$\sigma_{\alpha\beta}(\mathbf{r},t)=-\left\langle\frac{1}{4}\sum_i\{\hat{v}_\alpha,\{\hat{v}_\beta,\delta(\mathbf{r}-\mathbf{r}_i)\}\}\right\rangle. \tag{2.54}$$

The brackets $\langle ... \rangle$ represent the expectation value in the unprimed system at time t. An expression analogue to Eq. (2.52) can be written also for the primed system: the external electric and magnetic fields, the internal force, and the stress tensor become now primed. By assumption $\rho(\mathbf{r},t)=\rho'(\mathbf{r},t)$ and $\mathbf{j}(\mathbf{r},t)=\mathbf{j}'(\mathbf{r},t)$, thus taking the difference of the two equations we arrive at

$$\rho(\mathbf{r},t)\frac{1}{c}\frac{\partial\Delta\mathbf{A}(\mathbf{r},t)}{\partial t}=\frac{1}{c}\mathbf{j}(\mathbf{r},t)\times[\nabla\times\Delta\mathbf{A}(\mathbf{r},t)]+\mathbf{Q}(\mathbf{r},t)-\mathbf{Q}'(\mathbf{r},t), \tag{2.55}$$

where $\Delta\mathbf{A}(\mathbf{r},t)\equiv\mathbf{A}'(\mathbf{r},t)-\mathbf{A}(\mathbf{r},t)$ and

$$\mathbf{Q}(\mathbf{r},t)\equiv\mathbf{F}(\mathbf{r},t)+\nabla\cdot\sigma(\mathbf{r},t). \tag{2.56}$$

$\mathbf{Q}'(\mathbf{r},t)$ is the analogue of $\mathbf{Q}(\mathbf{r},t)$ in the primed system. If solved, this equation can give the vector potential $\mathbf{A}'(\mathbf{r},t)$ which produces the same current-density as the vector potential $\mathbf{A}(\mathbf{r},t)$ in the unprimed system. However, since $\mathbf{A}'(\mathbf{r},t)$ enters the equation also implicitly through $\mathbf{Q}'(\mathbf{r},t)$, it is not immediate to verify the existence and uniqueness of the solution of this equation. To overcome this difficulty one can follow an alternative approach. By hypothesis both $\mathbf{A}(\mathbf{r},t)$ and $\mathbf{A}'(\mathbf{r},t)$ are expandable in Taylor series around $t = t_0$, and the Taylor series of their difference is given by

$$\Delta\mathbf{A}(\mathbf{r},t) = \sum_{k=0}^{\infty} \Delta\mathbf{A}_k(\mathbf{r})(t-t_0)^k, \tag{2.57}$$

with

$$\Delta\mathbf{A}_k(\mathbf{r}) \equiv \frac{1}{k!}\left.\frac{\partial^k \Delta\mathbf{A}(\mathbf{r},t)}{\partial t^k}\right|_{t=t_0}. \tag{2.58}$$

Substituting this expansion in Eq. (2.55) and equating the lth term of the Taylor expansion on each side of it, we arrive at the final result

$$\begin{aligned}\rho_0(\mathbf{r})(l+1)\frac{1}{c}\Delta\mathbf{A}_{l+1}(\mathbf{r}) &= -\sum_{k=0}^{l-1}\rho_{l-k}(\mathbf{r})(k+1)\frac{1}{c}\Delta\mathbf{A}_{k+1}(\mathbf{r}) \\ &+ \frac{1}{c}\sum_{k=0}^{l}\{\mathbf{j}_{l-k}(\mathbf{r})\times[\nabla\times\Delta\mathbf{A}_k(\mathbf{r})]\} \\ &+ [\mathbf{Q}(\mathbf{r},t)]_l - [\mathbf{Q}'(\mathbf{r},t)]_l. \end{aligned}\tag{2.59}$$

Here we have considered that all the quantities appearing in Eq. (2.55) admit Taylor expansion in the neighbourhood of $t = t_0$, as consequence of the analyticity of the vector potential and the time-dependent Schrödinger equation. In general $[f(\mathbf{r},t)]_l$ indicates the lth coefficient (a function of $\mathbf{r}$ alone) in the Taylor expansion of the function $f(\mathbf{r},t)$. Moreover, we have used the relation $[\partial\Delta\mathbf{A}(\mathbf{r},t)/\partial t]_k = (k+1)\Delta\mathbf{A}(\mathbf{r})_{k+1}$. One can show that Eq. (2.59) is a recursion relation for the coefficients $\Delta\mathbf{A}_k(\mathbf{r})$ of the Taylor expansion of $\Delta\mathbf{A}(\mathbf{r},t)$. This means that the coefficient $\Delta\mathbf{A}_{l+1}(\mathbf{r})$ can be expressed in terms of $\Delta\mathbf{A}_k(\mathbf{r})$, with $k \leqslant l$. In order this to be true, the right-hand side of Eq. (2.59) must depend only on the coefficient $\Delta\mathbf{A}_k(\mathbf{r})$, with $k \leqslant l$. This is immediately clear for the terms in which this coefficient appears explicitly. There are also $\Delta\mathbf{A}_k(\mathbf{r})$s that enter the equation implicitly through the coefficients of the expansion of the expectation value of the stress tensor. However, the time-dependent Schrödinger equation, which is of first order in time, assures that the lth coefficient of the Taylor expansion of the quantum states $\Psi(t)$ and $\Psi'(t)$ is entirely determined by the coefficients of order $k < l$ in the expansion of the vector potentials $\mathbf{A}_k(\mathbf{r},t)$ and $\mathbf{A}'_k(\mathbf{r},t)$, respectively. We can then conclude that all the quantities on the right-hand side of Eq. (2.59) are completely determined by the coefficients $\Delta\mathbf{A}_k(\mathbf{r})$, with $k \leqslant l$. To use the recursion relation we also need to know the initial state $\Delta\mathbf{A}_0(\mathbf{r}) = \mathbf{A}'(\mathbf{r}, t_0) - \mathbf{A}(\mathbf{r}, t_0)$. This can be retrieved from the equality of densities and current-densities of the primed and unprimed systems,

$$\langle\Psi(t_0)|\hat{\mathbf{j}}(\mathbf{r})|\Psi(t_0)\rangle = \langle\Psi'(t_0)|\hat{\mathbf{j}}(\mathbf{r})|\Psi'(t_0)\rangle,$$

which leads to the following expression,

$$\rho(\mathbf{r}, t_0)\Delta\mathbf{A}_0(\mathbf{r}) = \langle\Psi'(t_0)|\hat{\mathbf{j}}_p(\mathbf{r})|\Psi'(t_0)\rangle - \langle\Psi(t_0)|\hat{\mathbf{j}}_p(\mathbf{r})|\Psi(t_0)\rangle, \qquad (2.60)$$

where $\hat{\mathbf{j}}_p(\mathbf{r}) = 1/2\sum_i\{-i\nabla_i, \delta(\mathbf{r} - \mathbf{r}_i)\}$ is the paramagnetic current-density operator. The recursion equation (2.59), together with the initial condition (2.60), completely determine the Taylor expansion of the vector potential $\mathbf{A}'(\mathbf{r}, t)$ which produces in the primed system the same current-density that $\mathbf{A}(\mathbf{r}, t)$ produces in the unprimed system. The knowledge of these coefficients uniquely defines the potential $\mathbf{A}'(\mathbf{r}, t)$ provided that the series itself converges within a nonvanishing convergence radius $t_c > 0$. Physically, the possibility of a vanishing radius can be safely discounted [20]. Under this assumption, the potential can be computed up to t_c and then the process can be iterated taking t_c as initial time.

Two special cases can now be discussed.

In the case in which the unprimed and primed systems are such that $U = U'$ and $\Psi(t_0) = \Psi'(t_0)$, Eq. (2.60) implies that $\Delta\mathbf{A}_0(\mathbf{r}) = 0$. From Eq. (2.59) it then follows that $\Delta\mathbf{A}_k(\mathbf{r}) = 0$ for all k, i.e., $\mathbf{A}(\mathbf{r}, t) = \mathbf{A}'(\mathbf{r}, t)$ at all times. This result is the analogue of the Runge-Gross theorem for the TDCDFT: two vector potentials that produce the same current-density in two systems evolving from the same initial state must be the same up to a gauge transformation. In other words the map between vector potentials and current-densities is invertible.

In the case in which the primed system is a noninteracting one, i.e., $U' = 0$, then the current-density produced in an interacting system under a vector potential $\mathbf{A}(\mathbf{r}, t)$ can be also reproduced in a noninteracting system evolving under a suitable vector potential $\mathbf{A}'(\mathbf{r}, t)$. This is possible if $\Psi'(t_0)$ is a Slater determinant which produces the initial density and current-density. It becomes clear that in this case we have a solid basis for the use of a time-dependent Kohn-Sham formalism. The time-dependent one-electron Kohn-Sham equations take the form

$$\left\{\frac{1}{2}[-i\nabla + \frac{1}{c}\mathbf{A}_s(\mathbf{r}, t)]^2 + v_s(\mathbf{r}, t)\right\}\psi_i(\mathbf{r}, t) = i\frac{\partial}{\partial t}\psi_i(\mathbf{r}, t). \qquad (2.61)$$

The effective potentials are uniquely determined up to a gauge transformation. In the Coulomb gauge ($\nabla \cdot \mathbf{A} = 0$), they can be decomposed in external, classical, and exchange-correlation potentials as follows,

$$v_s(\mathbf{r},t) = v(\mathbf{r},t) + \int \frac{\rho(\mathbf{r}',t)}{|\mathbf{r}-\mathbf{r}'|} d\mathbf{r}' + v_{xc}(\mathbf{r},t), \tag{2.62}$$

$$\mathbf{A}_s(\mathbf{r},t) = \mathbf{A}(\mathbf{r},t) + \frac{1}{c}\int \frac{\mathbf{j}_T(\mathbf{r}',t-|\mathbf{r}-\mathbf{r}'|/c)}{|\mathbf{r}-\mathbf{r}'|} d\mathbf{r}' + \mathbf{A}_{xc}(\mathbf{r},t), \tag{2.63}$$

where we have assumed the two-particle interaction to be the repulsive Coulomb potential. The vector potential defined in terms of the transverse current-density $\mathbf{j}_T(\mathbf{r},t)$ accounts for the properly retarded contribution to the total current and for the retardation effects which have not been included in the instantaneous Coulomb potential [21]. The density of the real system can be obtained in a similar way as in TDDFT by using Eq. (2.45). The current is obtained as

$$\begin{aligned}\mathbf{j}(\mathbf{r},t) &= -\frac{i}{2}\sum_{i=1}^{N}(\psi_i^*(\mathbf{r},t)\nabla\psi_i(\mathbf{r},t) - \nabla\psi_i^*(\mathbf{r},t)\psi_i(\mathbf{r},t)) \\ &\quad + \frac{1}{c}\rho(\mathbf{r},t)\mathbf{A}_s(\mathbf{r},t).\end{aligned} \tag{2.64}$$

Here the first and the second terms on the right-hand side represent the paramagnetic and diamagnetic currents, respectively. The time-dependent density and current-density are related *via* the continuity equation, whereas the initial values are fixed by the initial state.

2.4 Linear response

One of the main application of time-dependent (current)-density-functional theory is the study of the dynamics of a system, initially in the ground state, when an external small perturbation is applied. In the linear regime one considers only terms which are linear in the perturbation and neglects higher order ones. We consider a system which at $t \leq t_0$ is in the ground state Ψ_0 of the Hamiltonian $\hat{H}_0$. At $t = t_0$ we apply a small perturbation $\delta\hat{h}(t)$ and we study the linear response for an arbitrary physical observable $\hat{O}$ of the system as

$$\delta\langle\hat{O}\rangle(t) = \langle\Psi(t)|\hat{O}|\Psi(t)\rangle - \langle\Psi_0|\hat{O}|\Psi_0\rangle. \tag{2.65}$$

Here $\Psi(t)$ is the solution of the time-dependent Schrödinger equation

$$i\frac{\partial}{\partial t}\Psi(t) = [\hat{H}_0 + \delta\hat{h}(t)]\Psi(t). \tag{2.66}$$

This equation is better treated in the Heisenberg picture relative to $\hat{H}_0$, in which wavefunctions and operators are related to the corresponding wavefunctions and operators in the Schrödinger picture by an unitary transformation as follows,

$$\Psi_H(t) = e^{i(t-t_0)\hat{H}_0}\Psi(t), \tag{2.67}$$

$$\hat{O}_H(t) = e^{i(t-t_0)\hat{H}_0}\hat{O}e^{-i(t-t_0)\hat{H}_0}. \tag{2.68}$$

The wavefunction $\Psi_H(t)$ satisfies the following equation of motion,

$$i\frac{\partial}{\partial t}\Psi_H(t) = \delta\hat{h}_H(t)\Psi_H(t), \tag{2.69}$$

which can be reformulated as an integral equation

$$\Psi_H(t) = \Psi(t_0) - i\int_{t_0}^{t}\delta\hat{h}_H(t')\Psi_H(t')dt' \tag{2.70}$$

Here the causality constraint is automatically incorporated. Note that at $t = t_0$ the wavefunctions in the Heisenberg and Schrödinger pictures are the same. This integral equation can be solved by iteration. The solution up to the terms linear in the perturbation is given already by a single iteration, so that, together with Eq. (2.67), we obtain

$$\Psi(t) = e^{-i(t-t_0)\hat{H}_0}\left[1 - i\int_{t_0}^{t}\delta\hat{h}_H(t')dt'\right]\Psi_0 + O(\delta\hat{h}_H^2). \tag{2.71}$$

From this, the linear response equation (2.65) for the observable $\hat{O}$ becomes

$$\delta\langle\hat{O}\rangle(t) = -i\int_{t_0}^{t}\langle\Psi_0|\left[\hat{O}_H(t), \delta\hat{h}_H(t')\right]|\Psi_0\rangle dt', \tag{2.72}$$

where $[\hat{a}, \hat{b}]$ is the commutator of the operators $\hat{a}$ and $\hat{b}$. If we consider the perturbation $\delta\hat{h}_H(t)$ to be

$$\delta\hat{h}_H(t) = \sum_i \hat{O}_{iH}(t)\varphi_i(t), \tag{2.73}$$

with $\varphi_i(t)$ arbitrary time-dependent variables, then the linear response for the operators $\hat{O}_i$ is given as

$$\begin{aligned}\delta\langle\hat{O}_i\rangle(t) &= -i\int_{t_0}^{t}\langle\Psi_0|[\hat{O}_{iH}(t), \sum_j \hat{O}_{jH}(t')\varphi_j(t')]|\Psi_0\rangle dt' \\ &= \sum_j \int_{t_0}^{\infty}\chi_{ij}(t,t')\varphi_j(t')dt'.\end{aligned} \tag{2.74}$$

Here $\chi_{ij}(t,t')$ represent the response functions and are defined as

$$\chi_{ij}(t,t') = -i\Theta(t-t')\langle\Psi_0|[\hat{O}_{iH}(t), \hat{O}_{jH}(t')]|\Psi_0\rangle. \tag{2.75}$$

The Heaviside step-function $\Theta(\tau)$ ($\Theta(\tau > 0) = 1, \Theta(\tau \leqslant) = 0$) assures the causality of the response functions, since the system should not respond to the perturbation before this is applied. If the set $|\Psi_n\rangle$ is the complete set of eigenstates of $\hat{H}_0$, we may use the closure relation $\sum_n |\Psi_n\rangle\langle\Psi_n| = 1$ and write

$$\chi_{ij}(t,t') = -i\Theta(t-t')\sum_n \Big\{\langle\Psi_0|\hat{O}_{iH}(t)|\Psi_n\rangle\langle\Psi_n|\hat{O}_{jH}(t')|\Psi_0\rangle \\ -\langle\Psi_0|\hat{O}_{jH}(t')|\Psi_n\rangle\langle\Psi_n|\hat{O}_{iH}(t)|\Psi_0\rangle\Big\}. \tag{2.76}$$

Using (2.68) we can write,

$$\begin{aligned}\langle\Psi_0|\hat{O}_{iH}(t)|\Psi_n\rangle\langle\Psi_n|\hat{O}_{jH}(t')|\Psi_0\rangle &= \langle\Psi_0|e^{i(t-t_0)H_0}\hat{O}_i e^{-i(t-t_0)H_0}|\Psi_n\rangle \times \\ &\quad \langle\Psi_n|e^{i(t'-t_0)H_0}\hat{O}_j e^{-i(t'-t_0)H_0}|\Psi_0\rangle \\ &= e^{i(E_0-E_n)(t-t')}\langle\Psi_0|\hat{O}_i|\Psi_n\rangle\langle\Psi_n|\hat{O}_j|\Psi_0\rangle,\end{aligned} \tag{2.77}$$

with E_0 and E_n the eigenvalues corresponding to the eigenstates Ψ_0 and Ψ_n, respectively, of the Hamiltonian $\hat{H}_0$. A similar expression can be written for the other term of the commutator in Eq. (2.76). The response functions (2.76) depend thus only on the difference $(t-t')$ as follows,

$$\chi_{ij}(t-t') = -i\Theta(t-t')\sum_n \Big\{e^{i(E_0-E_n)(t-t')}\langle\Psi_0|\hat{O}_i|\Psi_n\rangle\langle|\Psi_n|\hat{O}_j|\Psi_0\rangle \\ -e^{-i(E_0-E_n)(t-t')}\langle\Psi_0|\hat{O}_j|\Psi_n\rangle\langle\Psi_n|\hat{O}_i|\Psi_0\rangle\Big\}. \tag{2.78}$$

Note that this is only true if the operators $\hat{O}_i$ and $\hat{O}_j$ are time-independent. By using the following expression for the Heaviside step-function $\Theta(\tau)$,

$$\Theta(\tau) = -\frac{1}{2\pi i}\lim_{\eta\to 0^+}\int_{-\infty}^{\infty}\frac{e^{-i\omega\tau}}{\omega+i\eta}d\omega, \tag{2.79}$$

we can arrive at

$$\chi_{ij}(t-t') = \lim_{\eta\to 0^+}\int_{-\infty}^{\infty}\frac{1}{2\pi}e^{-i\omega(t-t')}\chi_{ij}(\omega), \tag{2.80}$$

where

$$\chi_{ij}(\omega) = \lim_{\eta\to 0^+}\sum_n\left\{\frac{\langle\Psi_0|\hat{O}_i|\Psi_n\rangle\langle\Psi_n|\hat{O}_j|\Psi_0\rangle}{\omega-(E_n-E_0)+i\eta} - \frac{\langle\Psi_0|\hat{O}_j|\Psi_n\rangle\langle\Psi_n|\hat{O}_i|\Psi_0\rangle}{\omega+(E_n-E_0)+i\eta}\right\} \tag{2.81}$$

represent the response functions in the frequency domain. The limit in (2.81) can be rewritten as

$$\lim_{\eta\to 0^+}\frac{1}{\omega-(E_n-E_0)+i\eta} = P\left(\frac{1}{\omega-(E_n-E_0)}\right) - i\pi\delta(\omega-(E_n-E_0)), \tag{2.82}$$

where P represents the principal value of the limit. If the system has time-reversal invariance, then one can choose the quantities $\langle\Psi_0|\hat{O}_i|\Psi_n\rangle$ real, so that the real and imaginary parts of the response functions are given by

$$\begin{aligned}
\Re\{\chi_{ij}(\omega)\} &= \sum_n \langle\Psi_0|\hat{O}_i|\Psi_n\rangle\langle\Psi_n|\hat{O}_j|\Psi_0\rangle \times \\
&\quad \left\{P\left(\frac{1}{\omega-(E_n-E_0)}\right) - P\left(\frac{1}{\omega+(E_n-E_0)}\right)\right\}, \qquad (2.83)\\
\Im\{\chi_{ij}(\omega)\} &= -\pi\sum_n \langle\Psi_0|\hat{O}_i|\Psi_n\rangle\langle\Psi_n|\hat{O}_j|\Psi_0\rangle \times \\
&\quad \{\delta(\omega-(E_n-E_0)) - \delta(\omega+(E_n-E_0))\}. \qquad (2.84)
\end{aligned}$$

2.4.1 Linear response in TDCDFT

Within the TDCDFT framework we can now describe the response of an interacting many-electron system to a time-dependent external perturbation in terms of the response functions of the corresponding noninteracting Kohn-Sham systems. We consider as initial state the ground state of the stationary Kohn-Sham system corresponding to the external potentials $v_0(\mathbf{r}) = v(\mathbf{r}, t_0)$ and $\mathbf{A}_0(\mathbf{r}) = \mathbf{A}(\mathbf{r}, t_0) = \mathbf{0}$. The first-order perturbation of the ground state is governed by the perturbation Hamiltonian $\delta\hat{h}(\mathbf{r}, t)$ containing all terms linear in the field,

$$\delta\hat{h}(\mathbf{r}, t) = \hat{\rho}(\mathbf{r})\delta v_s(\mathbf{r}, t) + \frac{1}{c}\hat{\mathbf{j}}(\mathbf{r}) \cdot \delta\mathbf{A}_s(\mathbf{r}, t), \qquad (2.85)$$

where $\hat{\rho}(\mathbf{r}) = 1$ and $\hat{\mathbf{j}}(\mathbf{r}) = -i\left(\nabla - \nabla^\dagger\right)/2$. In chapter 4 we derive the equation of the linear response by including the spin of electrons as well. The Kohn-Sham perturbing potentials $\delta v_s(\mathbf{r}, t)$ and $\delta\mathbf{A}_s(\mathbf{r}, t)$ are given by

$$\begin{aligned}
\delta v_s(\mathbf{r}, t) &= \delta v(\mathbf{r}, t) + \int \frac{\delta\rho(\mathbf{r}', t)}{|\mathbf{r}-\mathbf{r}'|}d\mathbf{r}' + \delta v_{xc}(\mathbf{r}, t), \qquad (2.86)\\
\delta\mathbf{A}_s(\mathbf{r}, t) &= \delta\mathbf{A}(\mathbf{r}, t) + \frac{1}{c}\int \frac{\delta\mathbf{j}_T(\mathbf{r}', t-|\mathbf{r}-\mathbf{r}'|/c)}{|\mathbf{r}-\mathbf{r}'|}d\mathbf{r}' + \delta\mathbf{A}_{xc}(\mathbf{r}, t). \qquad (2.87)
\end{aligned}$$

The linear contributions to the exchange-correlation potentials depend on both the induced density and induced current-density. One can choose the gauge such that in the exchange-correlation scalar potential only terms linear in the induced density are retained, whereas all the terms linear in the induced current-density are gauge-transformed to the exchange-correlation vector potential. The terms linear in the induced density which contribute to the exchange-correlation vector potential can be considered as functional of the induced current-density, since density and current are related by the continuity equation (2.41). Thus the exchange-correlation vector potential is a functional of the induced current-density. In this gauge, the linear contribution to the scalar exchange-correlation potential can be defined *via* a response kernel $f_{xc}(\mathbf{r},\mathbf{r}',t-t')$ as

$$\delta v_{xc}(\mathbf{r},t) = \int_{t_0}^{t}\int f_{xc}(\mathbf{r},\mathbf{r}',t-t')\delta\rho(\mathbf{r}',t')d\mathbf{r}'dt'. \tag{2.88}$$

The exchange-correlation contribution to the vector potential is given in terms of a tensor kernel $\mathbf{f}_{xc}(\mathbf{r},\mathbf{r}',t-t')$ as

$$\delta \mathbf{A}_{xc}(\mathbf{r},t) = \int_{t_0}^{t}\int \mathbf{f}_{xc}(\mathbf{r},\mathbf{r}',t-t')\cdot\delta\mathbf{j}(\mathbf{r}',t')d\mathbf{r}'dt'. \tag{2.89}$$

The exchange-correlation kernels are, as expected, very complicated functionals of the density and current-density and need to be approximated. The induced density and current-density are then obtained, in the linear regime and in the frequency domain, as

$$\begin{aligned}
\delta\rho(\mathbf{r},\omega) &= \int\Big\{\chi_{s,\rho\rho}(\mathbf{r},\mathbf{r}',\omega)\cdot\delta v_s(\mathbf{r}',\omega) \\
&+ \frac{1}{c}\chi_{s,\rho\mathbf{j}}(\mathbf{r},\mathbf{r}',\omega)\cdot\delta\mathbf{A}_s(\mathbf{r}',\omega)\Big\}d\mathbf{r}' &\quad (2.90)\\
\delta\mathbf{j}(\mathbf{r},\omega) &= \int\Big\{\chi_{s,\mathbf{j}\rho}(\mathbf{r},\mathbf{r}',\omega)\cdot\delta v_s(\mathbf{r}',\omega) \\
&+ \frac{1}{c}\left[\chi_{s,\mathbf{jj}}(\mathbf{r},\mathbf{r}',\omega)+\rho_0\delta(\mathbf{r}-\mathbf{r}')\right]\cdot\delta\mathbf{A}_s(\mathbf{r}',\omega)\Big\}d\mathbf{r}', &\quad (2.91)
\end{aligned}$$

where $\rho_0(\mathbf{r})$ is the density in the ground state. The term $\delta\mathbf{j}_d(\mathbf{r},\omega) = \rho_0(\mathbf{r})\delta\mathbf{A}_s(\mathbf{r},t)/c$ is the diamagnetic contribution to the induced current-density, and can be related to the current-current Kohn-Sham response function $\chi_{s,\mathbf{jj}}(\mathbf{r},\mathbf{r}',\omega)$ *via* the conductivity sum rule

$$\chi_{s,\mathbf{jj}}(\mathbf{r},\mathbf{r}',\omega=0)+\rho_0(\mathbf{r})\delta(\mathbf{r}-\mathbf{r}') = 0. \tag{2.92}$$

In this expression we neglect a purely transverse contribution which gives rise to the weak Landau diamagnetism [1]. In the next chapter we give a detailed description of this sum-rule. The set of equations (2.86)-(2.91) needs to be solved self-consistently. To do this we need to approximate the exchange-correlation kernels.

2.4.2 The Adiabatic Local Density Approximation

The simplest approximation to the time-dependent exchange-correlation potentials is the adiabatic local density approximation (ALDA) [22], which is a straightforward extension of the local density approximation used in the stationary case. Within this approximation one neglects the exchange-correlation vector potential and evaluates the LDA expression for the ground-state exchange-correlation scalar potential at the time-dependent local density,

$$v_{xc}(\mathbf{r},t) = v_{xc}^{hom}(\rho(\mathbf{r},t)) = \frac{d}{d\rho}(\rho e_{xc}^{hom}(\rho))\bigg|_{\rho(\mathbf{r},t)}, \tag{2.93}$$

where $e_{xc}^{hom}(\rho)$ is the exchange-correlation energy per particle of the homogeneous electron gas with density ρ. The main characteristic of the ALDA is that it is local in time as well as in space. This approximation can be expected to be valid in nearly homogeneous systems in which densities change very slowly in time; in practice, however, it works quite well also beyond this domain of applicability. When the adiabatic approximation is used in the linear response approach, the exchange-correlation response kernel $f_{xc}(\mathbf{r},\mathbf{r}',t,t') = \delta v_{xc}(\mathbf{r},t)/\delta\rho(\mathbf{r}',t')$ takes the following simple form,

$$f_{xc}^{ALDA}(\mathbf{r},\mathbf{r}',t,t') = \delta(t-t')\delta(\mathbf{r}-\mathbf{r}')\,\frac{d^2}{d\rho^2}(\rho e_{xc}^{hom}(\rho))\bigg|_{\rho_0(\mathbf{r})}. \tag{2.94}$$

The kernel is real and local in space and time. When Fourier-transformed, the locality in time implies that f_{xc}^{ALDA} is frequency-independent. In order to improve this approximation one can incorporate the frequency-dependence of the exchange-correlation kernel. But it has been rigorously proved that the frequency-dependent $f_{xc}(\mathbf{r},\mathbf{r}',\omega)$ is long range in space and that frequency-dependence and locality are incompatible in an exchange-correlation potential that is expressed as functional of the density alone [23]. Vignale and Kohn showed that a consistent local approximation can be constructed if the theory is formulated in terms of the current-density as dynamical basic variable, with the vector potential as conjugate variable [24]. The main result is that one obtains a local current approximation for the exchange-correlation kernel for the vector potential.

2.4.3 The Vignale-Kohn functional

The exchange-correlation vector potential can be approximated as a local functional of the current by using the expression derived by Vignale and Kohn [24, 25],

$$\frac{i\omega}{c}\delta\mathbf{A}_{xc,i}(\mathbf{r},\omega) = -\frac{1}{\rho_0(\mathbf{r})}\sum_j \partial_j\sigma_{xc,ij}(\mathbf{r},\omega). \tag{2.95}$$

Here $\sigma_{xc,ij}(\mathbf{r},\omega)$ has the structure of a symmetric viscoelastic stress tensor,

$$\sigma_{xc,ij} = \tilde{\eta}_{xc}\left(\partial_j u_i + \partial_i u_j - \frac{2}{3}\delta_{ij}\sum_k \partial_k u_k\right) + \tilde{\zeta}\delta_{ij}\sum_k \partial_k u_k, \tag{2.96}$$

with $\mathbf{u}(\mathbf{r},\omega) = \delta\mathbf{j}(\mathbf{r},\omega)/\rho_0(\mathbf{r})$ the velocity field. The coefficients $\tilde{\eta}_{xc}(\mathbf{r},\omega)$ and $\tilde{\zeta}_{xc}(\mathbf{r},\omega)$ depend on the exchange-correlation energy $e_{xc}(\rho_0)$ and on the transverse and longitudinal exchange-correlation kernels $f_{xcT}(\rho_0(\mathbf{r}),\omega)$ and $f_{xcL}(\rho_0(\mathbf{r}),\omega)$ of the homogeneous electron gas with density $\rho_0(\mathbf{r})$. In chapter 7 we give a more detailed discussion on this functional and we show the performance in the linear response of noble metals.

Chapter 3

TD-CDFT for the Metallic Response of Solids

We formulate the linear response of metals within time-dependent current-density-functional theory. To achieve this, the Kohn-Sham response functions have to include both interband and intraband transitions with an accurate treatment of the Fermi surface in the Brillouin-zone integrations. The intraband contributions in particular have to be evaluated using a wavevector-dependent description. To test the method we calculate the optical properties of the two noble metals Cu and Ag. In general we find a good agreement with the experiments for the calculated results obtained within the adiabatic local density approximation. In order to describe the Drude-like absorption below the interband onset and the sharp plasma feature in silver exchange-correlation effects beyond the adiabatic local density approximation are needed.

3.1 Introduction

In time-dependent density-functional theory (TDDFT), developed by Runge and Gross [13] starting from the original ground-state Hohenberg-Kohn formulation [6, 8], the exact dynamical response of a many-particle system to an external perturbing time-dependent scalar potential can be obtained using an effective one-particle description [13, 15, 26, 27]. Many-particle effects enter in the time-dependent version of the so-called Kohn-Sham scheme [8] through the exchange-correlation contribution to the self-consistent and time-dependent effective scalar potential. Ghosh and Dhara [18, 19] extended the Runge-Gross theorem [13] to many-particle systems in a general time-dependent electromagnetic field. In their description the electron current-density enters, replacing the electron density of ordinary TDDFT as the fundamental dynamical variable, with the vector potential instead of the scalar potential as its natural conjugate variable [28]. This time-dependent current-density functional approach (TDCDFT) [24,27,29] is particularly well suited for the treatment of extended systems [30,31]. When such a system is perturbed by an external electric field, there will be a macroscopic response caused by charge accumulating at the outer surface that leads to a macroscopic screening field inside the bulk. The continuity relation implies that the density change at the surface of the system is accompanied by a current flowing through the interior with a nonzero average value for the current-density. When treating the response of a crystalline system by using periodic boundary conditions within TDDFT, the effect of this phenomenon called macroscopic polarization cannot be described using the periodic bulk density alone [32], and one has to introduce additional dynamical variables to account for the surface charge, c.q. the macroscopic polarization [33] or, equivalently, the macroscopic induced field [34]. In the TDCDFT approach the information on the surface charge is already contained in a natural way in the periodic current-density. For the longitudinal response of isotropic systems some of the difficulties can be circumvented by relating the long-wavelength limit of the density-density response to the longitudinal current-current response [1,2,35,36]. The (current-)density functional approach yields reasonable results for the dielectric constants and optical dielectric functions of various isotropic semiconductors and insulators when it is used within the adiabatic local density approximation (ALDA) for the exchange-correlation field [30,31,37–42], but more advanced schemes involving long-range kernels [43–48] or equivalently (semi)-local current functionals [24,25,49] are needed to account for excitonic effects in these systems. For anisotropic system and when calculating transverse response at $q > 0$ we have to use the TDCDFT approach, which can be applied to treat the optical properties of metals as well. Here, however, one should not only consider the interband contribution, involving transitions from (partially) occupied to (partially) unoccupied bands as in nonmetals, but also the intraband contribution due to transitions within the same band, more specifically, from just below the Fermi level to just above this level. The latter processes are responsible for the collective plasmon response typical for simple metallic systems [1]. For the noble metals like Ag and Cu the interplay between inter- and intraband processes involving d-electrons leads to a strong redshift of the Drude-like plasmon resonance [50–54].

In this chapter we give a general description of the response of a metallic system to an external electromagnetic field within the current-density functional scheme [30,31].

To achieve this we consider a general q- and ω-dependent perturbation,

$$\delta\hat{h}(\mathbf{r},t) = \delta\hat{h}_{\mathbf{q}}(\mathbf{r},\omega)e^{i(\mathbf{q}\cdot\mathbf{r}-\omega t)}, \tag{3.1}$$

where we choose $\delta\hat{h}_{-\mathbf{q}}(\mathbf{r},-\omega) = \delta\hat{h}^{\dagger}_{\mathbf{q}}(\mathbf{r},\omega)$ to ensure a real perturbation with $\delta\hat{h}_{\mathbf{q}}(\mathbf{r},\omega)$ lattice periodic. We derive the linear response of the system for vanishing q but finite ω. This is the regime describing optical properties. To evaluate the response in this limit three steps are essential. First we show that the inter- and intraband processes behave differently for small q. Then we show that we can still use the microscopic Coulomb gauge [30] to separate microscopic and macroscopic contributions to the effective scalar and vector potentials. Finally, we consider the self-consistent-field equations and show that inter- and intraband contributions to the response decouple in the optical limit when we make use of the adiabatic local density approximation. Here we outline the derivation, which can be found in full detail in the next section. We start by expressing the induced density and current-density using the q-dependent Kohn-Sham response functions. These take the following general form,

$$\begin{aligned}\chi_{ab\mathbf{q}}(\mathbf{r},\mathbf{r}',\omega) \quad = \quad & \frac{1}{N_k}\sum_{\mathbf{k}}\sum_{i,a}\frac{(f_{i\mathbf{k}}-f_{a\mathbf{k}+\mathbf{q}})}{1+\delta_{i,a}}\times \\ & \frac{(\psi^*_{i\mathbf{k}}(\mathbf{r})\hat{a}_{\mathbf{q}}\psi_{a\mathbf{k}+\mathbf{q}}(\mathbf{r}))\,(\psi^*_{a\mathbf{k}+\mathbf{q}}(\mathbf{r}')\hat{b}_{-\mathbf{q}}\psi_{i\mathbf{k}}(\mathbf{r}'))}{\epsilon_{i\mathbf{k}}-\epsilon_{a\mathbf{k}+\mathbf{q}}+\omega+i\eta} + c.c.(-\mathbf{q},-\omega),\end{aligned}$$

where η is a positive infinitesimal quantity, $\hat{a}_{\mathbf{q}}$ and $\hat{b}_{\mathbf{q}}$ refer to the operators $\hat{\rho}_{\mathbf{q}} = e^{-i\mathbf{q}\cdot\mathbf{r}}$ or $\hat{\mathbf{j}}_{\mathbf{q}} = -i(e^{-i\mathbf{q}\cdot\mathbf{r}}\nabla - \nabla^{\dagger}e^{-i\mathbf{q}\cdot\mathbf{r}})/2$, and the summation is over the (partially) occupied bands i and (partially) unoccupied bands a. Only ground-state orbitals $\psi_{n\mathbf{k}}$, orbital energies $\epsilon_{n\mathbf{k}}$, and occupation numbers $f_{n\mathbf{k}}$ enter in this expression, which takes into account the conservation of the crystal momentum. The Bloch functions are normalized on the Wigner-Seitz cell V_{WS}, and the number of $\mathbf{k}$ points in the summation is $N_k = V_{BvK}/V_{WS}$, in which V_{BvK} is the volume of the Born-von Kármán cell. The intraband (interband) contribution to the response functions is given by the terms with $a = i$ ($a \neq i$) in the summation over i and a. In the intraband case the factor $1/(1+\delta_{i,a})$ corrects for the double counting. Analysis of the q-dependence at finite ω indicates that the intraband contributions vanish in the limit $q \to 0$ except for $\chi_{\mathbf{jjq}}(\mathbf{r},\mathbf{r}',\omega)$. By considering the reverse order of limits, i.e. by evaluating the limit $\omega \to 0$ before taking $q \to 0$, we retrieve the conductivity sum rule which allows us to relate the diamagnetic and paramagnetic components of the current-density. Identifying the various contributions to the response functions makes it possible to separate the inter- and intraband contributions to the induced density and current-density,

$$\begin{aligned}\delta\rho(\mathbf{r},\omega) &= \delta\rho^{inter}(\mathbf{r},\omega)+\delta\rho^{intra}(\mathbf{r},\omega), \\ \delta\mathbf{j}(\mathbf{r},\omega) &= \delta\mathbf{j}^{inter}(\mathbf{r},\omega)+\delta\mathbf{j}^{intra}(\mathbf{r},\omega).\end{aligned} \tag{3.2}$$

The equations for the interband contribution to the density and current-density become identical to the original description of Kootstra *et al.* [30, 31] in the limit of q to zero. The description of the intraband contribution follows along the same lines as for the interband case. In the description of Kootstra *et al.* it is proven to be essential to choose the gauge such that the macroscopic component of the induced electric field that is due to the induced density and current-density is completely described using the vector potential. The scalar potential is thus purely microscopic. One can then obtain the response to a fixed macroscopic field instead of to an external field and thus treat the macroscopic optical response exactly [30]. This still holds in our q-dependent description, where it turns out that the density and current-density have the same q-dependence as the perturbing field. We can then define the macroscopic induced density as

$$\delta\rho_{mac}(\mathbf{r},\omega)=e^{i\mathbf{q}\cdot\mathbf{r}}\frac{1}{V}\int_V e^{-i\mathbf{q}\cdot\mathbf{r}}\delta\rho(\mathbf{r},\omega)d\mathbf{r}, \tag{3.3}$$

where V is the unit cell, and similarly we can define the macroscopic current-density. A careful analysis of the q-dependence at small q, but finite ω, reveals that we can include in the microscopic scalar potential the contribution due to the intraband part of the microscopic induced density,

$$\delta\rho^{intra}_{mic}(\mathbf{r},\omega)=\delta\rho^{intra}(\mathbf{r},\omega)-\delta\rho^{intra}_{mac}(\mathbf{r},\omega),$$

where $\delta\rho^{intra}_{mac}(\mathbf{r},\omega)$ is the macroscopic part of the intraband induced density. The other contributions that lead to a macroscopic field have to be included in the vector potential. Intraband contributions to both the microscopic scalar potential and macroscopic vector potential are now identified. The former vanishes in the limit of q to zero, and the latter is to be included in the definition of the fixed macroscopic field. Like in the description of Kootstra *et al.* we can neglect the very small microscopic magnetic contribution to the self-consistent field, which is due to the transverse current. Together with the classical potentials, we also have to consider the exchange-correlation contribution to the self-consistent field. We find that in the optical limit only the exchange-correlation contribution of the interband part of the induced density needs to be included in the microscopic scalar potential to arrive at the same adiabatic local density approximation (ALDA) used in the ordinary TDDFT approach. At the same time no exchange-correlation contributions to the macroscopic vector potential remain. In this chapter we neglect possible additional contributions from the induced current [25]. The microscopic effective scalar potential is thus completely determined by the microscopic interband induced density. Therefore we can obtain the response in the optical limit by first solving the equations for the interband part of the density and by subsequently obtaining the intraband part. We show that, whereas the interband density needs a self-consistent solution, in the second stage the intraband density and the current-density do not need to be calculated self-consistently. It follows that the intraband current can be obtained completely independent from the interband density and current-density and *vice versa*. Note, however, that for finite q and for exchange-correlation approximations that go beyond the ALDA the sets of equations are essentially coupled.

The remainder of the chapter is organized as follows. The main aspects of the implementation are given in a separate section. This implementation is based on the description of Kootstra *et al.* [30] for the q-independent nonmetallic case. Here we focus on the specific case of metals and refer the reader to Ref. [30] for the general framework used. Finally, we report our results for the dielectric and energy-loss functions for the crystals of Cu and Ag and compare them with the best available experimental data [50–54].

3.2 Theory

We treat the dynamic linear response of a metallic crystal to a perturbation described by both scalar and vector potentials within the time-dependent current-density-functional theory (TDCDFT) [18, 19, 24, 27, 29]. In the effective one-electron scheme of Kohn-Sham [8], noninteracting particles moving in a time-dependent effective electromagnetic field are described by Bloch functions that are solutions of the following equation,

$$i\frac{\partial}{\partial t}\psi_{n\mathbf{k}}(\mathbf{r},t) = \left(\frac{1}{2}\left[\hat{\mathbf{p}} + \frac{1}{c}\delta\mathbf{A}_{\mathit{eff}}(\mathbf{r},t)\right]^2 + v_{\mathit{eff},0}(\mathbf{r}) + \delta v_{\mathit{eff}}(\mathbf{r},t)\right)\psi_{n\mathbf{k}}(\mathbf{r},t). \qquad (3.4)$$

Here $v_{\mathit{eff},0}(\mathbf{r})$ is the effective scalar potential giving the initial density which we choose to be the ground-state density. It is, therefore, uniquely determined by the Hohenberg-Kohn theorem [6]. The time-dependent potentials $\delta v_{\mathit{eff}}(\mathbf{r},t)$ and $\delta\mathbf{A}_{\mathit{eff}}(\mathbf{r},t)$ produce the exact time-dependent density and current-density for the chosen initial state,

$$\rho(\mathbf{r},t) = \sum_{n,\mathbf{k}} f_{n\mathbf{k}}\psi^*_{n\mathbf{k}}(\mathbf{r},t)\psi_{n\mathbf{k}}(\mathbf{r},t), \qquad (3.5)$$

where $f_{n\mathbf{k}}$ are the occupation numbers, and

$$\mathbf{j}(\mathbf{r},t) = \sum_{n,\mathbf{k}} f_{n\mathbf{k}} \psi^*_{n\mathbf{k}}(\mathbf{r},t)\hat{\mathbf{j}}\psi_{n\mathbf{k}}(\mathbf{r},t) + \frac{1}{c}\rho(\mathbf{r},t)\delta\mathbf{A}_{\mathit{eff}}(\mathbf{r},t). \tag{3.6}$$

In Eq. (3.6) the first term is the paramagnetic component of the current-density, in which the auxiliary operator $\hat{\mathbf{j}}$ is defined as $-i(\nabla - \nabla^\dagger)/2$ where the dagger indicates that terms to the left have to be differentiated. The second term is the diamagnetic component. Since the initial state is the ground state, the occupation numbers $f_{n\mathbf{k}}$ are given by the Fermi-Dirac distribution function $f_{n\mathbf{k}} = f(\epsilon_{n\mathbf{k}}) = 2$ for $\epsilon_{n\mathbf{k}} \leq \epsilon_F$ and 0 otherwise, with $\epsilon_{n\mathbf{k}}$ the ground-state orbital energies and ϵ_F the Fermi level. The time-dependent potentials are uniquely determined up to an arbitrary gauge due to the Ghosh-Dhara theorem [18, 19]. Both the density and the current-density are gauge invariant. The first-order perturbation of the ground state is governed by the perturbation Hamiltonian $\delta\hat{h}_{\mathit{eff}}$ containing all terms linear in the field,

$$\delta\hat{h}_{\mathit{eff}}(\mathbf{r},t) = \frac{1}{2c}\left(\hat{\mathbf{p}}\cdot\delta\mathbf{A}_{\mathit{eff}}(\mathbf{r},t) + \delta\mathbf{A}_{\mathit{eff}}(\mathbf{r},t)\cdot\hat{\mathbf{p}}\right) + \delta v_{\mathit{eff}}(\mathbf{r},t). \tag{3.7}$$

We choose the gauge to be the microscopic Coulomb gauge of Kootstra *et al.* [30] in which the effective scalar and vector potentials are given by

$$\begin{aligned} \delta v_{\mathit{eff}}(\mathbf{r},t) &= \delta v_{H,mic}(\mathbf{r},t) + \delta v_{xc}(\mathbf{r},t), && (3.8)\\ \delta\mathbf{A}_{\mathit{eff}}(\mathbf{r},t) &= -c\int^t \mathbf{E}_{mac}(\mathbf{r},t')dt' + \delta\mathbf{A}_{xc}(\mathbf{r},t), && (3.9)\end{aligned}$$

where $\delta v_{H,mic}(\mathbf{r},t)$ and $\delta v_{xc}(\mathbf{r},t)$ are the microscopic component of the Hartree and exchange-correlation potentials, respectively, and $\mathbf{E}_{mac}(\mathbf{r},t')$ is the fixed macroscopic electric field, comprising both the external and the induced macroscopic components. The latter accounts for the long-range contribution of the Hartree potential, as well as for the properly retarded macroscopic contribution of the induced transverse current-density. We can neglect the microscopic part of the induced vector potential consistent with the Breit approximation used in the ground-state calculation [21, 30, 31, 55]. As described in the previous section we consider the macroscopic exchange-correlation contributions to be included in $\delta\mathbf{A}_{\mathit{eff}}$ *via* $\delta\mathbf{A}_{xc}$. We work in the frequency domain for simplicity,

$$\delta\mathbf{A}_{\mathit{eff}}(\mathbf{r},t) = \int e^{-i\omega t}\delta\mathbf{A}_{\mathit{eff}}(\mathbf{r},\omega)d\omega, \tag{3.10}$$

and consider a general perturbation characterized by wavevector $\mathbf{q}$ and frequency ω,

$$\delta\mathbf{A}_{\mathit{eff}}(\mathbf{r},\omega) = e^{i\mathbf{q}\cdot\mathbf{r}}\delta\mathbf{A}_{\mathbf{q},\mathit{eff}}(\mathbf{r},\omega), \tag{3.11}$$

in which $\delta\mathbf{A}_{\mathbf{q},\mathit{eff}}(\mathbf{r},\omega)$ is lattice periodic,

$$\delta\mathbf{A}_{\mathbf{q},\mathit{eff}}(\mathbf{r}+\mathbf{R},\omega) = \delta\mathbf{A}_{\mathbf{q},\mathit{eff}}(\mathbf{r},\omega), \tag{3.12}$$

for any Bravais lattice vector $\mathbf{R}$. Since the field given by Eqs (3.10) and (3.11) is real, we have

$$\delta\mathbf{A}_{\mathbf{q},\mathit{eff}}(\mathbf{r},\omega) = \delta\mathbf{A}^{*}_{-\mathbf{q},\mathit{eff}}(\mathbf{r},-\omega). \tag{3.13}$$

Similar expressions are assumed for the scalar potential $\delta v_{\mathit{eff}}(\mathbf{r},t)$. In the remainder we will only consider plane-wavevector potentials, i.e., $\delta\mathbf{A}_{\mathbf{q},\mathit{eff}}(\mathbf{r},\omega) = \delta\mathbf{A}_{\mathbf{q},\mathit{eff}}(\omega)$, unless stated otherwise.

3.2.1 Induced density

Using the Bloch theorem we show in App. A that in the linear regime the induced density can be written as

$$\delta\rho(\mathbf{r},\omega) = e^{i\mathbf{q}\cdot\mathbf{r}}\delta\rho_{\mathbf{q}}(\mathbf{r},\omega), \tag{3.14}$$

where $\delta\rho_{\mathbf{q}}(\mathbf{r},\omega)$ is lattice periodic, $\delta\rho_{\mathbf{q}}(\mathbf{r}+\mathbf{R},\omega) = \delta\rho_{\mathbf{q}}(\mathbf{r},\omega)$, given by

$$\begin{aligned}
\delta\rho_{\mathbf{q}}(\mathbf{r},\omega) \quad = \quad & \frac{1}{N_k}\sum_{\mathbf{k},\mathbf{k}'}\delta_{\mathbf{k}',\mathbf{k}+\mathbf{q}}\sum_{i,a}\frac{(f_{i\mathbf{k}}-f_{a\mathbf{k}'})}{1+\delta_{ia}} \times \\
& \frac{\psi^{*}_{i\mathbf{k}}(\mathbf{r})e^{-i\mathbf{q}\cdot\mathbf{r}}\psi_{a\mathbf{k}'}(\mathbf{r})\langle\psi_{a\mathbf{k}'}|\delta\hat{h}(\mathbf{q},\omega)|\psi_{i\mathbf{k}}\rangle}{\epsilon_{i\mathbf{k}}-\epsilon_{a\mathbf{k}'}+\omega+i\eta} \\
+ \quad & \frac{1}{N_k}\sum_{\mathbf{k},\mathbf{k}'}\delta_{\mathbf{k}',\mathbf{k}-\mathbf{q}}\sum_{i,a}\frac{(f_{a\mathbf{k}'}-f_{i\mathbf{k}})}{1+\delta_{ia}} \times \\
& \frac{\psi^{*}_{a\mathbf{k}'}(\mathbf{r})e^{-i\mathbf{q}\cdot\mathbf{r}}\psi_{i\mathbf{k}}(\mathbf{r})\langle\psi_{i\mathbf{k}}|\delta\hat{h}(\mathbf{q},\omega)|\psi_{a\mathbf{k}'}\rangle}{\epsilon_{a\mathbf{k}'}-\epsilon_{i\mathbf{k}}+\omega+i\eta},
\end{aligned} \tag{3.15}$$

in which we introduced the short-hand notation

$$\delta\hat{h}(\mathbf{q},\omega) = \frac{-i}{2c}\left(e^{i\mathbf{q}\cdot\mathbf{r}}\nabla - \nabla^{\dagger}e^{i\mathbf{q}\cdot\mathbf{r}}\right)\cdot\delta\mathbf{A}_{\mathbf{q},\mathit{eff}}(\omega) + e^{i\mathbf{q}\cdot\mathbf{r}}\delta v_{\mathbf{q},\mathit{eff}}(\mathbf{r},\omega). \tag{3.16}$$

For future reference we define the additional short-hand notations, $\hat{\mathbf{j}}_{\mathbf{q}} = -i(e^{-i\mathbf{q}\cdot\mathbf{r}}\nabla - \nabla^{\dagger}e^{-i\mathbf{q}\cdot\mathbf{r}})/2, \hat{\rho}_{\mathbf{q}} = e^{-i\mathbf{q}\cdot\mathbf{r}}$. The lattice-periodicity of $\delta\rho_{\mathbf{q}}(\mathbf{r},\omega)$ allows us to define the macroscopic induced density as

$$\delta\rho_{mac}(\mathbf{r},\omega) = e^{i\mathbf{q}\cdot\mathbf{r}}\frac{1}{V}\int_{V}\delta\rho_{\mathbf{q}}(\mathbf{r},\omega)d\mathbf{r}, \tag{3.17}$$

where the average is taken over the unit cell. In Eq. (3.15) the second term is the complex conjugate of the first one at $-\mathbf{q}$ and $-\omega$, so the induced density $\delta\rho(\mathbf{r},t)$ is real-valued, since $\delta\rho_{\mathbf{q}}(\mathbf{r},\omega) = \delta\rho^*_{-\mathbf{q}}(\mathbf{r},-\omega)$. Using time-reversal symmetry (see App. A) we can write Eq. (3.15) as

$$\begin{aligned}\delta\rho_{\mathbf{q}}(\mathbf{r},\omega) = \frac{1}{N_k}\sum_{\mathbf{k},\mathbf{k}'}\sum_{i,a} w_{i\mathbf{k}a\mathbf{k}',+}(\omega)\Bigg\{ & \delta_{\mathbf{k}',\mathbf{k}+\mathbf{q}}(\psi^*_{i\mathbf{k}}\hat{\rho}_{\mathbf{q}}\psi_{a\mathbf{k}'})\langle\psi_{a\mathbf{k}'}|\delta\hat{h}_e(\mathbf{q},\omega)|\psi_{i\mathbf{k}}\rangle + \\ & \delta_{\mathbf{k}',\mathbf{k}-\mathbf{q}}(\psi^*_{a\mathbf{k}'}\hat{\rho}_{\mathbf{q}}\psi_{i\mathbf{k}})\langle\psi_{i\mathbf{k}}|\delta\hat{h}_e(\mathbf{q},\omega)|\psi_{a\mathbf{k}'}\rangle\Bigg\} \\ +\frac{1}{N_k}\sum_{\mathbf{k},\mathbf{k}'}\sum_{i,a} w_{i\mathbf{k}a\mathbf{k}',-}(\omega)\Bigg\{ & \delta_{\mathbf{k}',\mathbf{k}+\mathbf{q}}(\psi^*_{i\mathbf{k}}\hat{\rho}_{\mathbf{q}}\psi_{a\mathbf{k}'})\langle\psi_{a\mathbf{k}'}|\delta\hat{h}_o(\mathbf{q},\omega)|\psi_{i\mathbf{k}}\rangle - \\ & \delta_{\mathbf{k}',\mathbf{k}-\mathbf{q}}(\psi^*_{a\mathbf{k}'}\hat{\rho}_{\mathbf{q}}\psi_{i\mathbf{k}})\langle\psi_{i\mathbf{k}}|\delta\hat{h}_o(\mathbf{q},\omega)|\psi_{a\mathbf{k}'}\rangle\Bigg\}. \end{aligned} \tag{3.18}$$

Here the $\mathbf{r}$-dependence of the Bloch orbitals has been implied and we have defined the "even" and "odd" components of the interaction Hamiltonian according to

$$\delta\hat{h}_e(\mathbf{q},\omega) = \frac{1}{2}[\delta\hat{h}(\mathbf{q},\omega) + \delta\hat{h}^*(-\mathbf{q},-\omega)] = \hat{\rho}_{-\mathbf{q}}\delta v_{\mathbf{q},\mathit{eff}}(\mathbf{r},\omega), \tag{3.19}$$

$$\delta\hat{h}_o(\mathbf{q},\omega) = \frac{1}{2}[\delta\hat{h}(\mathbf{q},\omega) - \delta\hat{h}^*(-\mathbf{q},-\omega)] = \frac{1}{c}\hat{\mathbf{j}}_{-\mathbf{q}}\cdot\delta\mathbf{A}_{\mathbf{q},\mathit{eff}}(\omega), \tag{3.20}$$

where $\delta\hat{h}^*(-\mathbf{q},-\omega)$ is the complex conjugate (not the Hermitian adjoint) of $\delta\hat{h}(\mathbf{q},\omega)$ at negative $\mathbf{q}$ and ω. The energy denominators and the occupation numbers in Eq. (3.15) are contained in the frequency-dependent weights,

$$w_{i\mathbf{k}a\mathbf{k}',\pm}(\omega) = \frac{f_{i\mathbf{k}} - f_{a\mathbf{k}'}}{2(1+\delta_{ia})}\left\{\frac{1}{\epsilon_{i\mathbf{k}} - \epsilon_{a\mathbf{k}'} + \omega + i\eta} \pm \frac{1}{\epsilon_{i\mathbf{k}} - \epsilon_{a\mathbf{k}'} - \omega - i\eta}\right\}. \tag{3.21}$$

In App. B we show that $w_{i\mathbf{k}a\mathbf{k}',+}(\omega)$ and $w_{i\mathbf{k}a\mathbf{k}',-}(\omega)$ are related,

$$w_{i\mathbf{k}a\mathbf{k}',-}(\omega) = -\frac{\epsilon_{i\mathbf{k}} - \epsilon_{a\mathbf{k}'}}{\omega}(w_{i\mathbf{k}a\mathbf{k}',+}(\omega) - (w_{i\mathbf{k}a\mathbf{k}',+}(0)) \tag{3.22}$$

$$w_{i\mathbf{k}a\mathbf{k}',+}(\omega) = -\frac{\epsilon_{i\mathbf{k}} - \epsilon_{a\mathbf{k}'}}{\omega}w_{i\mathbf{k}a\mathbf{k}',-}(\omega). \tag{3.23}$$

3.2.2 Induced current-density

For the induced current-density we can derive expressions along the same lines used for the induced density. The paramagnetic component of the induced current-density can be obtained as

$$\delta\mathbf{j}_p(\mathbf{r},\omega) = e^{i\mathbf{q}\cdot\mathbf{r}}\delta\mathbf{j}_{p\mathbf{q}}(\mathbf{r},\omega), \tag{3.24}$$

where $\delta\mathbf{j}_{p\mathbf{q}}(\mathbf{r},\omega)$ is lattice periodic as well, and follows from

$$\begin{aligned}
\delta\mathbf{j}_{p\mathbf{q}}(\mathbf{r},\omega) \quad = \quad & \frac{1}{N_k}\sum_{\mathbf{k},\mathbf{k}'}\delta_{\mathbf{k}',\mathbf{k}+\mathbf{q}}\sum_{i,a}\frac{(f_{i\mathbf{k}}-f_{a\mathbf{k}'})}{1+\delta_{ia}}\times \\
& \frac{\psi^*_{i\mathbf{k}}\hat{\mathbf{j}}_{\mathbf{q}}\psi_{a\mathbf{k}'}\langle\psi_{a\mathbf{k}'}|\delta\hat{h}(\mathbf{q},\omega)|\psi_{i\mathbf{k}}\rangle}{\epsilon_{i\mathbf{k}}-\epsilon_{a\mathbf{k}'}+\omega+i\eta} \\
+ \quad & \frac{1}{N_k}\sum_{\mathbf{k},\mathbf{k}'}\delta_{\mathbf{k}',\mathbf{k}-\mathbf{q}}\sum_{i,a}\frac{(f_{a\mathbf{k}'}-f_{i\mathbf{k}})}{1+\delta_{ia}}\times \\
& \frac{\psi^*_{a\mathbf{k}'}\hat{\mathbf{j}}_{\mathbf{q}}\psi_{i\mathbf{k}}\langle\psi_{i\mathbf{k}}|\delta\hat{h}(\mathbf{q},\omega)|\psi_{a\mathbf{k}'}\rangle}{\epsilon_{a\mathbf{k}'}-\epsilon_{i\mathbf{k}}+\omega+i\eta}.
\end{aligned} \tag{3.25}$$

Here the second term is the complex conjugate of the first term, but at the negative $\mathbf{q}$ and negative frequency. In the linear regime the diamagnetic contribution is given by

$$\delta\mathbf{j}_d(\mathbf{r},\omega) = e^{i\mathbf{q}\cdot\mathbf{r}}\delta\mathbf{j}_{d\mathbf{q}}(\mathbf{r},\omega), \tag{3.26}$$

where

$$\delta\mathbf{j}_{d\mathbf{q}}(\mathbf{r},\omega) = \frac{1}{c}\rho_0(\mathbf{r})\delta\mathbf{A}_{\mathbf{q},\mathit{eff}}(\omega), \tag{3.27}$$

with $\rho_0(\mathbf{r})$ real and lattice periodic. As result one finds also for the induced current-density the relation $\delta\mathbf{j}_{\mathbf{q}}(\mathbf{r},\omega) = \delta\mathbf{j}_{p\mathbf{q}}(\mathbf{r},\omega) + \delta\mathbf{j}_{d\mathbf{q}}(\mathbf{r},\omega) = \delta\mathbf{j}^*_{-\mathbf{q}}(\mathbf{r},-\omega)$ and thus a real-valued current-density $\delta\mathbf{j}(\mathbf{r},t)$. Using again the time-reversal symmetry the induced paramagnetic current-density can be written in a way very similar to Eq. (3.18),

$$\begin{aligned}
\delta\mathbf{j}_{p\mathbf{q}}(\mathbf{r},\omega) = \frac{1}{N_k}\sum_{\mathbf{k},\mathbf{k}'}\sum_{i,a} w_{i\mathbf{k}a\mathbf{k}',+}(\omega)\Bigg\{ & \delta_{\mathbf{k}',\mathbf{k}+\mathbf{q}}(\psi^*_{i\mathbf{k}}\hat{\mathbf{j}}_{\mathbf{q}}\psi_{a\mathbf{k}'})\langle\psi_{a\mathbf{k}'}|\delta\hat{h}_o(\mathbf{q},\omega)|\psi_{i\mathbf{k}}\rangle + \\
& \delta_{\mathbf{k}',\mathbf{k}-\mathbf{q}}(\psi^*_{a\mathbf{k}'}\hat{\mathbf{j}}_{\mathbf{q}}\psi_{i\mathbf{k}})\langle\psi_{i\mathbf{k}}|\delta\hat{h}_o(\mathbf{q},\omega)|\psi_{a\mathbf{k}'}\rangle)\Bigg\} \\
+\frac{1}{N_k}\sum_{\mathbf{k},\mathbf{k}'}\sum_{i,a} w_{i\mathbf{k}a\mathbf{k}',-}(\omega)\Bigg\{ & \delta_{\mathbf{k}',\mathbf{k}+\mathbf{q}}(\psi^*_{i\mathbf{k}}\hat{\mathbf{j}}_{\mathbf{q}}\psi_{a\mathbf{k}'})\langle\psi_{a\mathbf{k}'}|\delta\hat{h}_e(\mathbf{q},\omega)|\psi_{i\mathbf{k}}\rangle) - \\
& \delta_{\mathbf{k}',\mathbf{k}-\mathbf{q}}(\psi^*_{a\mathbf{k}'}\hat{\mathbf{j}}_{\mathbf{q}}\psi_{i\mathbf{k}})\langle\psi_{i\mathbf{k}}|\delta\hat{h}_e(\mathbf{q},\omega)|\psi_{a\mathbf{k}'}\rangle)\Bigg\},
\end{aligned} \tag{3.28}$$

where the weights are given by Eq. (3.21). Note that here the “even” and “odd” components of the perturbation, defined in Eqs (3.19) and (3.20), have changed positions with respect to Eq. (3.18).

For the implementation it turns out to be convenient to relate the diamagnetic component of the induced current-density to the paramagnetic one, and treat both contributions on an equal footing. Before doing this we want to refer to the case of a homogeneous electron gas perturbed by a monochromatic field $\delta\mathbf{A}(\mathbf{r},\omega)$ [1]. Indeed the induced total current-density is then given by

$$\delta\mathbf{j}(\mathbf{r},\omega) = \frac{1}{c}\int \chi_{\mathbf{jj}}(\mathbf{r},\mathbf{r}',\omega)\delta\mathbf{A}(\mathbf{r}',\omega)d\mathbf{r}' + \frac{1}{c}\rho_0(\mathbf{r})\delta\mathbf{A}(\mathbf{r},\omega), \tag{3.29}$$

where the exact current-current response function $\chi_{\mathbf{jj}}(\mathbf{r},\mathbf{r}',\omega)$ only depends on the distance $|\mathbf{r}-\mathbf{r}'|$. Its Fourier transform can be expressed in the following way,

$$\chi_{\mathbf{jj},\mu\nu}(\mathbf{q},\omega) = \chi_L(\mathbf{q},\omega)\frac{q_\mu q_\nu}{|\mathbf{q}|^2} + \chi_T(\mathbf{q},\omega)(\delta_{\mu\nu} - \frac{q_\mu q_\nu}{|\mathbf{q}|^2}), \tag{3.30}$$

with the longitudinal and the transverse components $\chi_L(\mathbf{q},\omega)$ and $\chi_T(\mathbf{q},\omega)$ satisfying [1]

$$\lim_{\mathbf{q}\to 0}\chi_T(\mathbf{q},\omega=0) = -\rho_0 \tag{3.31}$$

$$\chi_L(\mathbf{q},\omega=0) = -\rho_0. \tag{3.32}$$

For the value of $\chi_T(\mathbf{q},\omega=0)$ at finite q the corrections to this limit are of order q^2. In real space we can therefore write

$$\chi_{\mathbf{jj}}(\mathbf{r},\mathbf{r}',0) = -\rho_0\delta(\mathbf{r}-\mathbf{r}') + \triangle\chi_T(\mathbf{r},\mathbf{r}',0), \tag{3.33}$$

where $\triangle\chi_T(\mathbf{r},\mathbf{r}',0)$ is purely transverse, and hence responsible for the weak diamagnetism first calculated by Landau. Here we deal with two limits, lim $\mathbf{q}\to 0$ and lim $\omega\to 0$. The value of $\chi_T(\mathbf{q},\omega)$ depends on the order in which one takes the limits, since it is nonanalytic in the point $(0,0)$ in the q-ω plane. In order to relate the diamagnetic and the paramagnetic contributions to the current-current response function, one has to consider first the limit $\omega\to 0$ at finite q, and only then take $\mathbf{q}\to 0$, as reported in Fig. 3.1. Here the term $\left\{\chi_{\mathbf{jj}}(\mathbf{q}\to 0,\omega=0) - \chi_{\mathbf{jj}}(\mathbf{q},\omega=0)\right\}$ represents the term $\triangle\chi_T(\mathbf{r},\mathbf{r}',0)$ of Eq. (3.33) in its Fourier representation. In the absence of magnetic fields the vector potential is regular in $q=0$ for any ω, hence the term $\triangle\chi_T(\mathbf{q},0)$, which is proportional to q^2, does not contribute to the induced current-density for vanishing q. A relation similar to Eq. (3.33) holds for crystalline systems,

$$\chi_{\mathbf{jjq}}(\mathbf{r},\mathbf{r}',0) = -\rho_0\delta(\mathbf{r}-\mathbf{r}') + \triangle\chi_{\mathbf{q}}(\mathbf{r},\mathbf{r}',0), \tag{3.34}$$

where again $\triangle\chi_{\mathbf{q}}(\mathbf{r},\mathbf{r}',0)$ is transverse and of the order of q^2 [1, 56]. Therefore, we can introduce the following relation for the diamagnetic current-density,

$$\delta\mathbf{j}_{d\mathbf{q}}(\mathbf{r},\omega) = -\delta\mathbf{j}^0_{p\mathbf{q}}(\mathbf{r},\omega) + \triangle\mathbf{j}_{d\mathbf{q}}(\mathbf{r},\omega), \tag{3.35}$$

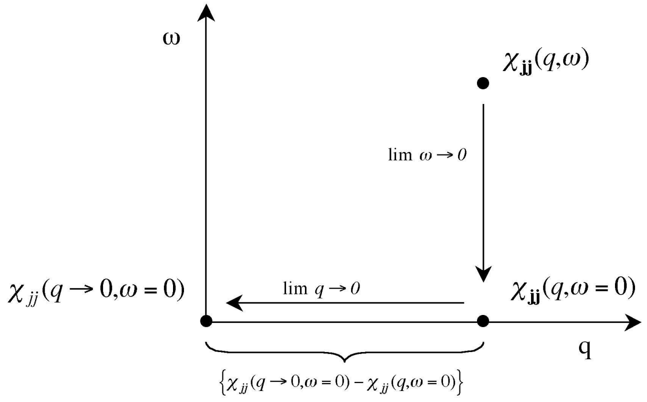

Figure 3.1: The order of the limits needed to relate diamagnetic and paramagnetic contributions to the current-current response function.

where $\delta\mathbf{j}^0_{p\mathbf{q}}(\mathbf{r},\omega)$ is the paramagnetic current-density obtained from the static response, at finite q, to the dynamic perturbation,

$$\begin{aligned}\delta\mathbf{j}^0_{p\mathbf{q}}(\mathbf{r},\omega) &= \frac{1}{N_k}\sum_{\mathbf{k},\mathbf{k}'}\sum_{i,a} w_{i\mathbf{k}a\mathbf{k}',+}(0)) \times \\ &\quad \Big\{\delta_{\mathbf{k}',\mathbf{k}+\mathbf{q}}(\psi^*_{i\mathbf{k}}\hat{\mathbf{j}}_{\mathbf{q}}\psi_{a\mathbf{k}'})\langle\psi_{a\mathbf{k}'}|\delta\hat{h}_o(\mathbf{q},\omega)|\psi_{i\mathbf{k}}\rangle + \\ &\quad \delta_{\mathbf{k}',\mathbf{k}-\mathbf{q}}(\psi^*_{a\mathbf{k}'}\hat{\mathbf{j}}_{\mathbf{q}}\psi_{i\mathbf{k}})\langle\psi_{i\mathbf{k}}|\delta\hat{h}_o(\mathbf{q},\omega)|\psi_{a\mathbf{k}'}\rangle\Big\}, \end{aligned} \tag{3.36}$$

and $\triangle\mathbf{j}_{d\mathbf{q}}(\mathbf{r},\omega)$ is by construction equal to $\delta\mathbf{j}_{d\mathbf{q}}(\mathbf{r},\omega) + \delta\mathbf{j}^0_{p\mathbf{q}}(\mathbf{r},\omega)$, and gives rise to contributions analogous to the Landau diamagnetism. Since we do not treat magnetic fields in this derivation, only the first term on the right-hand side of Eq. (3.35) is considered and $\triangle\mathbf{j}_{d\mathbf{q}}(\mathbf{r},\omega)$ is neglected in the sequel. Combining Eq. (3.36) with Eq. (3.28) for the paramagnetic current-density, the induced physical current is then obtained from

$$\begin{aligned}
\delta\mathbf{j}_{\mathbf{q}}(\mathbf{r},\omega) &= \frac{1}{N_k}\sum_{\mathbf{k},\mathbf{k}'}\sum_{i,a} w_{i\mathbf{k}a\mathbf{k}',-}(\omega)\times \\
&\quad \Big\{\delta_{\mathbf{k}',\mathbf{k}+\mathbf{q}}(\psi^*_{i\mathbf{k}}\hat{\mathbf{j}}_{\mathbf{q}}\psi_{a\mathbf{k}'})\langle\psi_{a\mathbf{k}'}|\delta\hat{h}_e(\mathbf{q},\omega)|\psi_{i\mathbf{k}}\rangle - \\
&\quad \delta_{\mathbf{k}',\mathbf{k}-\mathbf{q}}(\psi^*_{a\mathbf{k}'}\hat{\mathbf{j}}_{\mathbf{q}}\psi_{i\mathbf{k}})\langle\psi_{i\mathbf{k}}|\delta\hat{h}_e(\mathbf{q},\omega)|\psi_{a\mathbf{k}'}\rangle\Big\} \\
&+ \frac{1}{N_k}\sum_{\mathbf{k},\mathbf{k}'}\sum_{i,a}(w_{i\mathbf{k}a\mathbf{k}',+}(\omega) - w_{i\mathbf{k}a\mathbf{k}',+}(0))\times \\
&\quad \Big\{\delta_{\mathbf{k}',\mathbf{k}+\mathbf{q}}(\psi^*_{i\mathbf{k}}\hat{\mathbf{j}}_{\mathbf{q}}\psi_{a\mathbf{k}'})\langle\psi_{a\mathbf{k}'}|\delta\hat{h}_o(\mathbf{q},\omega)|\psi_{i\mathbf{k}}\rangle + \\
&\quad \delta_{\mathbf{k}',\mathbf{k}-\mathbf{q}}(\psi^*_{a\mathbf{k}'}\hat{\mathbf{j}}_{\mathbf{q}}\psi_{i\mathbf{k}})\langle\psi_{i\mathbf{k}}|\delta\hat{h}_o(\mathbf{q},\omega)|\psi_{a\mathbf{k}'}\rangle\Big\}. \qquad (3.37)
\end{aligned}$$

3.2.3 Response functions

Interband contribution

We will first consider the interband contributions to the induced density and current-density which are obtained from the terms with $a \neq i$ in Eqs (3.18) and (3.37). They can then be written in the following concise form,

$$\left(\begin{array}{c} \delta\rho^{inter}_{\mathbf{q}} \\ \hline i\delta\mathbf{j}^{inter}_{\mathbf{q}}/\omega \end{array}\right) = \left(\begin{array}{c|c} \chi^{inter}_{\rho\rho\mathbf{q}} & -i\chi^{inter}_{\rho\mathbf{j}\mathbf{q}}/\omega \\ \hline i\chi^{inter}_{\mathbf{j}\rho\mathbf{q}}/\omega & (\chi^{inter}_{\mathbf{j}\mathbf{j}\mathbf{q}} - \chi^{inter,0}_{\mathbf{j}\mathbf{j}\mathbf{q}})/\omega^2 \end{array}\right)\cdot\left(\begin{array}{c} \delta v_{\mathbf{q},\mathit{eff}} \\ \hline i\omega\delta\mathbf{A}_{\mathbf{q},\mathit{eff}}/c \end{array}\right), \qquad (3.38)$$

by inserting the equations for the "even" and for the "odd" perturbation, Eqs (3.19) and (3.20). Here the matrix-vector product also includes an integration over a real space coordinate, where the various response kernels take simple forms by using the relations (3.22) and (3.23) for $w_{i\mathbf{k}a\mathbf{k}',+}(\omega)$ and $w_{i\mathbf{k}a\mathbf{k}',-}(\omega)$. For the interband contribution to the density-density response function, $\chi^{inter}_{\rho\rho\mathbf{q}}$, we find

$$\begin{aligned}
\chi^{inter}_{\rho\rho\mathbf{q}}(\mathbf{r},\mathbf{r}',\omega) &= \frac{1}{N_k}\sum_{\mathbf{k},\mathbf{k}'}\sum_{ia} w_{i\mathbf{k}a\mathbf{k}',+}(\omega)\times \\
&\quad \Big\{\delta_{\mathbf{k}'\mathbf{k}+\mathbf{q}}(\psi^*_{i\mathbf{k}}(\mathbf{r})\hat{\rho}_{\mathbf{q}}\psi_{a\mathbf{k}'}(\mathbf{r}))\,(\psi^*_{a\mathbf{k}'}(\mathbf{r}')\hat{\rho}'_{-\mathbf{q}}\psi_{i\mathbf{k}}(\mathbf{r}')) + \\
&\quad \delta_{\mathbf{k}'\mathbf{k}-\mathbf{q}}(\psi^*_{a\mathbf{k}'}(\mathbf{r})\hat{\rho}_{\mathbf{q}}\psi_{i\mathbf{k}}(\mathbf{r}))\,(\psi^*_{i\mathbf{k}}(\mathbf{r}')\hat{\rho}'_{-\mathbf{q}}\psi_{a\mathbf{k}'}(\mathbf{r}'))\Big\}. \qquad (3.39)
\end{aligned}$$

For the contributions to the density-current and current-density response functions, $\chi^{inter}_{\rho\mathbf{jq}}$ and $\chi^{inter}_{\mathbf{j}\rho\mathbf{q}}$, the equations become

$$
\begin{aligned}
-\frac{i}{\omega}\chi^{inter}_{\rho\mathbf{jq}}(\mathbf{r},\mathbf{r}',\omega) &= \frac{1}{N_k}\sum_{\mathbf{k},\mathbf{k}'}\sum_{ia} w_{i\mathbf{k}a\mathbf{k}',+}(\omega)\times \\
&\left\{\delta_{\mathbf{k}'\mathbf{k}+\mathbf{q}}(\psi^*_{i\mathbf{k}}(\mathbf{r})\hat{\rho}_{\mathbf{q}}\psi_{a\mathbf{k}'}(\mathbf{r}))\,\frac{i\psi^*_{a\mathbf{k}'}(\mathbf{r}')\hat{\mathbf{j}}'_{-\mathbf{q}}\psi_{i\mathbf{k}}(\mathbf{r}')}{\epsilon_{i\mathbf{k}}-\epsilon_{a\mathbf{k}'}}+\right. \\
&\left.\delta_{\mathbf{k}'\mathbf{k}-\mathbf{q}}(\psi^*_{a\mathbf{k}'}(\mathbf{r})\hat{\rho}_{\mathbf{q}}\psi_{i\mathbf{k}}(\mathbf{r}))\,\frac{i\psi^*_{i\mathbf{k}}(\mathbf{r}')\hat{\mathbf{j}}'_{-\mathbf{q}}\psi_{a\mathbf{k}'}(\mathbf{r}')}{\epsilon_{a\mathbf{k}'}-\epsilon_{i\mathbf{k}}}\right\}, \qquad (3.40) \\
\frac{i}{\omega}\chi^{inter}_{\mathbf{j}\rho\mathbf{q}}(\mathbf{r},\mathbf{r}',\omega) &= \frac{1}{N_k}\sum_{\mathbf{k},\mathbf{k}'}\sum_{ia} w_{i\mathbf{k}a\mathbf{k}',+}(\omega)\times \\
&\left\{\delta_{\mathbf{k}'\mathbf{k}+\mathbf{q}}\frac{i\psi^*_{i\mathbf{k}}(\mathbf{r})\hat{\mathbf{j}}_{\mathbf{q}}\psi_{a\mathbf{k}'}(\mathbf{r})}{\epsilon_{a\mathbf{k}'}-\epsilon_{i\mathbf{k}}}\,(\psi^*_{a\mathbf{k}'}(\mathbf{r}')\hat{\rho}'_{-\mathbf{q}}\psi_{i\mathbf{k}}(\mathbf{r}'))+\right. \\
&\left.\delta_{\mathbf{k}'\mathbf{k}-\mathbf{q}}\frac{i\psi^*_{a\mathbf{k}'}(\mathbf{r})\hat{\mathbf{j}}_{\mathbf{q}}\psi_{i\mathbf{k}}(\mathbf{r})}{\epsilon_{i\mathbf{k}}-\epsilon_{a\mathbf{k}'}}\,(\psi^*_{i\mathbf{k}}(\mathbf{r}')\hat{\rho}'_{-\mathbf{q}}\psi_{a\mathbf{k}'}(\mathbf{r}'))\right\}, \qquad (3.41)
\end{aligned}
$$

and finally for the interband contribution to the combination of the current-current response function and its static value, respectively $\chi^{inter}_{\mathbf{jjq}}$ and $\chi^{inter,0}_{\mathbf{jjq}}$, the result is

$$
\begin{aligned}
\frac{1}{\omega^2}(\chi^{inter}_{\mathbf{jjq}}(\mathbf{r},\mathbf{r}',\omega)-\chi^{inter}_{\mathbf{jjq}}(\mathbf{r},\mathbf{r}',\omega=0)) &= \frac{1}{N_k}\sum_{\mathbf{k},\mathbf{k}'}\sum_{ia} w_{i\mathbf{k}a\mathbf{k}',+}(\omega)\times \\
\left\{\delta_{\mathbf{k}'\mathbf{k}+\mathbf{q}}\frac{i\psi^*_{i\mathbf{k}}(\mathbf{r})\hat{\mathbf{j}}_{\mathbf{q}}\psi_{a\mathbf{k}'}(\mathbf{r})}{\epsilon_{a\mathbf{k}'}-\epsilon_{i\mathbf{k}}}\otimes\frac{i\psi^*_{a\mathbf{k}'}(\mathbf{r}')\hat{\mathbf{j}}'_{-\mathbf{q}}\psi_{i\mathbf{k}}(\mathbf{r}')}{\epsilon_{i\mathbf{k}}-\epsilon_{a\mathbf{k}'}}+\right.& \\
\left.\delta_{\mathbf{k}'\mathbf{k}-\mathbf{q}}\frac{i\psi^*_{a\mathbf{k}'}(\mathbf{r})\hat{\mathbf{j}}_{\mathbf{q}}\psi_{i\mathbf{k}}(\mathbf{r})}{\epsilon_{i\mathbf{k}}-\epsilon_{a\mathbf{k}'}}\otimes\frac{i\psi^*_{i\mathbf{k}}(\mathbf{r}')\hat{\mathbf{j}}'_{-\mathbf{q}}\psi_{a\mathbf{k}'}(\mathbf{r}')}{\epsilon_{a\mathbf{k}'}-\epsilon_{i\mathbf{k}}}\right\}.& \qquad (3.42)
\end{aligned}
$$

The ω-dependence in the above expressions for the various interband contributions is governed by the common factor $w_{i\mathbf{k}a\mathbf{k}',+}(\omega)$, which is a well-behaved function of ω and q for ω smaller than the (indirect) energy gap between the different occupied and unoccupied bands. The various interband contributions to the response functions have then the following ω-dependence,

$$
\begin{aligned}
\chi^{inter}_{\rho\rho\mathbf{q}} &\propto 1, \\
\chi^{inter}_{\rho\mathbf{jq}}, \chi^{inter}_{\mathbf{j}\rho\mathbf{q}} &\propto \omega, \\
(\chi^{inter}_{\mathbf{jjq}} - \chi^{0,inter}_{\mathbf{jjq}}) &\propto \omega^2.
\end{aligned}
$$

In the limit of vanishing q the set of equations (3.39 - 3.42) reduces to the one used in the case of nonmetallic crystalline systems [30, 31] for which we need to consider only fully occupied bands i and fully unoccupied bands a. However, in metallic crystals, we have to consider also the contribution from partially occupied and/or unoccupied bands, for which $\mathbf{k}$-space integrations are restricted to just a part of the Brillouin zone cut off by the Fermi surface.

Intraband contribution

Let us consider now the intraband contributions to Eqs (3.18) and (3.37) that are given by the terms with $a = i$ in the summation over the energy bands. By changing variables from $\{\mathbf{k}', \mathbf{k}\} = \{\mathbf{k} - \mathbf{q}, \mathbf{k}\}$ to $\{\mathbf{k}, \mathbf{k} + \mathbf{q}\}$ in the second and fourth terms in Eq. (3.18) we obtain

$$\begin{aligned}
\delta\rho^{intra}_{\mathbf{q}}(\mathbf{r},\omega) &= \frac{1}{N_k}\sum_{i,\mathbf{k}} 2w_{i\mathbf{k}i\mathbf{k}+\mathbf{q},+}(\omega) \times \\
&\quad (\psi^*_{i\mathbf{k}}(\mathbf{r})\hat{\rho}_{\mathbf{q}}\psi_{i\mathbf{k}+\mathbf{q}}(\mathbf{r}))\,\langle\psi_{i\mathbf{k}+\mathbf{q}}|\delta\hat{h}_e(\mathbf{q},\omega)|\psi_{i\mathbf{k}}\rangle \\
&+ \frac{1}{N_k}\sum_{i,\mathbf{k}} 2w_{i\mathbf{k}i\mathbf{k}+\mathbf{q},-}(\omega) \times \\
&\quad (\psi^*_{i\mathbf{k}}(\mathbf{r})\hat{\rho}_{\mathbf{q}}\psi_{a\mathbf{k}+\mathbf{q}}(\mathbf{r}))\,\langle\psi_{i\mathbf{k}+\mathbf{q}}|\delta\hat{h}_o(\mathbf{q},\omega)|\psi_{i\mathbf{k}}\rangle, \qquad (3.43)
\end{aligned}$$

where we have used that $w_{i\mathbf{k}i\mathbf{k}+\mathbf{q},\pm}(\omega) = \pm w_{i\mathbf{k}+\mathbf{q}i\mathbf{k},\pm}(\omega)$. Operating in a similar way in Eq. (3.37) for the induced current-density we arrive at

$$\begin{aligned}
\delta\mathbf{j}^{intra}_{\mathbf{q}}(\mathbf{r},\omega) &= \frac{1}{N_k}\sum_{i,\mathbf{k}} 2w_{i\mathbf{k}i\mathbf{k}+\mathbf{q},-}(\omega) \times \\
&\quad (\psi^*_{i\mathbf{k}}(\mathbf{r})\hat{\mathbf{j}}_{\mathbf{q}}\psi_{i\mathbf{k}+\mathbf{q}}(\mathbf{r}))\,\langle\psi_{i\mathbf{k}+\mathbf{q}}|\delta\hat{h}_e(\mathbf{q},\omega)|\psi_{i\mathbf{k}}\rangle \\
&+ \frac{1}{N_k}\sum_{i,\mathbf{k}} 2(w_{i\mathbf{k}a\mathbf{k}+\mathbf{q},+}(\omega) - w_{i\mathbf{k}i\mathbf{k}+\mathbf{q},+}(0)) \times \\
&\quad (\psi^*_{i\mathbf{k}}(\mathbf{r})\hat{\mathbf{j}}_{\mathbf{q}}\psi_{i\mathbf{k}+\mathbf{q}}(\mathbf{r}))\,\langle\psi_{i\mathbf{k}+\mathbf{q}}|\delta\hat{h}_o(\mathbf{q},\omega)|\psi_{i\mathbf{k}}\rangle. \qquad (3.44)
\end{aligned}$$

These expressions can be written in the following concise form,

$$i\omega\left(\begin{array}{c} \omega/q\,\delta\rho^{intra}_{\mathbf{q}} \\ \hline \delta\mathbf{j}^{intra}_{\mathbf{q}} \end{array}\right) = \left(\begin{array}{c|c} \omega^2/q^2\,\chi^{intra}_{\rho\rho\mathbf{q}} & \omega/q\,\chi^{intra}_{\rho\mathbf{j}\mathbf{q}} \\ \hline \omega/q\,\chi^{intra}_{\mathbf{j}\rho\mathbf{q}} & \chi^{intra}_{\mathbf{j}\mathbf{j}\mathbf{q}} - \chi^{intra,0}_{\mathbf{j}\mathbf{j}\mathbf{q}} \end{array}\right)\cdot\left(\begin{array}{c} iq\delta v_{\mathbf{q},\mathit{eff}} \\ \hline i\omega\delta\mathbf{A}_{\mathbf{q},\mathit{eff}}/c \end{array}\right), \qquad (3.45)$$

where the various response kernels are given in the following set of equations. For the intraband contribution to the density-density response kernel, $\chi^{intra}_{\rho\rho\mathbf{q}}$, we get

$$\begin{aligned}
\frac{\omega^2}{q^2}\chi^{intra}_{\rho\rho\mathbf{q}}(\mathbf{r},\mathbf{r}',\omega) &= \frac{2}{N_k}\sum_{i\mathbf{k}} \frac{\omega^2}{q^2} w_{i\mathbf{k}i\mathbf{k}+\mathbf{q},+}(\omega) \times \\
&\quad (\psi^*_{i\mathbf{k}}(\mathbf{r})\hat{\rho}_{\mathbf{q}}\psi_{i\mathbf{k}+\mathbf{q}}(\mathbf{r}))\,(\psi^*_{i\mathbf{k}+\mathbf{q}}(\mathbf{r}')\hat{\rho}'_{-\mathbf{q}}\psi_{i\mathbf{k}}(\mathbf{r}')). \qquad (3.46)
\end{aligned}$$

Similarly for the contributions to the density-current and current-density kernels, $\chi_{\rho\mathbf{j}\mathbf{q}}^{intra}$ and $\chi_{\mathbf{j}\rho\mathbf{q}}^{intra}$, the expressions are

$$\begin{aligned}
\frac{\omega}{q}\chi_{\rho\mathbf{j}\mathbf{q}}^{intra}(\mathbf{r},\mathbf{r}',\omega) &= \frac{2}{N_k}\sum_{i\mathbf{k}}\frac{\omega^2}{q}\frac{w_{i\mathbf{k}i\mathbf{k}+\mathbf{q},+}(\omega)}{\epsilon_{i\mathbf{k}+\mathbf{q}}-\epsilon_{i\mathbf{k}}}\times \\
&\quad (\psi_{i\mathbf{k}}^*(\mathbf{r})\hat{\rho}_{\mathbf{q}}\psi_{i\mathbf{k}+\mathbf{q}}(\mathbf{r}))\,(\psi_{i\mathbf{k}+\mathbf{q}}^*(\mathbf{r}')\hat{\mathbf{j}}'_{-\mathbf{q}}\psi_{i\mathbf{k}}(\mathbf{r}')), \qquad (3.47)\\
\frac{\omega}{q}\chi_{\mathbf{j}\rho\mathbf{q}}^{intra}(\mathbf{r},\mathbf{r}',\omega) &= \frac{2}{N_k}\sum_{i\mathbf{k}}\frac{\omega^2}{q}\frac{w_{i\mathbf{k}i\mathbf{k}+\mathbf{q},+}(\omega)}{\epsilon_{i\mathbf{k}+\mathbf{q}}-\epsilon_{i\mathbf{k}}}\times \\
&\quad (\psi_{i\mathbf{k}}^*(\mathbf{r})\hat{\mathbf{j}}_{\mathbf{q}}\psi_{i\mathbf{k}+\mathbf{q}}(\mathbf{r}))\,(\psi_{i\mathbf{k}+\mathbf{q}}^*(\mathbf{r}')\hat{\rho}'_{-\mathbf{q}}\psi_{i\mathbf{k}}(\mathbf{r}')). \qquad (3.48)
\end{aligned}$$

Finally, for the intraband contribution to the combination of the current-current response function and its static value, respectively $\chi_{\mathbf{jjq}}^{intra}$ and $\chi_{\mathbf{jjq}}^{intra,0}$, we have

$$\begin{aligned}
\chi_{\mathbf{jjq}}^{intra}(\mathbf{r},\mathbf{r}',\omega)-\chi_{\mathbf{jjq}}^{intra}(\mathbf{r},\mathbf{r}',\omega=0) &= \frac{2}{N_k}\sum_{i\mathbf{k}}\omega^2\frac{w_{i\mathbf{k}i\mathbf{k}+\mathbf{q},+}(\omega)}{(\epsilon_{i\mathbf{k}+\mathbf{q}}-\epsilon_{i\mathbf{k}})^2}\times \\
&\quad (\psi_{i\mathbf{k}}^*(\mathbf{r})\hat{\mathbf{j}}_{\mathbf{q}}\psi_{i\mathbf{k}+\mathbf{q}}(\mathbf{r}))\otimes(\psi_{i\mathbf{k}+\mathbf{q}}^*(\mathbf{r}')\hat{\mathbf{j}}'_{-\mathbf{q}}\psi_{i\mathbf{k}}(\mathbf{r}')). \qquad (3.49)
\end{aligned}$$

In this thesis we will only consider the optical limit, i.e., the limit of vanishing q (but finite ω), for which we can evaluate the weights $w_{i\mathbf{k}i\mathbf{k}+\mathbf{q},+}(\omega)$ using the two relations

$$\begin{aligned}
(\epsilon_{i\mathbf{k}}-\epsilon_{i\mathbf{k}+\mathbf{q}}) &\simeq -q(\nabla_{\mathbf{k}}\epsilon_{i\mathbf{k}}\cdot\hat{\mathbf{q}}), \qquad (3.50)\\
(f_{i\mathbf{k}}-f_{i\mathbf{k}+\mathbf{q}}) = (f(\epsilon_{i\mathbf{k}})-f(\epsilon_{i\mathbf{k}+\mathbf{q}})) &\simeq -q\frac{df}{d\epsilon}(\nabla_{\mathbf{k}}\epsilon_{i\mathbf{k}}\cdot\hat{\mathbf{q}}). \qquad (3.51)
\end{aligned}$$

We can then write for the common factor $2\omega^2/q^2\,w_{i\mathbf{k}i\mathbf{k}+\mathbf{q},+}(\omega)$,

$$2\,\frac{\omega^2}{q^2}w_{i\mathbf{k}i\mathbf{k}+\mathbf{q},+}(\omega) \simeq \frac{df}{d\epsilon}\,\frac{\omega^2(\nabla_{\mathbf{k}}\epsilon_{i\mathbf{k}}\cdot\hat{\mathbf{q}})^2}{q^2(\nabla_{\mathbf{k}}\epsilon_{i\mathbf{k}}\cdot\hat{\mathbf{q}})^2-(\omega+i\eta)^2}. \qquad (3.52)$$

The nonanalytic behavior of the intraband response functions at the origin of the q-ω plane is now made explicit. In the limit of q to zero at finite ω this factor becomes independent of ω and equal to $df/d\epsilon\,(\nabla_{\mathbf{k}}\epsilon_{i\mathbf{k}}\cdot\hat{\mathbf{q}})^2$, whereas in the reverse order of limits the factor is zero. It immediately becomes clear that the intraband response functions show the following ω and q-dependence at small q but finite ω,

$$\begin{aligned}
\chi_{\rho\rho\mathbf{q}}^{intra} &\propto q^2/\omega^2,\\
\chi_{\rho\mathbf{j}\mathbf{q}}^{intra},\chi_{\mathbf{j}\rho\mathbf{q}}^{intra} &\propto q/\omega,\\
(\chi_{\mathbf{jjq}}^{intra}-\chi_{\mathbf{jjq}}^{0,intra}) &\propto 1.
\end{aligned}$$

3.2.4 The SCF equations

In the previous section we derived expressions for the induced density and current-density as result of a given set of vector and scalar potentials. To complete the self-consistent-field scheme of Kohn and Sham [8] we have to express the induced potentials in terms of the induced density and current-density. In order to do this it is important to separate microscopic and macroscopic components of these densities and to show how they lead to the microscopic and macroscopic contributions to the induced potentials. We will do this first for the Hartree term and then for the exchange-correlation contributions. We start by identifying the microscopic and macroscopic components of the density. Since both the inter- and intraband contributions to $\delta\rho_{\mathbf{q}}(\mathbf{r},\omega)$ are lattice periodic, we can write the total induced density as a Fourier series expansion,

$$\delta\rho(\mathbf{r},\omega) = e^{i\mathbf{q}\cdot\mathbf{r}}\delta\rho_{\mathbf{q}}(\mathbf{r},\omega) = e^{i\mathbf{q}\cdot\mathbf{r}}\sum_{\mathbf{G}}\delta\rho_{\mathbf{q}+\mathbf{G}}(\omega)e^{i\mathbf{G}\cdot\mathbf{r}}. \tag{3.53}$$

Here the term with $\mathbf{G} = 0$ is equal to the macroscopic density defined in Eq. (3.17). The remaining terms with $\mathbf{G} \neq 0$ together constitute the microscopic density. One usually assumes [2,35] that a similar expansion exists for the Hartree potential which can then be written as

$$\delta v_H(\mathbf{r},\omega) = 4\pi\, e^{i\mathbf{q}\cdot\mathbf{r}}\left(\frac{\delta\rho_{\mathbf{q}+\mathbf{0}}(\omega)}{q^2} + \sum_{\mathbf{G}\neq\mathbf{0}}\frac{\delta\rho_{\mathbf{q}+\mathbf{G}}(\omega)}{|\mathbf{q}+\mathbf{G}|^2}e^{i\mathbf{G}\cdot\mathbf{r}}\right). \tag{3.54}$$

One can then define the microscopic scalar potential $\delta v_{H,mic}$ as

$$\delta v_{H,mic}(\mathbf{r},\omega) = 4\pi e^{i\mathbf{q}\cdot\mathbf{r}}\sum_{\mathbf{G}\neq\mathbf{0}}\frac{\delta\rho_{\mathbf{q}+\mathbf{G}}(\omega)}{|\mathbf{q}+\mathbf{G}|^2}e^{i\mathbf{G}\cdot\mathbf{r}}, \tag{3.55}$$

whereas the term $e^{i\mathbf{q}\cdot\mathbf{r}}\delta v_{\mathbf{q}+\mathbf{0}} \doteq 4\pi e^{i\mathbf{q}\cdot\mathbf{r}}\delta\rho_{\mathbf{q}+\mathbf{0}}/q^2$ represents a macroscopic field. In the TDCDFT approach this term will be gauge transformed to a macroscopic vector potential,

$$\frac{i\omega}{c}\delta\mathbf{A}_{H,mac}(\mathbf{r},\omega) = \nabla(e^{i\mathbf{q}\cdot\mathbf{r}}\delta v_{\mathbf{q}+\mathbf{0}}(\omega)) = 4\pi i\hat{\mathbf{q}}\left(\frac{\delta\rho_{\mathbf{q}+\mathbf{0}}(\omega)}{q}\right)e^{i\mathbf{q}\cdot\mathbf{r}}. \tag{3.56}$$

As Kootstra *et al.* have shown, this field is sample-shape dependent. In their approach this contribution is, by construction, already contained in the total macroscopic vector potential, which describes the macroscopic electric field, and which is kept fixed (Eqs. (3.8) and (3.9)) [30]. Note that we do not evaluate the microscopic scalar potential using the Fourier series expansion, as this series converges extremely slowly for real densities. Instead we make use of the screening technique described by Kootstra *et al.* [30]. In the effective one-electron scheme of Kohn and Sham the effective potentials $\left\{\delta v_{\mathit{eff}}, \delta\mathbf{A}_{\mathit{eff}}\right\}$ also contain exchange-correlation contributions. For the total exchange-correlation scalar potential we write

$$\delta v_{xc}(\mathbf{r},\omega) = \int f_{xc}(\mathbf{r},\mathbf{r}',\omega)\delta\rho(\mathbf{r}',\omega)d\mathbf{r}', \tag{3.57}$$

in which we will use the adiabatic local density approximation (ALDA) for the exchange-correlation kernel $f_{xc}(\mathbf{r},\mathbf{r}',\omega)$,

$$f_{xc}(\mathbf{r},\mathbf{r}',\omega) = f_{xc}^{ALDA}(\mathbf{r},\mathbf{r}') = \delta(\mathbf{r}-\mathbf{r}')\left.\frac{dv_{xc}^{LDA}(\rho)}{d\rho}\right|_{\rho=\rho_0(\mathbf{r})}. \tag{3.58}$$

In our scheme all other exchange-correlation effects are to be included in the exchange-correlation vector potential. As the induced density is a functional of the induced current-density through the continuity equation, we can formally write this vector potential as a pure functional of the induce current-density,

$$\delta\mathbf{A}_{xc}(\mathbf{r},\omega) = \int \mathbf{f}_{xc}(\mathbf{r},\mathbf{r}',\omega)\cdot\delta\mathbf{j}(\mathbf{r}',\omega)d\mathbf{r}'. \tag{3.59}$$

As in Ref. [30], we split also these contributions into microscopic and macroscopic components. To achieve this we choose to retain only terms linear in the microscopic induced density in the microscopic exchange-correlation scalar potential, and to gauge transform all terms linear in the macroscopic induced density and those linear in the induced current-density to the exchange-correlation vector potential. This is possible because we consider only the linear response. In this way we keep contact with the ordinary TDDFT formulation. This vector potential will contain in general both microscopic and macroscopic components. In the gauge described above the effective potentials take the following form,

$$\delta v_{\mathit{eff},mic} = \delta v_{H,mic} + \delta v_{xc}^{ALDA}[\delta\rho_{mic}], \tag{3.60}$$

$$\delta\mathbf{A}_{\mathit{eff}} = \delta\mathbf{A}_{mac} + \delta\mathbf{A}_{xc}[\delta\mathbf{j}] - \frac{ic}{\omega}\nabla\delta v_{xc}^{ALDA}[\delta\rho_{mac}]. \tag{3.61}$$

Using Eq. (3.57) the last term in Eq. (3.61) can be written as

$$-\frac{ic}{\omega}\nabla\delta v_{xc}^{ALDA}[\delta\rho_{mac}](\mathbf{r},\omega) = -\frac{ic}{\omega}\left[(i\mathbf{q}+\nabla)\frac{dv_{xc}^{LDA}}{d\rho}(\rho_0(\mathbf{r}))\right]\delta\rho_{\mathbf{q}+\mathbf{0}}(\omega)e^{i\mathbf{q}\cdot\mathbf{r}}. \tag{3.62}$$

In the ALDA approximation used in this chapter we will neglect the exchange-correlation contribution $\delta\mathbf{A}_{xc}[\delta\mathbf{j}]$ in the effective vector potential, and retain only the macroscopic part of the other terms. Then Eq. (3.61) becomes

$$\delta\mathbf{A}_{\mathit{eff},mac}(\mathbf{r},\omega) = \delta\mathbf{A}_{mac}(\mathbf{r},\omega) + c\hat{\mathbf{q}}\frac{q}{\omega}\left(\frac{1}{V}\int_V \frac{dv_{xc}^{LDA}}{d\rho}(\rho_0(\mathbf{r}))d\mathbf{r}\right)\delta\rho_{\mathbf{q}+\mathbf{0}}e^{i\mathbf{q}\cdot\mathbf{r}}, \tag{3.63}$$

where in calculating the cell average the contribution of the gradient in Eq. (3.62) vanishes due to the lattice-periodicity of the ground-state density $\rho_0(\mathbf{r})$.

The separation of the induced potentials in microscopic and macroscopic terms as discussed above is based on the separation of the induced density into microscopic and macroscopic components. We will now describe how inter- and intraband processes contribute to the microscopic and macroscopic parts of the induced density. To achieve this we refer to Eq. (3.15) and analyze first the factor $\psi^*_{i\mathbf{k}}(\mathbf{r})\hat{\rho}_{\mathbf{q}}\psi_{a\mathbf{k}+\mathbf{q}}(\mathbf{r})$. Using the expression for the Bloch functions and the definition of the $\hat{\rho}_{\mathbf{q}}$ operator, it becomes evident that this factor is lattice periodic and can be written as a Fourier series expansion,

$$\begin{aligned}\psi^*_{i\mathbf{k}}(\mathbf{r})\hat{\rho}_{\mathbf{q}}\psi_{a\mathbf{k}+\mathbf{q}}(\mathbf{r}) &= u^*_{i\mathbf{k}}(\mathbf{r})e^{-i\mathbf{k}\cdot\mathbf{r}}\, e^{-i\mathbf{q}\cdot\mathbf{r}}\, u_{a\mathbf{k}+\mathbf{q}}(\mathbf{r})e^{i(\mathbf{k}+\mathbf{q})\cdot\mathbf{r}} \\ &= \frac{1}{V}\sum_{\mathbf{G}} C_{ia\mathbf{G}}(\mathbf{q})e^{i\mathbf{G}\cdot\mathbf{r}}. \end{aligned} \tag{3.64}$$

We can now use the following relation obtained using the $\mathbf{k}\cdot\mathbf{p}$ method [57],

$$u_{a\mathbf{k}+\mathbf{q}}(\mathbf{r}) = (1 + i\boldsymbol{\alpha}_{a\mathbf{k}}\cdot\mathbf{q})u_{a\mathbf{k}}(\mathbf{r}) + \sum_{n\neq a}\frac{\langle\psi_{n\mathbf{k}} \mid \hat{\mathbf{p}} \mid \psi_{a\mathbf{k}}\rangle\cdot\mathbf{q}}{\epsilon_{a\mathbf{k}} - \epsilon_{n\mathbf{k}}}\cdot u_{n\mathbf{k}}(\mathbf{r}) + \mathcal{O}(q^2), \tag{3.65}$$

where, in the nondegenerate case, $\boldsymbol{\alpha}_{a\mathbf{k}}$ can be chosen to be a continuous and periodic function of $\mathbf{k}$. For the coefficient $C_{ia\mathbf{G}=\mathbf{0}}(\mathbf{q})$, which determines the value of the macroscopic density $\delta\rho_{\mathbf{q}+\mathbf{0}}(\omega)$, in Eq. (3.53) we then get

$$\begin{aligned} C_{ia\mathbf{G}=\mathbf{0}}(\mathbf{q}) &= \int u^*_{i\mathbf{k}}(\mathbf{r})u_{a\mathbf{k}+\mathbf{q}}(\mathbf{r})d\mathbf{r} \\ &= (1 + i\boldsymbol{\alpha}_{a\mathbf{k}}\cdot\mathbf{q})\delta_{ia} + \frac{\langle\psi_{i\mathbf{k}} \mid \hat{\mathbf{p}} \mid \psi_{a\mathbf{k}}\rangle\cdot\mathbf{q}}{\epsilon_{a\mathbf{k}} - \epsilon_{i\mathbf{k}}}\cdot(1-\delta_{ia}) + \mathcal{O}(q^2), \end{aligned} \tag{3.66}$$

where we made use of the orthogonality of the Bloch functions. The coefficients $C_{ia\mathbf{G}\neq\mathbf{0}}(\mathbf{q})$ that determine the microscopic density are in general of order 1. We consider first the q-dependence of the interband contribution to the macroscopic induced density, by inspecting Eq. (3.38) for $\delta\rho^{inter}_{\mathbf{q}}$ and Eqs (3.39) and (3.40) for the interband contribution to the response functions. In these last two expressions the weights $w_{i\mathbf{k}a\mathbf{k}+\mathbf{q},+}$ have a leading term of order 1 in the expansion in orders of q, as $i \neq a$. From the expressions (3.64) and (3.66) it follows that for $i \neq a$ the uniform component of the factor $\psi^*_{i\mathbf{k}}\hat{\rho}_{\mathbf{q}}\psi_{a\mathbf{k}+\mathbf{q}} = C_{ia\mathbf{G}=\mathbf{0}}(\mathbf{q})$ is of order q. Hence the interband contribution to the macroscopic induced density is one order in q higher than the off-diagonal matrix elements of the perturbations $\hat{\rho}_{-\mathbf{q}}\delta v_{\mathbf{q},eff}$ and $i\omega/c\hat{\mathbf{j}}_{-\mathbf{q}}\cdot\delta\mathbf{A}_{\mathbf{q},eff}$. The microscopic part is, on the other hand, of the same order as these matrix elements. For the intraband case we refer to Eqs (3.45)-(3.47). Here the uniform component of $\psi^*_{i\mathbf{k}}\hat{\rho}_{\mathbf{q}}\psi_{a\mathbf{k}+\mathbf{q}}$ is of order 1, as here $i = a$ in Eq. (3.66), and also the common factor $\omega^2/q^2 w_{i\mathbf{k}i\mathbf{k}+\mathbf{q},+}(\omega)$, as defined in Eq. (3.52), is of this order. Together with Eq. (3.45) we can now conclude that both the microscopic and macroscopic components of the intraband induced density are two orders in q higher than the diagonal matrix elements of the perturbation $\hat{\rho}_{-\mathbf{q}}\delta v_{\mathbf{q},\mathit{eff}}$, and one order in q higher than those of the perturbation $i\omega/c\,\hat{\mathbf{j}}_{-\mathbf{q}} \cdot \delta\mathbf{A}_{\mathbf{q},\mathit{eff}}$. The relations derived above constitute a set of self-consistent-field equations for the induced density that are depicted schematically in Fig. 3.2. The self-consistent loops involving the macroscopic effective vector potential do not need to be completed as we keep this macroscopic potential fixed to calculate the optical response. Assuming that both the effective microscopic scalar potential and the effective macroscopic vector potential are of order 1, we can see that the contribution of the interband processes to the microscopic density is of order 1 and that to the macroscopic density is of order q. In a similar way we can conclude that the contributions of the intraband processes to the microscopic and macroscopic densities are both of order q. From Eqs (3.55) and (3.57) within the ALDA it immediately becomes clear that a microscopic density of order 1 leads to an effective microscopic scalar potential of order 1, consistent with the initial assumption. On the other hand, a macroscopic density of order q will lead according to Eq. (3.56) to a macroscopic contribution to the effective vector potential of order 1, again consistent with the initial assumption. Within the ALDA the contribution of a macroscopic density of order q will lead to an exchange-correlation vector potential of order q with a uniform component of order q^2 (Eq. 3.62). The latter two contributions hence vanish in the optical limit. Using the scaling introduced in Eq. (3.45) all the variables acquire the same order in q as depicted in Fig. 3.3. Now it also becomes clear that in the optical limit the self-consistent loops for the microscopic and macroscopic induced density become decoupled. Since the contribution to the scaled intraband induced density $\delta\rho^{intra}_{\mathbf{q}}/q$ that is due to the microscopic effective scalar potential is of order q, it vanishes in the optical limit. Accounting for the scaling, the intraband contribution to the microscopic density is of order q and vanishes for q going to zero. The interband contribution to the scaled macroscopic density $\delta\rho_{\mathbf{q},mac}/q$ is, however, of order 1. Therefore we can conclude that the SCF for the microscopic density can be solved independently from the SCF for the macroscopic density, but that the reverse is not true. It is now clear how we can solve the optical response of metallic systems within the ALDA. First, for a given macroscopic vector potential, we need to solve the equations for the microscopic induced density and microscopic effective scalar potential self-consistently. With both the perturbing potentials now known, we can calculate the macroscopic induced density and the induced current-density.

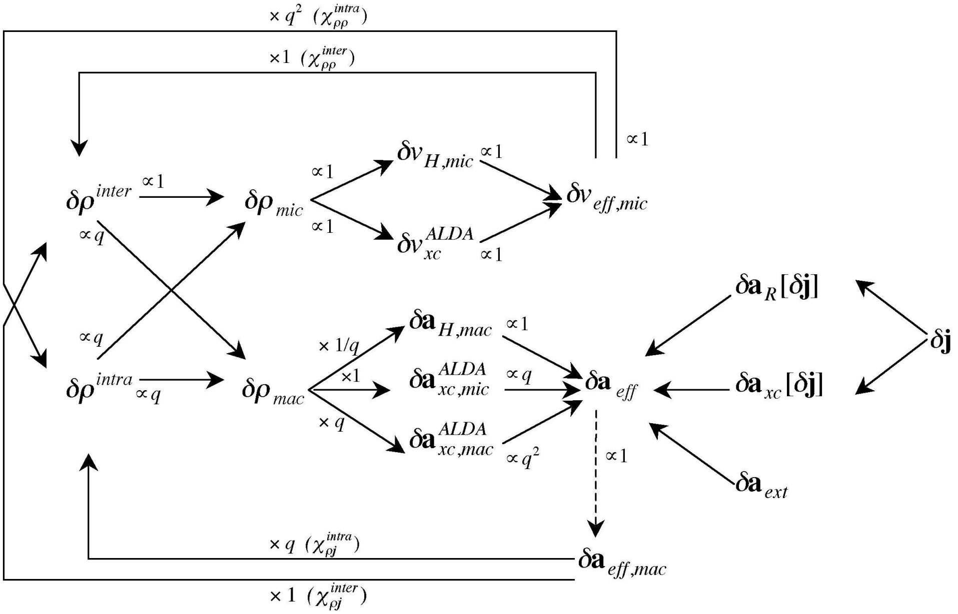

Figure 3.2: Schematic representation of the self-consistent-field (SCF) calculation of microscopic and macroscopic parts of the induced density. The leading order in powers of q is indicated near the variables by the "∝" sign. The arrows indicate the contributions to each variable, where the "×" sign indicates the order in q gained through some multiplicative factor. The inter- and intraband contributions to the induced density both contribute to the microscopic and macroscopic components of this density. In the microscopic Coulomb gauge only the microscopic density gives rise to the microscopic effective scalar potential *via* the microscopic Hartree term and the ALDA xc-term. The macroscopic density as well as the current-density contribute in various ways to the effective vector potential. The dashed line indicates that the self-consistent loop is not completed as we keep the macroscopic effective vector potential fixed. For more details and discussions see the text.

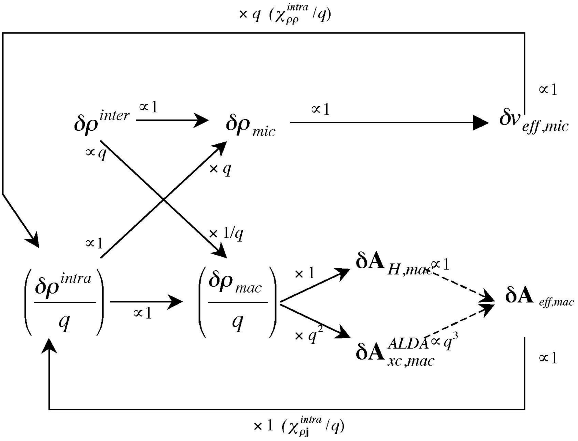

Figure 3.3: Schematic representation of the main changes in the calculation of the intraband induced density after the scaling to $\delta\rho^{intra}/q$ and $\delta\rho_{mac}/q$. The symbols used are similar as in Fig. 3.2. Note that not all the relations are indicated but only those involving the rescaled variables.

3.2.5 The macroscopic dielectric function

The macroscopic dielectric function $\epsilon(\mathbf{q},\omega)$ is a tensor that can be expressed as

$$\epsilon(\mathbf{q},\omega) = 1 + 4\pi\chi_e(\mathbf{q},\omega), \tag{3.67}$$

where the the macroscopic susceptibility $\chi_e(\mathbf{q},\omega)$ can be obtained in terms of the total induced macroscopic current *via*

$$\chi_e(\mathbf{q},\omega)\cdot\hat{\mathbf{e}} = \left(\frac{-i}{\omega V}\int \delta\mathbf{j}_{\mathbf{q}}(\mathbf{r},\omega)d\mathbf{r}\right)\Bigg|_{\frac{i\omega}{c}\delta\mathbf{A}_{mac,\mathbf{q}}=\hat{\mathbf{e}}}. \tag{3.68}$$

In Fig. 3.4 we report schematically the post-SCF calculation for the induced current-density. In the optical limit, i.e., for $q = 0$, the expression for the dielectric function takes a simple form. In the limit of $q \to 0$ the microscopic scalar potential does not contribute to the intraband current-density. Thus, in this limit and within the ALDA, the inter- and intraband contributions to the induced current-density can be calculated independently. From Eq. (3.38) we can obtain the interband contribution to the electric susceptibility by repeating the SCF calculation for the uniform macroscopic field in the three Cartesian directions $\hat{\mathbf{e}}$,

$$\chi_e^{inter}(\mathbf{q}=\mathbf{0},\omega)\cdot\hat{\mathbf{e}} = \left(\frac{-i}{\omega V}\int \delta\mathbf{j}^{inter}_{\mathbf{q}=\mathbf{0}}(\mathbf{r},\omega)d\mathbf{r}\right)\Bigg|_{\frac{i\omega}{c}\delta\mathbf{A}_{mac,\mathbf{q}=\mathbf{0}}=\hat{\mathbf{e}}}. \tag{3.69}$$

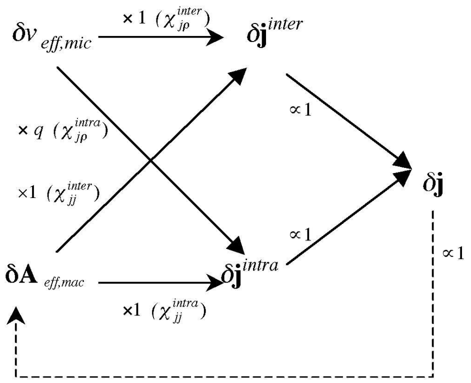

Figure 3.4: Schematic representation of post-SCF calculations of inter- and intraband contributions to the induced current-density. Here the dashed line indicates the additional SCF loop that needs to be considered when taking into account a current-dependent exchange-correlation functional.

From Eqs (3.45) and (3.63) the macroscopic part of the intraband contribution to the induced current can be written as

$$\sigma^{intra}(\mathbf{q}=\mathbf{0},\omega)\cdot\hat{\mathbf{e}} = \left(\frac{1}{V}\int \delta\mathbf{j}^{intra}_{\mathbf{q}=\mathbf{0}}(\mathbf{r},\omega)d\mathbf{r}\right)\Bigg|_{\frac{i\omega}{c}\delta\mathbf{A}_{mac,\mathbf{q}=\mathbf{0}}=\hat{\mathbf{e}}}, \tag{3.70}$$

where the intraband contribution to the macroscopic conductivity tensor, $\sigma^{intra}(\mathbf{q},\omega)$, at $\mathbf{q}=\mathbf{0}$ is given by

$$\sigma^{intra}(\mathbf{q}=\mathbf{0},\omega) = \frac{-i}{\omega V}\int\int \left(\chi^{intra}_{\mathbf{jjq=0}}(\mathbf{r},\mathbf{r}',\omega) - \chi^{intra,0}_{\mathbf{jjq=0}}(\mathbf{r},\mathbf{r}',\omega=0)\right)d\mathbf{r}d\mathbf{r}'. \tag{3.71}$$

We can then consider the following expression for the macroscopic dielectric function at $\mathbf{q}=0$,

$$\epsilon(\omega) = (1+4\pi\chi_e^{inter}(\omega)) - \frac{4\pi i}{\omega}\sigma^{intra}(\omega), \tag{3.72}$$

where the contribution in brackets is defined as the interband part of the dielectric function.

3.2.6 The energy-loss function

In transmission electron energy-loss spectroscopy one studies the inelastic scattering of a beam of high energy electrons by a target. The scattering rates obtained in these experiments are expressed in terms of the differential cross-section, which is obtained within the first Born approximation as [58]

$$\frac{d^2\sigma(\mathbf{k},\mathbf{k}',\omega)}{d\Omega d\omega} = \frac{2}{\pi q^4}\frac{k'}{k}S(\mathbf{q},\omega). \tag{3.73}$$

Here $\mathbf{k}$ and $\mathbf{k}'$ are the wavevectors of the incident and scattered electron, and $\mathbf{q}$ and ω are the transferred momentum and energy, respectively, with $\mathbf{q} = \mathbf{k} - \mathbf{k}'$ and $\omega = k^2/2 - k'^2/2$. The dynamical structure factor $S(\mathbf{q},\omega)$ is related to the imaginary part of the true density-density response function *via* the fluctuation-dissipation theorem,

$$S(\mathbf{q},\omega) = -2\Im \int\int e^{-i\mathbf{q}\cdot(\mathbf{r}-\mathbf{r}')}\chi(\mathbf{r},\mathbf{r}',\omega)d\mathbf{r}d\mathbf{r}'. \tag{3.74}$$

Here the true density-density response function relates the induced density to an external perturbing scalar field,

$$\delta\rho(\mathbf{r},\omega) = \int \chi(\mathbf{r},\mathbf{r}',\omega)\delta v_{ext}(\mathbf{r}',\omega)d\mathbf{r}'. \tag{3.75}$$

If we choose the external perturbing field as $\delta v_{ext}(\mathbf{r},\omega) = e^{i\mathbf{q}\cdot\mathbf{r}}$, then the dynamical structure factor can be expressed as $S(\mathbf{q},\omega) = \Im\tilde{s}(\mathbf{q},\omega)$, where

$$\begin{aligned}\tilde{s}(\mathbf{q},\omega) &= -2\int e^{-i\mathbf{q}\cdot\mathbf{r}}\delta\rho(\mathbf{r},\omega)d\mathbf{r}\Big|_{\delta v_{ext}(\mathbf{r},\omega)=e^{i\mathbf{q}\cdot\mathbf{r}}} \\ &= -2\int \delta\rho_{\mathbf{q}}(\mathbf{r},\omega)d\mathbf{r}\Big|_{\delta v_{ext,\mathbf{q}}=1}.\end{aligned} \tag{3.76}$$

Here we used Eq. (3.14) for the induced density and the external potential. In our scheme we have to work in the microscopic Coulomb gauge and therefore we want to gauge transform the external macroscopic scalar potential to an external vector potential: we can have $i\omega\delta\mathbf{a}_{ext}(\mathbf{r},\omega)/c = \hat{\mathbf{q}}\,e^{i\mathbf{q}\cdot\mathbf{r}}$ if we choose the external scalar potential as $\delta v_{ext}(\mathbf{r},\omega) = \frac{-i}{q}e^{i\mathbf{q}\cdot\mathbf{r}}$. Then the same dynamical structure factor can be obtained using

$$\tilde{s}(\mathbf{q},\omega) = -2iq\int \delta\rho_{\mathbf{q}}(\mathbf{r},\omega)d\mathbf{r}\;|_{\frac{i\omega}{c}\delta\mathbf{A}_{ext,\mathbf{q}}=\hat{\mathbf{q}}}\,. \tag{3.77}$$

Unlike in the case of the macroscopic dielectric function, here we need to consider the response to a given external field. Assuming Eq. (3.56) to hold, i.e., neglecting the sample-shape dependence of the induced field, the total macroscopic field can be related to the given external field according to

$$\begin{aligned}\frac{i\omega}{c}\delta\mathbf{A}_{mac,\mathbf{q}}(\mathbf{r},\omega) &= \hat{\mathbf{q}}\left(1+\frac{4\pi i}{qV}\int\delta\rho_{\mathbf{q}}(\mathbf{r},\omega)d\mathbf{r}\right) \\ &= \hat{\mathbf{q}}\left(1-\frac{2\pi}{q^2V}\tilde{s}(\mathbf{q},\omega)\right).\end{aligned} \tag{3.78}$$

In a completely similar way as for the calculation of the macroscopic dielectric function, we can now solve the SCF equations for a fixed macroscopic field and calculate the induced macroscopic density as linear response to this field,

$$\frac{i}{2q^2V}\tilde{s}(\mathbf{q},\omega) = \frac{1}{V}\int \frac{\delta\rho_{\mathbf{q}}(\mathbf{r},\omega)}{q}d\mathbf{r} = \frac{i\omega}{c}\int \mathbf{F}_{\mathbf{q}}(\mathbf{r},\omega)\cdot\delta\mathbf{A}_{mac,\mathbf{q}}(\mathbf{r},\omega)d\mathbf{r}. \tag{3.79}$$

By solving the SCF equations we obtain the lattice periodic response function $\mathbf{F}_{\mathbf{q}}(\mathbf{r},\omega)$. In the previous section we showed that for a finite macroscopic field the central term in the equation above is finite for vanishing q, and therefore also the terms on the left- and right-hand sides will be finite. By inserting Eq. (3.78) in Eq. (3.79) we can now account for the relation between the macroscopic and external fields to arrive at

$$\frac{i}{2q^2V}\tilde{s}(\mathbf{q},\omega) = \int \mathbf{F}_{\mathbf{q}}(\mathbf{r},\omega)\cdot\hat{\mathbf{q}}\left(1+4\pi i\frac{i}{2q^2V}\tilde{s}(\mathbf{q},\omega)\right)d\mathbf{r}, \tag{3.80}$$

from which we immediately obtain

$$\frac{i}{2q^2V}\tilde{s}(\mathbf{q},\omega) = \frac{\int \mathbf{F}_{\mathbf{q}}(\mathbf{r},\omega)\cdot\hat{\mathbf{q}}\,d\mathbf{r}}{1-4\pi i\int \mathbf{F}_{\mathbf{q}}(\mathbf{r},\omega)\cdot\hat{\mathbf{q}}\,d\mathbf{r}}. \tag{3.81}$$

Using now the definitions of the dynamical structure factor $S(\mathbf{q},\omega)$ and the response function $\mathbf{F}_{\mathbf{q}}(\mathbf{r},\omega)$, we can write

$$S(\mathbf{q},\omega) = -2q^2V\Re\left\{\frac{\frac{1}{V}\int\frac{\delta\rho_{\mathbf{q}}(\mathbf{r},\omega)}{q}d\mathbf{r}}{1-4\pi i\frac{1}{V}\int\frac{\delta\rho_{\mathbf{q}}(\mathbf{r},\omega)}{q}d\mathbf{r}}\right\}\Bigg|_{\frac{i\omega}{c}\delta\mathbf{A}_{mac,\mathbf{q}}=\hat{\mathbf{q}}}. \tag{3.82}$$

We can now consider the special case $\mathbf{q}=\mathbf{0}$ and show that it is related to the current-current response function, and hence the macroscopic dielectric function. Using Eqs (3.64) and (3.66) in Eqs (3.39) and (3.40) one can easily show that the following relations hold,

$$\begin{aligned}
\lim_{q\to 0}\frac{1}{q}\int\chi^{inter}_{\rho\rho\mathbf{q}}(\mathbf{r},\mathbf{r}',\omega)d\mathbf{r} &= \frac{\hat{\mathbf{q}}}{\omega}\cdot\int\chi^{inter}_{\mathbf{j}\rho\mathbf{q}=\mathbf{0}}(\mathbf{r},\mathbf{r}',\omega)d\mathbf{r}\\
\lim_{q\to 0}\frac{1}{q}\int\chi^{inter}_{\rho\mathbf{j}\mathbf{q}}(\mathbf{r},\mathbf{r}',\omega)d\mathbf{r} &=\\
\frac{\hat{\mathbf{q}}}{\omega}\cdot\int[\chi^{inter}_{\mathbf{jj}\mathbf{q}=\mathbf{0}}(\mathbf{r},\mathbf{r}',\omega) &- \chi^{inter}_{\mathbf{jj}\mathbf{q}\to\mathbf{0}}(\mathbf{r},\mathbf{r}',\omega=0)]d\mathbf{r}.
\end{aligned} \tag{3.83}$$

Therefore using Eq. (3.38) we can write

$$\lim_{q\to 0}\frac{1}{V}\int\frac{\delta\rho^{inter}_{\mathbf{q}}(\mathbf{r},\omega)}{q}d\mathbf{r} = \frac{\hat{\mathbf{q}}}{\omega}\cdot\frac{1}{V}\int\delta\mathbf{j}^{inter}_{\mathbf{q}=\mathbf{0}}(\mathbf{r},\omega)d\mathbf{r}. \tag{3.84}$$

A similar relation holds for the intraband contribution. Using again Eqs (3.64) and (3.66), but now in Eqs (3.46) and (3.47), and using in addition the following relation [57],

$$\epsilon_{i\mathbf{k}+\mathbf{q}} - \epsilon_{i\mathbf{k}} = \mathbf{q} \cdot \int \psi^*_{i\mathbf{k}}(\mathbf{r})\hat{\mathbf{j}}_{\mathbf{q}}\psi_{i\mathbf{k}+\mathbf{q}}(\mathbf{r})d\mathbf{r} + \mathcal{O}(q^2), \tag{3.85}$$

one finds

$$\begin{aligned}
\lim_{q\to 0}\frac{\omega^2}{q^2}\int \chi^{intra}_{\rho\rho\mathbf{q}}(\mathbf{r},\mathbf{r}',\omega)d\mathbf{r} &= \lim_{q\to 0}\frac{\omega}{q}\hat{\mathbf{q}} \cdot \int \chi^{intra}_{\mathbf{j}\rho\mathbf{q}=\mathbf{0}}(\mathbf{r},\mathbf{r}',\omega)d\mathbf{r}, \\
\lim_{q\to 0}\frac{\omega}{q}\int \chi^{intra}_{\rho\mathbf{j}\mathbf{q}}(\mathbf{r},\mathbf{r}',\omega)d\mathbf{r} &= \\
\hat{\mathbf{q}} \cdot \int (\chi^{intra}_{\mathbf{j}\mathbf{j}\mathbf{q}=\mathbf{0}}(\mathbf{r},\mathbf{r}',\omega) &- \chi^{intra}_{\mathbf{j}\mathbf{j}\mathbf{q}\to\mathbf{0}}(\mathbf{r},\mathbf{r}',\omega=0))d\mathbf{r}.
\end{aligned} \tag{3.86}$$

Therefore, using the Eq. (3.45) we can write

$$\lim_{q\to 0}\frac{1}{V}\int \frac{\delta\rho^{intra}_{\mathbf{q}}(\mathbf{r},\omega)}{q}d\mathbf{r} = \frac{\hat{\mathbf{q}}}{\omega} \cdot \frac{1}{V}\int \delta\mathbf{j}^{intra}_{\mathbf{q}=\mathbf{0}}(\mathbf{r},\omega)d\mathbf{r}. \tag{3.87}$$

From Eqs (3.84) and (3.87) the long-wavelength limit of Eq. (3.82) can be written as

$$\lim_{q\to 0}\frac{1}{2q^2V}S(\mathbf{q},\omega) = \Re\left\{\frac{-i\hat{\mathbf{q}} \cdot \frac{-i}{\omega V}\int \delta\mathbf{j}_{\mathbf{q}=\mathbf{0}}(\mathbf{r},\omega)d\mathbf{r}}{1 + 4\pi\hat{\mathbf{q}} \cdot \frac{-i}{\omega V}\int \delta\mathbf{j}_{\mathbf{q}=\mathbf{0}}(\mathbf{r},\omega)d\mathbf{r}}\right\}\Bigg|_{\frac{i\omega}{c}\delta\mathbf{A}_{mac,\mathbf{q}}=\hat{\mathbf{q}}}. \tag{3.88}$$

Using the results of the previous section Eqs (3.69)-(3.72), we arrive at the final result

$$\lim_{q\to 0}\frac{2\pi}{q^2V}S(\mathbf{q},\omega) = \Im\left\{\frac{-1}{\hat{\mathbf{q}} \cdot \epsilon(\omega) \cdot \hat{\mathbf{q}}}\right\}. \tag{3.89}$$

The dynamical structure factor for all q and ω as given in Eq. (3.82) includes all the local field effects and can be used for both isotropic and anisotropic systems. By making use of the continuity equation,

$$\nabla \cdot \mathbf{j}_{\mathbf{q}}(\mathbf{r},\omega) + i\mathbf{q} \cdot \mathbf{j}_{\mathbf{q}}(\mathbf{r},\omega) - i\omega\rho_{\mathbf{q}}(\mathbf{r},\omega) = 0, \tag{3.90}$$

we can relate the integral $\int \delta\rho_{\mathbf{q}}(\mathbf{r},\omega)/qd\mathbf{r}$ in Eq. (3.82) directly to $1/\omega\int \delta\mathbf{j}_{\mathbf{q}}(\mathbf{r},\omega)d\mathbf{r}$ for all q, and hence we generalize Eq. (3.89) with the result

$$\frac{2\pi}{q^2V}S(\mathbf{q},\omega) = \Im\left\{\frac{-1}{\hat{\mathbf{q}} \cdot \epsilon(\mathbf{q},\omega) \cdot \hat{\mathbf{q}}}\right\}. \tag{3.91}$$

In particular, in the limit of vanishing q the dynamical structure factor is directly related to the macroscopic dielectric function according to the relation given above.

3.3 Implementation

In this section we describe the main new aspects of the implementation for the dielectric function calculation in metallic systems. For the interband part we closely follow the implementation for nonmetallic crystalline systems described in Ref. [30]. The main difference here is in the numerical evaluation of the **k**-space integrals. The response integrals of the set of equations (3.39)-(3.42) involve integrations over the (irreducible wedge of the) Brillouin zone, in which the denominator can become singular. These singularities have been treated, as described in Ref. [30], using a Lehmann-Taut tetrahedron scheme [59]. With partially occupied bands the numerical evaluation of integrals over tetrahedra in which the first Brillouin zone is partitioned is restricted to a part cut off by the Fermi surface. Both the energy and the integrand at the new corners of the truncated simplices are obtained by linear interpolation within each tetrahedron (see App. C). The intraband contribution to the dielectric function is completely defined by Eq. (3.71). Inserting Eqs (3.49) and (3.52) and replacing the summation over the **k** points by an integral over the Brillouin zone $1/N_k \sum_{\mathbf{k}} \to V/8\pi^3 \int d\mathbf{k}$, we arrive at

$$\begin{aligned}\sigma^{intra}(\omega) \quad &= \quad \lim_{q\to 0}\left\{\frac{-i}{8\pi^3\omega}\sum_i \int d\mathbf{k}\frac{df}{d\epsilon}\,\frac{\omega^2}{q^2(\nabla_{\mathbf{k}}\epsilon_{i\mathbf{k}}\cdot\hat{\mathbf{q}})^2-(\omega+i\eta)^2}\right.\\ &\left.\langle\psi^*_{i\mathbf{k}}|\hat{\mathbf{j}}_{\mathbf{q}}|\psi_{i\mathbf{k}+\mathbf{q}}\rangle\otimes\langle\psi^*_{i\mathbf{k}+\mathbf{q}}|\hat{\mathbf{j}}'_{-\mathbf{q}}|\psi_{i\mathbf{k}}\rangle\right\}. \qquad (3.92)\end{aligned}$$

The integration will be reduced to an integral over the sheets S_i of the Fermi surface originating by the bands i, as the first derivative of the Fermi-Dirac distribution $f(\epsilon) = 2\Theta(\epsilon_F - \epsilon)$ peaks at $\epsilon = \epsilon_F$, $df/d\epsilon = -2\delta(\epsilon_F - \epsilon)$. For the frequency-dependent factor we can use the Cauchy theorem and write

$$\begin{aligned}&\frac{\omega^2}{(\nabla_{\mathbf{k}}\epsilon_{i\mathbf{k}}\cdot\mathbf{q})^2-(\omega+i\eta)^2} =\\ &\quad\mathcal{P}\frac{(\omega/q)^2}{(\nabla_{\mathbf{k}}\epsilon_{i\mathbf{k}}\cdot\hat{\mathbf{q}})^2-(\omega/q)^2}+\\ &\quad i\pi(\omega/q)^2(\delta(\nabla_{\mathbf{k}}\epsilon_{i\mathbf{k}}\cdot\hat{\mathbf{q}}-\omega/q)+\delta(\nabla_{\mathbf{k}}\epsilon_{i\mathbf{k}}\cdot\hat{\mathbf{q}}+\omega/q)). \qquad (3.93)\end{aligned}$$

In optical experiments ω/q is of the order of the velocity of light, $\omega/q \sim c$, which is much higher than the velocity in the direction of $\hat{\mathbf{q}}$ of valence electrons at the Fermi surface, $\nabla_{\mathbf{k}}\epsilon_{i\mathbf{k}}\cdot\hat{\mathbf{q}}$. Thus, the imaginary part in Eq. (3.93) is zero and the real part reduces to -1 in the limit of $q \to 0$. In other experiments, where ω/q is of the same order as the Fermi velocity, the imaginary part can become important. In this case the integrations in the **k**-space are reduced to integrations over closed loops resulting from the intersection of the Fermi surface with a surface of constant velocity ($= \omega/q$) parallel to $\mathbf{q}$. Using the principal value of Eq. (3.93) in the optical limit, Eq. (3.92) becomes

$$\sigma^{intra}(\omega) = \frac{-i}{4\pi^3\omega} \sum_i \int_{S_i} \frac{d^2\mathbf{k}}{|\nabla_{\mathbf{k}}\epsilon_{i\mathbf{k}}|} \langle\psi^*_{i\mathbf{k}}|\hat{\mathbf{j}}|\psi_{i\mathbf{k}}\rangle \otimes \langle\psi^*_{i\mathbf{k}}|\hat{\mathbf{j}}|\psi_{i\mathbf{k}}\rangle. \tag{3.94}$$

The integrations over the Fermi surface are evaluated numerically following the linear tetrahedron method proposed by Wiesenekker and Baerends [60].

3.4 Results and discussion

To test our method we calculated the optical dielectric functions $\epsilon(\omega)$ in the spectral range 0-10 eV and the energy-loss functions $-\Im\left\{\epsilon_L^{-1}(\omega)\right\}$ in the spectral range 0-40 eV for the isotropic crystals of copper and silver within the adiabatic local density approximation. Both metals have the fcc lattice type for which we used the experimental lattice constants 3.61 Å for Cu and 4.09 Å for Ag. All calculations were performed using a modified version of the ADF-BAND program [30, 31, 61–63]. We made use of a hybrid valence basis set consisting of Slater-type orbitals (STOs) in combination with the numerical solutions of a free-atom Herman-Skillman program [64]. Cores were kept frozen up to $3p$ and $4p$ for Cu and Ag, respectively. The spatial resolution of this basis is equivalent to a STO triple-zeta basis set augmented with two polarization functions. The Herman-Skillman program also provides us with the free-atom effective potential. The crystal potential was evaluated using an auxiliary basis set of STO functions to fit the deformation density in the ground-state calculation and the induced density in the response calculation. For the evaluation of the **k**-space integrals we used a quadratic numerical integration scheme with 175 symmetry-unique sample points in the irreducible wedge of the Brillouin zone, which was constructed by adopting a Lehmann-Taut tetrahedron scheme [59, 60]. We found that the convergency and accuracy are very similar to the previous formulation for nonmetals and we checked that our results were converged with respect to **k**-space sampling and basis set size. All results shown here were obtained using the Vosko-Wilk-Nusair parametrization [65] of the LDA exchange-correlation potential, which was also used to derive the ALDA exchange-correlation kernel. In Fig. 3.5 and Fig. 3.6 the calculated real and imaginary parts of the dielectric functions of Cu and Ag are compared with two sets of experimental data well known in literature [50, 51], and with more recent measurements [52]. The latter data have been obtained using ultrahigh vacuum spectroscopic ellipsometry, thus we consider them the best data available. Our results are in good overall agreement with the experiments. In particular, the onset

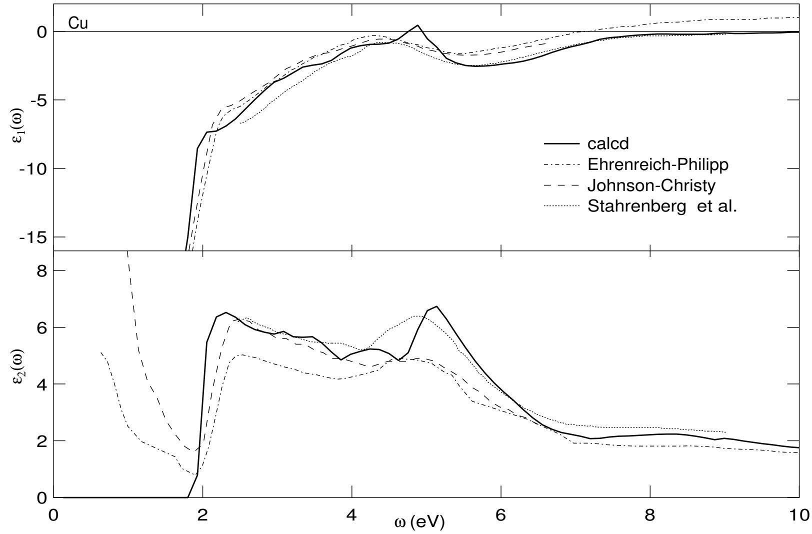

Figure 3.5: Real, $\epsilon_1(\omega)$, and imaginary, $\epsilon_2(\omega)$, parts of the dielectric function of Cu. The bold solid line shows our calculation, the others show the experimental data from Ref. [50–52].

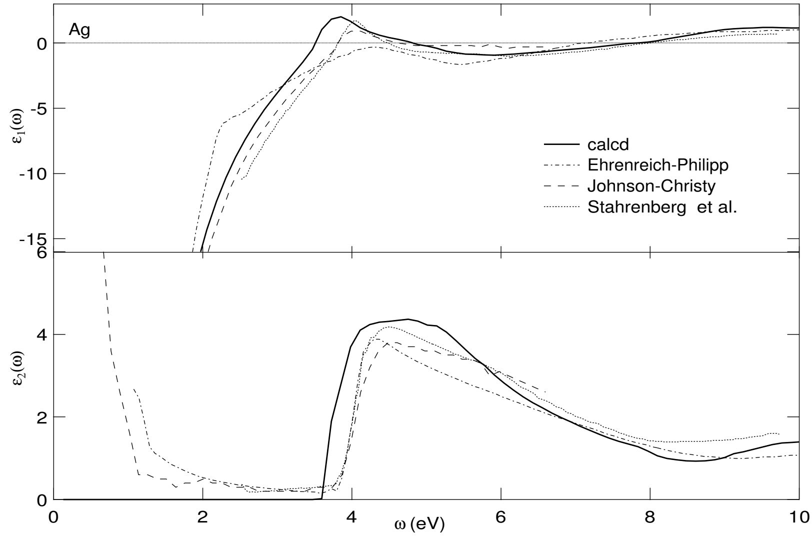

Figure 3.6: Real, $\epsilon_1(\omega)$, and imaginary, $\epsilon_2(\omega)$, parts of the dielectric function of Ag. The bold solid line shows our calculation, the others show experimental data from Ref. [50–52].

of the interband transitions at $\sim$ 1.9 eV (experimentally around 2.0 eV) for Cu as well as the overall shape of ϵ_2 are very well reproduced by our calculations. For Ag the onset at $\sim$ 3.7 eV (experimentally around 4.0 eV) is slightly shifted to lower frequency, but again the main features of ϵ_2 are well described by our method, in line with the general observation in semiconductors where the absorption gap is underestimated in the LDA. A feature clearly missing in our calculated spectra is the low-frequency tail in the imaginary part of the dielectric function. In perfect crystals this contribution comes from the scattering that free-conduction electrons have with phonons and with other electrons [66, 67]. These phenomena are not described by the ALDA, where a frequency-independent xc-kernel $f_{xc}(\mathbf{r}, \mathbf{r}')$ is used. In general, electron correlation effects (beyond ALDA) will lead to a frequency-dependent kernel $f_{xc}(\mathbf{r}, \mathbf{r}', \omega)$ which will, in general, be long range [24]. The electron-phonon interaction requires the use of a multicomponent-density functional approach [68]. The phonon-mediated electron correlation effects are then described by an extra contribution to the $f_{xc}(\mathbf{r}, \mathbf{r}', \omega)$ kernel. In particular the long-range frequency-dependent $f_{xc}(\mathbf{r}, \mathbf{r}', \omega)$ can take the form of a local functional of the current-density, which can be included in our scheme [24, 69]. In chapter 7 we will use such a frequency-dependent kernel. The separation of the inter- and intraband contributions to the dielectric function gives a deeper insight in the linear response of the two metals, in particular in the role of bound and conduction electrons and in the identification of the plasma resonances. Plasmon excitations can be identified by the characteristic maxima in the electron energy-loss spectra (EELS) occurring at energies where both ϵ_1 and ϵ_2 are small. In the measured dielectric functions of Ref. [50, 51] the Drude theory is used to estimate the free-electron contribution (intraband contribution). Within this model both the real and imaginary parts of the dielectric function in the free-electron region depend on the relaxation time τ and the plasma frequency ω_p,

$$\epsilon_1^D(\omega) = 1 - \frac{\omega_p^2 \tau^2}{1 + \omega^2 \tau^2}, \tag{3.95}$$

$$\epsilon_2^D(\omega) = \frac{\omega_p^2 \tau}{\omega(1 + \omega^2 \tau^2)}. \tag{3.96}$$

Here $\omega_p^2 = 4\pi N/m^*$ with N the density of conduction electrons and m^* their effective optical mass. In order to compare with our theory within the ALDA approach we have to consider the expressions (3.95) and (3.96) in the limit of τ to infinity. In this case, indeed, they become

$$\epsilon_1^D(\omega) = 1 - \frac{\omega_p^2}{\omega^2}, \tag{3.97}$$

$$\epsilon_2^D(\omega) = 0. \tag{3.98}$$

In our treatment the intraband contribution to ϵ_2 is zero, whereas Eqs (3.72) and (3.94) show that for isotropic systems the intraband contribution to ϵ_1 can be written as

$$\begin{aligned} -\frac{4\pi i}{\omega}\sigma^{intra}(\omega) &= -\frac{1}{3\pi^2\omega^2}\, Tr \sum_i \int_{S_i} \frac{d^2\mathbf{k}}{|\nabla_{\mathbf{k}}\epsilon_{i\mathbf{k}}|}(\nabla_{\mathbf{k}}\epsilon_{i\mathbf{k}}) \otimes (\nabla_{\mathbf{k}}\epsilon_{i\mathbf{k}}) \\ &= -\frac{1}{3\pi^2\omega^2}\sum_i \int_{S_i} d^2\mathbf{k}\nabla_{\mathbf{k}}\epsilon_{i\mathbf{k}} \cdot \hat{n}, \end{aligned} \tag{3.99}$$

where the gradient $\nabla_{\mathbf{k}}\epsilon_{i\mathbf{k}} = |\nabla_{\mathbf{k}}\epsilon_{i\mathbf{k}}| \cdot \hat{n}$ is a vector normal to the Fermi surface. The integrals over the Fermi surface can be written as an integral over the occupied part of the Brillouin zone, thus we arrive at

$$-\frac{4\pi i}{\omega}\sigma^{intra}(\omega) = -\frac{1}{6\pi^2\omega^2}\sum_i \int_{BZ} d\mathbf{k} f_{i\mathbf{k}} \nabla^2_{\mathbf{k}}\epsilon_{i\mathbf{k}}. \tag{3.100}$$

Since the isotropic average effective mass m^* of the conduction electrons can be defined *via* $N/m^* = (8\pi^3)^{-1}\sum_i \int_{BZ} d\mathbf{k} f_{i\mathbf{k}} \left(\nabla^2_{\mathbf{k}}\epsilon_{i\mathbf{k}}/3\right)$, where N is the density of the conduction electrons $N = (8\pi^3)^{-1}\sum_i \int_{BZ} d\mathbf{k} f_{i\mathbf{k}}$, we can write Eq. (3.100) as

$$-\frac{4\pi i}{\omega}\sigma^{intra}(\omega) = -\frac{1}{\omega^2}\frac{4\pi N}{m^*} = -\left(\frac{\omega_p}{\omega}\right)^2, \tag{3.101}$$

with indeed $\omega_p^2 = 4\pi N/m^*$. In order to compare our results with those obtained using the Drude model, we plotted $4\pi\chi^{inter}$ and $1 - 4\pi i\sigma^{intra}/\omega$ separately in Fig. 3.7, together with the decomposition of the experimental data proposed in Refs [50, 51]. We cannot compare with the data of Ref. [52], however, because the few values of the dielectric functions recorded at frequencies lower than the onset of the interband transitions makes it difficult to obtain the parameters τ and ω_p by fitting the experimental data. In Fig. 3.8 we report the energy-loss spectra for both metals in the range 0-40 eV. Here calculated and experimental data [50, 70] are compared. For both metals the calculated Drude-like part of the dielectric function crosses zero at frequencies around 8.9 eV and 8.8 eV, in good agreement with the free-electron plasma frequencies 9.3 eV for Cu and 9.2 eV for Ag found in Ref. [50]. In copper this is the only resonance observed and it has to be interpreted as a free-electron-like resonance [50, 53]. However, in silver ϵ_1 crosses zero three times, at frequencies 3.5 eV, 4.8 eV, and 7.8 eV close to the experimental values. Sharp energy-loss peaks are experimentally observed near the first and the third frequency [50, 52, 54]. The peak near the third frequency is a free-electron-like resonance as it is close to the Drude plasma frequency. Although ϵ_1 becomes zero twice near the onset of the interband transitions, only one peak appears in the EELS at a frequency near 3.8 eV where ϵ_2 is still small. Whereas the third

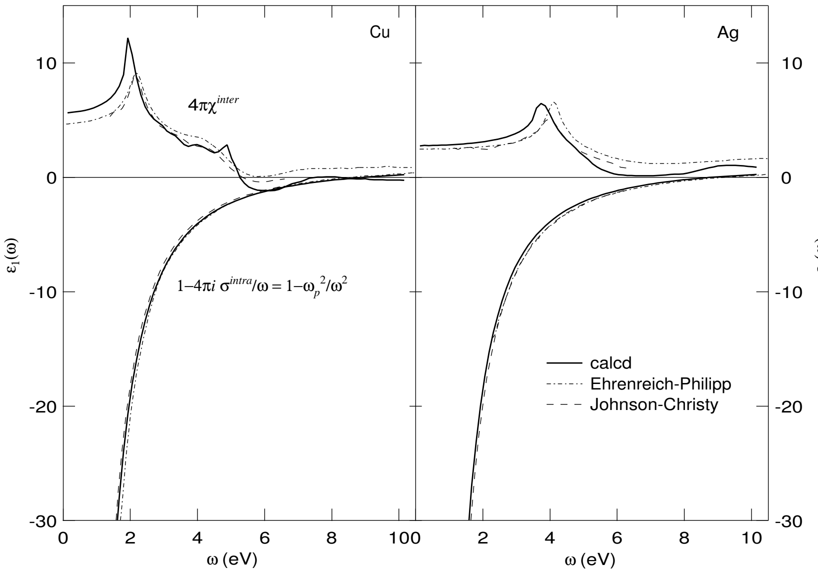

Figure 3.7: The $4\pi\chi^{inter}$ and $1 - 4\pi i\sigma^{intra}/\omega$ contributions to the real part of the dielectric function of Cu (left) and Ag (right). Included are the decompositions of the experimental data using the Drude model as reported in Ref. [50, 51].

resonance is well reproduced in the calculated spectrum, the first one is less intense than the one observed experimentally. Similar results have been found by Cazalilla *et al.* [54]. In order for the first peak to gain intensity it is necessary to have a small but nonvanishing imaginary part of the dielectric function at the frequency where the real part crosses the zero axes. As becomes clear from Fig. 3.7 in silver this crossing occurs where the inter- and intraband contributions compensate, which is always below the peak appearing in the interband contribution to the real part of the dielectric function corresponding to the absorption onset. In copper the situation is different as here this compensation will occur in a region around 4.8 eV where the absorption is already strong. Unlike Cazalilla *et al.* [54] we expect that the use of more advanced approximations to the xc-functional in the ground state, although changing the band structure, will not affect the peak intensity in the case of silver. Instead inclusion of relaxation effects through the xc-kernel $f_{xc}(\mathbf{r}, \mathbf{r}', \omega)$ is expected to strongly influence this peak. This is in keeping with the observation that the absorption is sensitive to the introduction of nonintrinsic sources of scattering [71, 72].

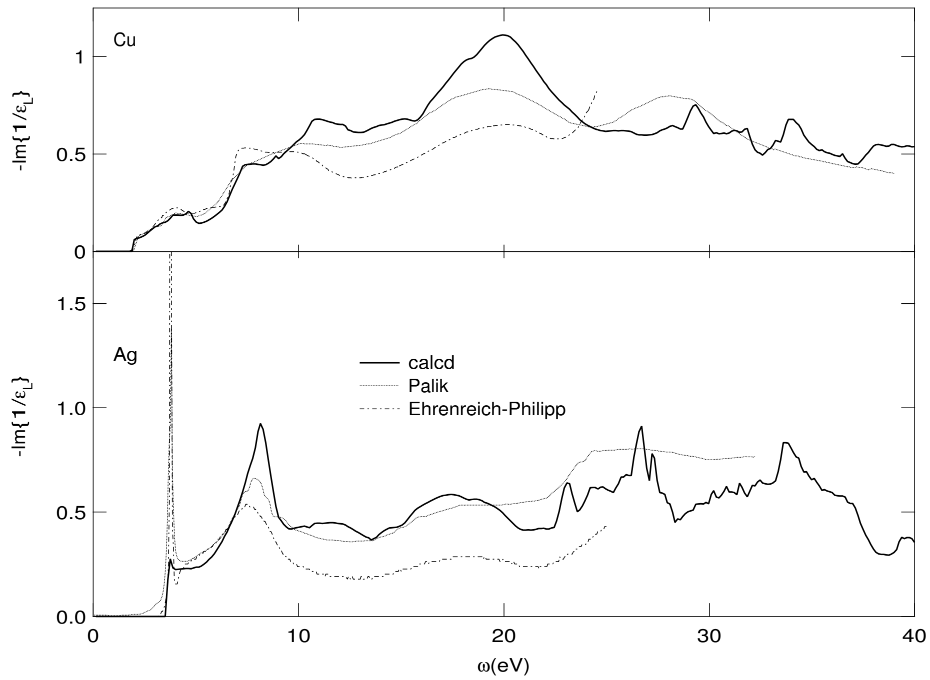

Figure 3.8: The energy-loss function of Cu (upper graph) and Ag (lower graph). The bold solid line shows our calculation, the others show the experimental data from Ref. [50, 70].

3.5 Conclusions

We have successfully extended the existing time-dependent current-density-functional approach, originally developed for the calculation of the dielectric response of non-metallic crystalline systems [30, 31], to treat metallic systems. We describe the linear response of a metallic system to a general q- and ω- dependent external electromagnetic field and arrive at closed expressions for the $q = 0$ limit at finite ω. We show how the macroscopic dielectric function and the energy-loss function can be derived as a function of $\mathbf{q}$ and ω in our scheme. Three steps are essential in this procedure. First we show how the inter- and intraband contributions to the induced density and current-density can be separated. Then the microscopic Coulomb gauge is used. In this gauge the effective scalar potential is completely microscopic and all macroscopic contributions due to the inter- and intraband parts of the induced density and current-density are gauge transformed to the effective vector potential. Finally, we consider the limit of vanishing q. Since the macroscopic inter- and intraband parts of the induced density as well as the microscopic intraband part vanish in the optical limit, they cannot lead to exchange-correlation contributions unless there is a long-range part in the exchange-correlation functional. Using the local exchange-correlation functional, there is only a contribution to the exchange-correlation scalar potential due to the microscopic interband part of the induced density. From the last step we conclude that, within the ALDA and at q=0, the self-consistent-field equations describing the inter- and intraband contributions to the response decouple. In general, however, for $q > 0$ and when going beyond the ALDA, inter- and intraband processes are interconnected. We have applied our approach to calculate the dielectric function and the energy-loss function for Cu and Ag. Comparison of the ALDA results with experimental data shows a good overall agreement. Even though the onset for the interband transitions is shifted to lower frequency for both metals by about 10 percent, the main features of the spectra are well reproduced above the onset. Within the ALDA no relaxation processes are included which results in the absence of the Drude-like absorption tail below the interband onset. For both metals we obtain a macroscopic dielectric function, with $|\epsilon| \approx 0$, near the experimentally observed Drude-like free electron plasma frequencies. In silver, in addition, a vanishing dielectric function is observed at 3.5 eV, just below the interband absorption edge, and close to the experimental plasma resonance. This is not a free-electron resonance but the results of the combined response due to inter- and intraband processes. In our calculated loss spectrum the intensity of this plasmon peak is strongly underestimated, which cannot be attributed to the local density approximation for the xc-potential of the ground state but is the result of the absence of relaxation processes in our ALDA description.

Chapter 4

Relativistic DFT

Systems of heavy atoms are not correctly described within a nonrelativistic quantum-mechanical model. In this case one has to consider the Dirac equation, which satisfies both the postulates of special relativity and those of quantum mechanics. In this chapter we give the main concepts of a relativistic density functional formulation and how to reduce the four-component Dirac-Kohn-Sham equations to two-component pseudorelativistic equations. We discuss in particular the two-component equations within the zeroth-order regular approximation, we extend this formulation to the time-domain, and we combine it with our formulation of linear response.

4.1 RDFT from quantum electrodynamics

The appropriate starting point for a fully relativistic description of the electronic structure of atoms, molecules, clusters, and solids is Quantum Electrodynamics (QED). However, in general, the QED equations represent a quite complex computational problem, thus approximations are unavoidable. An approximation is the Dirac equation. The quantum-mechanical evolution of a system of N interacting electrons in the presence of time-dependent scalar and vector potentials $v(\mathbf{r},t)$ and $\mathbf{A}(\mathbf{r},t)$, respectively, is described by the following Hamiltonian,

$$\sum_{i}^{N} \big(c\boldsymbol{\alpha}\cdot\boldsymbol{\pi}_i + \beta c^2 + v(\mathbf{r}_i,t)\big) + \sum_{i<j} U(\mathbf{r}_i - \mathbf{r}_j), \tag{4.1}$$

with $U(\mathbf{r}_i - \mathbf{r}_j)$ the electron-electron interaction and βc^2 the rest mass of the electron. Here $\boldsymbol{\pi}_i = \mathbf{p}_i + \mathbf{A}(\mathbf{r}_i, t)/c$, $\boldsymbol{\alpha}$ is the velocity operator,

$$\boldsymbol{\alpha} = \begin{pmatrix} 0 & \boldsymbol{\sigma} \\ \boldsymbol{\sigma} & 0 \end{pmatrix}, \tag{4.2}$$

with $\boldsymbol{\sigma}$ the vector of two-by-two Pauli matrices,

$$\sigma_x = \begin{pmatrix} 0 & 1 \\ 1 & 0 \end{pmatrix}, \sigma_y = \begin{pmatrix} 0 & -i \\ i & 0 \end{pmatrix}, \sigma_z = \begin{pmatrix} 1 & 0 \\ 0 & -1 \end{pmatrix}, \tag{4.3}$$

and β is the four-by-four matrix

$$\beta = \begin{pmatrix} I & 0 \\ 0 & -I \end{pmatrix}, \tag{4.4}$$

with I the two-by-two identity matrix. The Dirac Hamiltonian can, thus, be expressed as a four-by-four matrix which operates on the wavefunction Ψ. This means that solution of Eq. (4.1) leads to four-component wavefunctions or spinors. The Dirac equation admits both positive energy solutions, associated with electrons, and negative energy solutions, associated with positrons, i.e. particles with the same mass as the electrons, but opposite charge. Normally one is interested in the electronic states. If the rest mass energy for positive energy states is subtracted from the Dirac equation (change of gauge), the solutions of interest are those in which the upper two-component spinor of the wavefunction is predominant. This component is called large component, while the lower two-component spinor is called small component. The electron and positron states can be completely decoupled by means of unitary transformations, as, for example, the Fouldy-Wouthuysen transformation. The electronic states are then described by a two-component Hamiltonian.

4.1.1 The stationary and time-dependent Dirac-Kohn-Sham equations

Relativistic density functional theory (RDFT) has been formulated within the framework of quantum electrodynamics, where the renormalization procedure provides a minimum principle which makes possible the relativistic extension of the Hohenberg-Kohn theorem [73]. Recent reviews of the quantum electrodynamical basis of RDFT have been given by Engel *et al.* in Refs [74, 75]. Using the renormalized ground-state energy E_{0R} and the ground-state four-current $j^{\mu}_{R}(\mathbf{r})$, one can then prove that there exists a one-to-one correspondence between the class of external potentials just differing by gauge transformations, $V^{\mu}_{ext}(\mathbf{r}) = (v_{ext}(\mathbf{r}), \mathbf{A}_{ext}(\mathbf{r}))$, $(\mu = 0,1,2,3)$, the associated class of (nondegenerate) ground-state wavefunctions $|\Phi_0\rangle$, and ground-state four-current $j^{\mu}_{R}(\mathbf{r})$. This means that the ground-state wavefunction is a unique (and universal) functional of the ground-state four-current. As consequence, also the ground-state energy of the system is a functional of the ground-state current, $E_{0R}[j_R]$. The exact $j^{\mu}_{R}(\mathbf{r})$ minimizes $E_{0R}[j_R]$ under the condition of current conservation, and thus conservation of the total charge Q,

$$\sum_{\mu} \partial_{\mu} j^{\mu}_{R}(\mathbf{r}) \quad = \quad 0, \tag{4.5}$$

$$\frac{1}{c}\int j^{0}_{R}(\mathbf{r}) d\mathbf{r} \quad = \quad Q, \tag{4.6}$$

where we use the notation $\partial_{\mu} = (\partial_t/c, \nabla)$. In order to derive the relativistic Kohn-Sham equations [76, 77] one has to assume the existence of an auxiliary system of noninteracting particles in effective potentials $V^{\mu}_{s}(\mathbf{r})$ with exactly the same ground-state four-current as the interacting system. This assumption has not been examined in the relativistic case, but one expects analogous statements as in the nonrelativistic case. Within the relativistic Kohn-Sham scheme the ground-state four-current and energy can be represented in terms of auxiliary single-particle four-spinors ψ_i. This representation in general also includes vacuum polarization contributions. However, for most RDFT applications these electrodynamical effects are irrelevant, thus we will neglect them in the following for simplicity (no-pair approximation) [74, 75]. The four-current can then be expressed as

$$j^{\mu}(\mathbf{r}) = c \sum_{-mc^2 < \epsilon_i \leqslant \epsilon_F} \psi^{\dagger}_{i}(\mathbf{r}) \alpha^{\mu} \psi_i(\mathbf{r}), \tag{4.7}$$

where ϵ_F is the Fermi level of the auxiliary system and the summation is over the electronic states. In (4.7) the symbol "†" indicates the Hermitian adjoint, and $\alpha^{\mu} = (\alpha^0, \boldsymbol{\alpha})$ is a four-vector of four-by-four matrices, with $\alpha^0 = I$ the identity matrix and $\boldsymbol{\alpha}$ given in (4.2). Within the Kohn-Sham scheme the total ground-state energy functional $E_0[j^{\mu}]$ can be decomposed in terms of the kinetic energy of the auxiliary system, $T_s[j^{\mu}]$, the external potential energy, $E_{ext}[j^{\mu}]$, the Hartree energy, $E_H[j^{\mu}]$, and the exchange-correlation functional, $E_{xc}[j^{\mu}]$,

$$E_0[j^{\mu}] = T_s[j^{\mu}] + E_{ext}[j^{\mu}] + E_H[j^{\mu}] + E_{xc}[j^{\mu}]. \tag{4.8}$$

The minimization of the total ground-state energy $E_0[j^{\mu}]$ with respect to the single-particle four-spinors ψ_k leads to the Dirac-like relativistic KS-equations [74, 75],

$$\left\{ c\boldsymbol{\alpha} \cdot \boldsymbol{\pi} + \beta c^2 + v_s(\mathbf{r}) \right\} \psi_i(\mathbf{r}) = \epsilon_i \psi_i(\mathbf{r}), \tag{4.9}$$

where $\boldsymbol{\pi} = \mathbf{p} + \mathbf{A}_s(\mathbf{r})/c$. The Kohn-Sham four-potential $V_s^\mu(\mathbf{r}) = (v_s(\mathbf{r}), \mathbf{A}_s(\mathbf{r}))$ consists of the external, the Hartree, and the exchange-correlation four-potentials, respectively,

$$\begin{aligned} v_s(\mathbf{r}) &= v_{ext}(\mathbf{r}) + \int d\mathbf{r}' \frac{\rho(\mathbf{r}')}{|\mathbf{r}-\mathbf{r}'|} + v_{xc}(\mathbf{r}), && (4.10) \\ \mathbf{A}_s(\mathbf{r}) &= \mathbf{A}_{ext}(\mathbf{r}) + \frac{1}{c}\int d\mathbf{r}' \frac{\mathbf{j}_T(\mathbf{r}')}{|\mathbf{r}-\mathbf{r}'|} + \mathbf{A}_{xc}(\mathbf{r}), && (4.11) \end{aligned}$$

where $\mathbf{j}_T(\mathbf{r}')$ is the transverse current-density (see chapter 2). Here the exchange-correlation four-potential $V_{xc}^\mu(\mathbf{r}) = (v_{xc}(\mathbf{r}), \mathbf{A}_{xc}(\mathbf{r}))$ is defined by the relation

$$\lim_{\lambda\to 0} \frac{E_{xc}[j^\mu + \lambda\delta j^\mu] - E_{xc}[j^\mu]}{\lambda} = \int V_{xc}^\mu(\mathbf{r})\delta j^\mu(\mathbf{r})d\mathbf{r}, \tag{4.12}$$

where $V_{xc}^\mu(\mathbf{r})$ is determined up to a gauge transformation $V_{xc}^{\mu\prime}(\mathbf{r}) \to V_{xc}^\mu(\mathbf{r}) + \delta_\mu\Lambda_{xc}(\mathbf{r})$ as

$$\begin{aligned} \int V_{xc}^{\mu\prime}(\mathbf{r})\delta j^\mu(\mathbf{r})d\mathbf{r} &= \int V_{xc}^\mu(\mathbf{r})\delta j^\mu(\mathbf{r})d\mathbf{r} - \int \Lambda_{xc}(\mathbf{r})\left(\delta_\mu\delta j^\mu(\mathbf{r})\right)d\mathbf{r} \\ &= \int V_{xc}^\mu(\mathbf{r})\delta j^\mu(\mathbf{r})d\mathbf{r}. && (4.13) \end{aligned}$$

Here we have used the condition of current conservation given in (4.5). The set of Eqs (4.7), (4.9)-(4.11) has to be solved self-consistently in order to obtain the exact four-current $j^\mu(\mathbf{r})$ of the interacting system. One can extend Eq. (4.9) to the time-domain [78],

$$\left\{c\alpha\cdot\boldsymbol{\pi} + \beta c^2 + v_s(\mathbf{r},t)\right\}\psi_i(\mathbf{r},t) = i\frac{\partial}{\partial t}\psi_i(\mathbf{r},t), \tag{4.14}$$

where $\boldsymbol{\pi} = \mathbf{p} + \mathbf{A}_s(\mathbf{r},t)/c$. The four-component current $j^\mu(\mathbf{r},t)$ is now time-dependent and it is given by

$$j^\mu(\mathbf{r},t) = c\sum_i \psi_i^\dagger(\mathbf{r},t)\alpha^\mu\psi_i(\mathbf{r},t), \tag{4.15}$$

where the summation is over states which represent the evolution of the initial occupied electronic states with energies $-mc^2 < \epsilon_i \leqslant \epsilon_F$. The scalar component of the four-current is the density,

$$\rho(\mathbf{r},t) = j^0(\mathbf{r},t)/c = \sum_i \psi_i^\dagger(\mathbf{r},t)\psi_i(\mathbf{r},t), \tag{4.16}$$

whereas the vector component is

$$\mathbf{j}(\mathbf{r},t) = c\sum_i \psi_i^\dagger(\mathbf{r},t)\boldsymbol{\alpha}\psi_i(\mathbf{r},t), \tag{4.17}$$

where we have used the notation $j^\mu = (c\rho, \mathbf{j})$.

4.1.2 Gordon decomposition of the four-current

To keep contact with the nonrelativistic density functional approaches, we can make more explicit the content of the vector current by using the Gordon decomposition. We rewrite the expression of the vector current as

$$\mathbf{j}(\mathbf{r},t) = c\sum_i \Big(\frac{1}{2}\psi_i^\dagger(\mathbf{r},t)\boldsymbol{\alpha}\psi_i(\mathbf{r},t) + \frac{1}{2}\psi_i^\dagger(\mathbf{r},t)\boldsymbol{\alpha}\psi_i(\mathbf{r},t)\Big), \tag{4.18}$$

and the time-dependent DKS equation (4.14) as

$$\psi_i(\mathbf{r},t) = -\frac{1}{c}\beta\boldsymbol{\alpha}\cdot\boldsymbol{\pi}\psi_i(\mathbf{r},t) + \frac{i\partial/\partial t - v_s(\mathbf{r},t)}{c^2}\beta\psi_i(\mathbf{r},t). \tag{4.19}$$

We can then substitute Eq. (4.19) into the first term on the right-hand side of Eq. (4.18), and its Hermitian adjoint into the second term. After some elementary rearrangements exploiting the properties of the matricies $\boldsymbol{\alpha}$ and β, we arrive at

$$\mathbf{j}(\mathbf{r},t) \;=\; \mathbf{j}_p(\mathbf{r}.t) + \mathbf{j}_d(\mathbf{r},t) + \nabla\times\mathbf{s}(\mathbf{r},t) + \frac{\partial\mathbf{g}(\mathbf{r},t)}{\partial t}, \tag{4.20}$$

with

$$\mathbf{j}_p(\mathbf{r},t) \;=\; -\frac{i}{2}\sum_i(\psi_i^\dagger(\mathbf{r},t)\cdot\beta\nabla\psi_i(\mathbf{r},t) - \nabla\psi_i^\dagger(\mathbf{r},t)\cdot\beta\psi_i(\mathbf{r},t)), \tag{4.21}$$

$$\mathbf{j}_d(\mathbf{r},t) \;=\; \frac{1}{c}\mathbf{A}_s(\mathbf{r},t)\sum_i\psi_i^\dagger(\mathbf{r},t)\beta\psi_i(\mathbf{r},t), \tag{4.22}$$

$$\mathbf{s}(\mathbf{r},t) \;=\; \frac{1}{2}\sum_i\psi_i^\dagger(\mathbf{r},t)\cdot\beta\boldsymbol{\Sigma}\psi_i(\mathbf{r},t), \tag{4.23}$$

$$\mathbf{g}(\mathbf{r},t) \;=\; -\frac{i}{2c}\sum_i\psi_i^\dagger(\mathbf{r},t)\cdot\beta\boldsymbol{\alpha}\psi_i(\mathbf{r},t). \tag{4.24}$$

The four-by-four matrix $\boldsymbol{\Sigma}$ in (4.23) is defined as

$$\boldsymbol{\Sigma} = \begin{pmatrix} \boldsymbol{\sigma} & 0 \\ 0 & \boldsymbol{\sigma} \end{pmatrix}. \tag{4.25}$$

We can conclude that the vector current can be split into the paramagnetic and diamagnetic components $\mathbf{j}_p(\mathbf{r},t)$ and $\mathbf{j}_d(\mathbf{r},t)$, a spin contribution expressed as curl of the spin density $\mathbf{s}(\mathbf{r},t)$, and a term which couples large and small components of the DKS wavefunction. Two important considerations on Eq. (4.20) need to be mentioned. First, the contribution to the current due to the term $\partial\mathbf{g}(\mathbf{r},t)/\partial t$ is of the order of c^{-1}, unlike the other contributions which are of the order of 1, and it even vanishes for stationary systems. The other important point, more subtle, is that only the Dirac-Kohn-Sham total current is the same as in the real system, while the various Dirac-Kohn-Sham terms in which the current can be decomposed do not necessarily have any physical meaning.

4.2 The ZORA equations

Fully relativistic calculations based on a four-component Hamiltonian are time-consuming. Several two-component formalisms have been developed and one of the most simple and elegant approaches is the zeroth-order regular approximation (ZORA) [79, 80].

4.2.1 Time-independent case

After the gauge transformation $v_s \rightarrow v_s - c^2$, the one-electron Dirac-Kohn-Sham equation for the large and small components of the four-component wavefunction can be written as follows,

$$\begin{pmatrix} v_s & c\,\sigma\cdot\boldsymbol{\pi} \\ c\,\sigma\cdot\boldsymbol{\pi} & v_s - 2c^2 \end{pmatrix} \cdot \begin{pmatrix} \phi \\ \chi \end{pmatrix} = \epsilon \begin{pmatrix} \phi \\ \chi \end{pmatrix}. \tag{4.26}$$

A two-component Hamiltonian for electronic states can be generated by finding a unitary transformation U,

$$U = \begin{pmatrix} \frac{1}{\sqrt{1+X^\dagger X}} & \frac{1}{\sqrt{1+X^\dagger X}} X^\dagger \\ -\frac{1}{\sqrt{1+XX^\dagger}} X & \frac{1}{\sqrt{1+XX^\dagger}} \end{pmatrix}, \tag{4.27}$$

with $U^{-1} = U^\dagger$, that reduces the Dirac Hamiltonian to a block diagonal form. Foldy and Wouthuysen introduced a systematic method for progressively decoupling large and small components [81]. The transformed Hamiltonian $U\hat{H}^D U^{-1}$ is block-diagonal if we choose $\hat{X}$ to satisfy

$$-\hat{X} v_s - \hat{X} c\boldsymbol{\sigma}\cdot\boldsymbol{\pi}\hat{X} + c\boldsymbol{\sigma}\cdot\boldsymbol{\pi} + (v_s - 2c^2)\hat{X} = 0. \tag{4.28}$$

The upper-left block is the Foldy-Wouthuysen Hamiltonian $\hat{H}^{FW}$,

$$\begin{aligned} \hat{H}^{FW} \;\; = \;\; & \frac{1}{\sqrt{1+\hat{X}^\dagger\hat{X}}} \times (c\boldsymbol{\sigma}\cdot\boldsymbol{\pi}\hat{X} + \hat{X}^\dagger c\boldsymbol{\sigma}\cdot\boldsymbol{\pi} - 2c^2\hat{X}^\dagger\hat{X} + v_s + \hat{X}^\dagger v_s \hat{X}) \times \\ & \frac{1}{\sqrt{1+\hat{X}^\dagger\hat{X}}}. \end{aligned} \tag{4.29}$$

The Foldy-Wouthuysen equation,

$$H^{FW}\Phi^{FW} = \epsilon\Phi^{FW}, \tag{4.30}$$

has the same one-electron energies ϵ as the Dirac equation, but generates only the positive energy spectrum. The wavefunction Φ^{FW} is a two-component wavefunction that can be related to the large and small components using

$$\begin{pmatrix} \Phi^{FW} \\ 0 \end{pmatrix} = U \begin{pmatrix} \phi \\ \chi \end{pmatrix}, \tag{4.31}$$

so that,

$$\Phi^{FW} = \frac{1}{\sqrt{1+\hat{X}^\dagger\hat{X}}}\phi + \frac{1}{\sqrt{1+\hat{X}^\dagger\hat{X}}}\hat{X}^\dagger\chi, \tag{4.32}$$

$$0 = -\frac{1}{\sqrt{1+\hat{X}\hat{X}^\dagger}}\hat{X}\phi + \frac{1}{\sqrt{1+\hat{X}\hat{X}^\dagger}}\chi. \tag{4.33}$$

The last equation is an identity if the operator $\hat{X}$ satisfies $\chi = \hat{X}\phi$. One can then obtain an expression for this operator from the Dirac equation for the small component in (4.26),

$$\chi = \frac{1}{2c^2+\epsilon-v_s}c\boldsymbol{\sigma}\cdot\boldsymbol{\pi}\phi = \hat{X}\phi, \tag{4.34}$$

where $\hat{X}$ automatically satisfies the condition (4.28). If we considered $1/\sqrt{1+\hat{X}^\dagger\hat{X}} = \sum_{n=0}^{\infty} a_n(\hat{X}^\dagger\hat{X})^n$, and we approximate $\hat{X}$ by expanding the energy-dependent expression $(2c^2+\epsilon-v_s)^{-1}c\boldsymbol{\sigma}\cdot\boldsymbol{\pi}$ in $\epsilon/(2c^2-v_s)$, then the Foldy-Wouthuysen Hamiltonian will give at zeroth order the ZORA (zeroth-order regular approximation) Hamiltonian H^{ZORA},

$$\hat{H}^{ZORA} = \boldsymbol{\sigma}\cdot\boldsymbol{\pi}\frac{c^2}{2c^2-v_s}\boldsymbol{\sigma}\cdot\boldsymbol{\pi} + v_s. \tag{4.35}$$

Note that the $\epsilon/(2c^2-v_s)$ expansion is valid for Coulomb-like potentials everywhere, provided that the energy of the particle is not too large, $\epsilon < (2c^2-v_s)$, as it is always the case for chemical applications. Another important observation is that by making the zeroth-order regular approximation for the operator $\hat{X}$, the unitary transformation U is correct only to order $\epsilon/(2c^2-v_s)$. Thus the transformed Hamiltonian is not exactly block-diagonal, but there is a residual coupling that we neglect. The small component are not completely annihilated as we have assumed in Eq. (4.31). The

ZORA kinetic operator $T^{ZORA} = \boldsymbol{\sigma} \cdot \boldsymbol{\pi} c^2/(2c^2 - v_s)\boldsymbol{\sigma} \cdot \boldsymbol{\pi}$ can be split into a scalar and a two-component part, so that the one-electron ZORA equation can be written as,

$$\left\{ \boldsymbol{\pi} \cdot \frac{K(\mathbf{r})}{2} \boldsymbol{\pi} + \frac{K^2(\mathbf{r})}{4c^2} \boldsymbol{\sigma} \cdot [\nabla v_s \times \boldsymbol{\pi}] - \frac{1}{c} \frac{K(\mathbf{r})}{2} \boldsymbol{\sigma} \cdot \mathbf{B}_s + v_s \right\} \Phi^{ZORA} = \epsilon \Phi^{ZORA}, \quad (4.36)$$

where $K(\mathbf{r}) = (1 - v_s(\mathbf{r})/2c^2)^{-1}$ and $\mathbf{B}_s = \nabla \times \mathbf{A}_s$. The ZORA one-particle wavefunctions Φ^{ZORA} are two-component spinors and represent the electron-like solutions of the Dirac four-component wavefunctions. The last two terms in the equation represent the spin-orbit coupling and the coupling between the spin and the magnetic field, respectively.

4.2.2 Time-dependent case

If we want to derive the ZORA equation for time-dependent problems, we have to start from the time-dependent Dirac equation,

$$\hat{H}^D \psi(\mathbf{r}, t) = i\partial_t \psi(\mathbf{r}, t), \quad (4.37)$$

where we use the notation $\partial_t = \partial/\partial t$. The equations for the large and small components are as follows,

$$\begin{aligned} v_s \, \phi + c\boldsymbol{\sigma} \cdot \boldsymbol{\pi} \, \chi &= i\partial_t \phi, && (4.38) \\ c\boldsymbol{\sigma} \cdot \boldsymbol{\pi} \, \phi + (v_s - 2c^2) \, \chi &= i\partial_t \chi. && (4.39) \end{aligned}$$

If we express the small component in term of the large component as $\chi = \hat{X}\phi$, Eqs (4.38)-(4.39) become

$$\begin{aligned} \left(v_s + c\boldsymbol{\sigma} \cdot \boldsymbol{\pi} \hat{X} \right) \phi &= i\partial_t \phi, && (4.40) \\ \left(c\boldsymbol{\sigma} \cdot \boldsymbol{\pi} + (v_s - 2c^2)\hat{X} \right) \phi &= i\partial_t (\hat{X}\phi) \\ &= [i\partial_t, \hat{X}]\phi + i\hat{X}\partial_t \phi. && (4.41) \end{aligned}$$

By substituting Eq. (4.40) in Eq. (4.41) we arrive at the following equation of motion,

$$c\boldsymbol{\sigma} \cdot \boldsymbol{\pi} + [v_s - i\partial_t, \hat{X}] - 2c^2 \hat{X} - \hat{X} c\boldsymbol{\sigma} \cdot \boldsymbol{\pi} \hat{X} = 0. \quad (4.42)$$

To solve this equation we isolate a time-independent part $(v_{s,0} - \epsilon) < 2c^2$ in the potential v_s, with $v_{s,0}$ an arbitrary function of $\mathbf{r}$ and ϵ an arbitrary constant, so that we can rewrite,

$$\hat{X} = \left(2c^2 - v_{s,0} + \epsilon \right)^{-1} \left(c\boldsymbol{\sigma} \cdot \boldsymbol{\pi} + \Xi(\hat{X}) \right), \quad (4.43)$$

where we introduce

$$\Xi(\hat{X}) = [v_s - v_{s,0} + \epsilon - i\partial_t, \hat{X}] - \hat{X}\left(v_{s,0} - \epsilon + c\boldsymbol{\sigma}\cdot\boldsymbol{\pi}\hat{X}\right). \tag{4.44}$$

We can choose $(v_{s,0} - \epsilon)$ in such a way that $\Xi(\hat{X})$ is small when acting on ϕ, i.e.,

$$\Xi(\hat{X})\phi = (v_s - v_{s,0} + \epsilon - i\partial_t)\,\chi, \tag{4.45}$$

for electron-like states. For example we can choose $v_{s,0}$ such that $(v_s - v_{s,0})$ is small everywhere and ϵ close to the orbital energy of the relevant states. In this way Eq. (4.43) can be solved by iteration,

$$\hat{X}_n = \left(2c^2 - v_{s,0} + \epsilon\right)^{-1}\left(c\boldsymbol{\sigma}\cdot\boldsymbol{\pi} + \Xi(\hat{X}_{n-1})\right). \tag{4.46}$$

If we insert an initial term $\hat{X}_{-1}$ on the right-hand side of Eq. (4.46), then we obtain on the left-hand side the term $\hat{X}_0$. We can then insert $\hat{X}_0$ on the right-side and obtain $\hat{X}_1$ and so on. If we take $\hat{X}_{-1} = 0$ then $\hat{X}_0$ is similar to the operator used in the stationary case,

$$\hat{X}_0 = \left(2c^2 - v_{s,0} + \epsilon\right)^{-1} c\boldsymbol{\sigma}\cdot\boldsymbol{\pi}. \tag{4.47}$$

Similar to the stationary case, the time-dependent Dirac equation can be reduced to a two-component one by using a unitary transformation U which leads to a transformed equation,

$$\left(U\hat{H}^D U^{-1} - U[i\partial_t, U^{-1}]\right)\Phi(\mathbf{r},t) \quad = \quad i\partial_t\Phi(\mathbf{r},t), \tag{4.48}$$

where the transformed Hamiltonian is block diagonal. Here $\Phi(\mathbf{r},t) = U\psi(\mathbf{r},t)$. The upper-left part of the transformed Hamiltonian is the two-component time-dependent Foldy-Wouthuysen Hamiltonian,

$$\begin{aligned}\hat{H}^{FW} = {} & v_s + \frac{1}{\sqrt{1+\hat{X}^\dagger\hat{X}}} \times \left(c\boldsymbol{\sigma}\cdot\boldsymbol{\pi}\hat{X} + \hat{X}^\dagger c\boldsymbol{\sigma}\cdot\boldsymbol{\pi} - 2c^2\hat{X}^\dagger\hat{X} - \hat{X}^\dagger\left[i\partial_t - v_s, \hat{X}\right]\right) \times \\ & \frac{1}{\sqrt{1+\hat{X}^\dagger\hat{X}}} - \sqrt{(1+\hat{X}^\dagger\hat{X})} \times \left[i\partial_t - v_s, \frac{1}{\sqrt{1+\hat{X}^\dagger\hat{X}}}\right],\end{aligned} \tag{4.49}$$

where we have collected the terms containing the potential v_s together with the terms containing the time derivative $i\partial_t$. By using the equation of motion (4.42) to write $\left[i\partial_t - v_s, \hat{X}\right] = -\left[v_s - i\partial_t, \hat{X}\right] = c\boldsymbol{\sigma}\cdot\boldsymbol{\pi} - 2c^2\hat{X} - \hat{X}c\boldsymbol{\sigma}\cdot\boldsymbol{\pi}\hat{X}$, Eq. (4.49) can be written as

$$\begin{aligned}\hat{H}^{FW} &= v_s + c\boldsymbol{\sigma}\cdot\boldsymbol{\pi}\hat{X} \\ &+ \left[i\partial_t - v_s - c\boldsymbol{\sigma}\cdot\boldsymbol{\pi}\hat{X}, \sqrt{1+\hat{X}^\dagger\hat{X}}\right] \times \frac{1}{\sqrt{1+\hat{X}^\dagger\hat{X}}}.\end{aligned} \tag{4.50}$$

To evaluate the commutator in the last line of Eq. (4.50) we express the square root $\sqrt{1+\hat{X}^\dagger\hat{X}}$ in a Taylor expansion $\sum_{n=0}^{\infty} a_n(\hat{X}^\dagger\hat{X})^n$. We have that

$$\Big[i\partial_t - v_s - c\boldsymbol{\sigma}\cdot\boldsymbol{\pi}\hat{X}, (\hat{X}^\dagger\hat{X})^n\Big] = \sum_{m=0}^{n-1}(\hat{X}^\dagger\hat{X})^m\Bigg(\Big[i\partial_t - v_s - c\boldsymbol{\sigma}\cdot\boldsymbol{\pi}\hat{X}, \hat{X}^\dagger\Big]\hat{X} + \hat{X}^\dagger\Big[i\partial_t - v_s - c\boldsymbol{\sigma}\cdot\boldsymbol{\pi}\hat{X}, \hat{X}\Big]\Bigg)(\hat{X}^\dagger\hat{X})^{n-m-1}. \quad (4.51)$$

By using again Eq. (4.42) for $\Big[i\partial_t - v_s, \hat{X}\Big]$ and for $\Big[i\partial_t - v_s, \hat{X}^\dagger\Big] = -\Big[i\partial_t - v_s, \hat{X}\Big]^\dagger$, and by working out the other two commutators, we arrive at

$$\begin{aligned}\Big[i\partial_t - v_s - c\boldsymbol{\sigma}\cdot\boldsymbol{\pi}\hat{X}, (\hat{X}^\dagger\hat{X})^n\Big] &= \sum_{m=0}^{n-1}(\hat{X}^\dagger\hat{X})^m\Big(\hat{X}^\dagger c\boldsymbol{\sigma}\cdot\boldsymbol{\pi} - c\boldsymbol{\sigma}\cdot\boldsymbol{\pi}\hat{X}\Big)\times \\ &\quad (\hat{X}^\dagger\hat{X})^{n-m-1}(1+\hat{X}^\dagger\hat{X}). \end{aligned} \quad (4.52)$$

By combining (4.50) and (4.52) we arrive at the following expression for the time-dependent Foldy-Wouthuysen Hamiltonian,

$$\hat{H}^{FW} = v_s + \frac{1}{2}\Big(c\boldsymbol{\sigma}\cdot\boldsymbol{\pi}\hat{X} + \hat{X}^\dagger c\boldsymbol{\sigma}\cdot\boldsymbol{\pi}\Big) + \hat{Y}, \quad (4.53)$$

where the operator $\hat{Y}$ is given by

$$\begin{aligned}\hat{Y} &= \frac{1}{2}\Big(c\boldsymbol{\sigma}\cdot\boldsymbol{\pi}\hat{X} - \hat{X}^\dagger c\boldsymbol{\sigma}\cdot\boldsymbol{\pi}\Big) \\ &- \sum_{n=0}^{\infty}a_n\sum_{m=0}^{n-1}(\hat{X}^\dagger\hat{X})^m\Big(c\boldsymbol{\sigma}\cdot\boldsymbol{\pi}\hat{X} - \hat{X}^\dagger c\boldsymbol{\sigma}\cdot\boldsymbol{\pi}\Big)\times \\ &\quad (\hat{X}^\dagger\hat{X})^{n-m-1}\times\sqrt{1+\hat{X}^\dagger\hat{X}}. \end{aligned} \quad (4.54)$$

The expression (4.53) shows that the time-dependent Foldy-Wouthuysen Hamiltonian is the sum of a Hermitian part similar to the stationary ZORA Hamiltonian (4.35) and a remainder $\hat{Y}$. In App. D we show that this remainder is Hermitian as well and of the first order in $(\hat{X}^\dagger\hat{X})$. If we neglect terms of the order of $\Xi(\hat{X})$ in the expression (4.43), then $\hat{X} = \hat{X}_0$ and $\hat{Y} = 0$. Using this approximation in Eq. (4.53) we obtain the time-dependent ZORA Hamiltonian,

$$\hat{H}^{ZORA} = v_s + \boldsymbol{\sigma}\cdot\boldsymbol{\pi}\frac{c^2}{2c^2 - v_{s,0} + \epsilon}\boldsymbol{\sigma}\cdot\boldsymbol{\pi}. \quad (4.55)$$

4.2.3 Gauge invariance

The ZORA equation (4.35) is not gauge invariant under a gauge transformation

$$v_s(\mathbf{r}) \quad \rightarrow \quad v_s(\mathbf{r}) + \Delta, \tag{4.56}$$

with Δ a constant. As shown in Ref. [79] the ZORA equation for this potential will not have eigenvalues which are shifted by the same constant. The equation is, however, gauge invariant under the combined gauge transformation

$$\begin{aligned} \mathbf{A}_s(\mathbf{r}) &\quad \rightarrow \quad \mathbf{A}_s(\mathbf{r}) + \nabla\Lambda(\mathbf{r}), \\ \Phi^{ZORA}(\mathbf{r}) &\quad \rightarrow \quad \Phi^{ZORA}(\mathbf{r})e^{-i\Lambda(\mathbf{r})}, \end{aligned} \tag{4.57}$$

where $\Lambda(\mathbf{r})$ is any scalar function of position only. The time-dependent ZORA equation (4.55) is, instead, gauge invariant under the transformations

$$\begin{aligned} v_s(\mathbf{r},t) &\quad \rightarrow \quad v_s(\mathbf{r},t) + \frac{\partial\Lambda(\mathbf{r},t)}{\partial t}, \\ \mathbf{A}_s(\mathbf{r},t) &\quad \rightarrow \quad \mathbf{A}_s(\mathbf{r},t) + \nabla\Lambda(\mathbf{r},t), \\ \Phi^{ZORA}(\mathbf{r},t) &\quad \rightarrow \quad \Phi^{ZORA}(\mathbf{r},t)e^{-i\Lambda(\mathbf{r},t)}, \end{aligned} \tag{4.58}$$

provided that the potential $(v_{s,0}(\mathbf{r}) - \epsilon)$ is kept fixed. Here $\Lambda(\mathbf{r},t)$ is now a scalar function of space and time. This means that the time-dependent ZORA equation is gauge-invariant, but the results depend on the choice of $(v_{s,0}(\mathbf{r}) - \epsilon)$. In practical applications one can demand the potential $v_s(\mathbf{r},t_0)$ to go to zero at infinity. In this case one can choose $v_{s,0}(\mathbf{r}) = v_s(\mathbf{r},t_0) - v_s(\mathbf{r}=\infty,t_0)$ and $\epsilon = 0$, where v_s is calculated in the Coulomb gauge ($\nabla\cdot\mathbf{A}_s(\mathbf{r},t_0) = 0$), and the gauge-invariance (4.58) is guaranteed, but it still depends on our particular choice for $(v_{s,0}(\mathbf{r}) - \epsilon)$.

4.2.4 The relativistic ZORA density and current operators

The unitary transformation that is used to reduce the four-component Dirac equation to an effective two-component pseudorelativistic equation represents a picture change: we pass from the Dirac picture to a new picture, which is appropriately called Schrödinger picture. This picture change requires that not only the wavefunction is transformed but also the operators, in order to keep the physics unaltered. For example, the position operator $\hat{\mathbf{r}}$ represents in the new picture a new physical observable which is called the mean position or mass position $\hat{\mathbf{r}}_{mass}$ of the electron [81,82], while the transformed $U\hat{\mathbf{r}}U^{-1}$ operator represents the original position in the new picture. Neglecting the picture change results in an error, which is usually small but visible for core states [83]. We define the four-current operator in the Dirac picture as

$$\hat{j}^D_\mu(\mathbf{r}) = c\sum_i \delta(\mathbf{r}-\mathbf{r}_i)\alpha^\mu, \tag{4.59}$$

where the scalar component is the density operator $\hat{\rho}^D(\mathbf{r}) = \sum_i \delta(\mathbf{r}-\mathbf{r}_i)\alpha^0$, and the vector component the current operator $\hat{\mathbf{j}}^D(\mathbf{r}) = c\sum_i \delta(\mathbf{r}-\mathbf{r}_i)\boldsymbol{\alpha}$. If we transform $\hat{\rho}^D(\mathbf{r})$, the Foldy-Wouthuysen density operator $\hat{\rho}^{FW}$ is given by

$$\hat{\rho}^{FW}(\mathbf{r}) = \sum_i \frac{1}{\sqrt{1+\hat{X}^\dagger\hat{X}}}\left(\delta(\mathbf{r}-\mathbf{r}_i) + \hat{X}^\dagger\delta(\mathbf{r}-\mathbf{r}_i)\hat{X}\right)\frac{1}{\sqrt{1+\hat{X}^\dagger\hat{X}}}. \tag{4.60}$$

If we take the operator $\hat{X}$ to be the ZORA operator $\hat{X}_0$ and we neglect terms of order of $(\hat{X}^\dagger\hat{X})$ in Eq. (4.60), the approximate ZORA density operator is simply

$$\hat{\rho}^{ZORA}(\mathbf{r}) = \sum_i \delta(\mathbf{r}-\mathbf{r}_i). \tag{4.61}$$

This amounts to neglect the picture change for the density operator, in line with van Lenthe *et al.* [79], who showed that the approximate ZORA density reproduces very well the Dirac density, in particular for the valence region.

For the transformed current operator we proceed in a similar way, and the Foldy-Wouthuysen current operator $\hat{j}^{FW}_\mu(\mathbf{r})$ is given by

$$\hat{j}^{FW}_\mu(\mathbf{r}) = \sum_i \frac{1}{\sqrt{1+\hat{X}^\dagger\hat{X}}}\left(c\delta(\mathbf{r}-\mathbf{r}_i)\,\sigma_\mu\hat{X} + c\hat{X}^\dagger\delta(\mathbf{r}-\mathbf{r}_i)\,\sigma_\mu\right)\frac{1}{\sqrt{1+\hat{X}^\dagger\hat{X}}}. \tag{4.62}$$

In the zeroth-order regular approximation the ZORA current operator is given by

$$\hat{j}^{ZORA}_\mu(\mathbf{r}) = \sum_i \left(\delta(\mathbf{r}-\mathbf{r}_i)\sigma_\mu\frac{K(\mathbf{r}_i)}{2}(\boldsymbol{\sigma}\cdot\boldsymbol{\pi}_i) + (\boldsymbol{\sigma}\cdot\boldsymbol{\pi}_i)\frac{K(\mathbf{r}_i)}{2}\delta(\mathbf{r}-\mathbf{r}_i)\sigma_\mu\right). \tag{4.63}$$

By exploiting the property of the Pauli matrices, $\sigma_\mu\sigma_\nu = \delta_{\mu\nu} + i\sum_\tau \epsilon_{\mu\nu\tau}\sigma_\tau$, this expression can be rearranged as

$$\begin{aligned}
\hat{j}^{ZORA}_\mu(\mathbf{r}) &= \sum_{i\nu}\left(\delta(\mathbf{r}-\mathbf{r}_i)\frac{K(\mathbf{r}_i)}{2}\sigma_\mu\sigma_\nu\pi_{i\nu} + \sigma_\nu\pi_{i\nu}\sigma_\mu\frac{K(\mathbf{r}_i)}{2}\delta(\mathbf{r}-\mathbf{r}_i)\right) \\
&= \sum_{i\nu}\Big(\delta(\mathbf{r}-\mathbf{r}_i)\frac{K(\mathbf{r}_i)}{2}(\delta_{\mu\nu} + i\sum_\tau \epsilon_{\mu\nu\tau}\sigma_\tau)\pi_{i\nu} + \\
&\quad (\delta_{\mu\nu} + i\sum_{i\tau}\epsilon_{\nu\mu\tau}\sigma_\tau)\pi_{i\nu}\frac{K(\mathbf{r}_i)}{2}\delta(\mathbf{r}-\mathbf{r}_i)\Big) \\
&= \sum_i\left(\delta(\mathbf{r}-\mathbf{r}_i)\frac{K(\mathbf{r}_i)}{2}\pi_{i\mu} + \pi_{i\mu}\frac{K(\mathbf{r}_i)}{2}\delta(\mathbf{r}-\mathbf{r}_i)\right) + \\
&\quad \left(\delta(\mathbf{r}-\mathbf{r}_i)\frac{K(\mathbf{r}_i)}{2}i(\mathbf{p}_i\times\boldsymbol{\sigma})_\mu - i(\mathbf{p}_i\times\boldsymbol{\sigma})_\mu\frac{K(\mathbf{r}_i)}{2}\delta(\mathbf{r}-\mathbf{r}_i)\right).
\end{aligned} \tag{4.64}$$

From this expression it follows that the approximate ZORA current operator can be decomposed into a paramagnetic, a diamagnetic, and a spin contribution, given by

$$\begin{aligned} \hat{\mathbf{j}}_p(\mathbf{r}) &= -\frac{i}{2}K(\mathbf{r})\sum_i \left[\delta(\mathbf{r}-\mathbf{r}_i)\nabla_i - \nabla_i^{\dagger}\delta(\mathbf{r}-\mathbf{r}_i)\right], && (4.65)\\ \hat{\mathbf{j}}_d(\mathbf{r}) &= \frac{1}{c}K(\mathbf{r})\sum_i \delta(\mathbf{r}-\mathbf{r}_i)\mathbf{A}_s(\mathbf{r}_i,t), && (4.66)\\ \hat{\mathbf{j}}_s(\mathbf{r}) &= K(\mathbf{r})\nabla\times\hat{\mathbf{s}}(\mathbf{r}), && (4.67) \end{aligned}$$

where

$$\hat{\mathbf{s}}(\mathbf{r}) = \frac{1}{2}\sum_i \delta(\mathbf{r}-\mathbf{r}_i)\boldsymbol{\sigma}. \tag{4.68}$$

It now becomes clear that the composition of the ZORA current-density is similar to the one obtained in the Gordon decomposition of the Dirac current (see Eq. (4.20)-(4.24)). Note that one arrives at the same expression (4.64) for the ZORA current operator by starting from the following anticommutator,

$$\hat{\mathbf{j}}^{ZORA}(\mathbf{r}) = \frac{1}{2}\sum_i \left\{\hat{\mathbf{v}}_i^{ZORA}, \delta(\mathbf{r}-\mathbf{r}_i)\right\}, \tag{4.69}$$

with the approximate ZORA velocity operator given as

$$\hat{\mathbf{v}}_i^{ZORA} = -i\left[\mathbf{r}_i, H_i^{ZORA}\right]. \tag{4.70}$$

This relation guarantees the validity of the Thomas-Reiche-Kuhn f-sum rule, which is used in the form of the conductivity sumrule in our response calculations.

4.2.5 Linear response

We can now combine the ZORA formalism with the time-dependent current-density formulation of the linear response of solids to a macroscopic field given in chapter 3. We start from a Kohn-Sham system in the ground-state described by the stationary ZORA Hamiltonian

$$\hat{H}_0^{ZORA} = \sum_i \left(v_{\mathit{eff},0}(\mathbf{r}_i) + \boldsymbol{\sigma}\cdot\mathbf{p}_i \frac{c^2}{2c^2 - v_{\mathit{eff},0}(\mathbf{r}_i)}\boldsymbol{\sigma}\cdot\mathbf{p}_i\right), \tag{4.71}$$

and we study the response of the system to small perturbing potentials $\delta v_{\mathit{eff}}(\mathbf{r},t)$ and $\delta\mathbf{A}_{\mathit{eff}}(\mathbf{r},t)$. To do this we consider the time-dependent ZORA Hamiltonian (4.55) with

$$\begin{aligned} v_{\mathit{eff}}(\mathbf{r},t) &= v_{\mathit{eff},0}(\mathbf{r}) + \delta v_{\mathit{eff}}(\mathbf{r},t),\\ \mathbf{A}_{\mathit{eff}}(\mathbf{r},t) &= \delta\mathbf{A}_{\mathit{eff}}(\mathbf{r},t), \end{aligned}$$

where the effective potentials have been described in chapter 3. We then have

$$\begin{aligned}
\hat{H}^{ZORA}(t) &= \sum_i \left\{ \boldsymbol{\pi}_i \cdot \frac{K(\mathbf{r}_i)}{2}\boldsymbol{\pi}_i + i\boldsymbol{\sigma}\left(\boldsymbol{\pi}_i \times \frac{K(\mathbf{r}_i)}{2}\boldsymbol{\pi}_i\right) + v_{\mathit{eff},0}(\mathbf{r}_i) + \delta v_{\mathit{eff}}(\mathbf{r}_i,t)\right\} \\
&= \sum_i \left\{ \mathbf{p}_i \cdot \frac{K(\mathbf{r}_i)}{2}\mathbf{p}_i + v_{\mathit{eff},0}(\mathbf{r}_i) + \delta v_{\mathit{eff}}(\mathbf{r}_i,t) \right. \\
&+ \frac{1}{2c}\left[\mathbf{p}_i \cdot K(\mathbf{r}_i)\delta\mathbf{A}_{\mathit{eff}}(\mathbf{r}_i,t) + \delta\mathbf{A}_{\mathit{eff}}(\mathbf{r}_i,t)\cdot K(\mathbf{r}_i)\mathbf{p}_i\right] + \frac{K(\mathbf{r}_i)}{2c}\delta\mathbf{A}^2_{\mathit{eff}}(\mathbf{r}_i,t) \\
&+ \left. \frac{i}{2c}\left[\delta\mathbf{A}_{\mathit{eff}}(\mathbf{r}_i,t)K(\mathbf{r}_i)(\mathbf{p}_i\times\boldsymbol{\sigma}) - (\mathbf{p}_i\times\boldsymbol{\sigma})K(\mathbf{r}_i)\delta\mathbf{A}_{\mathit{eff}}(\mathbf{r}_i,t)\right]\right\}. \qquad (4.72)
\end{aligned}$$

This expression can be arranged further as follows,

$$\begin{aligned}
\hat{H}^{ZORA}(t) = &\sum_i \left(-\nabla_i \cdot \frac{K(\mathbf{r}_i)}{2}\nabla_i + v_{\mathit{eff},0}(\mathbf{r}_i)\right) + \int \left\{ d\mathbf{r} \sum_i \delta(\mathbf{r}-\mathbf{r}_i)\delta v_{\mathit{eff}}(\mathbf{r},t) \right. \\
&- \frac{i}{2c}\sum_i \left(\delta(\mathbf{r}-\mathbf{r}_i)K(\mathbf{r}_i)\nabla_i - \nabla_i^\dagger K(\mathbf{r}_i)\delta(\mathbf{r}-\mathbf{r}_i)\right)\delta\mathbf{A}_{\mathit{eff}}(\mathbf{r},t) \\
&+ \left. \sum_i \delta(\mathbf{r}-\mathbf{r}_i)\frac{K(\mathbf{r}_i)}{2c^2}\delta\mathbf{A}^2_{\mathit{eff}}(\mathbf{r},t) + \frac{K(\mathbf{r})}{c}\left(\nabla\times\hat{\mathbf{s}}(\mathbf{r})\right)\delta\mathbf{A}_{\mathit{eff}}(\mathbf{r},t)\right\} d\mathbf{r}, \quad (4.73)
\end{aligned}$$

where we have considered $\mathbf{p} = -i\nabla$, $v_{\mathit{eff}}(\mathbf{r}_i,t) = \int \delta(\mathbf{r}-\mathbf{r}_i)v_{\mathit{eff}}(\mathbf{r},t)d\mathbf{r}$, and $\mathbf{A}_{\mathit{eff}}(\mathbf{r}_i,t) = \int \delta(\mathbf{r}-\mathbf{r}_i)\mathbf{A}_{\mathit{eff}}(\mathbf{r},t)d\mathbf{r}$. The first two terms on the right-hand side of Eq. (4.73) represent the ground-state ZORA Hamiltonian (4.71), whereas the remaining terms represent the perturbation Hamiltonian $\delta\hat{h}(t)$, which can be written as

$$\begin{aligned}
\delta\hat{h}(t) &= \int \Big(\hat{\rho}(\mathbf{r})\delta v_{\mathit{eff}}(\mathbf{r},t) + \frac{1}{c}\hat{\mathbf{j}}_p(\mathbf{r})\cdot\delta\mathbf{A}_{\mathit{eff}}(\mathbf{r},t) \\
&+ \frac{1}{2c^2}\hat{\rho}K(\mathbf{r})\mathbf{A}^2_{\mathit{eff}}(\mathbf{r},t) + \frac{1}{c}\hat{\mathbf{j}}_s(\mathbf{r})\cdot\delta\mathbf{A}_{\mathit{eff}}(\mathbf{r},t)\Big)d\mathbf{r}. \qquad (4.74)
\end{aligned}$$

Note that the last term on the right-hand side of Eq. (4.74) represents the perturbation due to a magnetic field $\delta\mathbf{B}_{\mathit{eff}}(\mathbf{r},t) = \nabla\times\delta\mathbf{A}_{\mathit{eff}}(\mathbf{r},t)$,

$$\begin{aligned}
\frac{1}{c}\hat{\mathbf{j}}_s(\mathbf{r})\cdot\delta\mathbf{A}_{\mathit{eff}}(\mathbf{r},t) &= -\frac{1}{c}\hat{\mathbf{s}}(\mathbf{r})\left(\nabla\times K(\mathbf{r})\delta\mathbf{A}_{\mathit{eff}}(\mathbf{r},t)\right) \\
&= -\frac{1}{c}\hat{\mathbf{s}}(\mathbf{r})\left(\nabla K(\mathbf{r})\times\delta\mathbf{A}_{\mathit{eff}}(\mathbf{r},t)\right) - \frac{1}{c}K(\mathbf{r})\hat{\mathbf{s}}(\mathbf{r})\cdot\delta\mathbf{B}_{\mathit{eff}}(\mathbf{r},t). \quad (4.75)
\end{aligned}$$

We will not treat response to magnetic fields in this thesis, thus $\delta\mathbf{B}_{\mathit{eff}}(\mathbf{r},t) = 0$. Furthermore, for the systems of interest here $\nabla v_{s,0}(\mathbf{r}) \ll 2c^2$ everywhere except close to the nuclei. Therefore the term $\nabla K(\mathbf{r}) = K^2(\mathbf{r})\nabla v_{s,0}(\mathbf{r})/(2c^2)$ is smaller than one everywhere, except in a small volume around the nuclei which, however, has a negligible contribution to the integrals in which it appears. The last term in (4.74) will thus give a very small contribution to the perturbation. If we do not include spin-orbit coupling in the time-dependent ZORA Hamiltonian, and we consider only scalar relativistic effects, then this last term does not appear in the perturbation. We can conclude that the difference in the perturbation within the scalar ZORA and the ZORA approaches is small, and that the main effect of the spin-orbit coupling on the linear response is due to the changes in the ground-state orbital energies. It now becomes clear how we can solve the linear response for a Kohn-Sham system within the ZORA approximation. We first solve the time-independent ZORA equation (4.71) to obtain the ground-state orbitals and orbital energies. Given the perturbation (4.74), in which we retain only terms linear in the field, we can then evaluate the various response functions and solve self-consistently the equations describing the induced density and induced current-density.

Chapter 5

Optical Response of Gold

We treat the dominant scalar relativistic effects using the zeroth-order regular approximation in the ground-state density-functional theory calculations, as well as in the time-dependent response calculations of gold. As well known, relativistic effects strongly influence the color of gold. We find that the onset of interband transitions is shifted from around 3.5 eV, obtained in a nonrelativistic calculation, to around 1.9 eV when relativity is included. With the inclusion of the scalar relativistic effects there is an overall improvement of both real and imaginary parts of the dielectric function over the nonrelativistic ones. Nevertheless some important features in the absorption spectrum are not well reproduced, but can be explained in terms of spin-orbit coupling effects.

5.1 Introduction

In chapter 3 we have extended the time-dependent current-density-functional theory (TDCDFT) formulation for the response of nonmetallic crystals [30, 31] to treat metals [84]. We have shown that this approach works well within the adiabatic local density approximation for copper and silver. Even though for both metals the onset for the interband transitions is shifted to lower frequency over about 10 percent, the main features of the spectra are well reproduced, resulting in an overall good agreement of the dielectric function with the experimental data. When applied to gold the results are not as good as described above. This can be attributed mainly to the large relativistic effects that gold exhibits. Indeed, from calculations in atoms [64, 85] and in many other systems [86], it is well known that the nuclear charge of gold is so large (Z=79) that the relativistic effects become important. The same conclusion can be expected to hold true for the solid as well. We analyze the influence of relativistic effects on the linear response by including scalar relativistic effects within the zeroth-order regular approximation (ZORA) in our full-potential ground-state DFT as well as in the time-dependent response calculations. We can interpret the absorption spectrum in terms of direct interband transitions. The inclusion of the scalar relativistic effects in our ground-state DFT-LDA band structure calculation strongly stabilizes the s- and p-like conduction bands and, to a lesser extent, destabilizes the highest occupied d-like valence bands. The band gap between d-like bands and the conduction bands is, thus, reduced accounting for a redshift of the absorption edge of gold (associated with transitions from the highest occupied d-like band to the Fermi level near the high-symmetry points L and X). Similar results have been obtained by different authors and are well recognized [87–90]. Much more puzzling is the origin of the other absorption peaks. For example Winsemius *et al.* [91], analyzing the temperature dependence of the optical properties of Au, found that frequently proposed assignments of the spectrum in the region 3.6-5.4 eV are not complete. From our analysis of the absorption spectrum we also find that some of the previous assignments are not complete. Furthermore not so many discussions have been found in literature about the high-frequency region of 6-10 eV [88, 89, 92]. We discuss also this spectral region and find some discrepancies with some previous tentative assignments. The outline of the chapter is as follows. First we show the way in which scalar relativistic ZORA is implemented in the TDCDFT for the response of metals, following the same line used by Kootstra *et al.* [93] for the linear response of nonmetallic systems. In particular, we treat the intraband contribution to the linear response. The main aspects of the implementation are briefly explained. Finally, we report our results for the band structure and dielectric function of the crystal of Au and compare them with the experimental data found in literature [51, 70, 92] and with recent ellipsometric measurements [94].

5.2 Theory

The scalar relativistic (SR) effects have earlier been included in the response calculation of nonmetallic crystals by Kootstra *et al.* [93, 95]. We now treat these effects in the linear response of metals as well by using the zeroth-order regular approximation (ZORA) as described in chapter 4. In the long-wavelength limit ($q \to 0$) and within the ALDA, the macroscopic dielectric function of a metal can be defined as [84]

$$\epsilon(\omega) = (1 + 4\pi\chi_e^{inter}(\omega)) - \frac{4\pi i}{\omega}\sigma^{intra}(\omega), \tag{5.1}$$

where $\chi_e^{inter}(\omega)$ is the interband contribution to the electric susceptibility that can be derived from the current induced by a macroscopic field $\mathbf{E}_{mac} = \hat{\mathbf{e}}$ *via*

$$\chi_e^{inter}(\omega) \cdot \hat{\mathbf{e}} = \left(\frac{-i}{\omega V} \int \delta \mathbf{j}^{inter}_{\mathbf{q}=\mathbf{0}}(\mathbf{r}, \omega) d\mathbf{r} \right) \Bigg|_{\mathbf{E}_{mac}=\hat{\mathbf{e}}}, \tag{5.2}$$

and $\sigma^{intra}(\omega)$ is the intraband contribution to the macroscopic conductivity tensor at $\mathbf{q} = \mathbf{0}$,

$$\sigma^{intra}(\omega) = \frac{-i}{\omega V} \int \int \left(\chi^{intra}_{\mathbf{jjq=0}}(\mathbf{r}, \mathbf{r}', \omega) - \chi^{intra,0}_{\mathbf{jjq=0}}(\mathbf{r}, \mathbf{r}', \omega = 0) \right) d\mathbf{r} d\mathbf{r}', \tag{5.3}$$

which is independent from the interband response within the adiabatic local-density approximation (ALDA) [84]. The scalar relativistic effects in Eq. (5.2) have been introduced in the same way described by Kootstra *et al* [93]. We focus here on the intraband contribution $-4\pi i/\omega\, \sigma^{intra}(\omega)$ to the dielectric function. The combination of the current-current response function and its static value, respectively, $\chi^{intra}_{\mathbf{jjq}}$ and $\chi^{intra,0}_{\mathbf{jjq}}$, in Eq. (5.3) is given at $\mathbf{q} = \mathbf{0}$ by

$$\begin{aligned} \chi^{intra}_{\mathbf{jjq=0}}(\mathbf{r}, \mathbf{r}', \omega) - \chi^{intra}_{\mathbf{jjq=0}}(\mathbf{r}, \mathbf{r}', \omega = 0) = \frac{V}{4\pi^3} \sum_i \int_{S_i} \frac{d^2\mathbf{k}}{|\nabla_{\mathbf{k}} \epsilon_{i\mathbf{k}}|} \times \\ (\psi^*_{i\mathbf{k}}(\mathbf{r}) \hat{\mathbf{j}} \psi_{i\mathbf{k}}(\mathbf{r})) \otimes (\psi^*_{i\mathbf{k}}(\mathbf{r}') \hat{\mathbf{j}}' \psi_{i\mathbf{k}}(\mathbf{r}')), \end{aligned} \tag{5.4}$$

in which i runs over all partially occupied band indices and the integrations are over the sheets S_i of the Fermi-surface originating from the bands i. The Bloch functions $\psi_{i\mathbf{k}}(\mathbf{r})$ are the solutions of the ground-state ZORA equation with eigenvalues $\epsilon_{i\mathbf{k}}$,

$$\left[\mathbf{p} \cdot \frac{c^2}{2c^2 - v_{eff,0}(\mathbf{r})} \mathbf{p} + v_{eff,0}(\mathbf{r}) \right] \psi_{i\mathbf{k}}(\mathbf{r}) = \epsilon_{i\mathbf{k}} \psi_{i\mathbf{k}}(\mathbf{r}), \tag{5.5}$$

where $\mathbf{p} = -i\nabla$, c is the velocity of light, and $v_{eff,0}(\mathbf{r})$ is the self-consistent effective potential. The operator $\hat{\mathbf{j}}$ has the following scalar ZORA relativistic expression,

$$\hat{\mathbf{j}}^{ZORA} = -\frac{i}{2} \left(K(\mathbf{r}) \nabla - \nabla^\dagger K(\mathbf{r}) \right), \tag{5.6}$$

where $K(\mathbf{r}) = (1 - v_{eff,0}(\mathbf{r})/2c^2)^{-1}$. In nonrelativistic response calculations based on relativistic ground-state calculations the ordinary operator

$$\hat{\mathbf{j}}^{NR} = -\frac{i}{2} \left(\nabla - \nabla^\dagger \right) \tag{5.7}$$

is used. We use the time-dependent extension of the ground-state DFT approach [30, 31, 84] to treat the dynamic linear response of metallic crystals to a perturbation described by a scalar and a vector effective potential. We choose the gauge to be the microscopic Coulomb gauge, in which the effective scalar potential is completely microscopic, i.e., lattice periodic. All macroscopic contributions due to the inter and intraband parts of the induced density and current-density are gauge transformed to the effective vector potential. Using the local exchange-correlation approximation and considering the limit for vanishing q, only a contribution to the exchange-correlation scalar potential remains due to the microscopic interband part of the induced density. It then follows that, within the ALDA and at $q = 0$, the self-consistent-field equations describing the inter and intraband contributions to the response decouple [84]. These conditions remain valid also for the scalar relativistic case. Given a fixed effective vector potential, we first solve the equations for interband contribution to the induced density $\delta\rho^{inter}(\mathbf{r}, \omega)$, using an iterative scheme in which the microscopic scalar potential is updated at each cycle until self-consictency is established. With the self-consistent perturbing potentials obtained, we can calculate the inter and intraband contributions to the dielectric function $\epsilon(\omega)$ from the inter and intraband parts of the induced current-density, $\delta\mathbf{j}^{inter/intra}(\mathbf{r}, \omega)$. We used this method before to calculate the dielectric funtion of copper and silver crystals. The results reported in chapter 3 [84] show a reasonable overall agreement with the experimental data for both the real and imaginary parts of the dielectric functions.

5.3 Results and discussion

We present our results for the optical dielectric function in the spectral range of 0-10 eV of the isotropic crystal of gold. To analyze the importance of relativistic effects we compare the response calculated by including relativity in both the ground-state and time-dependent response calculations with those obtained by including the relativity only in the ground-state calculation, and with nonrelativistic results. The band structures calculated with and without scalar relativistic effects are also reported in order to interpret the spectra. We also report the band-structure obtained including the spin-orbit coupling in order to estimate its effect on the optical properties. The gold crystal has the fcc lattice type for which we used the experimental lattice constant 4.08 Å. All calculations were performed using a modified local version of the ADF-BAND program [30, 31, 61, 62, 84, 96, 97]. We made use of a hybrid valence basis set consisting of Slater-type orbitals (STOs) in combination with the numerical solutions of a relativistic free-atom Herman-Skillman program [64]. Cores were kept frozen up to $4f$. The spatial resolution of this basis is equivalent to a STO triple-zeta basis set augmented with two polarization functions. The Herman-Skillman program also provides us with the free-atom effective potential. The crystal potential was evaluated using an auxiliary basis set of STO functions to fit the deformation density in the ground-state calculation and the induced density in the response calculation. For the evaluation of the **k**-space integrals we used a quadratic numerical integration scheme with 175 symmetry-unique sample points in the irreducible wedge of the Brillouin zone, which was constructed by adopting a Lehmann-Taut tetrahedron scheme [59, 60]. In all our calculations we use the nonrelativistic local density approximation (LDA) for the exchange-correlation functional. The use of relativistic exchange-correlation functionals do not change the cohesive properties and the band structure beyond the 1 percent level for the $5d$ transition metal system gold [98]. In contrast with the $3d$ transition metals, in the $5d$ transition metals the generalized gradient approximations (GGAs) overcorrect the cohesive properties [99, 100]. For comparison we have performed the calculation of the dielectric function also at the GGA level, using the exchange-correlation functional proposed by Perdew and Wang (PW91) [101] and the one by Becke for the exchange [9] and Perdew for the correlation [10] (BP). The results, however, are very similar to those obtained at the LDA level, in line with the results found by Schmid *et al.* [98]. All results shown here were obtained using the Vosko-Wilk-Nusair parametrization [65] of the LDA exchange-correlation potential, which was also used to derive the ALDA exchange-correlation kernel.

5.3.1 Dielectric function and band structure

In Fig. 5.1 the nonrelativistic (NR) and scalar relativistic (SR) results calculated for the real and imaginary parts of the dielectric function of Au are compared with the experimental data from literature [51, 70, 92] and with recent measurements carried out using a spectroscopic ellipsometric method [94]. The inclusion of scalar relativistic effects causes a general redshift of both the real and imaginary parts of the dielectric function resulting in a reasonable agreement with the experimental data. In particular, the Drude-like tail in the real part is much better reproduced. We have also calculated the dielectric function by including the scalar relativistic effects only in the ground-state calculation and not in the response part. These results are very close to those with the relativistic effects included also in the response part and are therefore not depicted in Fig. 5.1. We can conclude that relativistic effects in the response of gold are mainly due to their influence on the band structure. In Fig. 5.2 we show the band structures calculated with and without the inclusion of scalar relativistic effects in the ground-state DFT calculation. In order to facilitate the comparison between the two band-structures we report all energy levels with respect to the Fermi energy of the scalar relativistic calculation. The valence bands are numbered at a given k-point starting from the lowest band. The occupied bands are predominantly $5d$-like, although they show hybridization with the $6s$ and $6p$ bands. The d bands are rather dispersionless and slightly destabilized by the scalar relativistic effects, except for band 1 at the zone center, which is strongly stabilized around Γ due to the strong s character. Contrary to the d bands, the sp-conduction bands are strongly stabilized by relativistic effects. This results in lowering the energy of the half-occupied band 6, which is predominantly p-like near the zone boundary, and with it the Fermi level. Also band 7, which is predominantly s-like near the zone boundary, is stabilized. The onset of the interband absorptions that is due to transitions from band 5 to the Fermi level in the optically active regions around the high-symmetry points L and X is then redshifted over about 1.6 eV with respect to the nonrelativistic case. This explains the shift of about 1.6 eV found for the onset and the double-peak feature in the absorption spectrum upon inclusion of the scalar relativistic effects.

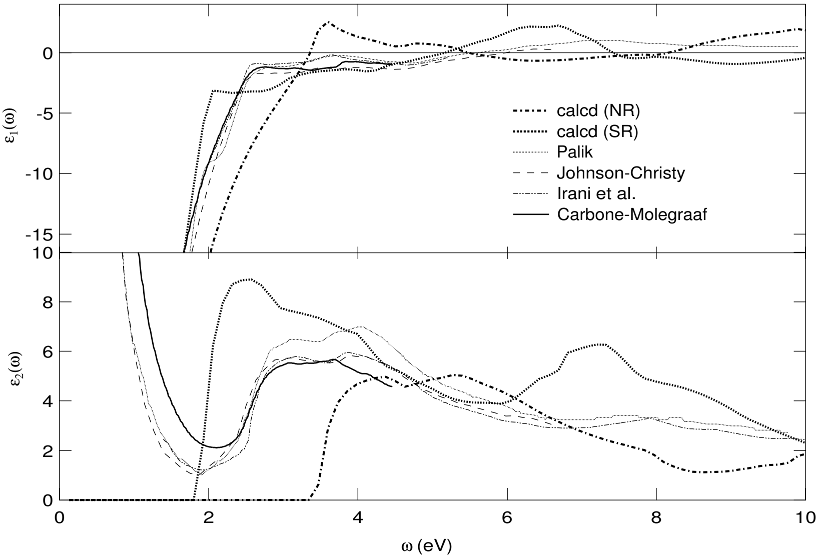

Figure 5.1: Real (upper graph) and imaginary (lower graph) parts of the dielectric function of Au. The bold dotted and dotted-dashed lines show our SR and NR results, the others the experimental data from Ref. [51, 70, 92, 94].

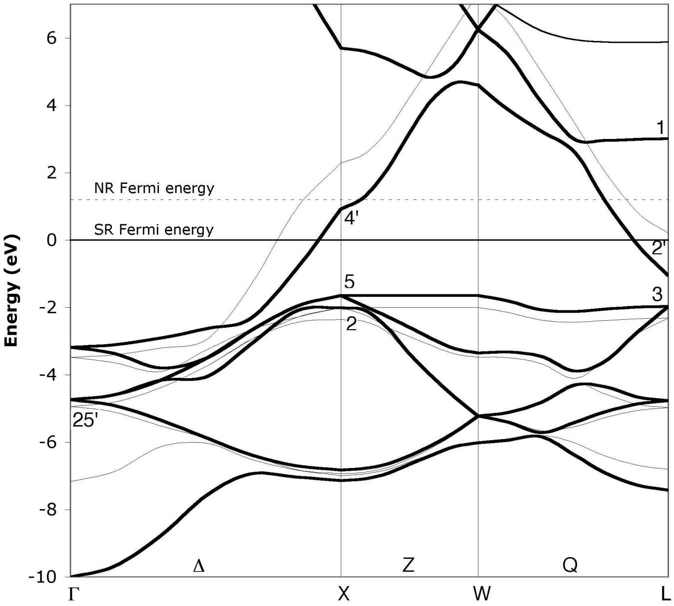

Figure 5.2: Band structure of gold (Au). The bold and thin lines refer to the scalar relativistic (SR) and the nonrelativistic (NR) ground-state calculations, respectively.

5.3.2 Analysis and assignment of the absorption spectrum

In order to better understand the origin of the absorption features we calculated the separate contributions to the absorption spectrum for selected pairs of bands and for different regions in the Brillouin zone. The various contributions that are due to direct transitions from the occupied valence bands to the two conduction bands 6 and 7 are shown in Fig. 5.3. We also analyzed our results by calculating the contributions of the transitions over the wedges of the Brillouin zone covering the L and the X direction, each accounting for roughly one quarter of the Brillouin-zone volume. This was done by including an extra weight factor in the Brillouin-zone integration,

$$w_X(\hat{\mathbf{k}}) = \langle \cos^2(2\phi)\cos^2(2\theta)\rangle, \tag{5.8}$$

$$w_L(\hat{\mathbf{k}}) = \langle \sin^2(2\phi)\sin^2(2\theta)\rangle, \tag{5.9}$$

where the average is taken over the three possible combinations with either $\hat{x}$, $\hat{y}$, or $\hat{z}$ being the polar axis. We find that the onset calculated at 1.9 eV is almost completely due to transitions from band 5 to band 6, as shown in panel a) of Fig. 5.3. About 60 percent of the intensity of this contribution, which is slightly more

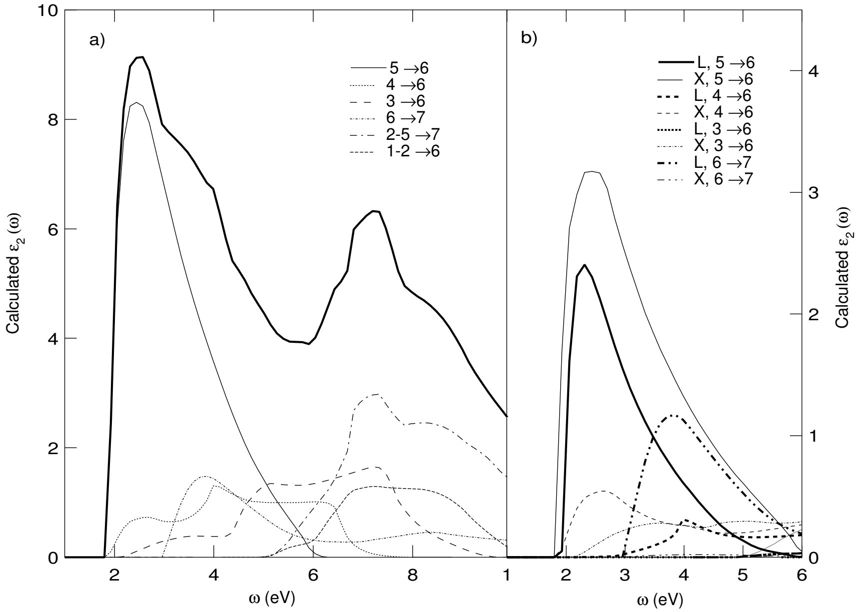

Figure 5.3: Contributions from various pairs of bands to the ϵ_2 spectrum calculated over the whole Brillouin zone, panel a), and selecting only the X and L directions, panel b).

than their combined volume fractions, is due to the regions near X and L, with the region around X accounting for 35 percent and the region around L for about 25 percent. In addition, we find that there are also small contributions from transitions from bands 3 and 4 to 6 that are completely due to the region around X. In previous assignments the experimental absorption edge of gold also has a composite nature with contributions due to the transitions near X and L (in particular, $L_3 \rightarrow L_{2'}$ and $X_2 \rightarrow X_{4'}$) [88–90]. However, the onsets in the two regions do not coincide. The experimental onset of the L transitions starts at about 2.5 eV [87,88,90], accounting for the steep rise in the absorption spectrum, whereas the onset of the X transitions has been located at about 1.9 eV [90,102], leading to the experimentally observed long tail which extends below 2 eV. The second experimental absorption peak occurring between 3.5 and 5 eV, and having a slightly higher intensity, appears in our scalar relativistic calculation as a broad shoulder between 3 and 5 eV. Around 3.6 eV this absorption has most frequently been attributed to transitions $6 \rightarrow 7$ near L and at slightly higher frequencies to transitions near X (in particular, $L_{2'} \rightarrow L_1$ and $X_5 \rightarrow X_{4'}$, respectively) [88, 89, 103]. Based on their analysis of the temperature dependence of the dielectric function, Winsemius *et al.* [91], on the other hand, concluded that these assignments are not complete. The panel a) of Fig. 5.3 shows that the peak can be attributed mainly to the transitions 6 → 7 and 4 → 6. The contribution of transition 6 → 7 comes mostly from the region near L: it has an onset at around 3 eV occurring for k points at the Fermi surface near L and peaks around 4 eV, which is about the gap between the bands 6 and 7 at L (transition $\mathrm{L}_{2'} \rightarrow \mathrm{L}_1$). The contribution due to the transitions from band 4 to band 6 is determined for only about 40 percent by transitions occurring in regions near L and X, which is less than their volume fraction. The structure at frequencies higher than 6 eV has not been extensively discussed. However, for the absorption around 8 eV we found some tentative assignments in literature to the $\mathrm{X}_1 \rightarrow \mathrm{X}_{4'}$ [88, 92] as well as to the $\mathrm{L}_1 \rightarrow \epsilon_F$ transitions [89]. In our calculations this absorption is overestimated and shifted to lower frequencies. Although the cited transitions contribute to the intensity of the absorption, we find that these alone cannot account for the absorption in this region, since also transitions from other occupied valence bands and from different parts of the Brillouin-zone contribute.

5.3.3 Spin-orbit effects

We expect that some of the discrepancies between our calculations and the experimental data are due to the spin-orbit effects. We cannot yet take into account the spin-orbit coupling in a full relativistic response calculation. Nevertheless the importance of spin-orbit relativistic effects for the response properties can be estimated by including the spin-orbit coupling in a relativistic calculation of the ground-state band structure. In Fig. 5.4 we report the most important changes upon inclusion of the spin-orbit effects in the relativistic ground-state band structure. Again we report all energy levels with respect to the Fermi energy of the scalar relativistic calculation. The spin-orbit coupling causes the splitting of the X_5 state into X_{6^+} and X_{7^+}. As a result the state X_2 (X_{7^+} in the double group symmetry), which was lower in energy than X_5 in the scalar relativistic case, becomes higher than both X_{6^+} and X_{7^+}. Unlike the electric dipole forbidden transition $\mathrm{X}_2 \rightarrow \mathrm{X}_{4'}$, $\mathrm{X}_7^+ \rightarrow \mathrm{X}_{6^-}$ is allowed. The gap between X_2 (X_{7^+}) and $\mathrm{X}_{4'}$ (X_{6^-}) becomes about 1 eV smaller than the one found in the scalar relativistic band-structure calculation. We can then expect that the contribution of transitions in the region near X from band 3 to band 6, in the scalar relativistic calculation, is shifted in energy to below 2 eV upon inclusion of spin-orbit coupling. This will result in a tail below the onset of the main absorption peak as observed in the experiments and as assigned to the transition X_2 (X_{7^+}) $\rightarrow \mathrm{X}_{4'}$

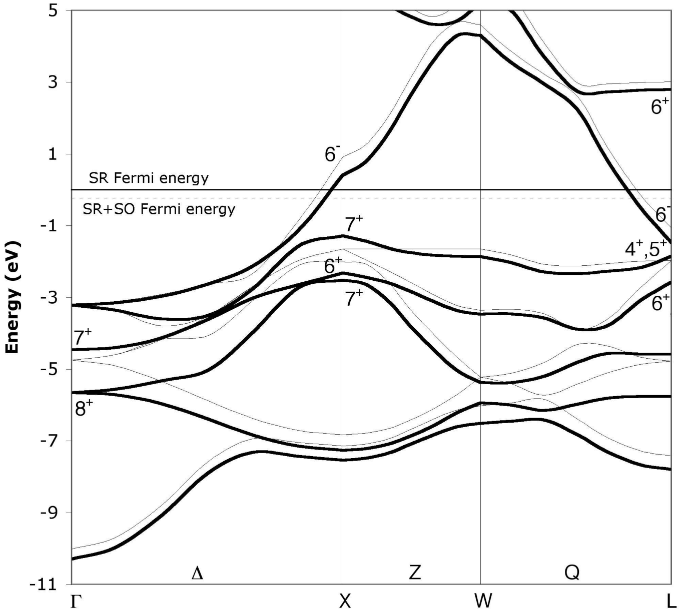

Figure 5.4: Band structure of gold (Au). The thin and bold lines refer to the scalar relativistic (SR) and the fully relativistic (scalar and spin-orbit effects) ground-state calculations, respectively.

(X_{6^-}) [89,90]. The contribution due to the transitions near X from band 5 to band 6 in the scalar relativistic case is slightly shifted to higher energies as the gap between X_5 (X_{7^+}) and $X_{4'}$ (X_{6^-}) increases by 0.2 eV. Although the change is only modest the shift is enough to decrease the intensity of the first calculated peak and increase that of the second one. Thus, we can conclude that this transition also contributes to the second absorption peak, together with the less intense transition $L_{2'} \rightarrow L_1$ that peaks at around 4 eV. Since the position of the latter transition is not affected by spin-orbit effects, we predict a different order than what is reported in literature. Due to the splitting in X_5, the contribution from transitions $4 \rightarrow 6$ in the region near X is expected to be blueshifted by about 0.4 eV. This increases the intensity of the second absorption peak even more. A large splitting involves the upper L_3 state lifting the degeneracy of band 4 and 5 with a magnitude of 0.7 eV. This splitting causes the gap between band 4 and band 6 at L in the scalar relativistic calculation to become about 0.6 eV larger. As becomes clear from Fig. 5.3, this is not expected to cause drastic changes in the absorption spectrum, since the contribution of the transitions $4 \rightarrow 6$

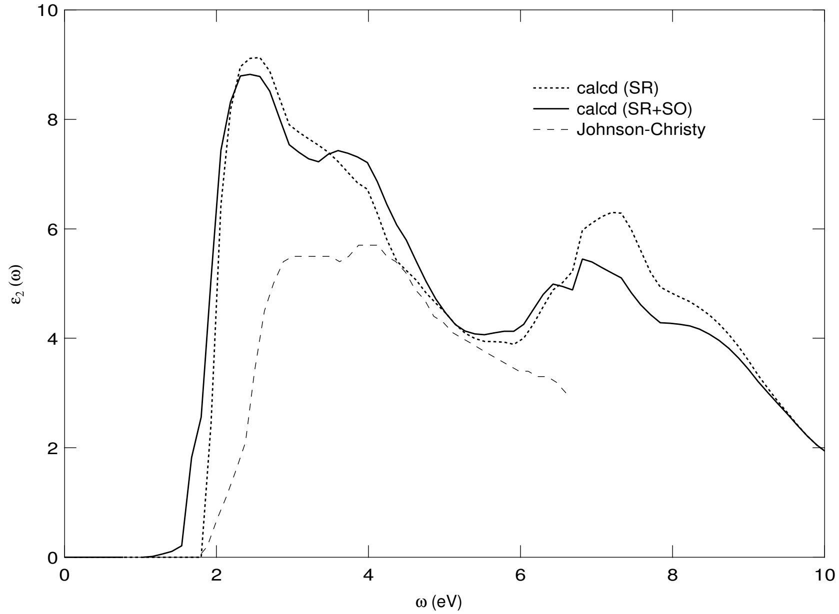

Figure 5.5: Qualitative description of the imaginary part of the dielectric function as expected upon the inclusion of the spin-orbit coupling in the response calculation. The experimental results are taken from Ref. [51].

near L is small even though it can contribute to make the second peak even more visible. The band 5 is lowered in energy by about 0.3 eV with respect to the Fermi level, thus blueshifting a bit the absorption edge and broadening the first peak. For the spectral region between 7 and 10 eV it is more complicated to predict which visible changes can be expected by including also the spin-orbit coupling, because of the complex composition of the absorption in terms of interband transitions. In Fig. 5.5 we give a qualitative prediction of the dielectric function as it can be expected from a response calculation including the spin-orbit effects. We modify the contributions due to the transitions from bands 1-6 to bands 6 and/or 7 in the region near L and X according to the analysis given above. All contributions are then summed and added to the unchanged contributions from the remaining part of the Brillouin zone giving the dielectric function. The modifications that we include are: $X_5 \rightarrow X_{4'}$ is blueshifted by about 0.2 and 0.4 eV for the transition $5 \rightarrow 6$ and $4 \rightarrow 6$, respectively, $X_2 \rightarrow X_{4'}$ is redshifted by 1 eV for the transition $3 \rightarrow 6$, $L_3 \rightarrow L_{2'}$ is redshifted by 0.3 eV for the transition $5 \rightarrow 6$ and blueshifted by 0.6 eV for the transition $4 \rightarrow 6$. In the same figure we also report the scalar relativistic dielectric function and the experimental interband contribution to the dielectric function that Johnson and Christy [51] obtained by removing the Drude free-electron contribution from their experimental data. Several spectral features are better described in the predicted absorption spectrum; in particular, the composite nature of the absorption edge and the second absorption maximum become visible. Even though we include only changes in the X and L contributions that are mainly responsible for the first and second absorption peaks, we also observe a decrease of the absorption intensity in the region around 8 eV. We can conclude that a full relativistic response calculation including the spin-orbit coupling is needed for an accurate description of several important spectral features of the dielectric function. Nevertheless even with the inclusion of the spin-orbit effects the interband onset and the two features at about 2.5 and 3.5 eV in the interband region of the absorption spectrum will remain redshifted by about 0.5 eV. Since most features involve transitions from $5d$-like bands to the Fermi level, which is completely determined by the $6p$-like band, this redshift suggests that the $5d$ bands should be lowered in energy with respect to the $6p$ band by roughly the same amount. The presumably incorrect position of the $5d$ bands may be due to the incorrect description of the ground-state exchange-correlation potential by the local density approximation. The use of standard available GGAs do not alter the position of the $5d$ bands, suggesting that more advanced functionals are needed for a correct description. This finding is in line with the overcorrection of the cohesive properties by standard GGAs in $5d$ transition metals [99]. Furthermore a feature clearly missing in our calculated absorption spectra is the low-frequency Drude-like tail. In perfect crystals this contribution comes from the scattering that free-conduction electrons have with phonons and with other electrons [66, 67]. These relaxation processes are not included within the ALDA, where a frequency-independent exchange-correlation (xc) kernel $f_{xc}(\mathbf{r}, \mathbf{r}')$ is used. To include these effects the use of a frequency-dependent approximation to this xc kernel that goes beyond the ALDA is needed. Such an $f_{xc}(\mathbf{r}, \mathbf{r}', \omega)$ kernel may also modify the intensity of the interband contribution to the absorption [69].

5.4 Conclusions

We have included scalar relativistic (SR) effects in the time-dependent current-density treatment of the optical response properties of metals by using the zeroth-order regular approximation (ZORA). We analyzed our results for the dielectric function of gold calculated in the spectral range of 0-10 eV with and without SR effects, and we estimated the effect of the spin-orbit coupling. The main effect of including the SR effects is a strong redshift of the absorption edge and the main spectral features, bringing both the real and imaginary parts of the dielectric function closer to the experiments. Nevertheless some features are not well reproduced: the absorption edge does not show the long tail observed experimentally below 2 eV and the second absorption peak appears only as a broad shoulder between 3 and 5 eV. The absorption in the region between 6 and 10 eV is overestimated. Moreover the interband absorption is redshifted with respect to the experiments by about 0.5 eV. By including relativity only in the ground-state DFT calculation or in both the ground-state and the response calculations we showed that the main influence of the relativistic effects is through the modification of the band structure in the optically active regions around X and L. Based on the scalar relativistic band structure, the analysis of the absorption spectrum shows some deviations from the most frequent assignments reported in literature. By including the spin-orbit coupling in the ground-state band-structure calculation we estimated its effect on the absorption features and their assignments. The general features and the assignments are now in good agreement with the literature. Therefore, the spin-orbit effects are essential to understand spectral features in gold. The predicted absorption spectrum remains, however, still redshifted with respect to the experiments, suggesting that the separation between the $6sp$ and $5d$ bands is underestimated in the local density approximation. The standard GGAs do not cure this problem and more advanced functionals may be needed. Furthermore a correct description of the Drude-like absorption in the low-frequency region requires approximations to the f_{xc} kernel beyond the ALDA.

5.5 Acknowledgments

The authors would like to thank Drs Fabrizio Carbone and Drs Hajo J.A. Molegraaf for the ellipsometric measurements of the dielectric function.

Chapter 6

Optical Properties of bcc Transition Metals

We present a systematic analysis of the optical properties of bcc transition metals in the groups VB: V, Nb, and Ta, and VIB: paramagnetic Cr, Mo, and W. The calculated dielectric and electron energy-loss functions are compared with new ellipsometry measurements and with data reported in literature, showing an overall good agreement. We calculate separately the inter- and intraband contributions to the absorption and we show using a $\mathbf{k}\cdot\mathbf{p}$ *analysis that, within the scalar relativistic approximation, interband transitions contribute to the absorption already at frequencies well below 0.5 eV. This finding makes questionable the Drude-like behavior normally assumed in the experimental analysis of the linear response. We find that the combination of the Drude model, in which we use the calculated plasma frequency and an optimized relaxation time, and the calculated interband response can well describe the experimental spectra. The electron energy-loss spectra are very well reproduced by our calculations showing in each metal a dominant plasmon peak at about 22-24 eV, well above the corresponding Drude-like free-electron plasma frequency, and additional features in the range 10-15 eV. We show that the renormalization of the plasma frequency is due to the interplay between inter- and intraband processes, and that the additional features arise from the rich structure in the dielectric function caused by interband transitions.*

6.1 Introduction

The electronic structure of transition metals is in general characterized by the overlap and hybridization of nearly free-electron-like *sp* bands with a relatively narrower *d*-band complex. This leads to a rather complex Fermi surface with in general multiple sheets. Moving across a period the binding energy of the *d* bands drops with respect to the low-lying *sp* bands while at the same time the Fermi level rises within the *d* bands due to the increasing filling fraction. The width of the *d* bands first increases, reaching a maximum for the Cr group where the *d* bands are approximately half filled, and then decreases again. At the noble metals the *d* bands are completely filled and very narrow. Furthermore, progressing within the same group the width of the *d* bands increases. These trends in the band structure have a large influence on the optical properties of the transition metals. Optical experiments [104–109] have shown that the high-energy optical properties ($\hbar\omega \gtrsim 10$ eV) are very similar from metal to metal, but that the low-energy behavior varies significantly with the filling of the *d* bands. Transitions within these bands are responsible for the absorption in this spectral region. In chapter 3 we have developed a method to treat the linear response of metal crystals within time-dependent current-density-functional theory (TDCDFT) [84]. This method gave good results for the dielectric function and the electron energy-loss function of copper and silver already within the adiabatic local density approximation (ALDA). Furthermore, by treating the dominant scalar relativistic effects (using the zeroth-order regular approximation) we obtained reasonable agreement with experiment also for the dielectric function of gold [110], as shown in chapter 5. In the case of these noble metals, two main deviations of the calculated dielectric functions from experiments were pointed out: an increasing redshift of the whole absorption spectrum passing from Cu *via* Ag to Au, and the absence of the low-frequency Drude-like absorption. We speculated that the redshift is mainly due to the deficiency of the local density approximation in describing the correct position of the *d*-band complex with respect to the Fermi level in our ground-state calculation. The other deviation, instead, is in part a failure of the adiabatic approximation to the exchange-correlation functional used in the response calculation. The low-frequency Drude-like absorption is due to relaxation processes such as electron-electron and electron-phonon scattering. The electron-electron scattering can not be described within the ALDA in which a frequency-independent exchange-correlation kernel is used. More advanced frequency-dependent functionals will be needed to describe these relaxation effects. The inclusion of electron-phonon scattering requires a theory that goes beyond the pure electron density-functional description [68]. In this chapter we use our method to investigate the optical properties of the bcc metals from group

VB: V, Nb, and Ta, and from the adjacent group VIB: Cr (in the paramagnetic phase), Mo, and W. Unlike the noble metals, where the d bands are completely filled, these metals have partially filled d bands, thus the analysis of their absorption spectra in terms of direct transitions between d bands can give an insight into the performance of the LDA in describing the dispersion and the width of the d bands in $3d$, $4d$, and $5d$ metals, and of the ALDA in describing the response properties. Furthermore these metals show interband absorption already at low frequencies, thus the separation in intra- and interband contributions to the absorption becomes difficult in the experimental analysis, where one often assumes the Drude-like behavior to hold at low frequency and well below the range of experimental data. Using the adiabatic local density approximation together with the long-wavelengh limit within our approach, we can calculate separately the inter- and intraband contributions to the dielectric function of these metals. We show that in these metals the interband absorption remains present at all frequencies, approaching a constant value for frequencies below $\simeq$0.5 eV, unless spin-orbit effects are taken into account. In the latter case a small absorption gap appears. These findings make the straightforward use of the bare Drude model for the low-frequency range questionable. In order to compare our calculations with reliable experimental data we performed also spectroscopic ellipsometry in the energy range between 0.7 and 4.5 eV. The spectra have been acquired at room temperature and ambient pressure. All samples were polished before the measurements and kept in a nitrogen atmosphere during the spectra acquisition, in order to prevent oxidization. The experimental procedure is described in more detail in Sec. 6.2. The rest of the chapter is organized as follows. The theory underlying the dielectric and electron energy-loss function calculations, and the treatment of the scalar relativistic effects within the zeroth-order regular approximation are briefly outlined in Sec. 6.3. Details of the computational method can be found in Sec. 6.4. The optical properties of the group-VB transition metals V, Nb, and Ta, and of the group-VIB transition metals Cr, Mo, and W are discussed in Sec. 6.5. Here, by comparing our theoretical results with our recent ellipsometry measurements and with other experiments found in literature, we give an insight into the trend of the optical properties of these metals with respect to the filling of the d-bands. Finally in Sec. 6.6 we draw conclusions about the performance of our method and of the exchange-correlation approximations used.

6.2 Experimental method

The optical constants of the transition metals studied in this chapter have been published in literature already several decades ago [104–109,111,112]. As these metals all have a bcc unit cell their optical constants are expected to be isotropic. Nestell, Johnson and Christy [111,112] measured polycrystalline thin films evaporated in situ, and performed reflection and transmission experiments at normal and 60 degrees angle of incidence to extract the optical constants n and k as a function of photon energy. Although this approach guarantees a negligible contribution from surface contamination, in particular from transition-metal oxides, still their optical constants showed a small but significant thickness dependence. Weaver and co-workers [104–109] measured the normal incidence reflectivity of polished single crystals and extracted the dielectric function *via* a standard Kramers-Kronig procedure. The dielectric functions presented by Weaver *et al.* deviate from Nestell and Christy's results mostly on the low-frequency side. However the reflectivity data that we obtained from Nestell and Christy's results agree well with those by Weaver *et al.* at least up to 3 eV. This apparent discrepancy may be due to the Drude-like extrapolation model used in the Kramers-Kronig procedure needed to extract the optical constants from the reflectivity data. In this chapter we question the validity of this Drude-like extrapolation for low frequency. The various sets of experiments show discrepancies in the absolute values of the optical constants, most notably for vanadium and chromium. Here we present our experimental results in the energy range between 0.7 and 4.5 eV obtained at room temperature using spectroscopic ellipsometry at an angle of incidence of 70 degrees with a resolution of approximately 12 meV. The polycrystalline samples used had a purity of 99.99 percent and were polished with a diamond sand paper of 0.1 micron grain size until a mirror-like surface was obtained. During the polishing process and the measurement the samples were kept in a pure nitrogen flow in order to prevent the oxidization of the surface. Our measurements are in excellent agreement with the results from Nestell and Christy for V and Cr where the various sets of experimental data differ most. For the other metals we find results in between the very similar data reported by Nestell and Christy and Weaver *et al.*. Some departures at high frequencies between our experiments and those reported by Nestell, Johnson, and Christy may be due to the non-negligible surface roughness and the film morphology. Our ellipsometry experiments and the combination of reflection and transmission measurements by Nestell and Christy directly provide the real and the imaginary parts of the dielectric function without assuming any model *a priori*. Due to the large spectral range of Nestell and Christy's measurements and to their good agreement with our results we will consider them to be the reference data.

6.3 Theory

In chapter 3 we have extended the formulation of the time-dependent current-density-functional theory describing the linear response of nonmetallic crystals to macroscopic fields [30, 31] to treat metals as well [84]. In this case not only transitions between occupied and unoccupied bands (interband contributions) contribute to the linear response, but also transitions within the same partially occupied band (intraband contributions) need to be considered. Within the adiabatic local density approximation (ALDA) and in the long-wavelength limit $q \to 0$ the two contributions remain separable, and we can calculate the dielectric function using the following expression [84],

$$\epsilon(\omega) = \left(1 + 4\pi\chi_e^{inter}(\omega)\right) - \frac{4\pi i}{\omega}\sigma^{intra}(\omega). \tag{6.1}$$

Here the contribution in brackets is referred to as the interband part of the dielectric function and the last term on the right-hand side as the intraband contribution. The tensor components of the interband contribution to the electric susceptibility $\chi_e^{inter}(\omega)$ can be obtained by repeating an SCF response calculation of the interband contribution to the induced current-density for the uniform macroscopic electric field in the three possible Cartesian directions $\hat{\mathbf{e}}$,

$$\chi_e^{inter}(\omega) \cdot \hat{\mathbf{e}} = \left(\frac{-i}{\omega V} \int \delta\dot{\mathbf{j}}^{inter}(\mathbf{r}, \omega) d\mathbf{r} \right) \Bigg|_{\mathbf{E}_{mac}=\hat{\mathbf{e}}}. \tag{6.2}$$

Analogously, the components of the intraband contribution to the macroscopic conductivity tensor $\sigma^{intra}(\omega)$ can be obtained from the intraband part *via*

$$\sigma^{intra}(\omega) \cdot \hat{\mathbf{e}} = \left(\frac{1}{V} \int \delta\dot{\mathbf{j}}^{intra}(\mathbf{r}, \omega) d\mathbf{r} \right) \Bigg|_{\mathbf{E}_{mac}=\hat{\mathbf{e}}}. \tag{6.3}$$

Once having calculated the macroscopic dielectric function $\epsilon(\omega)$, we can obtain also the electron energy-loss spectra by calculating the dynamical structure factor $S(\mathbf{q}, \omega)$. This factor expresses the scattering rates in transmission energy-loss spectroscopy where one studies the inelastic scattering of a beam of high-energy electrons by a target. This structure factor is related to the imaginary part of the true density-density response function *via* the fluctuation-dissipation theorem,

$$S(\mathbf{q}, \omega) = -2\Im \int\int e^{-i\mathbf{q}\cdot(\mathbf{r}-\mathbf{r}')} \chi(\mathbf{r}, \mathbf{r}', \omega) d\mathbf{r} d\mathbf{r}'. \tag{6.4}$$

We retrieve in our approach the well-known result [1] that in the limit of vanishing q the dynamical structure factor is directly related to the macroscopic dielectric function according to the following relation,

$$\lim_{q\to 0}\frac{2\pi}{q^2 V}S(\mathbf{q},\omega)=\Im\left\{\frac{-1}{\hat{\mathbf{q}}\cdot\epsilon(\omega)\cdot\hat{\mathbf{q}}}\right\}. \tag{6.5}$$

We have also included relativistic effects in our formulation [110] by using the zeroth-order regular approximation (ZORA) [79, 80, 113] as described in chapter 4. Scalar-relativistic effects are then considered by using the ground-state scalar ZORA equation,

$$\left[\mathbf{p}\cdot\frac{c^2}{2c^2-v_{\mathit{eff},0}(\mathbf{r})}\mathbf{p}+v_{\mathit{eff},0}(\mathbf{r})\right]\psi_{i\mathbf{k}}(\mathbf{r})=\epsilon_{i\mathbf{k}}\psi_{i\mathbf{k}}(\mathbf{r}), \tag{6.6}$$

to get the orbitals and the orbital energies needed in the response calculation, and by using the relativistic scalar ZORA operator,

$$\hat{\mathbf{j}}^{ZORA}=-\frac{i}{2}\left(K(\mathbf{r})\nabla-\nabla^{\dagger}K(\mathbf{r})\right), \tag{6.7}$$

with $K(\mathbf{r})=(1-v_{\mathit{eff},0}(\mathbf{r})/2c^2)^{-1}$, to calculate the induced current-density, and hence the response functions of Eqs. (6.2) and (6.3). Here c is the velocity of light, $v_{\mathit{eff},0}(\mathbf{r})$ is the self-consistent effective potential, and *H.a.* is the Hermitian adjoint expression. Spin-orbit effects have been studied only in the ground-state calculations by using the full ZORA Hamiltonian.

6.4 Computational method

We calculated the optical dielectric functions $\epsilon(\omega)$ in the spectral range 0-10 eV for the isotropic crystals of vanadium, niobium, tantalum, paramagnetic chromium, molybdenum, and tungsten in a bcc lattice. We used the experimental lattice constants as listed in tables 6.1 and 6.2. All calculations were performed using a modified version of the ADF-BAND program [30, 31, 61, 62, 84, 96]. We checked that our results were converged with respect to the basis set size and the sampling density of the irreducible Brillouin zone. We made use of a hybrid valence basis set consisting of Slater-type orbitals (STOs) in combination with the numerical solutions of a free-atom Herman-Skillman program [64]. Cores were kept frozen up to $2p$ for V and Cr, $3d$ for Nb and Mo, and $4f$ for Ta and W. The spatial resolution of this basis is equivalent to a STO triple-zeta basis set augmented with two polarization functions. The Herman-Skillman program also provides us with the free-atom effective potential. The crystal potential was evaluated using an auxiliary basis set of STO functions to fit the deformation density in the ground-state calculation and the induced density in the response calculation. For the evaluation of the k-space integrals in the ground-state calculations we used a quadratic numerical integration scheme, which was constructed by adopting a Lehmann-Taut tetrahedron method [59,60]. We found converged results using 84 sample points in the irreducible wedge of the Brillouin zone. In the response calculations the singular energy-dependent denominator in the response integrals is included in the quadrature weights of a linear tetrahedron method by using an analytic evaluation of the Cauchy principle value and residual parts. As we will show shortly below, in the scalar relativistic calculations these metals exhibit interband absorption already in the spectral range 0-0.5 eV, which involves transitions between bands degenerate at the Fermi level. A dense sampling of the Brillouin zone is then required in order to accurately describe the dispersions close to the Fermi surface. Therefore we used 1771 sample points for the response calculations in the low-frequency spectral region. Nevertheless, the results obtained for the lowest frequencies will still not be reliable due to the linear interpolation used in solving the k-space integrals. Therefore we made use of the $\mathbf{k} \cdot \mathbf{p}$ method of analytic continuation [57] near the points of degeneracy at the Fermi level to analyze the low-frequency interband transitions and the corresponding low-frequency behavior of the absorption. In all our ground-state calculations we used the local density approximation (LDA) for the exchange-correlation functional. In general the use of generalized-gradient approximations (GGAs) to the exchange-correlation functional is found to improve the ground-state properties of the $3d$ series [114, 115], whereas there have been mixed reports of their performance on the $4d$ and $5d$ series [116–118]. For comparison we have performed the calculation of the dielectric functions also by starting from ground states obtained at the GGA level, using the exchange-correlation functional proposed by Perdew and Wang (PW91) [101] and the one by Becke for the exchange [9] and Perdew for the correlation [10] (BP). The results, however, are very similar to those obtained at the LDA level. All results shown here were obtained using the Vosko-Wilk-Nusair parametrization [65] of the LDA exchange-correlation potential, which was also used to derive the ALDA exchange-correlation kernel for the response calculations.

6.5 Results and discussion

6.5.1 Band structure and Fermi surface

In Fig. 6.1 and Fig. 6.2 the calculated ground-state energy bands of V, Nb, and Ta (in the left panels), and of Cr, Mo, and W (in the right panels) have been displayed along high-symmetry directions. The energy levels are reported with respect to the respective Fermi levels, in order to facilitate the comparison between the band struc-

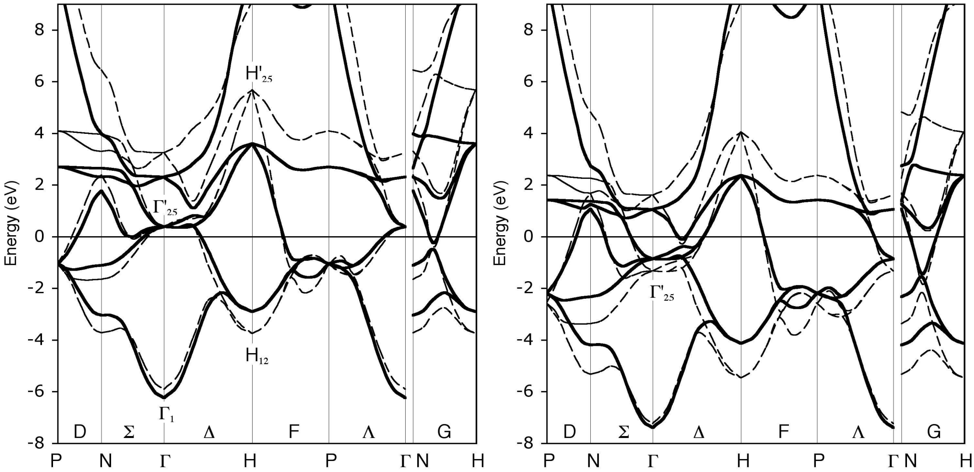

Figure 6.1: Theoretical LDA ground-state band structures. The left panel shows vanadium (solid line) and niobium (dashed line), whereas the right panel shows chromium (solid line) and molybdenum (dashed line). The band structures reported for Nb and Mo refer to scalar relativistic calculations.

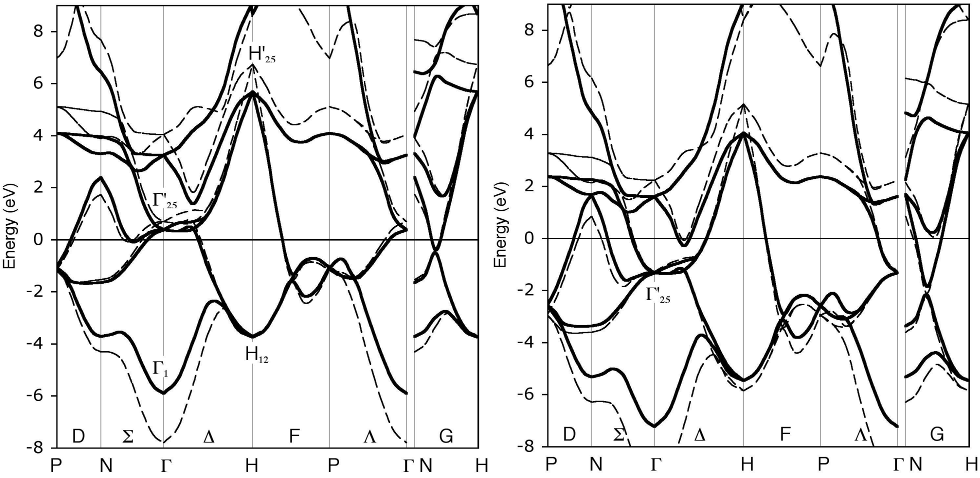

Figure 6.2: Theoretical scalar relativistic LDA ground-state band structures. The left panel shows niobium (solid line) and tantalum (dashed line), whereas the right panel shows molybdenum (solid line) and tungsten (dashed line).

tures. The valence bands are numbered at a given k point starting from the lowest band. Across the same group the band structures are quite similar, except that the d bands are broader, as immediately becomes clear by inspection of the d-band widths $E(\mathrm{H}'_{25})$-$E(\mathrm{H}_{12})$ in Fig. 6.1 and Fig. 6.2. Moving from the $3d$ series to the $5d$ series, the s-like Γ_1 state becomes more tightly bound, as result of a stronger stabilization by relativistic effects. The most noticeable difference between the band structures of the two groups is the position of the d-like Γ'_{25} states, which lie above the Fermi level for the group-VB metals but below this level for the group-VIB metals. The group-VB transition metals contain five valence electrons per atom, whereas the group-VIB ones contain six valence electrons. In the group-VB metals the lowest valence band and in the group-VIB metals the lowest two bands are completely filled. The second and third, respectively, the third, fourth, and fifth bands, are partially filled and contribute to the Fermi surfaces, which are characterized by multiple sheets. Cross sections of the Fermi surfaces are shown in Fig. 6.3 for the group-VB metals in the left panel and for the group-VIB metals in the right panel. The shaded areas indicate the regions of the Brillouin zone where the transitions between selected pairs of bands give the strongest contribution to the interband absorption. These couples are $2 \rightarrow 3$, $3 \rightarrow 4$, and $3 \rightarrow 5$ for the group-VB metals, and $4 \rightarrow 5$, $3 \rightarrow 4$, and $3 \rightarrow 5$ for the group-VIB metals. We will discuss them later in the chapter. In the group-VB metals closed hole pockets around Γ arise due to band 2, and around the symmetry points N due to band 3. Furthermore, band 3 gives rise to an open surface with arms in the Δ directions which is often referred to as the "jungle-gym". The pocket around Γ and the jungle-gym show a symmetry-induced degeneracy along the Λ line caused by the doubly degenerate Λ_3 states. This degeneracy will be lifted by spin-orbit effects. The three metals show also another point of contact inside the ΓHP plane (as depicted in Fig. 6.3), which is accidental and lifted by spin-orbit effects as well. The hole pockets situated around the symmetry points N are also found in the group-VIB metals, as can be expected from the band structures. However, a quite different picture of the Fermi surface emerges for these metals due to the position of the Γ'_{25} states, which now lie below the Fermi level. Hole pockets around H and an electron pocket around Γ appear due to bands 3 and 4, respectively. These two surfaces have a point of contact on the Δ line as the two bands show a symmetry-induced degeneracy, which again will be lifted by spin-orbit effects. In addition, another tiny pocket of electrons occurs along the Δ lines as contribution from band 5. As we will show later in this chapter, transitions near the symmetry-induced degeneracies are responsible for the low-frequency interband absorption.

The analysis shows that the band dispersions of all six metals are very similar. We observe only minor differences between metals which are adjacent in the Periodic

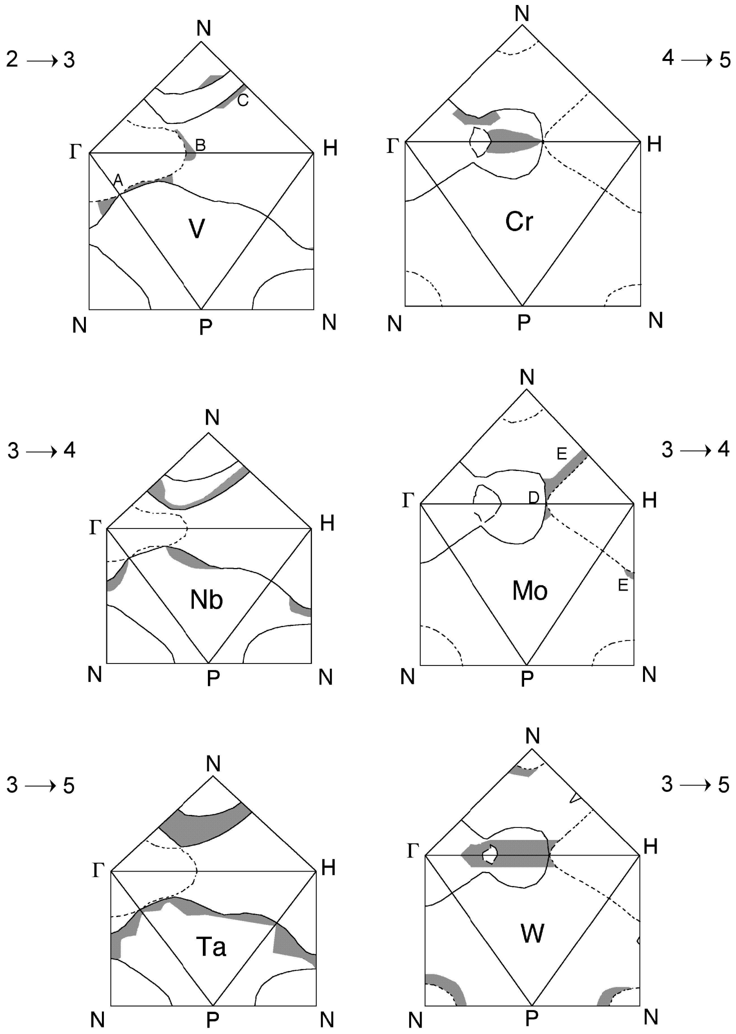

Figure 6.3: Theoretical Fermi surface cross sections for V, Nb, Ta (left panel), and for Cr, Mo, and W (right panel). The Brillouin zones have been plotted at the correct relative scale. The short dashed, the solid, and long dashed lines represent the contributions to the Fermi surface due to the bands 2, 3, and 4, respectively. The shaded areas indicate the regions in the Brillouin zone that contribute most to the absorption due to the transitions between the respective bands.

Table, but at the same time we see larger changes within each group, in particular in the d-band width. The main difference between the group-VB and -VIB metals is in the filling of the d-bands and, as result, in the topology of the Fermi surfaces. Since transitions between d-bands are responsible for the main structure in the optical absorption spectra, we expect to find common features shifting in energy corresponding to the increase of the d-band dispersion within the group. The adjacent group will have features in common at very similar frequencies, but also different features will result from the difference in filling of the d-bands and the topology of the Fermi surface.

6.5.2 Dielectric function

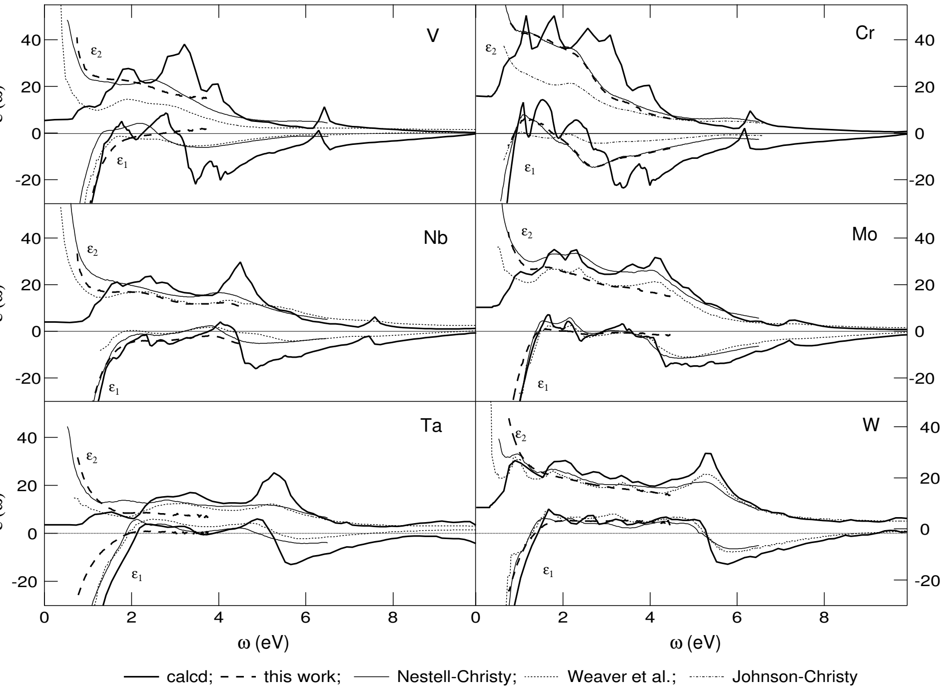

Figure 6.4: The calculated (bold solid line) and measured dielectric functions for vanadium, niobium, tantalum, chromium, molybdenum, and tungsten. Our measurements have been performed as described in section 6.1, the other experimental results are taken from Ref. [104–106, 111, 112]. The theoretical curves reported for Nb, Ta, Mo, and W are results of scalar relativistic calculations.

In Fig. 6.4 we report the calculated real and imaginary parts of the dielectric functions of V, Nb, and Ta in the left panels, and of Cr, Mo, and W in the right panels. The theoretical results are compared with our ellipsometry measurements and with other experiments present in literature [104–106, 111, 112]. For the $4d$ and $5d$ metals we found that relativistic effects are important. Therefore the results depicted for the $4d$ and $5d$ metals refer to scalar relativistic calculations. A comparison with the nonrelativistic calculations of the dielectric functions is reported in Fig. 6.5. Upon inclusion of scalar relativistic effects the dielectric functions of the group-VB metals Nb and Ta appear rigidly blueshifted and the intensity of some spectral features changes significantly with respect to the nonrelativistic spectra. In the group-VIB metals Mo and W, the absorption bandwidths become broader by including scalar relativistic effects. In particular for Mo the double-peak structure at about 2 eV then becomes visible. Similarly the absorption peak at about 1 eV and the main features in the real part of the dielectric function of Ware now correctly reproduced with respect

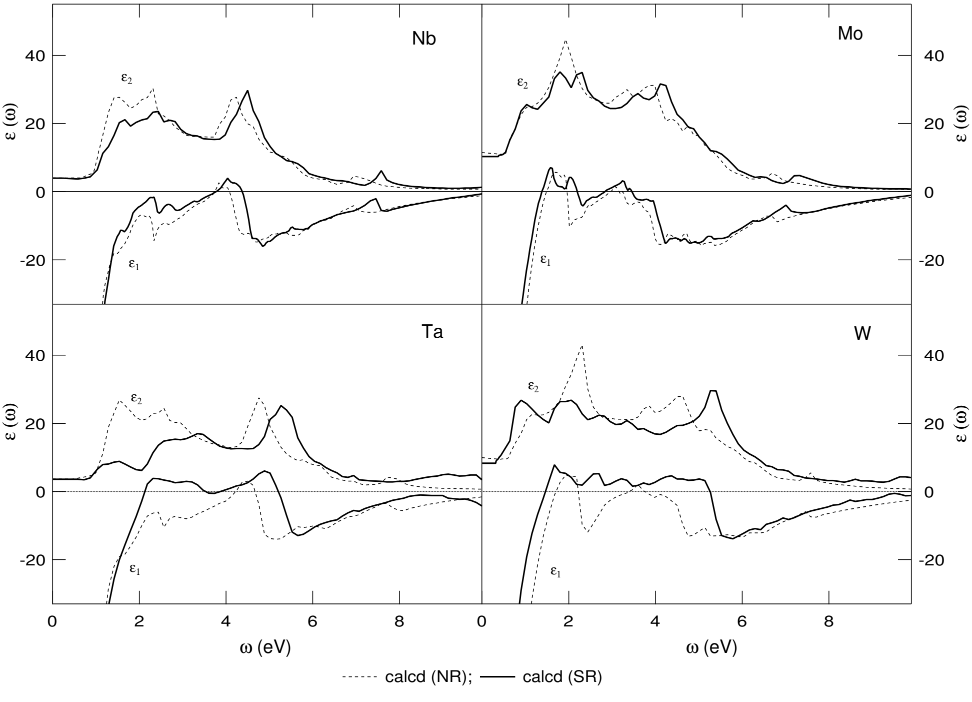

Figure 6.5: Comparison between nonrelativistic and scalar relativistic calculations of the dielectric functions of niobium, tantalum, molybdenum, and tungsten.

to the experiments. Spin-orbit effects are not treated at the moment in our response calculations, but they can be important, in particular for the $5d$ metals Ta and W. Indeed our results obtained by treating both the scalar and spin-orbit effects in the ground-state calculations show that the spin-orbit coupling removes the degeneracy between, for example, bands 2 and 3 along Λ in the group-VB metals and between bands 3 and 4 along Δ in the group-VIB metals. This will effectively remove all points of contact of the Fermi surface sheets, thus introducing a finite gap in the interband absorption spectra. In tungsten, for example, transitions near the Fermi surface between the two bands that would otherwise be degenerate but that are separated by about 0.60 eV upon inclusion of spin-orbit effects, are expected to be responsible for the sharp interband absorption onset found experimentally with a maximum at about 0.42 eV [106]. Our conclusions are in line with the findings of Antonov *et al.* [119], who calculated the optical properties of several $5d$ metals within the random phase approximation (RPA) and the fully relativistic linear muffin-tin-orbital (LMTO) method. In the absorption spectrum of tungsten the low-frequency peak and onset are absent in their calculations which excluded spin-orbit effects, whereas they appear in the fully relativistic calculation. They associated this to the direct transitions between the two bands crossing the Fermi level in the neighborhood of the high-symmetry point H (bands 3 and 4 in our calculations). The degeneracy of these two bands is lifted by the spin-orbit coupling and a small energy gap appears, resulting in a finite absorption onset. In our scalar relativistic calculations the use of a linear interpolation for the evaluation of the k-space integrals in the response calculations might result in an incorrect description of the response in the very low-frequency region. For this reason we analyzed the topology of the Fermi surface at the singular points by using the $\mathbf{k}\cdot\mathbf{p}$ method. This analysis indicates a constant interband contribution to the absorption in the low-frequency region for each of the six metals. We determined the value for the low-frequency absorption below 0.5 eV by extrapolating the linear relation found at higher frequencies for the current-current response function *versus* ω^2. In our scalar relativistic calculations the interband absorption extends all the way down to $\hbar\omega = 0$ eV. For most metals, however, two regions can be distinguished in the absorption spectrum, being the low-frequency region in which intraband transitions are assumed to be dominant and that is well described by a Drude model, and the visible region where the interband absorption is most important. In the ALDA approach there is no intraband contribution to the imaginary part of the dielectric function at finite frequency. Responsible for the Drude-like absorption are relaxation processes which are not described within the ALDA, in which a frequency-independent exchange-correlation kernel is used [68]. Therefore we can directly relate the calculated and experimental absorption spectra only at frequencies higher than ~1 eV where, for the metals studied here, the Drude-like absorption is found to be small [105, 111]. In the low-frequency region the comparison is more problematic. To overcome these difficulties we add to our calculated interband absorption an intraband contribution which we found to be well described by a simple Drude model,

$$\epsilon_2(\omega) = \epsilon_2^{inter}(\omega) + \epsilon_2^{D}(\omega), \tag{6.8}$$

where $\epsilon_2^{inter}(\omega)$ is the calculated interband contribution to the imaginary part of the dielectric function and $\epsilon_2^{D}(\omega)$ is the Drude contribution given by

$$\epsilon_2^{D}(\omega) = \frac{\omega_p^2 \tau}{\omega(1+\omega^2\tau^2)}, \tag{6.9}$$

with ω_p the plasma frequency and τ the relaxation time. Normally these two pa-

Table 6.1: Model parameters for the group-VB metals. The plasma frequencies have been calculated directly from intraband response functions in the ALDA approximation. The relaxation times have been fitted to experiments in the frequency range 0-1 eV (see text). In our calculations we used the experimental lattice parameters listed here.

	V	Nb	Ta
a (Å)	3.02	3.30	3.31
ω_p (eV)	8.06	9.24	8.88
τ ($\times 10^{-15}$ s)	5.0 ± 0.2[a]	$4.09 \pm .12$[a]	6.2 ± 0.2[a]

---

[a] standard deviation

Table 6.2: Model parameters for the group-VIB metals. The plasma frequencies have been calculated directly from intraband response functions in the ALDA approximation. The relaxation times have been fitted to experiments in the frequency range 0-1 eV (see text). In our calculations we used the experimental lattice parameters listed here.

	Cr	Mo	W
a (Å)	2.88	3.15	3.16
ω_p (eV)	6.99	8.66	7.81
τ ($\times 10^{-15}$ s)	3.78 ± 0.03[a]	5.57 ± 0.10[a]	12.2 ± 0.6[a]

---

[a] standard deviation

rameters are determined by fitting the bare Drude model to the experimental data below the onset of the interband transitions, where one assumes that the absorption is predominantly Drude-like. In the present case, however, the Drude model alone cannot describe the low-frequency absorption, since even for the lowest frequency in the experimental window the interband absorption is non-negligible. Our calculated constant low-frequency absorption will lead to an extra term with a logarithmic divergence at small frequencies in the real part of the dielectric function. Indeed for Nb, Ta, Mo, and W the plasma frequencies obtained by fitting the bare Drude model to experiments differ appreciably from the theoretical values [120–122]. This was associated with a renormalization of the optical mass by Fermi-liquid effects [120] rather than to interband processes. We found that Eq. (6.8) still holds and that Eq. (6.9)

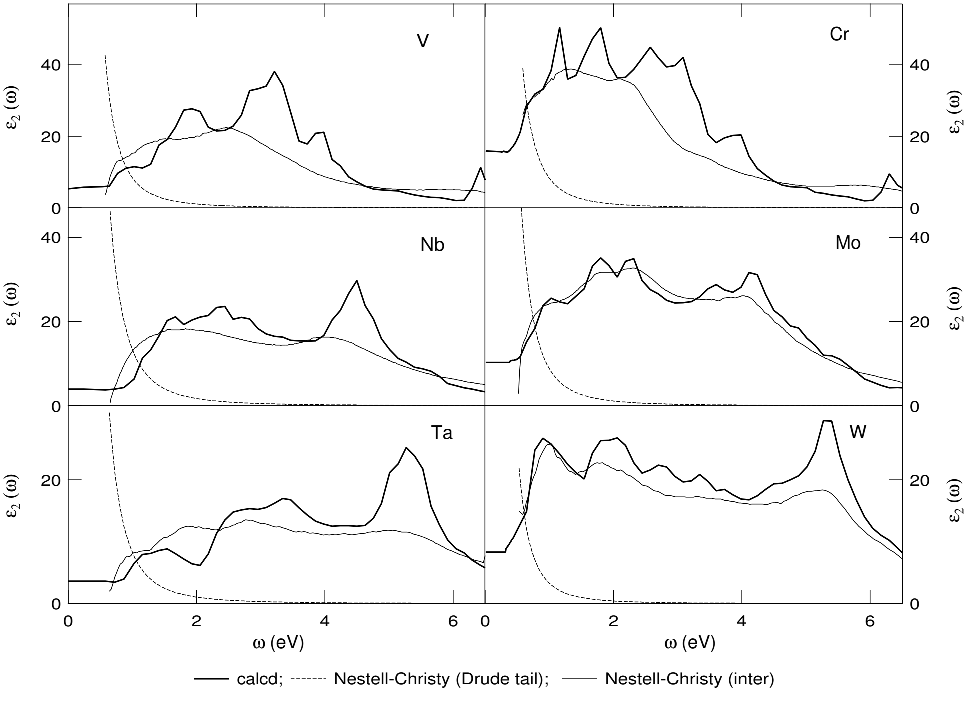

Figure 6.6: Comparison between the measured and calculated interband contribution to the absorption spectra of vanadium, niobium, tantalum, chromium, molybdenum, and tungsten. The Drude absorption (intraband contribution to the experimental absorption, see text) is also reported. The experimental spectra used are taken from Ref. [111].

can describe the intraband part of the low-frequency absorption. Here the Drude parameters are obtained in the following way. We subtract the calculated interband absorption from the experimental curve (comprising both inter- and intraband contributions) and fit Eq. (6.9) to the remaining part. In this fit we use the calculated value for ω_p, which is directly related to the intraband contribution to the macroscopic optical conductivity [84], $\omega_p^2 = -4\pi i\omega\,\sigma^{intra}(\omega)$, and we obtain the optimal relaxation time *via* a least-squares procedure. The Drude parameters thus obtained are listed in tables 6.1 and 6.2. In order to test the quality of our calculations we want to compare the calculated interband absorption with the experiments. To do this we subtract from the experimental absorption the intraband contribution described by Eq. (6.9) in which we use the theoretical value for the plasma frequency and the fitted relaxation time.The result of this procedure is depicted in Fig. 6.6, where we have also reported the Drude-like tail. We are now ready to assign the spectral features to interband processes. The position of the main features in the experimental spectra were obtained by using the extrema in the second derivative of the interband spectrum and they are given in tables 6.3 and 6.4.

Table 6.3: Position (in eV) of the main features in the experimental and theoretical spectra and their assignment in terms of transitions between pairs of bands for the group-VB metals.

Peak	V		Nb		Ta	
	Exp[a]	ALDA	Exp[a]	ALDA	Exp[a]	ALDA
$2 \to 3$, A	-	< 0.5[b]	-	< 0.5[b]	-	< 0.5[b]
$2 \to 3$, B,C	0.70	1.15	1.04	1.15[c], 1.54	0.85, 1.50[d]	1.41
$3 \to 4$	1.25-1.48	1.92	2.20	2.31	1.81, 2.86	2.82, 3.34[e]
$3 \to 5$	2.50	3.11	4.04	4.49	5.33[f]	5.26
$1 \to 4$, $2 \to 5$	3.47	3.98	-	5.53	-	6.17
$1 \to 6$	-	6.43	-	7.60	-	9.40[g]

---

[a] peak positions obtained using data from Ref. [111]

[b] constant absorption: ϵ_2=5.33, 3.94, and 3.60 for V, Nb, and Ta, respectively

[c] shoulder

[d] very weak shoulders

[e] here also the transitions $2 \to 4$ contribute

[f] broad peak

[g] broad; here also transitions $3 \to 6$ contribute

Table 6.4: Position (in eV) of the main features in the experimental and theoretical spectra and their assignment in terms of transitions between pairs of bands for the group-VIB metals.

Peak	Cr		Mo		W	
	Exp[a]	ALDA	Exp[a]	ALDA	Exp[a]	ALDA
$3 \rightarrow 4$, D	-, 0.70	<0.5[b], 0.77	-, 0.65	<0.5[b], 1.08	-, 0.95	<0.5[b], 0.90
$3 \rightarrow 4$, E	1.24	1.16, 1.80	1.77, 2.34	1.80, 2.31	1.78, 2.20[c], 3.40 [c]	1.90, 2.69, 3.34[d]
$3 \rightarrow 5$	2.32	2.57, 3.08	3.44, 4.08	3.60, 4.11	- , 4.98[c] , 5.36	3.72, 4.50, 5.40
$1 \rightarrow 4$	3.46[e]	3.85	-	5.39	-	6.81[f]
$1 \rightarrow 6$	5.83[e]	6.30	-	7.33	-	9.8[g]

---

[a] peak positions obtained using data from Ref. [111]

[b] constant absorption: ϵ_2=15.87, 10.27, and 8.33 for Cr, Mo, and W, respectively

[c] very week shoulder

[d] here also the transitions $3 \rightarrow 5$ contribute

[e] weak

[f] weak; here also transitions $2 \rightarrow 5$ and $3 \rightarrow 6$ contribute

[g] here also transitions $3 \rightarrow 6$ contribute

Assignment of the interband spectra

In order to facilitate the comparison of the spectral features we interpreted the absorption spectra in terms of direct transitions between couples of bands. In Fig. 6.7 we report the main contributions to the absorption spectra. The first and second peaks common to the $3d$ and $4d$ metals can be attributed mainly to the transitions $3 \rightarrow 4$ and $3 \rightarrow 5$, respectively, whereas the shoulder at low frequency is mainly due to the transitions $2 \rightarrow 3$ for the group-VB metals and to the transitions $4 \rightarrow 5$ for the group-VIB metals. It becomes clear that in Ta the broad peak centered at about 3.1 eV can be related to the first absorption peak which appears also in the $3d$ and $4d$ metals, whereas the peak at about 1.4 eV can be related to the shoulder present in the other group-VB metals. We find again that the same couples of bands, which are mainly responsible for the first absorption peak observed for the group-VIB metals

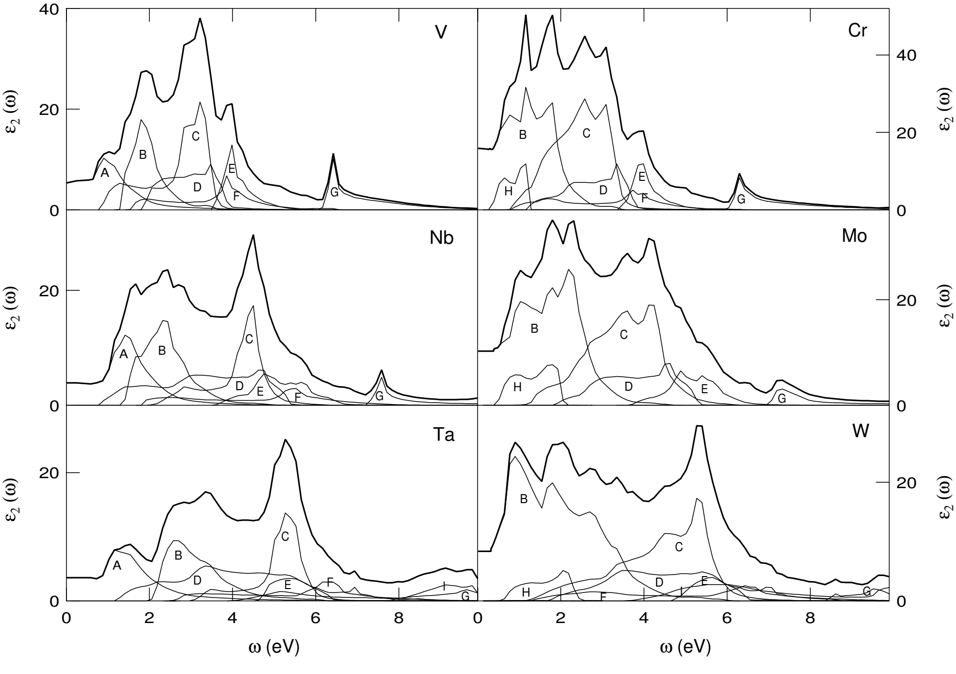

Figure 6.7: Assignment of the absorption spectra. The figure shows the total intensity (bold solid line) and the decomposition in terms of the different contributions due to direct transitions between the indicated pairs of bands.

Cr and Mo, are also involved in the absorption spectrum of W below 4 eV. Here different peaks are visible, revealing that a broader range of energies is covered by transitions between the two bands in different parts of the Brillouin zone. This is in keeping with the larger dispersion of the *d* bands in W as compared to Cr and Mo. All these metals show strong interband absorption also at very low frequencies, in line with absorbance measurements on Nb and Mo [123], and calculations on Nb [124]. At frequencies below ~ 0.5 eV, the interband absorption becomes constant in our calculation, being larger in the group-VIB than in the group-VB metals. This very low-frequency interband absorption reveals a degeneracy of energy bands at the Fermi surface. We will analyze later the topology of the Fermi surface around the points of degeneracy which are involved in the low-frequency absorption. Unfortunately, not much experimental data is available at so low frequencies since optical experiments are difficult to perform as here the reflectivity is close to 1. However, structure in the low-frequency region $\omega < 1$ eV has been observed in Nb [104, 125], but it has been found to vary with sample preparation. By analyzing the transition dipole moments for transitions between pairs of bands we can visualize the regions of the Brillouin zone where the transitions give the strongest contribution to the interband absorption. In Fig. 6.3 the shaded areas indicate the regions where transitions give rise to the strongest absorption. We found that for metals within a group the same areas are involved, but also that the regions are somewhat more diffuse for the heaviest metals.

In the group-VB metals the absorption below 0.5 eV is due to the transitions $2 \rightarrow 3$ in the region which is indicated as A in Fig. 6.3, near the symmetry-induced degeneracy. Transitions between the same bands in the regions B and C are the main contribution to the shoulder at about 1 eV. The absorption in this low-frequency region is very similar for all three metals as the dispersion of bands 2 and 3 is only weakly modified within the group. The transitions $3 \rightarrow 4$ and $3 \rightarrow 5$ contribute mainly in the region just outside the jungle-gym part of the Fermi surface. Here, however, the corresponding absorption peaks will move within the group towards higher energies as result of the larger dispersion of the *d*-bands, and hence of the increasing energy separation. These trends are clearly visible in the experiments and are well reproduced in our calculations, be it that the calculated peak positions are a few tenths to one half of an eV too high.

In the group-VIB metals the transitions $3 \rightarrow 4$ contribute strongly to the low-frequency absorption in the region D around the point of degeneracy. The high-frequency part of the absorption that is due to these two bands originates from the region E. Passing *via* Mo to W the contribution from D in the ΓHP plane becomes stronger, resulting in a peak at about 1 eV instead of a shoulder, while the zone E becomes broader, resulting in a broad absorption over the whole spectral range 0-5 eV. The shoulder is also due to transitions $4 \rightarrow 5$ mainly near the line Δ. From the same region, but also from the regions just outside the pockets around N transitions $3 \rightarrow 5$ give rise to the absorption in the high-frequency side of the spectrum. Again the increasing dispersion of the d-bands within the group leads to a considerable shift of the spectral features. The trends in the experimental and theoretical spectra are again very similar as in the group-VB case. However, here the peak positions are generally well reproduced except for the high-frequency range in Cr, where the peak positions are again overestimated by about one half of an eV.

Our assignment of the spectra is in line with those reported in literature [105, 106, 111, 126, 127]. For the group-VB metals the first peak is mainly attributed to the transitions $\Sigma_1 \rightarrow \Sigma_1$, which involves the third and fourth bands along the Σ line. Different transitions might contribute to the second peak: $\Delta_1 \rightarrow \Delta_2'$ ($1 \rightarrow 5$ transitions), $D_4 \rightarrow D_1'$ ($2 \rightarrow 4$ transitions), and $G_1 \rightarrow G_4'$ ($1 \rightarrow 5$ transitions). However, this structure seems to arise from large regions of the Brillouin zone away from symmetry lines; in particular Pickett *et al.* [125] found that in Nb and Mo the peak is mainly due to $3 \rightarrow 5$ transitions near $\mathbf{k} = \left(\frac{1}{2}, \frac{1}{4}, \frac{1}{4}\right)$. In the group-VIB metals the transition $\Delta_5 \rightarrow \Delta_2'$ ($3, 4 \rightarrow 5$ transitions) contributing to the absorption below 2 eV is common to the three metals. In Mo and W other transitions along the Δ line are found involving the third and fourth bands for Mo and W, and the fourth and fifth bands for W. Bands 3, 4, and 5 along Σ are found to be responsible for the structures at about 2.35 eV in Mo and at about 3.42 eV in W. The second peak in Cr is attributed to the transitions $\Delta_5 \rightarrow \Delta_1$ ($3 \rightarrow 6$ transitions) and $\Sigma_1 \rightarrow \Sigma_4$ ($3 \rightarrow 5$ transitions), whereas in Mo and W bands along F, G, Σ, and Λ, in particular the couples of bands 3 and 4, and 3 and 5, could all be contributing.

Our analysis shows that the spectra of the six metals are in general well reproduced by our calculations. Nevertheless, the locations of some absorption peaks deviate from the experimental ones, in particular in the $3d$ metals. The assignments of the absorption spectra in terms of d-d transitions and the analysis of the regions in the Brillouin zone where they mainly occur indicate that transitions from the Fermi level to virtual bands 4 and 5 yield absorption peaks that are blueshifted with respect to the experiments. The deviation is mainly observed in the $3d$ metals and decreases within a group. In the $4d$ and $5d$ group-VIB metals Mo and W these deviations are almost nonexisting. From the band structures it becomes clear that the energy separation with the Fermi level of these virtual bands strongly increases, while their dispersions remain almost unchanged, resulting within a group in a shift of the absorption peaks towards higher frequencies. On the other hand, absorption peaks are better reproduced if they are due to transitions between bands close to the Fermi level, namely bands 2 and 3, which show very similar dispersions for the metals within the same group. These findings suggest that virtual d bands are too weakly bound by using the local density approximation (or standard gradient corrected approximations) to the ground-state exchange-correlation functional, in particular in the $3d$ metals.

$\mathbf{k}\cdot\mathbf{p}$ analysis of the low-frequency interband transitions

We mentioned above that the linear tetrahedron method is not very reliable to solve the k-integrals in our response calculations for the absorption spectra in the very low-frequency region. The low-frequency absorption, indeed, involves bands degenerate at the Fermi surface, for which a more accurate description of the dispersion is required. In order to fully understand the low-frequency behavior of the absorption spectra and the differences between the group-VB and -VIB transition metals, we studied the interband contribution to the imaginary part of the dielectric function. If we neglect the local-field effects and the relativistic corrections in our method, this contribution is given for isotropic systems by [84]

$$\Im\{\epsilon^{inter}(\omega)\} = \frac{1}{6\pi}\sum_{i,a}\int d\mathbf{k}\frac{\left|\langle\psi_{i\mathbf{k}}|\hat{\mathbf{j}}|\psi_{a\mathbf{k}}\rangle\right|^2}{(\epsilon_{i\mathbf{k}}-\epsilon_{a\mathbf{k}})^2}\left(\delta(\epsilon_{i\mathbf{k}}-\epsilon_{a\mathbf{k}}+\omega)-\delta(\epsilon_{i\mathbf{k}}-\epsilon_{a\mathbf{k}}-\omega)\right), \tag{6.10}$$

where i labels the occupied states, $\epsilon_{i\mathbf{k}} \leq \epsilon_F$, and a labels the unoccupied states, $\epsilon_{a\mathbf{k}} \geq \epsilon_F$, with ϵ_F the Fermi energy. We analyzed the dispersion of the touching bands 2 and 3 in group VB and of bands 3 and 4 in group VIB around their points of degeneracy at the Fermi level (as depicted in Fig. 6.3). At these points the integrand in Eq. (6.10) becomes singular. To evaluate the integrals in these points we made use of the $\mathbf{k}\cdot\mathbf{p}$ method of analytic continuation [57]. In this method the Bloch functions at $\mathbf{k}+\mathbf{q}$ can be expressed in terms of the eigenstates at the reference point $\mathbf{k}$ using

$$\psi_{\mathbf{k}+\mathbf{q}}(\mathbf{r}) = \exp(i\mathbf{q}\cdot\mathbf{r})\sum_m \psi_{m\mathbf{k}}(\mathbf{r})c_{mn}(\mathbf{q}), \tag{6.11}$$

where the coefficients $c_{mn}(\mathbf{q})$ are solutions of the following eigenvalue equation,

$$\sum_m \left[\left(\frac{1}{2}q^2 - \epsilon_{n\mathbf{k}+\mathbf{q}} + \epsilon_{m\mathbf{k}}\right)\delta_{lm} + \langle\psi_{l\mathbf{k}}|\mathbf{q}\cdot\mathbf{p}|\psi_{m\mathbf{k}}\rangle\right]c_{mn}(\mathbf{q}) = 0, \tag{6.12}$$

with $\mathbf{p} = -i\nabla$. The coefficients explicitly depend on the length and direction of $\mathbf{q}$. In our case the reference points are the points of degeneracy. The corresponding eigenvalues $\epsilon_{n\mathbf{k}+\mathbf{q}}$ give the energy dispersions, which can be expressed in a unidirectional Taylor series with $q \geq 0$ as

$$\epsilon_{n\mathbf{k}+\mathbf{q}} \;=\; \epsilon_{n\mathbf{k}} + qP_n(\hat{\mathbf{q}}) + \frac{1}{2}q^2M_n^{-1}(\hat{\mathbf{q}}) + \cdots, \tag{6.13}$$

where we introduced the group velocity $P_n(\hat{\mathbf{q}})$ and the effective mass $M_n(\hat{\mathbf{q}})$. By inserting $\mathbf{q} = \mathbf{0}$ in Eq. (6.12), it immediately follows that the coefficients $c_{mn}(\mathbf{0})$ can only be different from zero if $\epsilon_{m\mathbf{k}} = \epsilon_{n\mathbf{k}}$, hence we can limit the analysis to the degenerate subspace. By retaining only the terms linear in q it also follows that the coefficients diagonalize the subblock of the $\hat{\mathbf{q}}\cdot\mathbf{p}$ matrix built by the degenerate states, resulting in

$$P_n(\hat{\mathbf{q}}) = \langle \psi_{n\mathbf{k}+\delta\mathbf{q}} | \hat{\mathbf{q}} \cdot \mathbf{p} | \psi_{n\mathbf{k}+\delta\mathbf{q}} \rangle. \tag{6.14}$$

For states that remain degenerate to first order in q these coefficients also diagonalize the corresponding subblock of the effective-mass matrix giving

$$M_n^{-1}(\hat{\mathbf{q}}) = 1 + 2 \sum_{i,\epsilon_{n\mathbf{k}} \neq \epsilon_{i\mathbf{k}}} \frac{\langle \psi_{n\mathbf{k}+\delta\mathbf{q}} | \hat{\mathbf{q}} \cdot \mathbf{p} | \psi_{i\mathbf{k}} \rangle \langle \psi_{i\mathbf{k}} | \hat{\mathbf{q}} \cdot \mathbf{p} | \psi_{n\mathbf{k}+\delta\mathbf{q}} \rangle}{\epsilon_{n\mathbf{k}} - \epsilon_{i\mathbf{k}}}, \tag{6.15}$$

which contains the terms of order q^2. Here, for notational convenience, we have introduced the analytically continued eigenstates for the direction $\hat{\mathbf{q}}$,

$$\psi_{n\mathbf{k}+\delta\mathbf{q}} = \sum_m \psi_{m\mathbf{k}} c_{mn}^{(0)}(\hat{\mathbf{q}}), \tag{6.16}$$

where the coefficients $c_{mn}^{(0)}(\hat{\mathbf{q}})$ are given by

$$c_{mn}^{(0)}(\hat{\mathbf{q}}) = \lim_{q \to 0} c_{mn}(q\hat{\mathbf{q}}). \tag{6.17}$$

Using the same expansion Eq. (6.11) one readily derives

$$\begin{aligned} \langle \psi_{i\mathbf{k}+\mathbf{q}} \mid \hat{\mathbf{j}} \mid \psi_{a\mathbf{k}+\mathbf{q}} \rangle &= \langle \psi_{i\mathbf{k}+\delta\mathbf{q}} \mid \hat{\mathbf{j}} \mid \psi_{a\mathbf{k}+\delta\mathbf{q}} \rangle + \mathbf{q}\delta_{ia} + \\ & \sum_{n,\epsilon_{n\mathbf{k}} \neq \epsilon_{i\mathbf{k}}} \frac{\mathbf{q} \cdot \langle \psi_{i\mathbf{k}+\delta\mathbf{q}} | \mathbf{p} | \psi_{n\mathbf{k}} \rangle \langle \psi_{n\mathbf{k}} | \mathbf{p} | \psi_{a\mathbf{k}+\delta\mathbf{q}} \rangle}{\epsilon_{i\mathbf{k}} - \epsilon_{n\mathbf{k}}} + \\ & \sum_{n,\epsilon_{n\mathbf{k}} \neq \epsilon_{a\mathbf{k}}} \frac{\langle \psi_{i\mathbf{k}+\delta\mathbf{q}} | \mathbf{p} | \psi_{n\mathbf{k}} \rangle \langle \psi_{n\mathbf{k}} | \mathbf{p} | \psi_{a\mathbf{k}+\delta\mathbf{q}} \rangle \cdot \mathbf{q}}{\epsilon_{a\mathbf{k}} - \epsilon_{n\mathbf{k}}} + \cdots \end{aligned} \tag{6.18}$$

Details of this analysis for the six bcc metals can be found in App. E. We only state the results here. We find that in the group-VB metals bands 2 and 3 give rise to a linear conical intersection with the contact point as result of the symmetry-induced degeneracy positioned on the line Λ, which is also the axis of the cone. The degeneracy is lifted to first order in q for directions perpendicular to the axis, but it remains present for directions along the axis. From the $\mathbf{k}\cdot\mathbf{p}$ analysis it follows that the contribution to the absorption at low frequency due to the transitions 2 → 3 is constant. Similar results are found also for the point of accidental degeneracy. For the group-VIB metals the bands 3 and 4 also give rise to a conical intersection with the axis of the cone along Δ (taken here as the $\hat{\mathbf{y}}$ direction). However, the degeneracy is lifted only to second order in q within the $\hat{\mathbf{x}}\hat{\mathbf{z}}$ plane, whereas it remains present to all orders in q along Δ due to symmetry. The contribution to the absorption at low frequency due to the transitions $3 \rightarrow 4$ is found to be constant. We conclude that in our scalar relativistic calculations the interband contribution to the absorption does not vanish at low frequencies but remains finite in these metals.

6.5.3 Electron energy-loss function

In Fig. 6.8 the calculated energy-loss function at $\mathbf{q} = \mathbf{0}$, $\Im\{-\epsilon(\omega)^{-1}\}$, is depicted in the range 0-40 eV for the six metals together with experiments reported in literature [104–106, 128]. Three main regions can be identified in the electron energy-loss spectra (EELS): a low-frequency region up to 10 eV with small EELS intensities, a medium-frequency range starting with peak structures at about 10 eV and extending up to about 20 eV, and finally a high-frequency region that is dominated by a single intense peak at about 24 eV. The main peaks in the medium- and high-frequency regions have been identified as volume plasmons, be it of different nature [104–106]: the one at high frequency corresponding to the collective motion of all valence electrons and the medium-frequency ones involving only groups of electrons. For all metals a single peak in the medium-frequency region is usually identified as plasmon-like, except for tungsten where a second peak can be seen at about 15.2 eV. In view of the occurrence of this second peak Weaver *et al.* [106] indicated that also in the other group-VIB metals and in the group-VB metals a second plasmon resonance should appear. Our ALDA calculations reproduce very well the experimental spectra in the low- and medium-frequency ranges: both the relative intensity and the position of the plasmon peaks are correctly described. The calculated plasmon-peak in the high-frequency range, however, is too intense as compared to experiments for the 4d and 5d metals, but it appears at the correct position. Also in the 3d metals the position is correct, but here we can not comment on the intensity as the experiments are given in arbitrary units. The main resonances are listed in tables 6.5 and 6.6. The agreement between calculations and measurements is better for the electron energy-loss functions than for the dielectric functions. Although closely related, the two quantities depend in a different way on the long-range Coulomb interaction [36]. Whereas the dielectric function measures the macroscopic response to the macroscopic field, which includes the long-range screening of the external field, the EELS measures the macroscopic response to an unscreened external field. By calculating the self-consistent

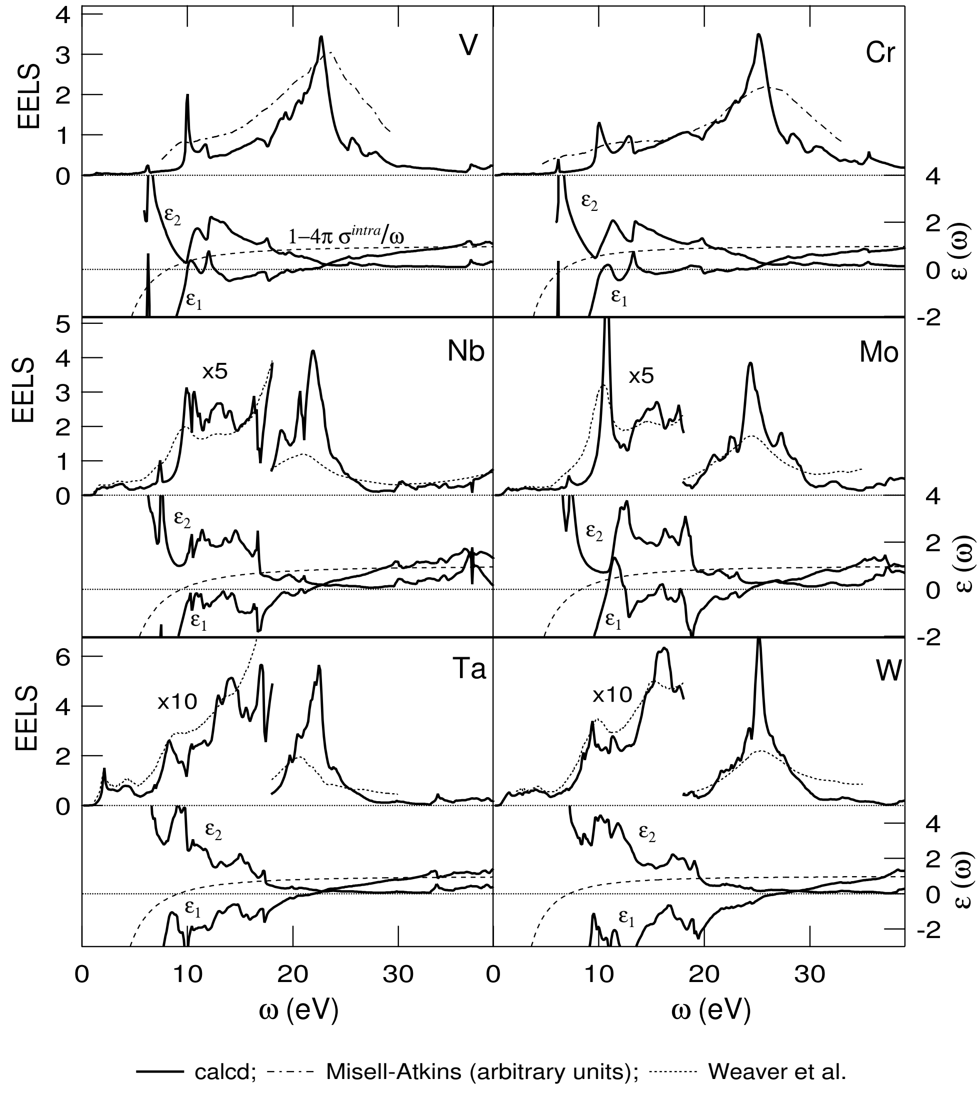

Figure 6.8: Calculated electron energy-loss spectra (bold solid line) for vanadium, niobium, tantalum, chromium, molybdenum, and tungsten. The experimental results are taken from Ref. [104–106, 128]. The calculated real and imaginary parts of the dielectric function are also reported in the range 6-40 eV. The calculated results reported for Nb, Ta, Mo, and W refer to scalar relativistic calculations.

Table 6.5: Position (in eV) of the main features in the experimental and theoretical electron energy-loss spectra for the group-VB metals. Ω_p= free-electron-like plasmon peak; $\Omega_{1,2}$=other main features.

Peak	V		Nb		Ta	
	Exp[a]	ALDA	Exp[a]	ALDA	Exp[a]	ALDA
Ω_p	23.6	22.7	20.8	21.8	20.7	22.6
Ω_1	9.6	10.0	9.7	10.4	8.9	8.8
Ω_2	-	-	13.0	13.3	13.6	14.0

---

[a] peak positions obtained using data from Ref. [104, 105, 128]

Table 6.6: Position (in eV) of the main features in the experimental and theoretical electron energy-loss spectra for the group-VB metals. Ω_p= free-electron-like plasmon peak; $\Omega_{1,2}$=other main features.

Peak	Cr		Nb		W	
	Exp[a]	ALDA	Exp[a]	ALDA	Exp[a]	ALDA
Ω_p	25.7	25.2	24.4	24.5	25.3	25.1
Ω_1	12.0	11.7	10.4	10.8	10.0	9.9
Ω_2	-	-	14.6	15.4	15.2	15.5

---

[a] peak positions obtained using data from Ref. [105, 106, 128]

response to the macroscopic field the long-range part of the Coulomb interaction is effectively removed from the self-consistent field [30]. In the EELS this dominant contribution to the self-consistent field remains present. As result the dielectric function will be more sensitive to the quality of the approximations used for the much smaller exchange-correlation part of the self-consistent potentials. In many cases the ALDA approximation already gives a good description of the EELS, whereas more sophisticated approximations are required to describe correctly the dielectric function.

In all six metals the dominant plasmon resonance appears in the experiments at much higher frequency than the Drude free-electron plasma frequency. From our calculations it becomes clear that the shift in energy is completely due to the interplay between inter- and intraband effects. The free-electron resonance is renormalized due to the polarizable background that is introduced by the low-frequency interband processes. If only intraband processes were to be included, the bulk plasmon resonance would occur at just below 10 eV. Upon inclusion of interband processes this resonance is shifted by approximately 10-15 eV to much higher energies. In the low-frequency region the intraband processes give rise to a very strong response, thus suppressing the EELS intensity. At about 10 eV, i.e., at the Drude free-electron plasma frequency, the intraband response is minimal and interband processes start to dominate. Interband transitions give rise to a rich structure in the dielectric function, which in turn leads to additional plasmon-like features in the EELS. At frequencies where both ϵ_1 and ϵ_2 are small such plasmon-like resonances are clearly observed in the calculated and measured spectra. Even though these resonances are close to the Drude plasma frequency, they are not free-electron-like resonances in nature, but they are caused by strongly mixed inter- and intraband processes. These features as well as the main plasmon resonances are very well reproduced in our calculations, in which local-field effects are fully included and exchange-correlation effects are treated within the adiabatic local density approximation.

6.6 Conclusions

We have systematically analyzed the optical properties of the group-VB bcc transition metals V, Nb, and Ta, and the group-VIB bcc transition metals Cr (in the paramagnetic phase), Mo, and W by comparing theoretical and experimental results. The dielectric and electron energy-loss functions of these metals have been calculated by using our formulation of the linear response of metals within the time-dependent current-density-functional theory. Our calculations have been compared with our ellipsometry measurements of the dielectric functions and with other experiments reported in literature. The two sets of experimental data by Nestell, Johnson, and Christy and by Weaver and co-workers differ mostly on the low-frequency side. We attribute this discrepancy to the Drude-like extrapolation model used by Weaver *et al.* in their Kramers-Kronig procedure, which is needed to extract the optical constants from the reflectivity data. This is confirmed by the very good agreement up to about 3 eV between the reflectivities that we extracted from the optical constants obtained by Nestell and Christy with those reported by Weaver *et al.*. Our experiments are in good agreement with Nestell and Christy's data.

We found that metals belonging to the same group show common spectral features which are shifted in energy with the increase of the d-band dispersion. On the other hand, features common to metals which are adjacent in the Periodic Table are found at similar energies, but also different features result from the different filling of the d bands. By carefully treating the topology of the Fermi surface, we calculated interband absorption already at frequencies below 0.5 eV, and hence deviations from the Drude behavior that is often assumed in the experimental analysis of the linear response are expected for these metals. In general both the real and imaginary parts of the dielectric functions are well reproduced by our calculations. However, some calculated peaks in the absorption spectra are blueshifted with respect to the experiments, in particular in the $3d$ metals. We observed that peaks that are mainly due to transitions between bands close to the Fermi level are reasonably well described in our calculations. These bands show similar dispersions within a group. Absorptions involving transitions from the Fermi level to virtual bands are calculated at energies higher than the experimental ones, in particular in the $3d$ metals. The energy separation of these virtual bands with the Fermi level strongly changes within a group while the dispersion roughly remains the same. This finding indicates that the virtual bands are too weakly bound in the ground state described by using the LDA and equally by the standard GGAs. A better functional should shift down these virtuals almost rigidly over $\sim$0.5 eV with respect to the LDA in order to correctly describe the response features. The use of exchange-correlation functionals beyond the adiabatic local density approximation should introduce the relaxation effects in the response calculations, that is lacking in the ALDA. Such nonadiabatic functionals are expected to give a better agreement between calculations and experiments by describing the electron-electron scattering part of the low-frequency Drude-like absorption and by broadening and smoothing the spectral features as effects of a finite relaxation time. The EELS are very well reproduced by our method. The six metals show a dominant plasmon resonance at about 22-24 eV, well above the Drude free-electron plasma frequency. Our analysis shows that the shift in energy is completely due to the interplay of inter- and intraband effects. Additional plasmon-like features are calculated in the range 10-15 eV and are due to the rich structure in the dielectric functions resulting from interband transitions.

Chapter 7

Performance of the Vignale-Kohn Functional in the Linear Response of Metals

We include the Vignale-Kohn current functional in the formulation of the linear response of metallic solids given in chapter 3. Within this approximation the exchange-correlation kernel $f_{xc}(\mathbf{r}, \mathbf{r}', \omega)$ *is* ω*-dependent, thus relaxation effects due to electron-electron scattering can now be taken into account and some deficiencies of the adiabatic local density approximation, as the absence of the low-frequency Drude-like absorption, can be cured. The self-consistent equations for the inter- and intraband contributions to the induced density and current-density, which are completely decoupled within the ALDA and in the long-wavelength limit, become now coupled. We treat the dominant scalar relativistic effects using the zeroth-order regular approximation in the ground-state density-functional theory calculations, as well as in the time-dependent response calculations. We present our results calculated for the optical properties of the noble metals Cu, Ag, and Au, and we compare them with measurements found in literature.*

7.1 Introduction

In treating the linear response of metals to a macroscopic electric field one has to consider both the interband contribution to the response, involving transitions from (partially) occupied to (partially) unoccupied bands as in nonmetals, and the intraband contribution due to transitions within the same partially occupied bands, more specifically, from just below the Fermi level to just above this level. In chapter 3 we have considered the linear response of the system to a general q- and ω-dependent perturbation. We have found that inter- and intraband processes behave differently for small q and that the self-consistent-field equations for the inter- and intraband contributions to the response decouple in the optical limit (vanishing q but finite ω) when we make use of the adiabatic local density approximation (ALDA). In this approximation the exchange-correlation scalar potential $v_{xc}(\mathbf{r}, t)$ is just a local functional of the density. Within the ALDA this method yields good results for the dielectric and the electron energy-loss functions of several transition metals. However the adiabatic approximation fails in describing the low-frequency Drude-like absorption, which is missing in all the calculated absorption spectra. This absorption is due to relaxation processes such as electron-electron and electron-phonon scattering. The description of the electron-phonon interaction requires the use of a multicomponent-density functional approach. The electron-electron scattering can be described within our method by using more advanced exchange-correlation functionals where a frequency-dependent xc-kernel $f_{xc}(\mathbf{r}, \mathbf{r}', \omega)$ is used.

In this chapter we go beyond the ALDA and we employ an exchange-correlation vector potential, $\mathbf{A}_{xc}(\mathbf{r}, t)$, which we approximate as a local functional of the current-density using the expression derived by Vignale and Kohn [24, 25]. The evaluation of the VK expression requires knowledge of some properties of the homogeneous electron gas, i.e., the exchange-correlation energy $e_{xc}(\rho_0)$, and the longitudinal and transverse exchange-correlation kernels, $f_{xcL}(\rho_0, \omega)$ and $f_{xcT}(\rho_0, \omega)$, respectively, where ρ_0 is the electron density of the electron gas. Knowledge of the first is already required in the ALDA and can be obtained from the accurate results of Monte Carlo calculations [65, 129]. The xc kernels, on the other hand, are not known accurately. There are two works in which parametrizations are given for both $f_{xcL}(\rho_0, \omega)$ and $f_{xcT}(\rho_0, \omega)$. One work is by Conti, Nifosì, and Tosi (CNT) [131], and the other is by Qian and Vignale (QV) [130]. An important difference between the paramatrizations of CNT and QV occurs in the $\omega \to 0$ limit of $f_{xcT}(\rho_0, \omega)$. Whereas $f_{xcT}(\rho_0, \omega)$ of CNT vanishes in that limit, the QV parametrization does not, i.e., it has a small but finite value. The fact that $f_{xcT}(\rho_0, \omega)$ vanishes in the $\omega \to 0$ limit in the case of the CNT parametrization has the important consequence that the VK expression for $\delta\mathbf{A}_{xc}(\mathbf{r}, \omega)$ reduces to that of the ALDA in that limit. The value of $f_{xcT}(\rho_0, 0)$ is related to μ_{xc}, the exchange-correlation part of the shear modulus, a quantity that is known only approximately. In previous work it has been shown that this difference in behavior of the two parametrizations in the zero-frequency limit leads to very different absorption spectra of bulk semiconductors [69]. Whereas spectra obtained with the CNT parametrization are relatively close to spectra obtained within the ALDA, spectra obtained with the QV parametrization are very different from the ALDA results and from the experiments. Since Qian and Vignale give an expression for their parametrization in which $f_{xcL,T}(\rho_0, 0)$ enter, the QV parametrization can easily be adapted for the case $f_{xcT}(\rho_0, 0)$=0. By using the resulting parametrization the absorption spectra for silicon are again close to the spectra obtained with the CNT parametrization and those obtained within the ALDA [69, 132]. In view of the obtained results mentioned above and the fact that we are mainly interested in the ω-dependence of the VK functional in order to describe relaxation effects due to electron-electron scattering, we choose to set $f_{xcT}(\rho_0, 0)$=0 also in the QV parametrization. In Sec. II we describe the theory we use. We introduce the self-consistent set of equations which describes the linear response of metallic crystals and how to include the Vignale-Kohn functional. In the end of the section we give the main equations we use to treat the dominant scalar relativistic effects within the zeroth order regular approximation (ZORA). The ZORA formalism will be used to treat the scalar relativistic effects in the linear response of Au. The main aspects of the implementation are presented in Sec. III. Finally, we show our results for the dielectric and energy-loss functions of the crystals of Cu, Ag, and Au, and we compare them with the best available experimental data [50–52, 70, 133–135].

7.2 Theory

7.2.1 Linear response

To derive the linear response of metals to a macroscopic field (see chapter 3) we consider a general q- and ω-dependent perturbation,

$$\delta\hat{h}(\mathbf{q},\omega) = \frac{-i}{2c}\left(e^{i\mathbf{q}\cdot\mathbf{r}}\nabla - \nabla^{\dagger}e^{i\mathbf{q}\cdot\mathbf{r}}\right)\cdot\delta\mathbf{A}_{\mathbf{q},\mathit{eff}}(\mathbf{r},\omega) + e^{i\mathbf{q}\cdot\mathbf{r}}\delta v_{\mathbf{q},\mathit{eff}}(\mathbf{r},\omega). \tag{7.1}$$

In the following we will use the notation $\hat{\rho}_{\mathbf{q}} = e^{-i\mathbf{q}\cdot\mathbf{r}}$ and $\hat{\mathbf{j}}_{\mathbf{q}} = -i(e^{-i\mathbf{q}\cdot\mathbf{r}}\nabla - \nabla^{\dagger}e^{-i\mathbf{q}\cdot\mathbf{r}})/2$. The perturbing potentials $\delta v_{\mathit{eff}}(\mathbf{r},\omega) = e^{i\mathbf{q}\cdot\mathbf{r}}\delta v_{\mathbf{q},\mathit{eff}}(\mathbf{r},\omega)$ and $\delta\mathbf{A}_{\mathit{eff}}(\mathbf{r},\omega) = e^{i\mathbf{q}\cdot\mathbf{r}}\delta\mathbf{A}_{\mathbf{q},\mathit{eff}}(\mathbf{r},\omega)$, with $\delta v_{\mathbf{q},\mathit{eff}}(\mathbf{r},\omega)$ and $\delta\mathbf{A}_{\mathbf{q},\mathit{eff}}(\mathbf{r},\omega)$ lattice periodic [84], are defined in the microscopic Coulomb gauge of Kootstra *et al.* [30] as

$$\delta v_{\mathit{eff}}(\mathbf{r},\omega) = \delta v_{H,mic}(\mathbf{r},\omega) + \delta v_{xc}(\mathbf{r},\omega), \tag{7.2}$$

$$\delta\mathbf{A}_{\mathit{eff}}(\mathbf{r},\omega) = \delta\mathbf{A}_{mac}(\mathbf{r},\omega) + \delta\mathbf{A}_{xc}(\mathbf{r},\omega). \tag{7.3}$$

Here $\delta v_{H,mic}(\mathbf{r},t)$ and $\delta v_{xc}(\mathbf{r},t)$ are the microscopic component of the Hartree and exchange-correlation potentials, respectively, $\delta\mathbf{A}_{mac}(\mathbf{r},\omega) = -ic/\omega\,\mathbf{E}_{mac}(\mathbf{r},\omega)$, with

$\mathbf{E}_{mac}(\mathbf{r},\omega)$ the fixed macroscopic electric field, comprising both the external and the induced macroscopic components, and $\delta\mathbf{A}_{xc}(\mathbf{r},\omega)$ is the exchange-correlation vector potential. The linear response of the system is then obtained for vanishing q but finite ω, which is the regime describing optical properties. An essential point of the formulation is that inter- and intraband processes behave differently for small q. At finite q the equations for the induced density $\delta\rho(\mathbf{r},\omega) = e^{i\mathbf{q}\cdot\mathbf{r}}\delta\rho_{\mathbf{q}}(\mathbf{r},\omega)$ and current-density $\delta\mathbf{j}(\mathbf{r},\omega) = e^{i\mathbf{q}\cdot\mathbf{r}}\delta\mathbf{j}_{\mathbf{q}}(\mathbf{r},\omega)$, with $\delta\rho_{\mathbf{q}}(\mathbf{r},\omega)$ and $\delta\mathbf{j}_{\mathbf{q}}(\mathbf{r},\omega)$ lattice periodic, can be written in the following concise form,

$$\left(\begin{array}{c} \delta\rho_{\mathbf{q}}^{inter} \\ \hline i\delta\mathbf{j}_{\mathbf{q}}^{inter}/\omega \end{array}\right) = \left(\begin{array}{c|c} \chi_{\rho\rho\mathbf{q}}^{inter} & -i\chi_{\rho\mathbf{j}\mathbf{q}}^{inter}/\omega \\ \hline i\chi_{\mathbf{j}\rho\mathbf{q}}^{inter}/\omega & (\chi_{\mathbf{j}\mathbf{j}\mathbf{q}}^{inter} - \chi_{\mathbf{j}\mathbf{j}\mathbf{q}}^{inter,0})/\omega^2 \end{array}\right) \cdot \left(\begin{array}{c} \delta v_{\mathbf{q},\mathit{eff}} \\ \hline i\omega\delta\mathbf{A}_{\mathbf{q},\mathit{eff}}/c \end{array}\right), \tag{7.4}$$

for the interband contributions, and

$$i\omega\left(\begin{array}{c} \omega/q\,\delta\rho_{\mathbf{q}}^{intra} \\ \hline \delta\mathbf{j}_{\mathbf{q}}^{intra} \end{array}\right) = \left(\begin{array}{c|c} \omega^2/q^2\,\chi_{\rho\rho\mathbf{q}}^{intra} & \omega/q\,\chi_{\rho\mathbf{j}\mathbf{q}}^{intra} \\ \hline \omega/q\,\chi_{\mathbf{j}\rho\mathbf{q}}^{intra} & \chi_{\mathbf{j}\mathbf{j}\mathbf{q}}^{intra} - \chi_{\mathbf{j}\mathbf{j}\mathbf{q}}^{intra,0} \end{array}\right) \cdot \left(\begin{array}{c} iq\delta v_{\mathbf{q},\mathit{eff}} \\ \hline i\omega\delta\mathbf{A}_{\mathbf{q},\mathit{eff}}/c \end{array}\right), \tag{7.5}$$

for the intraband part. Here the matrix-vector products also include an integration over a real space coordinate. All matrix elements in these expressions are finite in the limits $q,\omega \to 0$. The various interband contributions to the response functions have the following ω-dependence,

$$\begin{aligned} \chi_{\rho\rho\mathbf{q}}^{inter} &\propto 1, \\ \chi_{\rho\mathbf{j}\mathbf{q}}^{inter}, \chi_{\mathbf{j}\rho\mathbf{q}}^{inter} &\propto \omega, \\ (\chi_{\mathbf{j}\mathbf{j}\mathbf{q}}^{inter} - \chi_{\mathbf{j}\mathbf{j}\mathbf{q}}^{0,inter}) &\propto \omega^2, \end{aligned} \tag{7.6}$$

whereas the intraband response functions show the following ω and q-dependence at small q but finite ω,

$$\begin{aligned} \chi_{\rho\rho\mathbf{q}}^{intra} &\propto q^2/\omega^2, \\ \chi_{\rho\mathbf{j}\mathbf{q}}^{intra}, \chi_{\mathbf{j}\rho\mathbf{q}}^{intra} &\propto q/\omega, \\ (\chi_{\mathbf{j}\mathbf{j}\mathbf{q}}^{intra} - \chi_{\mathbf{j}\mathbf{j}\mathbf{q}}^{0,intra}) &\propto 1. \end{aligned}$$

Inspection of (7.5) makes immediately clear that in the long-wavelengh limit the effective scalar potential does not contribute to the intraband induced density and current-density. In chapter 3 we have used $\delta v_{xc}^{ALDA}(\mathbf{r},t)$ for the exchange-correlation scalar potential and we have neglected the exchange-correlation vector potential. In this case the effective vector potential is completely defined by the macroscopic electric field which is kept fixed. We then need to solve only the equation for the interband induced density self-consistently, and afterwards the inter- and intraband contributions to the induced current can be calculated. Approximations beyond the ALDA imply a self-consistent solution for both the inter- and intraband induced density and induced current-density equations, which will be coupled.

7.2.2 The Vignale-Kohn functional

The general expression for the exchange-correlation vector potential is to first order

$$\delta \mathbf{A}_{xc}(\mathbf{r},\omega) = \int \mathbf{f}_{xc}(\mathbf{r},\mathbf{r}',\omega) \cdot \delta \mathbf{j}(\mathbf{r}',\omega) d\mathbf{r}'. \tag{7.7}$$

This expression defines the tensor kernel $\mathbf{f}_{xc}(\mathbf{r},\mathbf{r}',\omega)$. By studying a weakly perturbed electron gas with wavevector $\mathbf{k}$ under the influence of an external perturbation with wavevector $\mathbf{q}'$, Vignale and Kohn derived an approximation for $\delta \mathbf{A}_{xc}(\mathbf{r},\omega)$ [24,25]. By construction the VK functional obeys several exact constraints. The VK functional satisfies the zero-force and zero-torque constraints, which state that the exchange-correlation potentials cannot exert a net force or a net torque on the system. Furthermore, it obeys the requirement of generalized translational invariance, which states that a rigid translation of the current-density implies a rigid translation of the exchange-correlation potentials. Finally, it satisfies the Onsager symmetry relation, which restricts the form of exchange-correlation kernel $\mathbf{f}_{xc}(\mathbf{r},\mathbf{r}',\omega)$. Vignale, Ullrich, and Conti showed that the complicated VK-expression for $\delta \mathbf{A}_{xc}(\mathbf{r},\omega)$ could be written in the following physically transparent form [136],

$$\frac{i\omega}{c} \delta \mathbf{A}_{xc,i}(\mathbf{r},\omega) = \nabla \delta v_{xc}^{ALDA}(\mathbf{r},\omega) - \frac{1}{\rho_0(\mathbf{r})} \sum_j \partial_j \sigma_{xc,ij}(\mathbf{r},\omega), \tag{7.8}$$

where the first term on the right-hand side is just the linearization of the ALDA xc scalar potential. Using a gauge transformation this longitudinal part of $\delta \mathbf{A}_{xc}(\mathbf{r},\omega)$ can be included in the scalar potential. The second term is the divergence of a tensor field $\sigma_{xc}(\mathbf{r},\omega)$, which has the structure of a symmetric viscoelastic stress tensor,

$$\sigma_{xc,ij} = \tilde{\eta}_{xc} \left(\partial_j u_i + \partial_i u_j - \frac{2}{3} \delta_{ij} \sum_k \partial_k u_k \right) + \tilde{\zeta} \delta_{ij} \sum_k \partial_k u_k, \tag{7.9}$$

where the velocity field $\mathbf{u}(\mathbf{r},\omega)$ is given by

$$\mathbf{u}(\mathbf{r},\omega) = \frac{\delta \mathbf{j}(\mathbf{r},\omega)}{\rho_0(\mathbf{r})}. \tag{7.10}$$

The coefficients $\tilde{\eta}_{xc}(\mathbf{r},\omega)$ and $\tilde{\zeta}_{xc}(\mathbf{r},\omega)$ are determined by the longitudinal and transverse response coefficients $f_{xcL}(\rho_0(\mathbf{r}),\omega)$ and $f_{xcT}(\rho_0(\mathbf{r}),\omega)$ of the homogeneous electron gas evaluated at the density $\rho_0(\mathbf{r})$,

$$\tilde{\eta}_{xc}(\mathbf{r},\omega) = \frac{i}{\omega}\rho_0^2(\mathbf{r}) f_{xcT}(\rho_0(\mathbf{r}),\omega), \tag{7.11}$$

and

$$\tilde{\zeta}_{xc}(\mathbf{r},\omega) = \frac{i}{\omega}\rho_0^2(\mathbf{r}) \left(f_{xcL}(\rho_0(\mathbf{r}),\omega) - \frac{4}{3} f_{xcT}(\rho_0(\mathbf{r}),\omega) - \frac{d^2 e_{xc}}{d\rho^2}(\rho_0(\mathbf{r})) \right), \tag{7.12}$$

where $e_{xc}(\rho_0(\mathbf{r}))$ is the exchange-correlation energy per unit volume of the homogeneous electron gas. The quantities $\tilde{\eta}_{xc}(\mathbf{r},\omega)$ and $\tilde{\zeta}_{xc}(\mathbf{r},\omega)$ can be interpreted as viscoelastic coefficients [136, 137]. The coefficients $f_{xcL,T}(\rho_0(\mathbf{r}),\omega)$ are defined by the identity [25, 138]

$$f_{xcL,T}(\rho_0(\mathbf{r}),\omega) = \lim_{\mathbf{q}'\to 0} f_{xcL,T}(\rho,\mathbf{q}',\omega)|_{\rho=\rho_0(\mathbf{r})}. \tag{7.13}$$

Note that $f_{xcL}(\rho,\mathbf{q}',\omega)$ is defined in such a way that coincides with $f_{xc}(\rho,\mathbf{q}',\omega)$ from scalar TDDFT. These exchange-correlation kernels have been extensively studied and some exact features are well known [130, 131, 137, 139, 140]. In particular Conti and Vignale [137] obtained the following identities for the three-dimensional electron gas,

$$\lim_{\omega\to 0}\lim_{\mathbf{q}'\to 0} f_{xcL}(\mathbf{q}',\omega) = \frac{1}{\rho_0^2}\left(K_{xc} + \frac{4}{3}\mu_{xc}\right), \tag{7.14}$$

$$\lim_{\omega\to 0}\lim_{\mathbf{q}'\to 0} f_{xcT}(\mathbf{q}',\omega) = \frac{\mu_{xc}}{\rho_0^2}, \tag{7.15}$$

where K_{xc} and μ_{xc} are the real-valued exchange-correlation parts of the bulk and shear moduli, respectively. Since $K_{xc} = \rho_0^2(d^2 e_{xc}(\rho_0)/d\rho^2)$, from Eqs. (7.14) and (7.15) one obtains that [136, 137]

$$\lim_{\omega\to 0}\frac{-i\omega\tilde{\zeta}_{xc}(\mathbf{r},\omega)}{\rho_0^2} = 0, \tag{7.16}$$

$$\lim_{\omega\to 0}\frac{-i\omega\tilde{\eta}_{xc}(\mathbf{r},\omega)}{\rho_0^2} = f_{xcT}(\rho_0,0). \tag{7.17}$$

Note that only if $\mu_{xc} = 0$ the VK expression (7.8) reduces to the ALDA in the limit $\omega \to 0$, otherwise it does not.

Conti, Nifosì, and Tosi (CNT) calculated $f_{xcL,T}(\rho_0,\omega)$ within a mode coupling approximation scheme [131]. Furthermore, CNT introduced parametrizations for $\mathrm{Im} f_{xcL,T}(\omega)$ that reproduce their numerical results. The real parts of $f_{xcL,T}(\rho_0,\omega)$

can then be obtained from the standard Kramers-Kronig symmetry relations. Their results reduce to the exact values in the limit $\omega \to \infty$, the high-frequency limit of $f_{xcL}(\rho_0, \omega)$ being that of Glick and Long [141]. However, they do not reduce to the exact values in the limit $\omega \to 0$ because they invoke the compressibility sum rule for $f_{xcL}(\omega)$,

$$\lim_{\mathbf{q}' \to 0} \lim_{\omega \to 0} f_{xcL}(\mathbf{q}', \omega) = \frac{K_{xc}}{\rho_0^2}, \tag{7.18}$$

thereby interchanging the order of the limits with respect to the exact result (7.14). This is equivalent to the approximation $\mu_{xc} = 0$. Because of the uncertainty in the precise values of μ_{xc}, the fact that it is small compared to K_{xc} and the appeal of a theory that reduces to the ALDA in the limit $\omega \to 0$, they prefer to enforce equality of the order of limits [131].

Qian and Vignale [130] introduced interpolation formulae for $\mathrm{Im} f_{xcL,T}(\omega)$ in which the coefficients were determined by exact constraints in the high- and low-frequency limits. The real parts of $f_{xcL,T}(\rho_0, \omega)$ can again been obtained from the Kramers-Kronig relations. Their results for $f_{xcL,T}(\omega)$ reduce to the correct high-frequency limits as well as to to the correct low-frequency limits (7.14) and (7.15). Furthermore, their results for $\mathrm{Im} f_{xcL,T}(\omega)$ also have the correct slope in the limit $\omega \to 0$, unlike the CNT results. Since QV give an expression for their parametrization in which $f_{xcL,T}(\rho_0, 0)$ enter, their parametrization can easily be adapted for the case $f_{xcT}(\rho_0, 0)$=0. For reasons mentioned in the Introduction we, like CNT, prefer to use a theory that reduces to the ALDA in the limit $\omega \to 0$. This means that we will use the QV parametrization only with $\mu_{xc} = f_{xcT}(\rho_0, 0) = 0$.

7.2.3 Relativistic corrections

Scalar-relativistic effects can be treated in our formulation by using the zeroth-order regular approximation (ZORA) [79, 80, 113] as described in chapter 4. In particular the nonrelativistic operator $\hat{\mathbf{j}}_{\mathbf{q}}$ will become

$$\hat{\mathbf{j}}_{\mathbf{q}}^{ZORA} = -\frac{i}{2} \left(e^{-i\mathbf{q}\cdot\mathbf{r}} K(\mathbf{r}) \nabla - \nabla^{\dagger} K(\mathbf{r}) e^{-i\mathbf{q}\cdot\mathbf{r}} \right), \tag{7.19}$$

in scalar ZORA calculations. Here $K(\mathbf{r}) = (1 - v_{\mathit{eff},0}(\mathbf{r})/2c^2)^{-1}$, with c the velocity of light and $v_{\mathit{eff},0}(\mathbf{r})$ the ground-state self-consistent effective potential. Furthermore, as we will show in the next section, in the implementation of the VK functional we will need the curl of the induced current-density $\delta\mathbf{m}(\mathbf{r}, \omega) = \nabla \times \delta\mathbf{j}(\mathbf{r}, \omega)$. An expression for $\delta\mathbf{m}(\mathbf{r}, \omega) = e^{-i\mathbf{q}\cdot\mathbf{r}} \delta\mathbf{m}_{\mathbf{q}}(\mathbf{r}, \omega)$ can be obtained by taking the curl of the induced current-density given in Eqs. (7.4) and (7.5). This amounts to the substitution of the operator $\hat{\mathbf{m}}_{\mathbf{q}} = -i(\nabla^\dagger \times e^{-i\mathbf{q}\cdot\mathbf{r}}\nabla)$ for $\hat{\mathbf{j}}_{\mathbf{q}}$ in the corresponding Kohn-Sham response functions. The scalar ZORA expression for the operator $\hat{\mathbf{m}}_{\mathbf{q}}$ results to be

$$\begin{aligned} \hat{\mathbf{m}}_{\mathbf{q}}^{ZORA} &= -i(\nabla^\dagger \times e^{-i\mathbf{q}\cdot\mathbf{r}}K(\mathbf{r})\nabla) \\ &- \frac{i}{2}\left(e^{-i\mathbf{q}\cdot\mathbf{r}}\nabla K(\mathbf{r}) \times \nabla + \nabla^\dagger \times e^{-i\mathbf{q}\cdot\mathbf{r}}\nabla K(\mathbf{r})\right). \end{aligned} \tag{7.20}$$

For the materials discussed in this chapter $K(\mathbf{r}) \approx 1$ and $\nabla v_{s,0}(\mathbf{r}) \ll 2c^2$ everywhere except close to the nuclei. The term $\nabla K(\mathbf{r}) = K^2(\mathbf{r})\nabla v_{s,0}(\mathbf{r})/(2c^2)$ is thus smaller than one everywhere, except in a small volume around the nuclei which, however, has a negligible contribution to the integrals in which it appears. Therefore we will neglect the second term on the right-hand side of Eq. (7.20).

7.3 Implementation

Berger *et al.* [69] have shown that the exchange-correlation vector potentials $\delta\mathbf{A}_{xc}(\mathbf{r},\omega)$ as expressed in Eqs (7.8)-(7.10) can be written in the following more convenient way,

$$\delta\mathbf{A}_{xc}(\mathbf{r},\omega) = -\frac{ic}{\omega}\nabla\delta u_{xc}(\mathbf{r},\omega) + \delta\mathbf{a}_{xc}(\mathbf{r},\omega) + \nabla \times \delta\mathbf{b}_{xc}(\mathbf{r},\omega). \tag{7.21}$$

Here $\delta u_{xc}(\mathbf{r},\omega)$ is a scalar field, $\delta\mathbf{a}_{xc}(\mathbf{r},\omega)$ is a polar vector field, and $\delta\mathbf{b}_{xc}(\mathbf{r},\omega)$ is an axial vector field. These contributions can be chosen to have a form that involves only the local values of $\delta\mathbf{j}(\mathbf{r},\omega)$, $\nabla\cdot\delta\mathbf{j}(\mathbf{r},\omega) = i\omega\delta\rho(\mathbf{r},\omega)$, and $\nabla\times\delta\mathbf{j}(\mathbf{r},\omega) = \delta\mathbf{m}(\mathbf{r},\omega)$. In this case one can write the following compact matrix vector product,

$$\begin{pmatrix} \delta u_{xc} \\ i\omega\delta\mathbf{a}_{xc}/c \\ i\omega\delta\mathbf{b}_{xc}/c \end{pmatrix} = \begin{pmatrix} y_{\rho\rho} & y_{\rho\mathbf{j}} & 0 \\ y_{\mathbf{j}\rho} & y_{\mathbf{jj}} & y_{\mathbf{jm}} \\ 0 & y_{\mathbf{mj}} & y_{\mathbf{mm}} \end{pmatrix} \cdot \begin{pmatrix} \delta\rho \\ i\delta\mathbf{j}/\omega \\ i\delta\mathbf{m}/\omega \end{pmatrix}, \tag{7.22}$$

where matrix entries are given as

$$\begin{aligned}
y_{\rho\rho} &= -i\omega\frac{\frac{4}{3}\tilde{\eta}_{xc}+\tilde{\zeta}_{xc}}{\rho_0^2}, && (7.23)\\
y_{\rho\mathbf{j}} = y_{\mathbf{j}\rho}^T &= -i\omega\left(\frac{\frac{4}{3}\tilde{\eta}_{xc}+\tilde{\zeta}_{xc}}{\rho_0^2} - 2\frac{\tilde{\eta}'_{xc}}{\rho_0}\right)\frac{\nabla\rho_0}{\rho_0}, && (7.24)\\
y_{\mathbf{jj}} &= -i\omega\left(\frac{\frac{1}{3}\tilde{\eta}_{xc}+\tilde{\zeta}_{xc}}{\rho_0^2} - 4\frac{\tilde{\eta}'_{xc}}{\rho_0} + 2\tilde{\eta}''_{xc}\right)\frac{\nabla\rho_0\otimes\nabla\rho_0}{\rho_0^2}\\
&\quad -i\omega\left(2\frac{\tilde{\eta}'_{xc}}{\rho_0}\frac{\nabla\otimes\nabla\rho_0}{\rho_0} + \frac{\tilde{\eta}_{xc}}{\rho_0^2}\frac{|\nabla\rho_0|^2}{\rho_0^2}\mathbf{I}\right), && (7.25)\\
y_{\mathbf{jm}} = y_{\mathbf{mj}}^T &= -i\omega\frac{\tilde{\eta}_{xc}}{\rho_0^2}\left[\frac{\nabla\rho_0}{\rho_0}\times\right], && (7.26)\\
y_{\mathbf{mm}} &= -i\omega\frac{\tilde{\eta}_{xc}}{\rho_0^2}\mathbf{I}. && (7.27)
\end{aligned}$$

Here we define the antisymmetric 3×3 matrix $[\nabla\rho_0/\rho_0\times]_{ij} = -\sum_k \epsilon_{ijk}(\partial_k\rho_0)/\rho_0$, and $\tilde{\eta}'_{xc}(\mathbf{r},\omega)$ and $\tilde{\eta}''_{xc}(\mathbf{r},\omega)$ are the first and second order derivatives of $\tilde{\eta}_{xc}(\mathbf{r},\omega)$ with respect to the ground-state density. The matrix in Eq.(7.22) is a local function of the ground-state density and its first and second order gradients, and has additional ω-dependence through the coefficients $\tilde{\eta}_{xc}(\mathbf{r},\omega)$ and $\tilde{\zeta}_{xc}(\mathbf{r},\omega)$.

By using Eq. (7.21) the xc contribution to the perturbation (7.1) can be written as

$$\begin{aligned}
\delta\hat{h}_{xc}(\mathbf{q},\omega) &= \hat{\rho}_{-\mathbf{q}}\delta v^{ALDA}_{\mathbf{q},xc}(\mathbf{r},\omega) + \hat{\rho}_{-\mathbf{q}}\delta u_{\mathbf{q},xc}(\mathbf{r},\omega)\\
&+ \frac{1}{c}\hat{\mathbf{j}}_{-\mathbf{q}}\cdot\delta\mathbf{a}_{\mathbf{q},xc}(\mathbf{r},\omega) + \frac{1}{c}\hat{\mathbf{m}}_{-\mathbf{q}}\cdot\delta\mathbf{b}_{\mathbf{q},xc}(\mathbf{r},t). \qquad (7.28)
\end{aligned}$$

The operators $\hat{\mathbf{j}}_{\mathbf{q}}$ and $\hat{\mathbf{m}}_{\mathbf{q}}$ have been discussed in Sec. (7.2.3). Using Eq. (7.28) the self-consistent linear-response equations (7.4) and (7.5) can be written in the following form,

$$\begin{aligned}
\begin{pmatrix} \delta\rho^{inter}_{\mathbf{q}} \\ i\delta\mathbf{j}^{inter}_{\mathbf{q}}/\omega \\ i\delta\mathbf{m}^{inter}_{\mathbf{q}}/\omega \end{pmatrix} &= \begin{pmatrix} \chi^{inter}_{\rho\rho\mathbf{q}} & -i\chi^{inter}_{\rho\mathbf{jq}}/\omega & -i\chi^{inter}_{\rho\mathbf{mq}}/\omega \\ i\chi^{inter}_{\mathbf{j}\rho\mathbf{q}}/\omega & \Delta\chi^{inter}_{\mathbf{jjq}}/\omega^2 & \Delta\chi^{inter}_{\mathbf{jmq}}/\omega^2 \\ i\chi^{inter}_{\mathbf{m}\rho\mathbf{q}}/\omega & \Delta\chi^{inter}_{\mathbf{mjq}}/\omega^2 & \Delta\chi^{inter}_{\mathbf{mmq}}/\omega^2 \end{pmatrix}\cdot\\
&\quad\begin{pmatrix} \delta v_{\mathbf{q},H,mic} + \delta v^{ALDA}_{\mathbf{q},xc,mic} + \delta u_{\mathbf{q},xc} \\ i\omega(\delta\mathbf{A}_{\mathbf{q},mac} + \delta\mathbf{a}_{\mathbf{q},xc})/c \\ i\omega\delta\mathbf{b}_{\mathbf{q},xc}/c \end{pmatrix}, \qquad (7.29)
\end{aligned}$$

for the interband parts, and as

$$i\omega\begin{pmatrix}\omega/q\delta\rho^{intra}_{\mathbf{q}}\\ \delta\mathbf{j}^{intra}_{\mathbf{q}}\\ \delta\mathbf{m}^{intra}_{\mathbf{q}}\end{pmatrix}=\begin{pmatrix}\omega^2/q^2\chi^{intra}_{\rho\rho\mathbf{q}} & \omega/q\chi^{intra}_{\rho\mathbf{jq}} & \omega/q\chi^{intra}_{\rho\mathbf{mq}}\\ \omega/q\chi^{intra}_{\mathbf{j}\rho\mathbf{q}} & \Delta\chi^{intra}_{\mathbf{jjq}} & \Delta\chi^{intra}_{\mathbf{jmq}}\\ \omega/q\chi^{intra}_{\mathbf{m}\rho\mathbf{q}} & \Delta\chi^{intra}_{\mathbf{mjq}} & \Delta\chi^{intra}_{\mathbf{mmq}}\end{pmatrix}\cdot\begin{pmatrix}iq(\delta v_{\mathbf{q}H,mic}+\delta v^{ALDA}_{\mathbf{q},xc,mic}+\delta u_{\mathbf{q},xc})\\ i\omega(\delta\mathbf{A}_{\mathbf{q},mac}+\delta\mathbf{a}_{\mathbf{q},xc})/c\\ i\omega\delta\mathbf{b}_{\mathbf{q},xc}/c\end{pmatrix}, \qquad (7.30)$$

for the intraband contributions, with $\Delta\chi^{inter/intra}_{\mathbf{abq}}=(\chi^{inter/intra}_{\mathbf{ab}}(\omega)-\chi^{inter/intra}_{\mathbf{ab}}(\omega=0))$. These relations have been written in such a way that all matrix elements are real and finite in the limit $q,\omega\to 0$. The expressions for the response kernels have been given in chapter 3. The new kernels involving the operator $\hat{\mathbf{m}}$ have the same form as those involving the operator $\hat{\mathbf{j}}$, but with the substitution of $\hat{\mathbf{m}}$ for $\hat{\mathbf{j}}$. In the limit of vanishing q the set of equations (7.29) reduces to that one used in the case of nonmetallic crystalline systems [69] for which we need to consider only fully occupied bands i and fully unoccupied bands a. In this limit the term $iq(\delta v_{\mathbf{q}H,mic}+\delta v^{ALDA}_{\mathbf{q},xc,mic}+\delta u_{\mathbf{q},xc})$ on the right-hand side of Eqs (7.30) vanishes [84], thus the intraband contributions to the induced density, current-density, and its curl only depend on the response to the vector potential in the optical limit $q\to 0$. Once the two sets of Eqs (7.29) and (7.30) are solved, we can calculate the macroscopic dielectric function from $\epsilon(\omega)=1+4\pi\chi_e(\omega)$, with $\chi_e(\omega)$ the electric susceptibility, and the electron energy-loss function as $-\Im\{\hat{\mathbf{q}}\cdot\epsilon(\omega)\cdot\hat{\mathbf{q}}\}^{-1}$ in the optical limit $q\to 0$ [84]. In chapter 3 we have shown [84] that within the ALDA and the optical limit the intraband contribution to the dielectric function is real, thus there is no intraband contribution to the absorption spectrum within this approximation. By using the Vignale-Kohn functional it is not possible anymore to separate inter- and intraband contributions to the dielectric function. Inter and intraband processes are coupled through the exchange-correlation potentials $\delta u_{\mathbf{q}xc}$, $\delta\mathbf{a}_{\mathbf{q}xc}$, and $\delta\mathbf{b}_{\mathbf{q}xc}$, which are complex vectors and give rise to the Drude-like tail on the low-frequency side of the absorption spectrum.

7.4 Results

We calculated the optical dielectric functions $\epsilon(\omega)$ and the electron energy-loss functions $-\Im\{\epsilon(\omega)\}^{-1}$ in the spectral range 0-10 eV for the isotropic crystals of copper, silver, and gold in a fcc lattice. We used the experimental lattice constants 3.61 Å for Cu, 4.09 Å for Ag, and 4.08 Å for Au. All calculations were performed using a modified version of the ADF-BAND program [30,31,61–63,84]. We made use of a hybrid valence basis set consisting of Slater-type orbitals (STOs) in combination with the numerical solutions of a free-atom Herman-Skillman program [64]. Cores were kept frozen up to $3p$ for Cu, $4p$ for Ag, and $4f$ for Au. The spatial resolution of this basis is equivalent to a STO triple-zeta basis set augmented with two polarization functions. The Herman-Skillman program also provides us with the free-atom effective potential. The crystal potential was evaluated using an auxiliary basis set of STO functions to fit the deformation density in the ground-state calculation and the induced density in the response calculation. For the evaluation of the k-space integrals we found converged results using a quadratic (linear for the response calculation) numerical integration scheme based on 175 sample points in the irreducible wedge of the Brillouin zone, which was constructed by adopting a Lehmann-Taut tetrahedron scheme [59,60]. In all our ground-state calculations we used the local density approximation (LDA) for the exchange-correlation functional. In the response calculations we employed the Vignale-Kohn functional. All results shown here were obtained using the Vosko-Wilk-Nusair parametrization [65] of the LDA exchange-correlation potential, which was also used to derive the ALDA exchange-correlation kernel, and both the QV and CNT parametrizations for the longitudinal and transverse kernels $f_{xcL/T}(\omega)$ which enter the VK expression. In the QV parametrization we used the

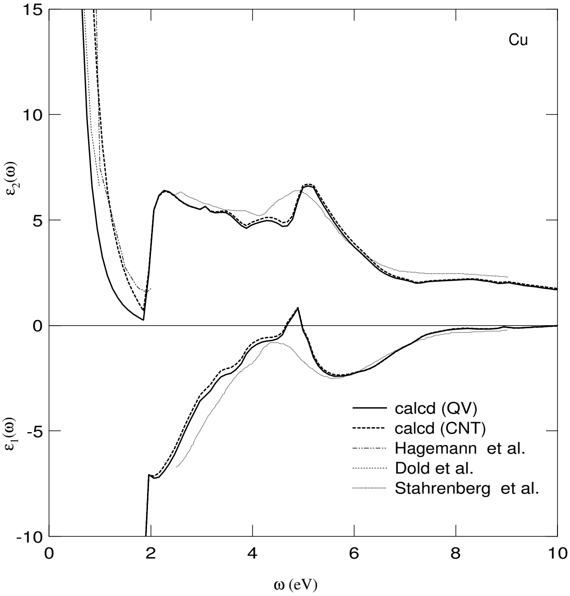

Figure 7.1: The calculated and measured real, $\epsilon_1(\omega)$, and imaginary, $\epsilon_2(\omega)$, parts of the dielectric function of Cu. Experiments are taken from Ref. [52,133,134].

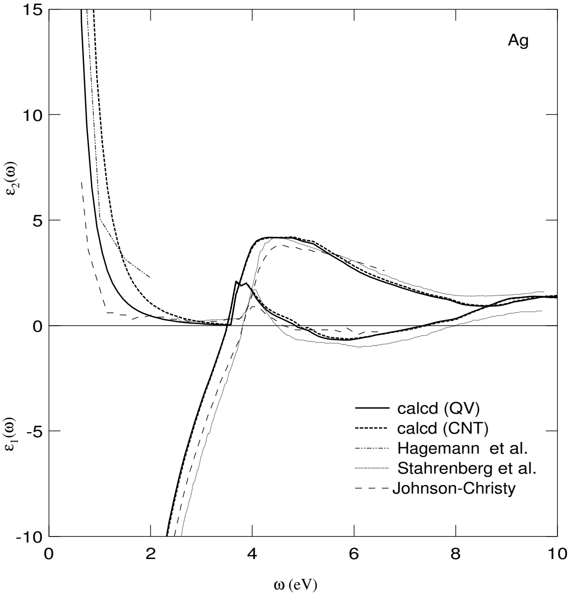

Figure 7.2: The calculated and measured real, $\epsilon_1(\omega)$, and imaginary, $\epsilon_2(\omega)$, parts of the dielectric function of Ag. Experiments are taken from Ref. [51, 52, 133].

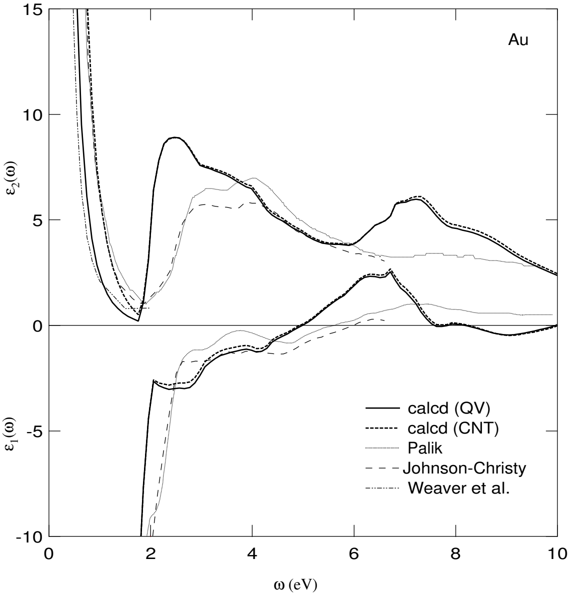

Figure 7.3: The calculated and measured real, $\epsilon_1(\omega)$, and imaginary, $\epsilon_2(\omega)$, parts of the dielectric functions of Au. Experiments are taken from Ref. [51, 70, 135]. The theoretical curves are results of scalar relativistic calculations.

extra constraint $f_{xcT}(\omega = 0) = 0$. In Figs 7.1-7.3 the real and imaginary parts of the dielectric functions of Cu, Ag, and Au are reported. The two parametrizations to the VK functional yield similar results, with the main difference in the Drude-like absorption tail where the two results are roughly 0.25 eV apart. For convenience we do not report the ALDA results [84, 110], which are very close to the VK results for the real part and for the region in the absorption spectra where the interband contribution is dominant. The low-frequency Drude-like absorption is missing in the ALDA absorption spectra, since ALDA is a functional local in time and, therefore, cannot describe electron-electron scattering, which is in part responsible for this absorption. In App. F we analyze the low-frequency behavior of the dielectric function within our method. There we show that if we use the Vignale-Kohn functional with $\mu_{xc} = 0$, then for frequencies higher than a characteristic frequency ω_1, which we defined in the appendix, the real part of the dielectric function diverges as ω^{-2}, whereas the imaginary part should decay as ω^{-3}. For frequencies below ω_1 the real part of the dielectric function is finite and the imaginary part diverges as ω^{-1}. If on the other hand we use the Vignale-Kohn functional with $\mu_{xc} \neq 0$, we obtain the same low-frequency behavior found above with the important difference that for frequencies lower than a characteristic frequency $\omega_0 < \omega_1$, which we defined in the appendix, the imaginary part of the dielectric function will go to zero as ω. Therefore, instead of a Drude-like tail we observe a low-frequency peak around ω_1 in the calculated absorption spectra. The low-frequency behavior obtained by using the Vignale-Kohn functional with $\mu_{xc} = 0$ is compatible with the description of the intraband contribution to the dielectric function within the classical Drude model. Within this simple model the real and imaginary parts of the dielectric functions, $\epsilon_1(\omega)$ and $\epsilon_2(\omega)$, respectively, are given by

$$\epsilon_1^D(\omega) = 1 - \frac{\omega_p^2 \tau^2}{1 + \omega^2 \tau^2}, \tag{7.31}$$

$$\epsilon_2^D(\omega) = \frac{\omega_p^2 \tau}{\omega(1 + \omega^2 \tau^2)}, \tag{7.32}$$

with ω_p the plasma frequency and the τ the relaxation time. The latter is in general frequency-dependent [142–145]. For $\omega\tau \gg 1$, which is true for the near infrared, Eqs. (7.31) and (7.31) become,

$$\epsilon_1^D(\omega) = 1 - \frac{\omega_p^2}{\omega^2}, \tag{7.33}$$

$$\epsilon_2^D(\omega) = \frac{\omega_p^2}{\omega^3 \tau}. \tag{7.34}$$

The real part of the dielectric function scales as ω^{-2}, whereas the imaginary part scales as ω^{-3} for a frequency-independent τ, in agreement with our calculations. For

$\omega\tau \ll 1$, the Drude equations reduce to

$$\epsilon_1^D(\omega) = 1 - \omega_p^2\tau^2, \tag{7.35}$$

$$\epsilon_2^D(\omega) = \frac{\omega_p^2\tau}{\omega}. \tag{7.36}$$

Again we find a qualitative agreement between the Drude description and our model: a finite real part and an imaginary part which diverges as ω^{-1}. It is important to note that in our calculations we only take into account relaxation processes due to electron-electron scattering, whereas the Drude model also describes relaxation processes due to other phenomena such as electron-phonon scattering. However, the analysis given above does not depend on the precise value of τ. Our results are also in good agreement with the experimental results although the spectra obtained for gold show some discrepancies, especially the first peak in the absorption spectrum is not well described. The Drude-like tail in the absorption spectra seems to be well

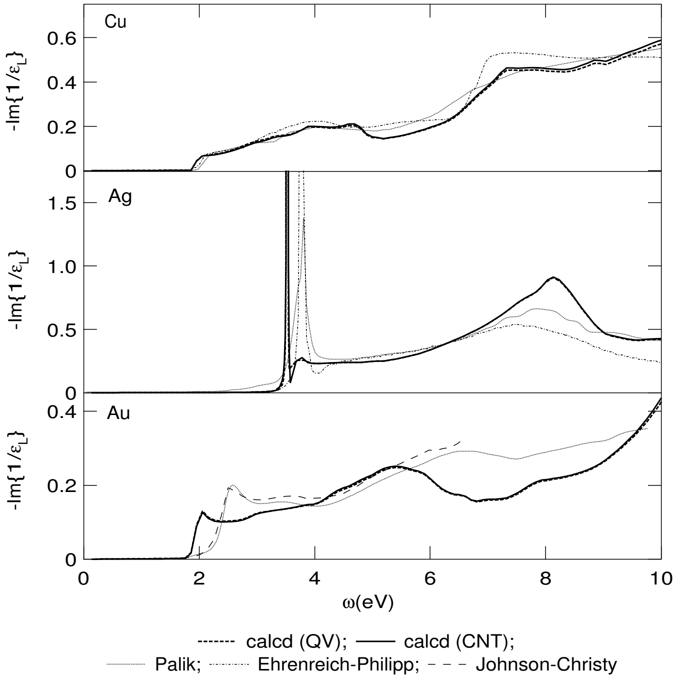

Figure 7.4: Electron energy-loss spectra of copper, silver, and gold. The experimental results are taken from Ref. [50, 51, 70]. The calculated results reported for Au refer to scalar relativistic calculations.

described for all the three materials. However, since we only consider relaxation processes due to electron-electron scattering and not those due to electron-phonon scattering, our results should be below the experimental ones. We therefore expect that the results we obtain for the Drude-like tail using the VK functional with the QV parametrization are the closest to the exact Drude-like tail due to electron-electron scattering only.

In Fig. 7.4 we have reported the electron energy-loss spectra (EELS) of the three metals. The EELS of the Cu and Ag are already well described within the ALDA [84], with one notable discrepancy: this approximation fails to reproduce the finite width of the sharp plasmon peak at about 3.8 eV in the electron energy-loss spectrum of silver [50, 70]. This feature is well described by the VK functional with both the QV and CNT parametrizations for $f_{xcL,T}(\omega)$. The appearance of this peak is due to the fact that now there is a small but non vanishing imaginary part in the dielectric function at the frequency where the real part crosses the zero axes. Also for gold the VK performs very similar to ALDA and with a good agreement with the experiments by using both the parametrizations. For convenience we do not report the ALDA results. Note that for Au we have obtained the experimental electron energy-loss spectra from optical measurements.

7.5 Conclusions

In this chapter we have included the Vignale-Kohn expression for the the exchange-correlation vector potential in our formulation of the linear response of metals within the time-dependent current-density approach. This functional is nonlocal in time and therefore relaxation effects due to electron-electron scattering can be taken into account. The evaluation of the VK functional requires the knowledge of the exchange-correlation kernels of the homogeneous electron gas $f_{xcL,T}(\rho_0, \omega)$ as a function of the density and of the frequency. We have used in this chapter two existing parametrizations of these xc kernels: that one proposed by Qian and Vignale (QV) and the other one by Conti, Nifosì, and Tosi (CNT). In the optical limit $q \to 0$ and by using the VK functional the two sets of equations describing the inter- and intraband contributions to the response are coupled. We have calculated the dielectric and electron energy-loss functions of copper, silver, and gold and we have compared them with measurements reported in literature and with our previous calculations within the adiabatic local density approximation. The VK functional yields results which are in good agreement with the experiments. The real parts of the dielectric functions and the regions in the absorption spectra where the interband processes are dominant are similarly described by the two approximations and are close to previous results obtained within the ALDA. In addition the VK functional reproduces the low-frequency Drude-like tail in the absorption spectra, which was missing in the previous ALDA calculations. The electron energy-loss spectra obtained with the VK functional are close to the spectra obtained within the ALDA with a notable difference in the case of silver: whereas the first sharp plasmon peak found in the experimental EELS was absent in the ALDA spectrum, this feature is well described in the spectrum obtained with the VK functional.

Chapter 8

Effect of the Spin-Orbit Coupling on the Linear Response of Solids

In this chapter we incorporate the ZORA equations (describing both scalar and spin-orbit relativistic effects) developed in chapter 4 in the formulation of the linear response of solids within TDCDFT. We obtain a spin-dependent version of the linear response formalism, which makes possible its further extension to the response to magnetic fields as well. As immediate application we can include the treatment of spin-orbit coupling in the optical property calculations. We test the method on metallic and nonmetallic systems. First we present the ZORA results for the dielectric functions of Au and W. With the treatment of the spin-orbit coupling new spectral features appear that are missing in the scalar ZORA spectra of these two metals, and that are in agreement with the experiment and with our speculations in chapters 5 and 6. Then we study the linear response of the zincblende semiconductors ZnTe, CdTe, and semimetal HgTe. We compare nonrelativistic, scalar ZORA, and ZORA relativistic results to show the impact of the scalar and spin-orbit effects on the spectra. Comparison of our ZORA results with experimental data shows an overall good agreement.

8.1 Introduction

In chapters 5, 6, and 7 we included the treatment of scalar relativistic effects in the linear response of heavy metals within the zeroth-order regular approximation [93, 95, 110]. Although the scalar relativistic effects induced major corrections in the spectra [110, 146], some important features were still missing due to the neglect of spin-orbit coupling. For example, in the group VB and VIB bcc transition metals we have seen that the treatment of spin-orbit coupling is expected to yield an onset in the interband contribution to the absorption spectrum, while in the scalar relativistic calculations a constant absorption results at low frequency, even close to $\hbar\omega = 0$ [146]. In this chapter we will take into account also the effect of spin-orbit coupling in the linear response of extended systems, following our derivation given in chapter 4. Besides this immediate application, the inclusion of the spin in the formulation of the linear response of solids is a first step for the treatment of the magnetic response. Indeed, the spin-dependent Hamiltonian, which governs the linear perturbation of the Kohn-Sham ground state, contains the coupling between a spin-density operator and the magnetic field. At present we do not treat the response to magnetic fields. We give the ZORA equations, comprising both the dominant scalar relativistic effects and spin-orbit coupling, which we solve in the ground-state and in the liner response calculations. The response functions, which depend only on the ground-state orbitals and orbital energies, are to be changed in order to consider two-component spinors. To test our method we first calculate the ZORA dielectric functions of Au and W. As discussed in more detail in chapters 5 and 6, these two metals are expected to show visible changes in the spectra upon the inclusion of spin-orbit coupling in the ground-state and response calculations. Indeed the ZORA calculations show a smooth onset and a better visible second peak in the absorption of Au, and an onset with a sharp peak at about 0.46 eV in the absorption of W, in good agreement with the experimental data and with our predictions. We further apply the method to the most common II-VI semiconductors ZnTe and CdTe, and semimetal HgTe in the zincblende structure. These compounds have been extensively studied both experimentally and theoretically [147–157]. Their electronic structure is characterized by a moderately narrow ($\lesssim$1 eV), fully occupied metal d band-complex inside the valence bands around 7-11 eV below the Fermi level, which are visible in the photoemission spectra of all II-VI semiconductors [158–160]. The highest-lying d bands play an important role in the electronic structure and optical properties of these materials. In particular they affect the fundamental band gap by mixing with the p-like states at the top of the valence band, resulting in wide and medium energy-gaps of 2.39 eV and 1.59 eV for ZnTe and CdTe, respectively [156]. Magnetoreflection data provide strong evidence that HgTe is a zero-gap semimetal with inverted band-stucture at Γ point, i.e., an inverted order of the bands at Γ_6 (s-like) and Γ_8 (p-like) with a resulting negative energy-gap of -0.30 eV [156], unlike ZnTe, CdTe, and most other zinc-blende compounds [147]. Spin-orbit coupling has a strong impact on the electronic structure, and thus on the optical spectra, of these compounds. Splittings appear at the top valence bands and for the *sp*-like conduction bands at Γ, L, and X high-symmetry points. The experimental observation of such splittings, usually as double peaks in the optical spectra, has been very useful in the assignement of the optical spectra in terms of interband transitions [161]. We show the importance of scalar and spin-orbit relativistic effects on the ground-state band structures as well as on the optical properties of the three compounds. While the first two compounds are described as semiconductors both in nonrelativistic and relativistic calculations, HgTe appears as semiconductors in nonrelativistic calculations, but as semimetals in a relativistic description. The changes in the electronic structures due to the inclusion of relativity has a drastic effect on the dielectric constant and dielectric function of HgTe. In the frequency range 0-10 eV we find an overall good agreement between the ZORA results and experiments reported in literature. First we give the main ZORA equations discussed in chapter 4, which can be used to include relativistic effects in the linear response of solids within TDCDFT. Next we present our results for the dielectric functions of Au and W, and for the band structures, the dielectric constants, and the dielectric functions of ZnTe, CdTe, and HgTe, and compare these with available experimental data.

8.2 Theory

We combine the ZORA formalism (comprising both scalar and spin-orbit relativistic effects) with the time-dependent current-density formulation of the linear response of solids to a macroscopic field. The first-order perturbation of the ground state of a Kohn-Sham system described by the ZORA equation

$$H^{ZORA}\Psi_{i\mathbf{k}}(\mathbf{r}) = \left[v_{\mathit{eff},0}(\mathbf{r}) + \boldsymbol{\sigma}\cdot\mathbf{p}\frac{c^2}{2c^2 - v_{\mathit{eff},0}(\mathbf{r})}\boldsymbol{\sigma}\cdot\mathbf{p}\right]\Psi_{i\mathbf{k}}(\mathbf{r}), \tag{8.1}$$

is governed by the perturbation

$$\begin{aligned} \delta\hat{h}(\mathbf{r},t) &= \int \Big(\hat{\rho}(\mathbf{r}')\delta v_{\mathit{eff}}(\mathbf{r}',t) + \frac{1}{c}\hat{\mathbf{j}}_p(\mathbf{r}')\cdot\delta\mathbf{A}_{\mathit{eff}}(\mathbf{r}',t) \\ &+ \frac{1}{c}K(\mathbf{r}')\nabla\times\hat{\mathbf{s}}(\mathbf{r}')\cdot\delta\mathbf{A}_{\mathit{eff}}(\mathbf{r}',t)\Big)d\mathbf{r}', \end{aligned} \tag{8.2}$$

where,

$$\hat{\rho}(\mathbf{r}') = \delta(\mathbf{r}-\mathbf{r}'), \tag{8.3}$$

$$\hat{\mathbf{j}}_p(\mathbf{r}') = -\frac{i}{2}\left[\hat{\rho}(\mathbf{r}')K(\mathbf{r}')\nabla - \nabla^{\dagger}K(\mathbf{r}')\hat{\rho}(\mathbf{r}')\right], \tag{8.4}$$

$$\hat{\mathbf{s}}(\mathbf{r}') = \frac{1}{2}\hat{\rho}(\mathbf{r}')\boldsymbol{\sigma}. \tag{8.5}$$

Here c is the velocity of light, $v_{\mathit{eff},0}(\mathbf{r})$ is the ground-state self-consistent effective potential, $\boldsymbol{\sigma}$ is the vector of Pauli matrices, and $K(\mathbf{r}) = (1 - v_{\mathit{eff},0}(\mathbf{r})/2c^2)^{-1}$. One can then calculate the linear response of the system to this perturbation by solving self-consistently the sets of equations describing the induced density and induced current-density. These two quantities are expressed in terms of q-dependent Kohn-Sham response functions, which only depend on the ground-state orbitals, orbital energies, and occupations numbers,

$$\chi_{ab\mathbf{q}}(\mathbf{r},\mathbf{r}',\omega) = \frac{1}{N_k}\sum_{\mathbf{k}}\sum_{ia}\frac{(f_{i\mathbf{k}} - f_{a\mathbf{k}+\mathbf{q}})}{1+\delta_{i,a}} \times \\ \frac{\langle\Psi^*_{i\mathbf{k}}|\hat{a}_{\mathbf{q}}(\mathbf{r})|\Psi_{a\mathbf{k}+\mathbf{q}}\rangle\,\langle\Psi^*_{a\mathbf{k}+\mathbf{q}}|\hat{b}_{-\mathbf{q}}(\mathbf{r}')|\Psi_{i\mathbf{k}}\rangle}{\epsilon_{i\mathbf{k}} - \epsilon_{a\mathbf{k}+\mathbf{q}} + \omega + i\eta} + c.c.(-\mathbf{q},-\omega), \quad (8.6)$$

where the summation is over the (partially) occupied bands i, with occupation number $f_{i\mathbf{k}} = 1$, and the unoccupied bands a, with occupation number $f_{i\mathbf{k}} = 0$. The operators $\hat{a}_{\mathbf{q}}(\mathbf{r})$ and $\hat{b}_{\mathbf{q}}(\mathbf{r})$ can be either $\hat{\rho}_{\mathbf{q}}(\mathbf{r}) = e^{-i\mathbf{q}\cdot\mathbf{r}}\hat{\rho}(\mathbf{r})$ or $\hat{\mathbf{j}}_{\mathbf{q}}(\mathbf{r}) = \hat{\mathbf{j}}_{p\mathbf{q}}(\mathbf{r}) + e^{-i\mathbf{q}\cdot\mathbf{r}}K(\mathbf{r})\nabla\times\hat{\mathbf{s}}(\mathbf{r})$, with $\hat{\mathbf{j}}_{p\mathbf{q}}(\mathbf{r}) = -i\left(\hat{\rho}_{\mathbf{q}}(\mathbf{r})K(\mathbf{r})\nabla - \nabla^{\dagger}K(\mathbf{r})\hat{\rho}_{\mathbf{q}}(\mathbf{r})\right)/2$. The Bloch orbitals $\Psi_{i\mathbf{k}}(\mathbf{r})$ are now two-component spinors and are solutions of the ground-state ZORA equation (8.1). Note that for scalar relativistic calculations the ground-state Hamiltonian in Eq. (8.1) does not contain the Pauli vector $\boldsymbol{\sigma}$, and the perturbation (8.2) does not contain the last term on the right-hand side. Furthermore, in the response functions (8.6) the Bloch orbitals are scalar functions, and the occupation numbers are $f_{i\mathbf{k}} = 2$ for occupied bands and $f_{a\mathbf{k}} = 0$ for unoccupied bands.

From the macroscopic induced current one can calculate the macroscopic dielectric function, which (at a wavevector $\mathbf{q} = \mathbf{0}$ and in the adiabatic local density approximation) can be defined as [84]

$$\epsilon(\omega) = (1 + 4\pi\chi_e^{inter}(\omega)) - \frac{4\pi i}{\omega}\sigma^{intra}(\omega). \quad (8.7)$$

Here the term in bracket on the right-hand side represents the interband contribution to the dielectric function, while the other term is the intraband contribution. The former is due to transitions between occupied and unoccupied bands, while the latter is due to transitions within the same partially occupied bands. Clearly, these last transitions are not possible in nonmetallic systems, which are characterized by bands that are either fully occupied or fully unoccupied.

8.3 Results and discussion

8.3.1 Computational details

We performed ZORA calculations of the dielectric functions of Au and W in the spectral range 0-10 eV. We used the experimental lattice constants 4.08 Å for Au in a fcc lattice, and 3.16 Å for W in a bcc lattice. Furthermore, we calculated the ground-state band structures and the optical dielectric functions $\epsilon(\omega)$ in the spectral range 0-10 eV for the isotropic crystals of ZnTe, CdTe, and HgTe in a zincblebde lattice. We used the experimental lattice constants 6.09 Å for ZnTe, 6.48 Å for CdTe, and 6.08 Å for HgTe. All calculations were performed using a modified version of the ADF-BAND program [30, 31, 61–63, 84]. We checked that our results were converged with respect to the basis set size and the sampling density of the irreducible Brillouin zone. We made use of a hybrid valence basis set consisting of Slater-type orbitals (STOs) in combination with the numerical solutions of a free-atom Herman-Skillman program [64]. Cores were kept frozen up to $3p$ for Zn, $4p$ for Cd and Te, and $4f$ for Hg, Au, and W. The spatial resolution of this basis is equivalent to a STO triple-zeta basis set augmented with two polarization functions. The Herman-Skillman program also provides us with the free-atom effective potential. The crystal potential was evaluated using an auxiliary basis set of STO functions to fit the deformation density in the ground-state calculation and the induced density in the response calculation. For the evaluation of the k-space integrals we used a quadratic (linear in the response calculations) numerical integration scheme, which was constructed by adopting a Lehmann-Taut tetrahedron method [59, 60]. We found converged results using 175 sample points in the irreducible wedge of the Brillouin zone for Au, W, ZnTe, and for CdTe and HgTe in the nonrelativistic calculations. Relativistic calculation results for W in the frequency range 0-3 eV converged using 1771 sample points, and for CdTe and HgTe using 1695 sample points. All the dielectric constants were obtained by using 1695 sample points. In all our ground-state calculations we used the Vosko-Wilk-Nusair parametrization [65] of the LDA exchange-correlation potential, which was also used to derive the ALDA exchange-correlation kernel for the response calculations.

8.3.2 Metals: spin-orbit effects

The electronic band structures and optical properties of Au and W have been analyzed in detail in chapters 5 and 6, respectively. In particular, in those chapters, we have discussed the effect of the scalar relativistic corrections in the linear response of the two metals. Some deviations from experiments have been attributed to the neglect of the spin-orbit coupling in the response calculations. Analysis of the band structure

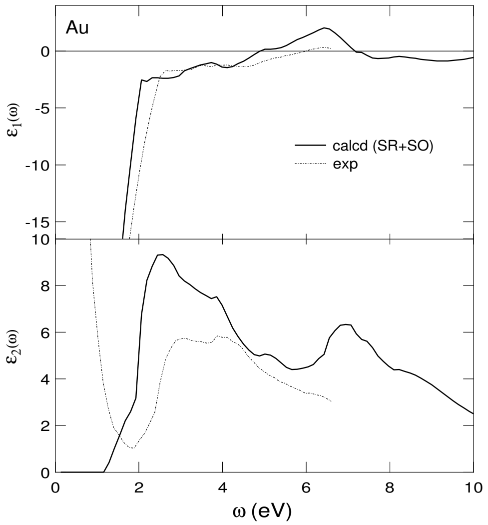

Figure 8.1: Real (upper graph) and imaginary (lower graph) parts of the dielectric function of Au. The ZORA relativistic calculations (bold solid lines) are compared with experimental results (dotted-dashed lines) taken from Ref. [51].

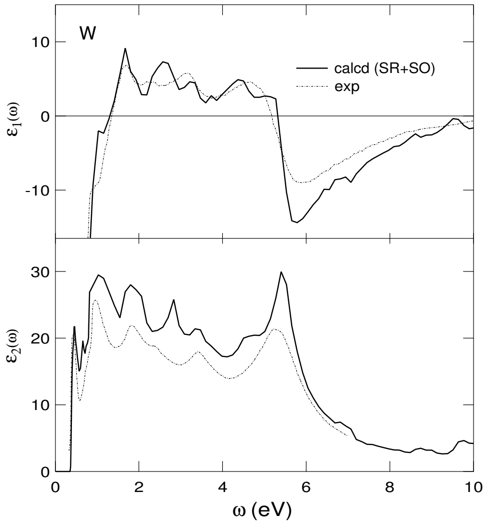

Figure 8.2: Real (upper graph) and imaginary (lower graph) parts of the dielectric function of W. The ZORA relativistic calculations (bold solid lines) are compared with experimental results (dotted-dashed lines) taken from Ref. [106]. To show the peak at 0.42 eV in the experimental absorption we have reported only the interband contribution to the absorption, as extrapolated from experiments in Ref. [106].

calculated by including scalar and spin-orbit coupling effects, and assignment of the spectral features in terms of pairs of bands suggested an improvement in the low-frequency onset of the interband transitions and second main peak in the absorption of Au, and the appearance of a finite onset and a peak around 0.60 eV in W with the inclusion of the spin-orbit coupling in the response calculations. Here we present the results of the dielectric functions of Au and W calculated by including scalar and spin-orbit effects both in the ground-state and response calculations. Inspection of Figs 8.1 and 8.2 confirm our previous speculations, and show a good agreement with the experiments. Note that in Fig. 8.2 we report the experimental interband absorption of W, as extrapolated by Weaver *et al.* by their experiments [106], in order to show the onset and peak at 0.42 eV.

8.3.3 Nonmetals: band structures and dielectric functions

In Figs 8.3, 8.4, and 8.5 we report the ground-state band structures of ZnTe, CdTe, and HgTe, respectively. Each figure comprises results from nonrelativistic, scalar ZORA relativistic, and ZORA relativistic calculations. In order to facilitate the comparison among the three band structures, the energy levels are reported with respect

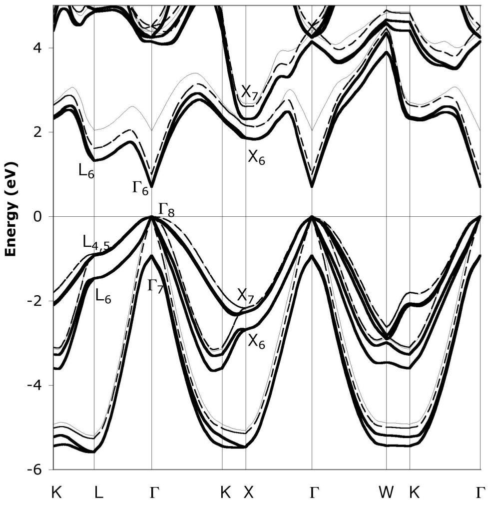

Figure 8.3: Theoretical LDA ground-state band structures of ZnTe. The thin dotted lines refer to nonrelativistic calculations, the dashed lines refer to scalar ZORA relativistic calculations, and the bold solid lines refer to ZORA relativistic calculations.

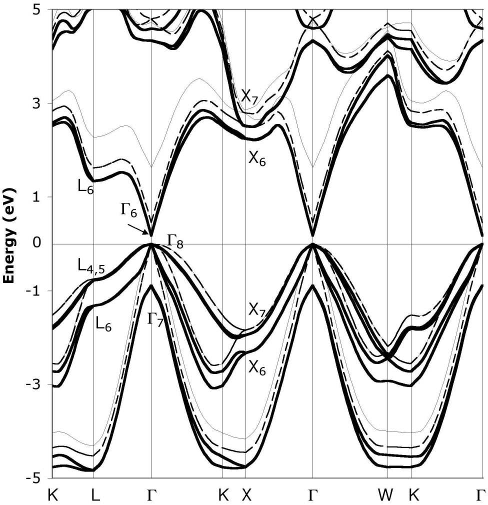

Figure 8.4: Theoretical LDA ground-state band structures of CdTe. The thin dotted lines refer to nonrelativistic calculations, the dashed lines refer to scalar ZORA relativistic calculations, and the bold solid lines refer to ZORA relativistic calculations

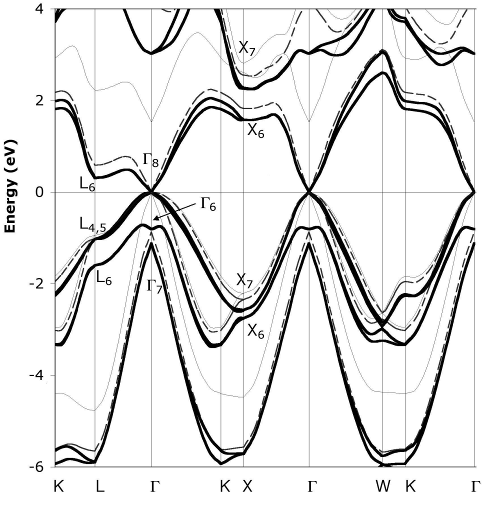

Figure 8.5: Theoretical LDA ground-state band structures of HgTe. The thin dotted lines refer to nonrelativistic calculations, the dashed lines refer to scalar ZORA relativistic calculations, and the bold solid lines refer to ZORA relativistic calculations

to the respective Fermi levels. The valence and conduction bands are numbered at a given k point starting from the lowest band. Some particular states at various high-symmetry points are labeled according to the respective double group representations. The d-band complexes, which for simplicity we have not reported in the figures, are located around 6-9 eV below the Fermi energy, and are almost dispersionless. As expected, scalar relativistic effects shift the band energies with respect to the non-relativistic results. In ZnTe and CdTe the dispersion of the valence and conduction bands is similar both in nonrelativistic and scalar relativistic band structures, thus nonrelativistic and scalar relativistic optical spectra can be expected to differ only in the energy position of the main spectral features. In HgTe relativistic effects induce drastic changes in the electronic structure and, thus, in the optical properties: already the inclusion of scalar relativistic effects changes the character of this compound from semiconductor, as appears to be in nonrelativistic calculations, to semimetal with an inverted band order. Indeed, the s-like (6s Hg) states at Γ_{1v} (Γ_6 in the double group representation) are stabilized more than the p-like (5p Te) states at Γ_{15v} (Γ_8 in the double group representation), resulting in a vanishing band gap and an inversion of the typical band order [162]. The inclusion of spin-orbit coupling leads in particular

Table 8.1: Calculated energy gaps (eV), centers of the d-band energies ϵ_d (eV), and spin-orbit splittings (eV) of valence bands at Γ (Δ_0) and L (Δ_1) for ZnTe, CdTe, and HgTe. The experiments are taken from Ref. [156].

		NR	SR	SR+SO	Exp[a]
ZnTe	Γ_8-Γ_6	2.03	0.99	0.71	2.39
	ϵ_d	-7.21	-6.97	-7.29	-9.84
	Δ_0			0.93	0.91
	Δ_1			0.54	0.53
CdTe	Γ_8-Γ_6	1.62	0.45	0.18	1.59
	ϵ_d	-8.45	-8.06	-8.49	-10.49
	Δ_0			0.89	0.90
	Δ_1			0.54	0.54
HgTe	Γ_8-Γ_6	1.52	-0.88	-0.81	-0.30
	ϵ_d	-8.15	-6.84	-6.56	-8.58
	Δ_0			1.12	1.08
	Δ_1			0.57	0.62

---

[a] data taken from Ref. [156].

to a splitting of the states at L_{3v} point (in the single group representation), as well as along the line Γ_{15v}-L_{3v}, in L_6 and $L_{4,5}$ (in the double group representations), at Γ_{15v} point in Γ_7 and Γ_8, and at X_{5v} point in X_6 and X_7. Some of these splittings are well visible in the optical spectra as we will shortly show. In table 8.1 we compare nonrelativistic, scalar ZORA, and ZORA band gaps, centers of the d-band energies ϵ_d, and spin-orbit splittings at Γ_{15v} and L_{3v} with the observed values collected in Ref. [156] for ZnTe, CdTe, and HgTe. Inspection of this table reveals the well-known underestimation of the band gap in semiconductors by using the local density approximation. The inclusion of relativity decreases even more the band gap. In HgTe

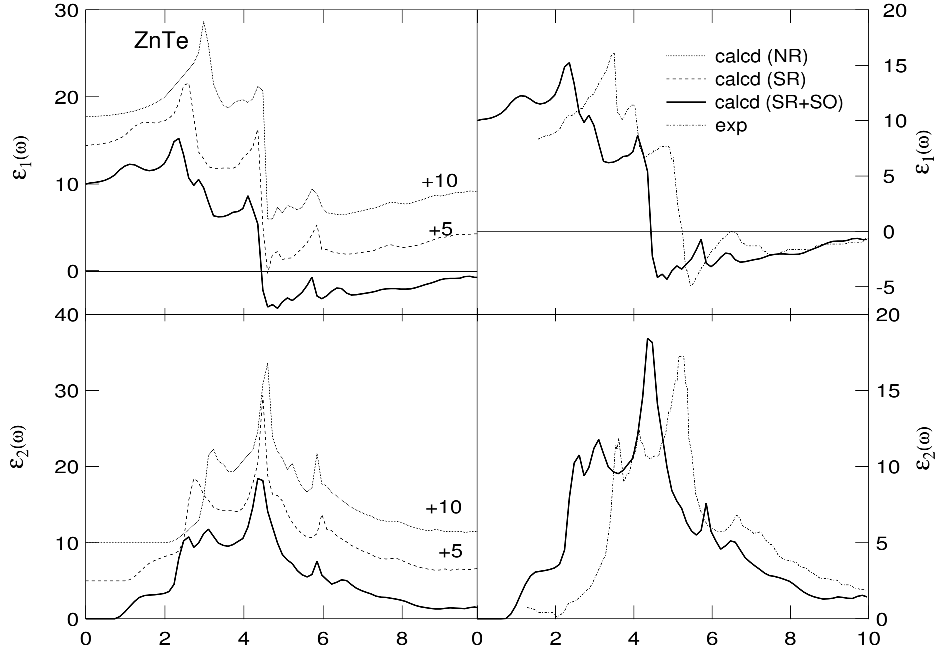

Figure 8.6: Real (upper graph) and imaginary (lower graph) parts of the dielectric function of ZnTe. In the left panel we compare nonrelativistic calculations (thin lines), scalar ZORA relativistic calculations (dashed lines), and ZORA relativistic calculations (bold lines). To facilitate the comparison we have rigidly shifhed upwards nonrelativistic ($\epsilon(\omega) + 10$) and scalar relativistic ($\epsilon(\omega) + 5$) curves. In the right panel we compare the ZORA relativistic calculations with the experiments (dotted-dashed lines) from Ref. [163].

relativity is essential to describe the negative band gap, which is, however, overestimated in the calculations with respect to the observed value. The energies of the d-band complexes improve with the inclusion of scalar and spin-orbit relativistic effects in ZnTe and CdTe, whereas in HgTe the nonrelativistic results are the closest to the experiments. However, in the calculations the d-band complexes are less bound than the observed ones. This has already been observed in previous calculations on gold and bcc metals from the groups VB and VIB [110, 146], and it is a failure of the local density approximation. The main important splittings are well reproduced in our calculations. In Figs 8.6-8.8 we report the calculated and measured [149, 163] real

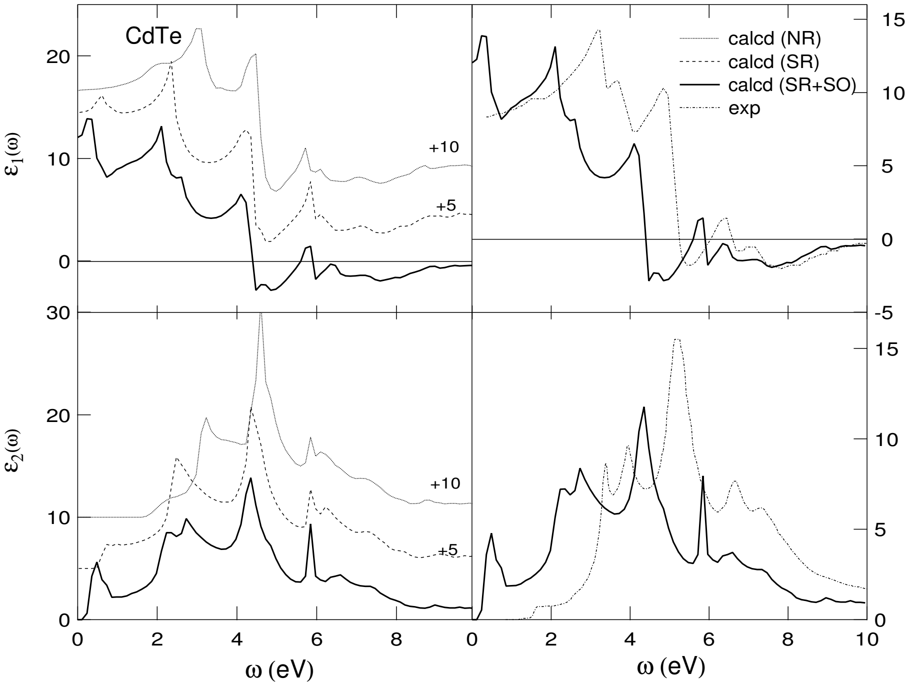

Figure 8.7: Real (upper graph) and imaginary (lower graph) parts of the dielectric function of CdTe. In the left panel we compare nonrelativistic calculations (thin lines), scalar ZORA relativistic calculations (dashed lines), and ZORA relativistic calculations (bold lines). To facilitate the comparison we have rigidly shifhed upwards nonrelativistic ($\epsilon(\omega) + 10$) and scalar relativistic ($\epsilon(\omega) + 5$) curves. In the right panel we compare the ZORA relativistic calculations with the experiments (dotted-dashed lines) from Ref. [163].

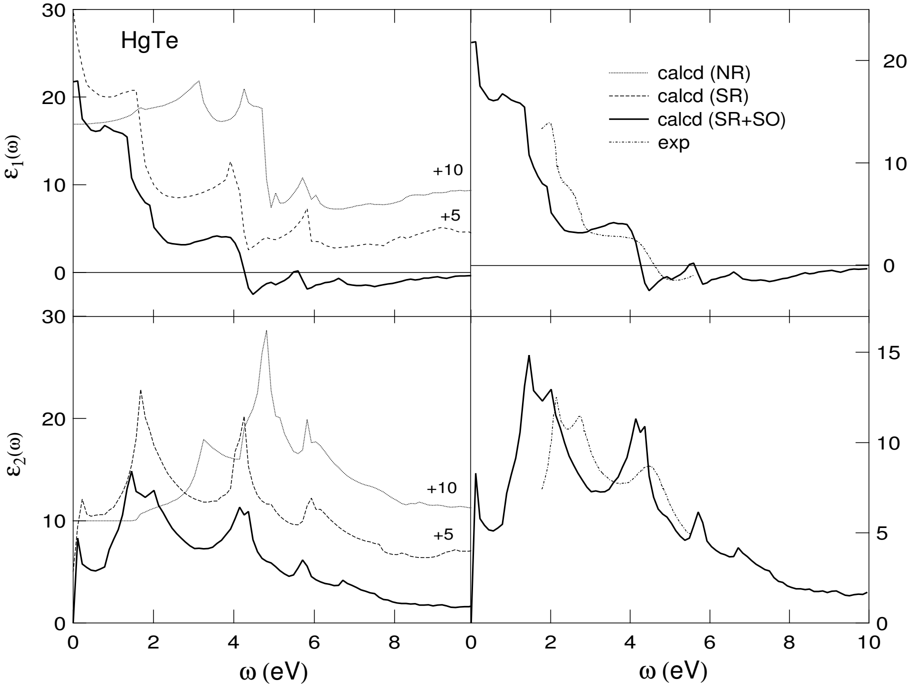

Figure 8.8: Real (upper graph) and imaginary (lower graph) parts of the dielectric function of HgTe. In the left panel we compare nonrelativistic calculations (thin lines), scalar ZORA relativistic calculations (dashed lines), and ZORA relativistic calculations (bold lines). To facilitate the comparison we have rigidly shifhed upwards nonrelativistic ($\epsilon(\omega) + 10$) and scalar relativistic ($\epsilon(\omega) + 5$) curves. In the right panel we compare the ZORA relativistic calculations with the experiments (dotted-dashed lines) from Ref. [149].

and imaginary parts of the dielectric function for the three compounds. The nonrelativistic, scalar ZORA, and ZORA spectra of ZnTe and CdTe are red-shifted by about 0.6-0.9 eV with respect to the experimental curves. Note that there is not a direct relation between the shift of the optical spectra and the error in the calculated band gaps, in line with previous findings [31,93]. In particular the ZORA spectra of CdTe show a low-frequency peak, whose high intensity is due to the too low frequencies at which it occurs. The spectra of HgTe reflect the strong impact of relativity on the electronic-structure: in particular, the relativistic absorption spectra show the onset at $\hbar\omega$=0 eV, while the nonrelativistic one shows the onset at a finite frequency and is quite different from the experiments. In the ZORA spectra all the main spectral features are present and well described in intensity, although they are red-shifted with respect to the experimental curves by ~ 1 eV. The same red-shift is also present in the scalar ZORA spectra. A striking feature common to the ZORA spectra is the doublet at about 2.7 eV for ZnTe, 2.5 eV for CdTe, and 1.7 eV for HgTe. This is mainly due to transitions between bands $5, 6 \rightarrow 7, 8$ and $3, 4 \rightarrow 7, 8$, expected to occur at the L point and along the Γ-L line [148–150]. Transitions $5, 6 \rightarrow 9, 10$ and $3, 4 \rightarrow 9, 10$ are responsible for the absorptions around 6 eV. The remaining main peak at about 4-5 eV is mainly due to transitions $5, 6 \rightarrow 7, 8$, which are expected to occur at or close the X point [148–150]. The calculated and measured [164] dielectric constants are reported in table 8.2. We find that in the two semiconductors the nonrelativistic results are in better agreement with the experiments than the relativistic ones. Scalar-ZORA and ZORA calculations overestimate the dielectric constants. For HgTe, instead, we find a strong improvement of the calculated dielectric constant if the relativity is included.

Table 8.2: Nonrelativistic, scalar ZORA relativistic, and ZORA relativistic dielectric constants (eV) calculated for ZnTe, CdTe, and HgTe. The experiments are taken from Ref. [164].

	ZnTe	CdTe	HgTe
NR	7.71	6.62	6.90
SR	9.21	9.48	24.80
SR+SO	9.49	12.04	21.60
Exp [a]	7.3	7.2	21.0

---

[a] dielectric constants taken from Ref. [164]

8.4 Conclusions

In this chapter we have proposed a spin-dependent version of the formulation of the linear response of solids within TDCDFT. The final goal of this extension is a future treatment of magnetic response as well. Here we have used the method to include the spin-orbit coupling, beside the dominant scalar relativistic effects, within the zeroth-order regular approximation in linear response calculations. We have shown that our method performs well for both metallic and nonmetallic systems. The calculated ZORA spectra of Au and W show the predicted spectral features which were missing in the scalar ZORA calculations discussed in chapter 5 and 6: a smooth onset of the interband transitions and a more visible second peak in the absorption spectrum of Au, and a sharp onset with peak at about 0.46 eV in the absorption spectrum of W, in agreement with the experiments. We further analyzed the impact of the relativity in the ground-state and response calculations, in particular the additional changes induced by the spin-orbit coupling with respect to the scalar relativistic results, of the semiconductors ZnTe, CdTe, and the semimetal HgTe. The main splittings of states in the band structures and in the spectral features are very well described. The local density approximation used in the ground-state calculations underestimates the band gap due to s- and p-like bands in ZnTe and CdTe. Scalar-relativistic corrections make this worse, which becomes evident in the bad results for the static dielectric constants. Relativity is, instead, essential in the case of HgTe, where the ZORA results are in good agreement with experiments.

Appendix A

Symmetry of the Response Functions

We consider a crystalline system perturbed by a potential $\delta\hat{\mathbf{h}}(\mathbf{r},\omega)$ with a periodicity that is consistent with the Born-von Kármán boundary condition. Using linear response theory and the following transformation for the perturbation, $\delta\hat{\mathbf{h}}(\mathbf{r}'+\mathbf{R},\omega) = e^{i\mathbf{q}\cdot\mathbf{R}}\delta\hat{\mathbf{h}}(\mathbf{r},\omega)$, the first order change in the density is given by

$$\delta\rho(\mathbf{r},\omega) = e^{i\mathbf{q}\cdot\mathbf{r}}\delta\rho_{\mathbf{q}}(\mathbf{r},\omega), \tag{A.1}$$

in which the lattice periodic $\delta\rho_{\mathbf{q}}(\mathbf{r}+\mathbf{R},\omega) = \delta\rho_{\mathbf{q}}(\mathbf{r},\omega)$ is given by

$$\begin{aligned} \delta\rho_{\mathbf{q}}(\mathbf{r},\omega) &= \frac{1}{N_k}\sum_{\mathbf{k},\mathbf{k}'}\sum_{n,n'}\delta_{\mathbf{k}',\mathbf{k}+\mathbf{q}}(f_{n\mathbf{k}} - f_{n'\mathbf{k}'}) \times \\ & \quad \frac{\psi^*_{n\mathbf{k}}(\mathbf{r})e^{-i\mathbf{q}\cdot\mathbf{r}}\psi_{n'\mathbf{k}'}(\mathbf{r})\langle\psi_{n'\mathbf{k}'}|\delta\hat{h}(\mathbf{q},\omega)|\psi_{n\mathbf{k}}\rangle}{\epsilon_{n\mathbf{k}} - \epsilon_{n'\mathbf{k}'} + \omega + i\eta}. \end{aligned} \tag{A.2}$$

Here η is an infinitesimal quantity. In the following we will use the perturbation given in Eq. (3.16) and consider the time-reversal symmetry. Since only combinations of (partially) occupied, i, and (partially) unoccupied, a, orbitals contribute, we can write

$$\begin{aligned}
\delta\rho_{\mathbf{q}}(\mathbf{r},\omega) &= \frac{1}{N_k}\sum_{\mathbf{k},\mathbf{k}'}\delta_{\mathbf{k}',\mathbf{k}+\mathbf{q}}\sum_{i,a}\frac{(f_{i\mathbf{k}}-f_{a\mathbf{k}'})}{1+\delta_{ia}}\times \\
&\quad \frac{\psi^*_{i\mathbf{k}}(\mathbf{r})e^{-i\mathbf{q}\cdot\mathbf{r}}\psi_{a\mathbf{k}'}(\mathbf{r})\langle\psi_{a\mathbf{k}'}|\delta\hat{h}(\mathbf{q},\omega)|\psi_{i\mathbf{k}}\rangle}{\epsilon_{i\mathbf{k}}-\epsilon_{a\mathbf{k}'}+\omega+i\eta} \\
&+ \frac{1}{N_k}\sum_{\mathbf{k},\mathbf{k}'}\delta_{\mathbf{k}',\mathbf{k}-\mathbf{q}}\sum_{i,a}\frac{(f_{a\mathbf{k}'}-f_{i\mathbf{k}})}{1+\delta_{ia}}\times \\
&\quad \frac{\psi^*_{a\mathbf{k}'}(\mathbf{r})e^{-i\mathbf{q}\cdot\mathbf{r}}\psi_{i\mathbf{k}}(\mathbf{r})\langle\psi_{i\mathbf{k}}|\delta\hat{h}(\mathbf{q},\omega)|\psi_{a\mathbf{k}'}\rangle}{\epsilon_{a\mathbf{k}'}-\epsilon_{i\mathbf{k}}+\omega+i\eta}.
\end{aligned} \tag{A.3}$$

In the second line we interchanged the role of $\mathbf{k}$ and $\mathbf{k}'$ and used that $\delta_{\mathbf{k},\mathbf{k}'+\mathbf{q}} = \delta_{\mathbf{k}',\mathbf{k}-\mathbf{q}}$. Furthermore, we introduced the factor $1/(1+\delta_{ia})$ to correct for the double counting of the diagonal terms with $i = a$. Introducing the time-reversed partners of $\psi_{i\mathbf{k}}$ and $\psi_{a\mathbf{k}'}$, namely $\psi^*_{i\mathbf{k}} = \psi_{i-\mathbf{k}}$ and $\psi^*_{a\mathbf{k}'} = \psi_{a-\mathbf{k}'}$, for which $\epsilon_{i\mathbf{k}} = \epsilon_{i-\mathbf{k}}$, $\epsilon_{a\mathbf{k}'} = \epsilon_{a-\mathbf{k}'}$ and $f_{i\mathbf{k}} = f(\epsilon_{i\mathbf{k}}) = f(\epsilon_{i-\mathbf{k}}) = f_{i-\mathbf{k}}$ etc. [57], we can write

$$\begin{aligned}
\delta\rho_{\mathbf{q}}(\mathbf{r},\omega) &= \frac{1}{N_k}\sum_{\mathbf{k},\mathbf{k}'}\delta_{\mathbf{k}',\mathbf{k}+\mathbf{q}}\sum_{i,a}\frac{(f_{i\mathbf{k}}-f_{a\mathbf{k}'})}{2(1+\delta_{ia})}\times \\
&\quad \frac{\psi^*_{i\mathbf{k}}(\mathbf{r})e^{-i\mathbf{q}\cdot\mathbf{r}}\psi_{a\mathbf{k}'}(\mathbf{r})\langle\psi_{a\mathbf{k}'}|\delta\hat{h}(\mathbf{q},\omega)|\psi_{i\mathbf{k}}\rangle}{\epsilon_{i\mathbf{k}}-\epsilon_{a\mathbf{k}'}+\omega+i\eta} \\
&+ \frac{1}{N_k}\sum_{\mathbf{k},\mathbf{k}'}\delta_{\mathbf{k}',\mathbf{k}+\mathbf{q}}\sum_{i,a}\frac{(f_{i-\mathbf{k}}-f_{a-\mathbf{k}'})}{2(1+\delta_{ia})}\times \\
&\quad \frac{\psi_{i-\mathbf{k}}(\mathbf{r})e^{-i\mathbf{q}\cdot\mathbf{r}}\psi^*_{a-\mathbf{k}'}(\mathbf{r})\langle\psi^*_{a-\mathbf{k}'}|\delta\hat{h}(\mathbf{q},\omega)|\psi^*_{i-\mathbf{k}}\rangle}{\epsilon_{i-\mathbf{k}}-\epsilon_{a-\mathbf{k}'}+\omega+i\eta} \\
&+ \frac{1}{N_k}\sum_{\mathbf{k},\mathbf{k}'}\delta_{\mathbf{k}',\mathbf{k}-\mathbf{q}}\sum_{i,a}\frac{(f_{i\mathbf{k}}-f_{a\mathbf{k}'})}{2(1+\delta_{ia})}\times \\
&\quad \frac{\psi^*_{a\mathbf{k}'}(\mathbf{r})e^{-i\mathbf{q}\cdot\mathbf{r}}\psi_{i\mathbf{k}}(\mathbf{r})\langle\psi_{i\mathbf{k}}|\delta\hat{h}(\mathbf{q},\omega)|\psi_{a\mathbf{k}'}\rangle}{\epsilon_{i\mathbf{k}}-\epsilon_{a\mathbf{k}'}-\omega-i\eta} \\
&+ \frac{1}{N_k}\sum_{\mathbf{k},\mathbf{k}'}\delta_{\mathbf{k}',\mathbf{k}-\mathbf{q}}\sum_{i,a}\frac{(f_{i-\mathbf{k}}-f_{a-\mathbf{k}'})}{2(1+\delta_{ia})}\times \\
&\quad \frac{\psi_{a-\mathbf{k}'}(\mathbf{r})e^{-i\mathbf{q}\cdot\mathbf{r}}\psi^*_{i-\mathbf{k}}(\mathbf{r})\langle\psi^*_{i-\mathbf{k}}|\delta\hat{h}(\mathbf{q},\omega)|\psi^*_{a-\mathbf{k}'}\rangle}{\epsilon_{i-\mathbf{k}}-\epsilon_{a-\mathbf{k}'}-\omega-i\eta}.
\end{aligned} \tag{A.4}$$

After a change of variables from $-\mathbf{k}$ and $-\mathbf{k}'$ to $\mathbf{k}$ and $\mathbf{k}'$ in the second and fourth terms, we can gather the factors $(\psi^*_{i\mathbf{k}}e^{-i\mathbf{q}\cdot\mathbf{r}}\psi_{a\mathbf{k}'})$ from the first and fourth terms and the factor $(\psi^*_{a\mathbf{k}'} e^{-i\mathbf{q}\cdot\mathbf{r}} \psi_{i\mathbf{k}})$ from the second and third. Now, using the relations

$$\begin{aligned} \langle \psi^*_{i\mathbf{k}} | \delta\hat{h}(\mathbf{q},\omega) | \psi^*_{a\mathbf{k}'} \rangle &= \langle \psi_{i\mathbf{k}} | \delta\hat{h}^*(\mathbf{q},\omega) | \psi_{a\mathbf{k}'} \rangle^* \\ &= \langle \psi_{a\mathbf{k}'} | (\delta\hat{h}^*(\mathbf{q},\omega))^\dagger | \psi_{i\mathbf{k}} \rangle \\ &= \langle \psi_{a\mathbf{k}'} | \delta\hat{h}^*(-\mathbf{q},-\omega) | \psi_{i\mathbf{k}} \rangle, \end{aligned} \tag{A.5}$$

in which $\delta\hat{h}(\mathbf{q},\omega) = \delta\hat{h}^\dagger(-\mathbf{q},-\omega)$, and reorganizing the terms a little, we arrive at Eq. (3.18). In a fully analogous way, but now taking into account the following relations,

$$\psi^*_{i\mathbf{k}} \hat{\mathbf{j}} \psi_{a\mathbf{k}'} = -\psi_{a\mathbf{k}'} \hat{\mathbf{j}} \psi^*_{i\mathbf{k}} = \left(\psi^*_{a\mathbf{k}'} \hat{\mathbf{j}} \psi_{i\mathbf{k}} \right)^* = -\left(\psi_{i\mathbf{k}} \hat{\mathbf{j}} \psi^*_{a\mathbf{k}'} \right)^*, \tag{A.6}$$

we arrive at the response functions for the paramagnetic part of the induced current-density, Eq. (3.28).

Appendix B

Integral Weights

We define integral weights $w_\pm(\Delta, \omega + i\eta)$,

$$w_\pm(\Delta, \omega + i\eta) = \frac{1}{2}\left(\frac{1}{\Delta + \omega + i\eta} \pm \frac{1}{\Delta - \omega - i\eta}\right), \tag{B.1}$$

to be used in the following meaning,

$$F_\pm(\omega) = \lim_{\eta \to 0} \int_0^\infty d\Delta\, f(\Delta) w_\pm(\Delta, \omega + i\eta). \tag{B.2}$$

It is easy to prove the following algebraic relations,

$$\begin{aligned} w_+(\Delta, \omega + i\eta) &= -\frac{\Delta}{\omega + i\eta} w_-(\Delta, \omega + i\eta), & \text{(B.3)} \\ w_-(\Delta, \omega + i\eta) &= -\frac{\Delta}{\omega + i\eta}(w_+(\Delta, \omega + i\eta) - w_+(\Delta, 0)). & \text{(B.4)} \end{aligned}$$

In order to treat the order of limits correctly, we will write

$$w_+(\Delta, 0) = w_+(\Delta, i\eta) + \frac{\eta^2}{\Delta(\Delta^2 + \eta^2)}. \tag{B.5}$$

The latter term will not contribute to the integral in the limit $\eta \to 0$, and in this limit the factor $(\omega + i\eta)^{-1}$ can be replaced by ω^{-1}. We thus get the simplified relations

$$\begin{aligned} w_+(\Delta, \omega^+) &= -\frac{\Delta}{\omega} w_-(\Delta, \omega^+), & \text{(B.6)} \\ w_-(\Delta, \omega^+) &= -\frac{\Delta}{\omega}(w_+(\Delta, \omega^+) - w_+(\Delta, 0^+)), & \text{(B.7)} \end{aligned}$$

where ω^+ means that i times a positive infinitesimal is added to the real number ω.

Appendix C

Integration in the Irreducible Brillouin Zone

The interband contribution to the Kohn-Sham response functions, as given in Sec. (3.2.3), involves integrations over the irreducible Brillouin zone, in which the integrand can become singular. The singular energy-dependent denominator in these response integrals is then included in the quadrature weights of a linear tetrahedron method by using an analytic evaluation of the Cauchy principle value and residual parts [30]. To keep it simple, if $\int f(\mathbf{k})d\mathbf{k}$ is an integral over the Brillouin zone, then for its quadrature one can write

$$\int f(\mathbf{k})d\mathbf{k} = \sum_{l=1}^{N}\sum_{i=1}^{4} w_{\mathbf{k}_i^l} f(\mathbf{k}_i^l), \tag{C.1}$$

where N is the number of tetrahedra in which the Brillouin zone is divided, $f(\mathbf{k}_i^l)$ is the value of the function in each corner of the l^{th} tetrahedron, and $w_{\mathbf{k}_i^l}$ are the quadrature weights. If partially occupied bands are involved in these integrals, then the integration is restricted only to a part of each tetrahedron cut off by the Fermi surface. The boundary planes $\epsilon(\mathbf{k}) = \epsilon_F$, with ϵ_F the Fermi energy, are shown in Fig. C.1 for the following three cases: $\epsilon_1 \leq \epsilon_F \leq \epsilon_2$ (I); $\epsilon_3 \leq \epsilon_F \leq \epsilon_4$ (II); $\epsilon_2 \leq \epsilon_F \leq \epsilon_3$ (III). In case I one obtains a small tetrahedron with corners $\mathbf{k}_1$, $\mathbf{k}_{12}^I$, $\mathbf{k}_{13}^I$, $\mathbf{k}_{14}^I$, and energies $\epsilon_1(\mathbf{k}_1)$, $\epsilon_{12}^I(\mathbf{k}_{12}^I)$, $\epsilon_{13}^I(\mathbf{k}_{13}^I)$, $\epsilon_{14}^I(\mathbf{k}_{14}^I)$. The corners $\mathbf{k}_{1i}^I$ of the new tretrahedron are obtained by the following linear expression,

$$\mathbf{k}_{1i}^I = c_1\mathbf{k}_1 + c_i\mathbf{k}_i, \tag{C.2}$$

where the coefficients c_1 and c_i are given by

$$c_1 = \frac{\epsilon_i - \epsilon_F}{\epsilon_i - \epsilon_1},\; c_i = \frac{\epsilon_F - \epsilon_1}{\epsilon_i - \epsilon_1}. \tag{C.3}$$

One can generate this set of coefficients for each of the N tetrahedra constituting the Brillouin zone, and use them to linear interpolate the function $f(\mathbf{k})$ over the new tetrahedra,

$$\int f(\mathbf{k})d\mathbf{k} = \sum_{l=1}^{N}\sum_{i,j=1}^{4} c^l_{ij} w_{\mathbf{k}^l_j} f(\mathbf{k}^l_i), \tag{C.4}$$

with $\mathbf{k}^l_i$ the corners of the l^{th} old tehrahedron, and $\mathbf{k}^l_j$ the corners of the l^{th} new tehrahedron. In case I the total number of tetrahedra remains the same and no extra tetrahedra are generated.

In case II the integral covers almost the whole tetrahedron except the small one with corners $\mathbf{k}_4$, $\mathbf{k}^{II}_{41}$, $\mathbf{k}^{II}_{42}$, $\mathbf{k}^{II}_{43}$. The troncated tretrahedron gives rise to other three secondary tetrahedra for which one can proceed as in case I.

In case III the primary tetrahedron is divided in two secondary ones by the shaded plane in Fig. C.1. One of the two secondary tetrahedra can be treated as in case I, whereas the other one as in case II.

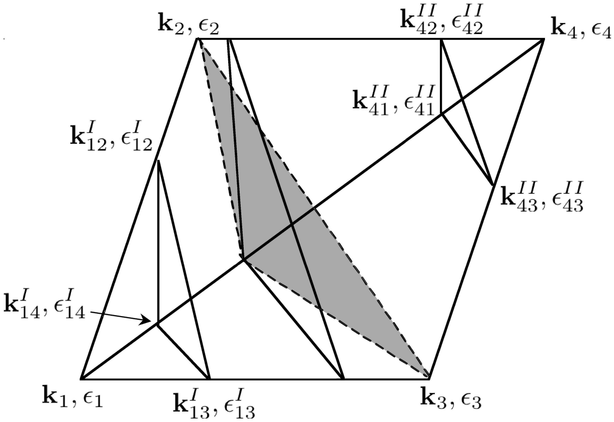

Figure C.1: Planes $\epsilon(\mathbf{k}){=}\epsilon_F$ cutting the basic tetrahedron. The shaded plane (used for the case III) divides the tetrahedron in two secondary tetrahedra. One can be treated as in case I and the other as in case II.

Appendix D

Hermiticity of the TD-ZORA Hamiltonian

We prove now that the time-dependent Foldy-Wouthuysen Hamiltonian (4.53) is Hermitian. To do this we show that the remainder $\hat{Y}$ is Hermitian. If we consider $\sqrt{1+\hat{X}^\dagger\hat{X}} = \sum_n a_n(\hat{X}^\dagger\hat{X})^n$, then we have

$$\hat{Y} \quad = \quad \sum_{n,k}(a_n a_k - \frac{1}{2}\delta_{n1}\delta_{k0}) \sum_{m=0}^{n-1}(\hat{X}^\dagger\hat{X})^{n-m-1}(\hat{X}^\dagger c\sigma\cdot\pi - c\sigma\cdot\pi\hat{X})(\hat{X}^\dagger\hat{X})^{m+k}.$$

By introducing $p = m+k$ with $m \geq 0$, and $q = n-m-1 \geq 0$ we can rewrite

$$\hat{Y} \quad = \quad \sum_{p,q}\sum_{m=0}^{q}(a_{p+m+1}a_{q-m} - \frac{1}{2}\delta_{p0}\delta_{q0})(\hat{X}^\dagger\hat{X})^p(\hat{X}^\dagger c\sigma\cdot\pi - c\sigma\cdot\pi\hat{X})(\hat{X}^\dagger\hat{X})^q.$$

Using

$$(\sqrt{1+\hat{X}^\dagger\hat{X}})^2 = \sum_{n,m} a_n a_m (\hat{X}^\dagger\hat{X})^{n+m} = 1 + \hat{X}^\dagger\hat{X}, \tag{D.1}$$

it follows that

$$\sum_{n=0}^{k} a_{k-n}a_n = \delta_{k0} + \delta_{k1}. \tag{D.2}$$

Hence

$$\begin{aligned}
c_{pq} &= \sum_{m=0}^{q} a_{p+1+m} a_{q-m} - \frac{1}{2}\delta_{p0}\delta_{q0} = \sum_{m'=0}^{q} a_{(p+q+1)-m'} a_{m'} - \frac{1}{2}\delta_{p0}\delta_{q0} \\
&= \delta_{p+q+1,0} + \delta_{p+q+1,1} - \sum_{m'=q+1}^{p+q+1} a_{(p+q+1)-m'} a_{m'} - \frac{1}{2}\delta_{p0}\delta_{q0} \\
&= \frac{1}{2}\delta_{p0}\delta_{q0} - \sum_{m''=0}^{p} a_{p-m''} a_{q+1+m''} \\
&= -c_{qp}.
\end{aligned}$$

We can then conclude that $\hat{Y}^{\dagger} = \hat{Y}$. Moreover all diagonal elements $c_{pp} = 0$, and in particular $c_{00} = 0$. As result $\hat{Y}$ is of the first order in $\hat{X}^{\dagger}\hat{X}$.

Appendix E

Fermi-Surface Topology

E.1 Group-VB metals: symmetry-induced degeneracy along Λ

We first analyze bands 2 and 3 of the group-VB metals around their point of degeneracy along Λ. The results given here are obtained from our numerical ground-state calculations. By taking the vector $\mathbf{q}$ along the Λ direction, $\hat{\mathbf{q}}_{||} = 1/\sqrt{3}\,(1,\,1,\,1)^T$, the projection along $\hat{\mathbf{q}}_{||}$ of the momentum matrix $\mathbf{p}$ entering in Eq. (6.12) becomes, for this degenerate subspace,

$$\hat{\mathbf{q}}_{||} \cdot \mathbf{p} = a\sqrt{3}\left(\begin{array}{c|c} 1 & 0 \\ \hline 0 & 1 \end{array}\right), \tag{E.1}$$

with double degenerate eigenvalues $\lambda_1 = \lambda_2 = a\sqrt{3}$. This means that bands 2 and 3 remain degenerate along this direction at least to first order in q as can be expected from symmetry. We now analyze the angular dependence of the two energy bands in the direction perpendicular to the $\hat{\mathbf{w}} = \hat{\mathbf{q}}_{||}$ axis, by considering the vector $\mathbf{q}$ as

$$\hat{\mathbf{q}}_{\perp}(\phi) = \cos(\phi)\hat{\mathbf{u}} + \sin(\phi)\hat{\mathbf{v}}, \tag{E.2}$$

where $\hat{\mathbf{u}} = 1/\sqrt{2}\,(1, -1,\,0)^T$ and $\hat{\mathbf{v}} = 1/\sqrt{6}\,(1,\,1, -2)^T$ are the other two unit vectors of the new system of coordinates ($\hat{\mathbf{u}}$, $\hat{\mathbf{v}}$, $\hat{\mathbf{w}}$) with the origin in the degeneracy of bands 2 and 3. In this case we obtain

$$\hat{\mathbf{q}}_{\perp}(\phi) \cdot \mathbf{p} = b\sqrt{\frac{3}{2}}\left(\begin{array}{c|c} 0 & -ie^{i\phi} \\ \hline ie^{-i\phi} & 0 \end{array}\right), \tag{E.3}$$

with eigenvalues $\lambda_\pm = \pm b\sqrt{3/2}$ independent from the angle ϕ, and eigenvectors $\hat{\mathbf{c}}_\pm = 1/\sqrt{2}\,(\mp i e^{i\phi},\, 1)^T$. As we move away from the Λ symmetry line the degeneracy is lifted as described by Eq. (6.13): one band increases in energy and the other one decreases with the same amount independent from the angle ϕ. We can conclude that bands 2 and 3 give rise to a linear conical intersection with the contact point on the symmetry line Λ, which is also the axis of the cone. The energy dispersion is then given by

$$\epsilon_\pm(q_\parallel, q_\perp) = \epsilon_F + a\sqrt{3}\,q_\parallel \pm b\sqrt{\frac{3}{2}}\,q_\perp + \mathcal{O}(q_\perp^2, q_\parallel^2), \tag{E.4}$$

which is characteristic of a conical intersection. The new eigenvalues $\epsilon_{i\mathbf{k}+\mathbf{q}}$ and $\epsilon_{a\mathbf{k}+\mathbf{q}}$ of bands 2 and 3 then give rise to the form

$$\epsilon_{i\mathbf{k}+\mathbf{q}} - \epsilon_{a\mathbf{k}+\mathbf{q}} = -b\sqrt{6}\,q_\perp + \mathcal{O}(q_\perp^2, q_\parallel^2), \tag{E.5}$$

where we made use of the cylindrical coordinates $(q_\perp, q_\parallel, \phi)$. We find for a generic direction that the off-diagonal elements of the momentum matrix $\mathbf{p}$ are a nonzero constant to zeroth order in q, and thus we obtain

$$|\langle \psi_{i\mathbf{k}+\mathbf{q}} \mid \hat{\mathbf{j}} \mid \psi_{a\mathbf{k}+\mathbf{q}} \rangle| = \sqrt{\frac{3}{2}}b + \mathcal{O}(q_\perp). \tag{E.6}$$

From our $\mathbf{k}\cdot\mathbf{p}$ analysis of the degeneracies in the group-VB metals we can evaluate the integrand in Eq. (6.10), which then becomes

$$\begin{aligned} \Im\left\{\epsilon^{inter}(\omega)\right\} \quad \propto \quad & \frac{4}{3\pi}\int_0^{2\pi} d\phi \int_0^{q} q_\perp dq_\perp \int_{-|b/a\sqrt{2}|q_\perp}^{|b/a\sqrt{2}|q_\perp} dq_\parallel \,\times \\ & \delta\left(-b\sqrt{6}q_\perp + \omega\right) \cdot \frac{1}{4q_\perp^2} = \frac{2}{|a|3\sqrt{3}}, \end{aligned} \tag{E.7}$$

where we have considered that the contribution from the Λ line is 8-fold. A similar accidental conical intersection occurs in the ΓHP plane, and we arrive at similar conclusions as the case discussed above. Here the intensity is lower than the other degeneracy, but the contribution is 24-fold.

E.2 Group-VIB metals: symmetry-induced degeneracy along Δ

The first two partially occupied bands 3 and 4 show a point of degeneracy along the Δ symmetry line taken here in the $\hat{\mathbf{y}}$ direction. By taking the vector $\mathbf{q}$ along the Δ

direction, $\hat{\mathbf{q}}_{\|} = (0,\, 1,\, 0)^T$, the projection along $\hat{\mathbf{q}}_{\|}$ of the momentum matrix $\mathbf{p}$ in Eq. (6.12) for this degenerate subspace becomes

$$\hat{\mathbf{q}}_{\|} \cdot \mathbf{p} = p_{\|} \left(\begin{array}{c|c} 1 & 0 \\ \hline 0 & 1 \end{array} \right), \tag{E.8}$$

whereas in the $\hat{\mathbf{x}}\hat{\mathbf{z}}$ plane we have, with $\hat{\mathbf{q}}_{\perp}(\phi) = \cos(\phi)\hat{\mathbf{x}} + \sin(\phi)\hat{\mathbf{z}}$,

$$\hat{\mathbf{q}}_{\perp} \cdot \mathbf{p} = \left(\begin{array}{c|c} 0 & 0 \\ \hline 0 & 0 \end{array} \right). \tag{E.9}$$

It is immediately clear that along the Δ symmetry line the degeneracy is not lifted and the two energies change linearly with $q_{\|}$. In the $\hat{\mathbf{x}}\hat{\mathbf{z}}$ plane the energies do not change to first order in $q_{\perp}$, but the degeneracy may still be lifted to second order. Therefore we analyze the effective mass matrix, which has the following form in the symmetry-induced degeneracy along the symmetry line Δ,

$$M_{\|}^{-1} = m_{\|}^{-1} \left(\begin{array}{c|c} 1 & 0 \\ \hline 0 & 1 \end{array} \right), \tag{E.10}$$

$$M_{\perp}^{-1}(\phi) = \left(\begin{array}{c|c} \bar{m}_{\perp}^{-1} + \Delta_1 \cos(2\phi) & \tilde{\Delta}_2 \sin(2\phi) \\ \hline \tilde{\Delta}_2^{*} \sin(2\phi) & \bar{m}_{\perp}^{-1} - \Delta_1 \cos(2\phi) \end{array} \right), \tag{E.11}$$

with $\bar{m}_{\perp}$, $m_{\|}$, and Δ_1 real numbers, and $\tilde{\Delta}_2$ a complex number. It is immediate to verify that in the $\hat{\mathbf{y}}$ direction the degeneracy is not lifted even to second order, whereas it is lifted in the $\hat{\mathbf{x}}\hat{\mathbf{z}}$ plane as becomes clear from the form of the matrix in Eqs (E.10) and (E.11). The energy dispersion is then given by

$$\epsilon_{\pm}(q_{\|}, q_{\perp}, \phi) = \epsilon_F + p_{\|} \cdot q_{\|} + \frac{1}{2} m_{\|}^{-1} \cdot q_{\|}^2 + \frac{1}{2} m_{\perp,\pm}^{-1}(\phi) \cdot q_{\perp}^2 + \mathcal{O}(q_{\perp}^3, q_{\|}^3), \tag{E.12}$$

where

$$m_{\perp,\pm}^{-1}(\phi) = \bar{m}_{\perp}^{-1} \pm \sqrt{\Delta_1^2 \cos^2(2\phi) + |\Delta_2|^2 \sin^2(2\phi)}. \tag{E.13}$$

Since $|\Delta_2| \approx \Delta_1 = \Delta$, we can consider $\Delta_2 = \Delta e^{i\zeta}$ without losing the validity of this analysis. In this case the eigenvectors have the form $\hat{\mathbf{c}}_{\pm} = 1/\sqrt{2 \mp 2\cos(2\phi)}(\pm 1 - \cos(2\phi), -\sin(2\phi)e^{-i\zeta})^T$. The new eigenvalues $\epsilon_{i\mathbf{k}+\mathbf{q}}$ and $\epsilon_{a\mathbf{k}+\mathbf{q}}$ of bands 3 and 4 then lead to

$$\epsilon_{i\mathbf{k}+\mathbf{q}} - \epsilon_{a\mathbf{k}+\mathbf{q}} = -\Delta \cdot q_{\perp}^2 + \mathcal{O}(q_{\perp}^3), \tag{E.14}$$

where we again used the cylindrical coordinates. We find for a generic direction that the off-diagonal elements of the momentum matrix $\mathbf{p}$ are linear in q, and thus we obtain

$$|\langle \psi_{i\mathbf{k}+\mathbf{q}} \mid \hat{\mathbf{j}} \mid \psi_{a\mathbf{k}+\mathbf{q}} \rangle| = \Delta \cdot q_{\perp} + \mathcal{O}(q_{\perp}^2). \tag{E.15}$$

We are now ready to evaluate Eq. (6.10) giving

$$\begin{aligned}\Im\left\{\epsilon^{inter}(\omega)\right\} \quad &\propto \quad \frac{1}{\pi}\int_0^{2\pi} d\phi \int_0^{q} q_\perp dq_\perp \int_{\alpha_- q_\perp^2}^{\alpha_+ q_\perp^2} dq_\| \times \\ &\qquad \delta\left(-\Delta\cdot q_\perp^2+\omega\right)\cdot\frac{1}{q_\perp^2}=\frac{1}{p_\|}, \end{aligned} \tag{E.16}$$

with $\alpha_\pm = -1/2(\bar{m}_\perp \pm \Delta)/p_\|$. Here we have considered that the contribution from the Δ symmetry line is 6-fold.

Appendix F

Low-Frequency Behavior of the Dielectric Function

We define two vectors $\mathbf{P}$ and $\mathbf{F}$ as

$$\mathbf{P} = \begin{pmatrix} \delta\rho \\ i\delta\mathbf{j}/\omega \\ i\delta\mathbf{m}/\omega \end{pmatrix}, \tag{F.1}$$

containing the densities, in which the inter- and intraband contributions are added, i.e., $\delta\rho = \delta\rho^{inter} + \delta\rho^{intra}$ and similarly for $\delta\mathbf{j}$ and $\delta\mathbf{m}$, and

$$\mathbf{F} = \begin{pmatrix} 0 \\ i\omega\delta\mathbf{A}_{mac}/c \\ 0 \end{pmatrix} + \begin{pmatrix} \delta v_{Hxc,mic}^{ALDA} \\ 0 \\ 0 \end{pmatrix} + \begin{pmatrix} \delta u_{xc} \\ i\omega\delta\mathbf{a}_{xc}/c \\ i\omega\delta\mathbf{b}_{xc}/c \end{pmatrix}, \tag{F.2}$$

which contains all first order contributions to the perturbing potentials. Here the perturbation $\mathbf{F}$ is decomposed into three terms: $\mathbf{F}_{mac}$ containing only the macroscopic field, $\mathbf{F}_a$ containing the adiabatic parts given by the microscopic Hartree potential and the ALDA exchange-correlation potential, $\delta v_{Hxc,mic}^{ALDA} = \delta v_{H,mic} + \delta v_{xc,mic}^{ALDA}$, and $\mathbf{F}_d$ containing the dynamic part of the exchange-correlation vector potential. From Eqs (7.29) and (7.30) it becomes clear that we can write

$$\mathbf{P} = \left(X^{inter} + \frac{1}{\omega^2} Q^\dagger \cdot X^{intra} \cdot Q \right) \cdot \mathbf{F}, \tag{F.3}$$

where

$$Q = \begin{pmatrix} iq & 0 & 0 \\ 0 & 1 & 0 \\ 0 & 0 & 1 \end{pmatrix}, \tag{F.4}$$

and X^{inter} and X^{intra} are the matrices of the inter- and intraband Kohn-Sham response functions given in Eqs (7.29) and (7.30). In the linear response regime we can write $\mathbf{F}_a = Y_a \cdot \mathbf{P}$ for the adiabatic part of the potential vector, and $\mathbf{F}_d = Y_d \cdot \mathbf{P}$ for the dynamic part. Here the matrix Y_d is given in (7.22) and Y_a is defined as

$$Y_a = \begin{pmatrix} y_a & 0 & 0 \\ 0 & 0 & 0 \\ 0 & 0 & 0 \end{pmatrix}, \tag{F.5}$$

with the frequency independent kernel y_a defined by the relation $y_a \delta\rho = \delta v^{ALDA}_{Hxc,mic}$. The total perturbing potential is then given by

$$\mathbf{F} = \mathbf{F}_{mac} + (Y_a + Y_d) \cdot \mathbf{P}. \tag{F.6}$$

The low-frequency behavior of the matrix Y_d is determined by the low-frequency behavior of the viscoelastic coefficients $\tilde{\eta}_{xc}(\mathbf{r},\omega)$ and $\tilde{\zeta}_{xc}(\mathbf{r},\omega)$, which in turn is determined by the low-frequency behavior of $f_{xcL,T}(\omega)$. Since $f_{xcL,T}(\omega) = f^*_{xcL,T}(-\omega)$ and considering the results obtained in Eqs (7.16) and (7.17), we can write the following expressions for the low-frequency behavior of $\tilde{\eta}_{xc}(\mathbf{r},\omega)$ and $\tilde{\zeta}_{xc}(\mathbf{r},\omega)$,

$$\frac{-i\omega\tilde{\zeta}_{xc}}{\rho_0^2} = i\omega A + \omega^2 B + O(\omega^3), \tag{F.7}$$

$$\frac{-i\omega\tilde{\eta}_{xc}}{\rho_0^2} = \frac{\mu_{xc}}{\rho_0^2} + i\omega C + \omega^2 D + O(\omega^3), \tag{F.8}$$

where A, B, C, and D are real. Furthermore, Qian and Vignale showed [130] that the slope of the imaginary parts of $f_{xcL,T}(\omega)$ is finite in the limit $\omega \to 0$. This means that in the above expressions A and C are finite. By using Eqs (F.7) and (F.8), we can write the following low-frequency expansion for Y_d,

$$Y_d = \sum_p (i\omega)^p Y_{d,p}, \tag{F.9}$$

where $Y_{d,p}$ are real and $Y_{d,0} \propto \mu_{xc}$.

It now becomes clear that we can obtain $\mathbf{P}$ by solving Eqs (F.3) and (F.6) self-consistently. We have carefully formulated these response equations such that a regular solution can be found for $\lim_{\mathbf{q}\to 0} \mathbf{P}(\mathbf{q}) = \mathbf{P}$, with $\mathbf{P}$ the solution of Eq. (F.3) at

$\mathbf{q} = \mathbf{0}$. In this limit we can write the following low-frequency expression of Eq. (F.3),

$$\left[\omega^2 I - \left(\omega^2 \sum_p (i\omega)^p X_p^{inter} + \tilde{X}^{intra}\right) \cdot \left(Y_a + \sum_p (i\omega)^p Y_{d,p}\right)\right] \cdot \mathbf{P} = \left(\omega^2 \sum_p (i\omega)^p X_p^{inter} + \tilde{X}^{intra}\right) \cdot \mathbf{F}_{mac}, \qquad \text{(F.10)}$$

where, since $X^{inter}(\omega) = X^{inter*}(-\omega)$, we have used the series expansion $X^{inter} = \sum_p (i\omega)^p X_p^{inter}$. Here the matrices X_{2p+1}^{inter} vanish if ω is below the interband absorption edge, and the matrix $\tilde{X}^{intra}$ is frequency-independent and defined as

$$\tilde{X}^{intra} = \lim_{q \to 0} Q^\dagger \cdot X^{intra} \cdot Q = \begin{pmatrix} 0 & 0 & 0 \\ 0 & \Delta\chi_{\rho\mathbf{jj}}^{intra} & \Delta\chi_{\rho\mathbf{jm}}^{intra} \\ 0 & \Delta\chi_{\rho\mathbf{mj}}^{intra} & \Delta\chi_{\rho\mathbf{mm}}^{intra} \end{pmatrix}. \qquad \text{(F.11)}$$

All matrices are real-valued. Note that due to their matrix structure the product $\tilde{X}^{intra} \cdot Y_a$ vanishes. From Eq. (F.10) it immediately becomes clear that the low-frequency behavior of the solution is largely determined by $\tilde{X}^{intra}$ and the low-frequency coefficients of Y_d.

Since $\mathbf{P}(\omega) = \mathbf{P}^*(-\omega)$, we can use the series expansion $\mathbf{P} = \sum_{n=n_0}^{\infty} (i\omega)^n \mathbf{P}_n$, where we assume that the expansion truncates at a certain value n_0 since we are interested in the low-frequency behavior of $\mathbf{P}$. We can then write Eq. (F.10) as

$$\left(\sum_{p=0}^{\infty} (i\omega)^p X_p\right) \left(\sum_{n=n_0}^{\infty} (i\omega)^n \mathbf{P}_n\right) = \sum_{m=0}^{\infty} (i\omega)^m \mathbf{F}_m, \qquad \text{(F.12)}$$

with

$$X_p = -\delta_{p,2} I + X_{p-2}^{inter} \cdot Y_a - \tilde{X}^{intra} \cdot Y_{d,p} + \sum_{s=0}^{p-2} X_{p-s-2}^{inter} \cdot Y_{d,s}, \qquad \text{(F.13)}$$

$$\mathbf{F}_m = \left(-X_{m-2}^{inter} + \delta_{m,0} \tilde{X}^{intra}\right) \cdot \mathbf{F}_{mac}. \qquad \text{(F.14)}$$

Note that the odd-indexed potential coefficients vanish, $\mathbf{F}_{2m+1} = \mathbf{0}$. We want to mention the first two matrix and vector elements in particular,

$$X_0 = -\tilde{X}^{intra} \cdot Y_{d,0}, \qquad \mathbf{F}_0 = \tilde{X}^{intra} \cdot \mathbf{F}_{mac} \qquad \text{(F.15)}$$

$$X_1 = -\tilde{X}^{intra} \cdot Y_{d,1}, \qquad \mathbf{F}_1 = \mathbf{0}. \qquad \text{(F.16)}$$

By equating all orders in Eq. (F.12) separately, we obtain the general structure of the m^{th}-order of the low-frequency expansion of the response equation, which is given by the relation

$$\sum_{n=n_0}^{m} X_{m-n}\mathbf{P}_n = \mathbf{F}_m \tag{F.17}$$

with $\mathbf{F}_{m<m_0} = \mathbf{0}$, in which we need to choose $n_0 \leq m_0$ such that there is a unique solution. The dimension of the matrices and vectors is d. This infinite set of equations can be written in the following triangular block matrix form,

$$\begin{bmatrix} X_0 & 0 & 0 & \cdots \\ X_1 & X_0 & 0 & \ddots \\ X_2 & X_1 & X_0 & \ddots \\ \vdots & \ddots & \ddots & \ddots \end{bmatrix} \left[\begin{array}{c} \mathbf{P}_{n_0} \\ \vdots \\ \mathbf{P}_{m_0-1} \\ \hline \mathbf{P}_{m_0} \\ \vdots \end{array}\right] = \left[\begin{array}{c} \mathbf{0} \\ \vdots \\ \mathbf{0} \\ \hline \mathbf{F}_{m_0} \\ \vdots \end{array}\right],$$

from which it becomes clear that there is a unique solution if X_0 is invertible, with $n_0 = m_0$ and $\mathbf{P}_{n<n_0} = 0$, generated by

$$\mathbf{P}_n = X_0^{-1}(\mathbf{F}_n - \sum_{m=m_0}^{n-1} X_{n-m}P_m).$$

If on the other hand X_0 is singular as in our case, we proceed to find a solution by constructing the singular value decomposition $X_0 = VDU^\dagger$ with the diagonal matrix D containing singular values $d_1 \cdots d_s = 0$ and $d_{i>s} \neq 0$ with $s > 0$, and the unitary matrices U and V built from the right and left singular vectors spanning the domain, null space, and range of X_0. We can multiply each line from the left by $V^\dagger$, and thus remove the first s rows from each diagonal block of the triangular matrix. These rows become replaced by the first s rows of the line below, yielding again a triangular form,

$$\begin{bmatrix} \begin{bmatrix} 0 \\ \tilde{D}U^\dagger \end{bmatrix} & 0 & 0 & \cdots \\ V^\dagger X_1 & \begin{bmatrix} 0 \\ \tilde{D}U^\dagger \end{bmatrix} & 0 & \ddots \\ V^\dagger X_2 & V^\dagger X_1 & \begin{bmatrix} 0 \\ \tilde{D}U^\dagger \end{bmatrix} & \ddots \\ \vdots & \ddots & \ddots & \ddots \end{bmatrix} \left[\begin{array}{c} \mathbf{P}_{n_0} \\ \vdots \\ \mathbf{P}_{m_0-1} \\ \hline \mathbf{P}_{m_0} \\ \vdots \end{array}\right] = \left[\begin{array}{c} \mathbf{0} \\ \vdots \\ \mathbf{0} \\ \hline V^\dagger\mathbf{F}_{m_0} \\ \vdots \end{array}\right].$$

Here $\tilde{D}$ is the matrix D with the first s rows removed. The first s lines of the equation can be removed as these are trivially satisfied. We can do this by defining new blocks

$$[X'_n]_{i,j} = \begin{cases} [V^\dagger X_n]_{i+s,j} & \textit{for } i \leq d-s \\ [V^\dagger X_{n+1}]_{i+s-d,j} & \textit{for } i > d-s \end{cases} \tag{F.18}$$

and similarly new vectors

$$[\mathbf{F}'_n]_i = \begin{cases} [V^\dagger \mathbf{F}_n]_{i+s} & \mathit{for}\ i \leq d-s \\ [V^\dagger \mathbf{F}_{n+1}]_{i+s-d} & \mathit{for}\ i > d-s \end{cases} \tag{F.19}$$

such that we retrieve the original structure, however in general with a nonzero vector $\mathbf{F}'_{m_0-1}$. Therefore we have to set $m'_0 = m_0 - 1$. If $\mathbf{F}_{m_0}$ is in the range of X_0, then $\mathbf{F}'_{m_0-1}$ will still be zero and we can set $m'_0 = m_0$. By iterating this procedure k times, until we have found a diagonal block $X_0^{\prime\cdots\prime}$ that is invertible, we have constructed a unique solution that truncates from below at $n_0 \geq m_0 - k$ with $\mathbf{P}_{n<n_0} = \mathbf{0}$.

We will now discuss three separate cases, being the adiabatic approximation, in which Y_d is set to zero, the dynamic exchange-correlation case with vanishing static limit and hence $Y_{d,0} = 0$, but $Y_{d,1} \neq 0$, and the dynamic case with finite static value $Y_{d,0} \neq 0$.

In the simplest case (the adiabatic approximation) we have $X_0 = X_1 = X_{2n+1} = 0$, and $\mathbf{F}_{2n+1} = \mathbf{0}$. From Eq. (F.17) it immediately follows that in this case the equations for even and odd indexed $\mathbf{P}$ decouple, with the partial result $\mathbf{P}_{2n+1} = \mathbf{0}$. The singular value decompositions for the first two iterations become trivial, $V = U = I$ and $D = 0$, and we obtain $n_0 = -2$ with the unique even-indexed solutions given by

$$\mathbf{P}_{2n} = X_2^{-1}(\mathbf{F}_{2n+2} - \sum_{m=-1}^{n-1} X_{2(n-m+1)} P_{2m}), \tag{F.20}$$

where we have assumed that X_2 is invertible. The susceptibility is therefore purely real valued and is diverging like ω^{-2}.

In the dynamic case with vanishing static limit for Y_d, we have $X_0 = 0$, X_1 singular, $\mathbf{F}_0 \neq \mathbf{0}$ but in the range of X_1 (provided that $Y_{d,1}$ is invertible), and again $\mathbf{F}_{2n+1} = \mathbf{0}$. The first iteration is again trivial, with $V = U = I$ and $D = 0$. In the second iteration we can remove the singularity of the new diagonal block $X'_0 = X_1$, by appying the SVD again. However, if indeed $\mathbf{F}'_{-1} = \mathbf{F}_0$ is in the range of X_1 (which is the case if $Y_{d,1}$ is invertible), then we do not have to decrease m_0 further and we obtain $n_0 = -1$, otherwise we do, and find $n_0 = -2$. Assuming that the second iteration yields an invertible diagonal block, we have found the solution which truncates at $n_0 = -1(-2)$. We can thus conclude that the susceptibility acquires an imaginary part that diverges like ω^{-1}, and a real value that is finite, unless the first order dynamic exchange-correlation kernel $Y_{d,1}$ is singular.

In the dynamical case with finite static limit an extra complication arises. In the first iteration the multiplication from the left with $V^\dagger$ reduces not only the diagonal blocks X_0, but removes also rows from the subdiagonal blocks. This is due to the fact that $X_{0(1)}$ is of the form $\tilde{X}^{intra} \cdot Y_{d,0(1)}$ in which $\tilde{X}^{intra}$ is singular as is clear from its matrix structure. If the ranges of X_0 and X_1 coincide (which is the case if $Y_{d,0(1)}$ is invertible), then an equal amount of rows is removed in the diagonal and subdiagonal blocks, and also in the vector $\mathbf{F}_0$ for invertible $Y_{d,0(1)}$. As always $\mathbf{F}_{2n+1} = \mathbf{0}$. One can check readily that in both iterations we do not need to decrease m_0, and we find a solution with $n_0 = 0$, assuming that after the second step an invertible diagonal block is generated. In this case the susceptibility is real and finite in the low frequency range. If on the other hand (one of) the matrices $Y_{d,0(1)}$ is singular still a divergence may result.

The analysis given above forms the basis for understanding the solution at finite frequency. Retaining only the lowest order terms of the interband response function in Eq. (F.10) it becomes clear that we can consider the contribution of $Y_{d,0(1)}$ as small perturbations if $\omega \gg \omega_{0(1)}$, where

$$\omega_0 = \sqrt{\| X_2^{-1} X_0 \|} \tag{F.21}$$

and

$$\omega_1 = \| X_2^{-1} X_1 \| \tag{F.22}$$

are two characteristic frequencies defined in terms of the X-matrices given in Eq. (F.13). Here $\| A \| = \max_i |\lambda_i|$ indicates the spectral norm of the matrix A, being equal to its largest eigenvalue. The first order correction to the adiabatic solution gives

$$\mathbf{P} \approx \big(-\frac{1}{\omega^2} X_2^{-1} - \frac{1}{\omega^4} X_2^{-1} (i\omega X_1 + X_0) X_2^{-1} \big) (\omega^2 X^{inter} + \tilde{X}^{intra}) \mathbf{F}_{mac},$$

and leads to an imaginary part for the susceptibility that decays like $1/\omega^3$ for $\omega < \omega_p$ as then $\omega^2 \| X^{inter} \| < \| \tilde{X}^{intra} \|$. For $\omega \lesssim \omega_{0(1)}$ the contributions of $Y_{d,0(1)}$ become dominant and determine the solutions as in the analysis given above. Going from high to low frequency we expect a transition from the adiabatic to the dynamic case at around $\max(\omega_0, \omega_1)$, and if $\omega_0 < \omega_1$ from the dynamic behavior with vanishing static limit to the case with finite static limit at around ω_0. The results of this analysis are summarized in the following,

$$\chi_e(\omega) \propto \begin{cases} \alpha_1 + i\omega\beta_2 & \textit{for } \omega < \omega_0 \\ \alpha_1' + i\beta_2'/\omega & \textit{for } \omega_0 < \omega < \omega_1 \\ \alpha_1''/\omega^2 + i\beta_2''/\omega^3 & \textit{for } \omega > \omega_0, \omega_1 \end{cases} \tag{F.23}$$

As special case $\omega_0 = 0$ if $\mu_{xc} = 0$.

Summary

Materials have been used throughout history for their structural properties, e.g. ductility, elasticity, hardness etc., and later also for their physical properties, i.e., for their characteristic response to external perturbances. These last properties have been investigated in this thesis by using quatumechanics. The mutual interactions of the many-particles which constitute matter complicate its theoretical description enormously. Time-dependent density-functional theory provides a powerful tool to investigate these dynamic properties in atoms, molecules, and clusters. Indeed this theory maps the many-particle problem of interacting electrons in a time-dependent external field onto an auxiliary system of noninteracting particles in an effective field. The many-particle effects enter through so-called exchange-correlation contributions to the effective potentials describing this field. These effective potentials are uniquely determined by the time-dependent density for a given initial state. Essential in this formulation is that the time-dependent density is exactly the same in the real and auxiliary system. The time-dependent density can thus be obtained from the auxiliary system once we know the effective potentials, which in turn are functionals of the time-dependent density. This requires a self-consistent procedure in which one updates the approximate densities and potentials in an iterative way. In this thesis we have only considered systems, initially in the ground state, which are perturbed only weakly by an external electromagnetic field. In this so-called linear response regime the induced density is proportional to the applied field. The exchange-correlation potentials depend on the density in a nontrivial way: the potentials at time t and position $\mathbf{r}$ depend in general on the density at all earlier times t' and at all positions $\mathbf{r}'$. In the linear response regime this relation is expressed through a so-called exchange-correlation response kernel. The most common approximation for the exchange-correlation potentials is the adiabatic local density approximation (ALDA), in which these potentials are instantaneous and local functionals of the density. The scenario becomes more complicated for solids, which can be treated as 'open' systems, i.e., systems without boundary. To fully describe these systems, the density is replaced by the current-density leading to time-dependent current-density-functional theory (TDCDFT). In this thesis we have formulated the linear response of metallic crystalline systems to an electric field within this theoretical framework. The method gives already reasonable results for the dielectric and electron energy-loss functions within the ALDA. Although this approximation describes well the interband region of the spectra, it is less satisfying in the intraband region, where relaxation processes, such as electron-electron and electron-phonon scattering, become more important. Indeed the ALDA fails to reproduce the Drude-like tail in the absorption spectra. Approximations to the exchange-correlation potentials which are local-functionals of the current-density and hence nonlocal-functionals of the density can be included in a natural way in our formulation. In these approximations the exchange-correlation kernels can have memory, and thus relaxation processes due to electron-electron scattering can be taken into account. Other types of deviations from experiments can be observed in systems containing heavy elements, if relativistic corrections are neglected. Our method can treat scalar relativistic effects and spin-orbit coupling both in the ground-state and response calculations by using the zeroth-order regular approximation (ZORA). The spin-dependent formulation of the method, which allows to treat spin-orbit coupling, represents a first step to describe the linear response to an external magnetic field.

In chapter 1 we have given a brief introduction to optical properties of solids, namely the dielectric function and the electron energy-loss function. These two quantities describe the response of the system to a macroscopic and to an external electric field, respectively. Although the experiments which measure these two quantities can appear so different, they actually contain the same information in the long-wavelength limit, i.e., for external fields characterized by wavelengths that are long if compared to the interatomic distance. In chapter 2 an overview of the theoretical framework used has been presented. Time-dependent current-density-functional theory is an extension of the earlier density functional theory. What makes a density functional approach so attractive for theoretical analysis is the use of the density as basic quantity. The density, rather than the many-particle wavefunction, is used to describe a quantumechanical system, since the ground-state properties of the system can be expressed as functional of this quantity. First we have discussed the fundamental theorems of Hohenberg and Kohn and the practical set of one-particle equations introduced later by Kohn and Sham. These equations describe an auxiliary system of noninteracting particles in an effective potential which reproduces the same density as in the real interacting system. We have then described the formulation of a density functional approach for systems subjected to time-dependent external longitudinal fields, by giving the statement and the proof of the Runge-Gross theorem. Finally we have introduced time-dependent current-density-functional theory, that allows to treat also transverse fields and to treat the linear response in extended systems. The theory was first formulated by Ghosh and Dhara, but we have reported the main steps of a more recent demonstration given by Vignale. The current-density is the basic variable and uniquely determines the scalar and vector potentials which act on the system. This approach has been used by Kootstra *et al.* to formulate in an elegant way the linear response of nonmetallic systems to a macroscopic electric field. The dynamical response of the system is described by solving the time-dependent one-electron Kohn-Sham equations for the auxiliary noninteracting system in effective induced scalar and vector potentials which give the same density and current-density of the real system. One can express the density and the current-density induced by the perturbing potentials in terms of Kohn-Sham response functions, which only depend on the ground-state orbitals and orbital energies. Upon solving self-consistently the set of equations that describe the induced density and current-density, the dielectric function can be calculated from the macroscopic current. We have extended this formulation in order to treat the linear response of metallic crystalline systems as well. The derivation of the method is given in chapter 3. In treating the response of a metal to an external perturbation the Kohn-Sham response functions have to include both interband and intraband transitions with accurate treatment of the Fermi surface in the Brillouin-zone integrations. The intraband contributions, in particular, have to be evaluated using a wavevector-dependent description. To achieve this we have considered a general perturbation with wavevector $\mathbf{q}$ and frequency ω, and we have derived the linear response of the system for vanishing q, but finite ω. This is the regime describing optical properties. We have found that within the ALDA and in the optical limit $q \to 0$ we can solve separately the self-consistent-field equations which describe the inter- and intraband contributions to the response. Upon solving these equations, one can calculate the dielectric function $\epsilon(\omega) = [1 + 4\pi\chi_e^{inter}(\omega)] - 4\pi i/\omega\, \sigma^{intra}(\omega)$, with $\chi_e^{inter}(\omega)$ the interband contribution to the electric susceptibility, and $\sigma^{intra}(\omega)$ the intraband contribution to the macroscopic conductivity tensor. We have also shown that we retrieve in our approach the well-known relation between the electron energy-loss function and the dielectric function, i.e., $2\pi/(q^2V)\, S(\mathbf{q},\omega) = \Im\{-1/\epsilon_L(\mathbf{q},\omega)\}$, with $S(\mathbf{q},\omega)$ the dynamical structure factor, and $\epsilon_L(\mathbf{q},\omega)$ the longitudinal dielectric function. We have applied the method to calculate the dielectric and electron energy-loss functions of copper and silver and the agreement with the experiments is very good. However, strong deviations from the experimental spectra can be expected for heavy metals. Here relativistic effects play an important role. In chapter 4 we have given an introduction to a relativistic formulation of density functional theory, which is based on quantum electrodynamics. Analogously to the nonrelativistic stationary case, one can prove a one-to-one mapping between the external four-component potential and the four-component current of the system. We have described how to arrive at the Dirac-Kohn-Sham equations and how to reduce the four-component Hamiltonian to a two-component pseudorelativistic one by using the zeroth-order regular approximation. The ZORA Hamiltonian contains, already at zeroth order, the dominant relativistic effects. In chapter 5 we have combined this approach with our formulation of linear response and we have calculated the dielectric function of gold. We have shown that in a nonrelativistic calculation gold has the onset of interband absorption at about 3.5 eV, while the treatment of scalar relativistic effects red-shifts the onset at $\sim$1.9 eV, very close to the experiments, thus explaining the yellow color of gold. In chapter 6 we have analyzed in detail the band structures, the Fermi cross-sections, and the optical properties of the group VB and VIB bcc transition metals V, Nb, Ta, and (paramagnetic) Cr, Mo, and W, respectively. Here it becomes clear how accurate and versatile our method is. Some deviations from experiments can be due to the neglect of spin-orbit coupling. In the chapter 8 we have presented a preliminary spin-dependent formulation of the method, which has the aim to treat the linear response to magnetic fields as well. As immediate application we have included the spin-orbit coupling both in the ground-state and response calculations. We have shown the main changes that need to be done in the response functions in order to be expressed in terms of two-component spinors. We have tested the method on metallic and nonmetallic systems. The ZORA calculations of the dielectric functions of Au and W show some spectral features which were missing in the scalar ZORA spectra, and are in agreement with our predictions (chapters 5 and 6) and with the experiments. We have analyzed the impact of the relativity on the ground state and optical properties of ZnTe, CdTe, and HgTe. Whereas the first two of the series are semiconductors both in nonrelativistic and relativistic calculations, HgTe becomes a semimetal when relativity is considered. The inclusion of spin-orbit coupling is immediately visible in the spectra, since a splitting of the low-frequency peak appears, which reproduces very well the experiments, although the spectra are red-shifted by $\sim$ 1 eV with respect to the experiments.

Although the calculated spectra are in overall good agreement with experiments, the low-frequency Drude like absorption is missing in our calculations. This absorption is due to relaxation processes, and thus cannot be described within the adiabatic local density approximation where the response kernel is instantaneous. In chapter 7 we have used a functional which goes beyond the ALDA: the exchange-correlation vector potential is approximated as a local functional of the current-density using the expression derived by Vignale and Kohn. The self-consistent-field equations describing the inter- and intraband contributions to the response become coupled. Within this approximation the response kernel has memory, hence it can take into account relaxation processes due to electron-electron scattering. We have calculated the dielectric and electron energy-loss functions of the noble metals Cu, Ag, and Au and our results reproduce reasonably well the experiments.

Samenvatting

Materialen zijn de hele geschiedenis door gebruikt voor hun structurele eigenschappen, b.v. rekbaarheid, elasticiteit, hardheid, enz., en later ook voor hun fysieke eigenschappen, d.w.z. voor hun kenmerkende reactie op externe verstoringen. Deze laatste eigenschappen zijn in dit proefschrift onderzocht door gebruik te maken van kwantummechanica. De wederzijdse wisselwerking van de vele deeltjes waaruit materie bestaat compliceert de theoretische beschrijving aanzienlijk. Tijdsafhankelijke dichtheidsfunctionaaltheorie is een krachtig hulpmiddel om eigenschappen van atomen, moleculen, en clusters te onderzoeken. Deze theorie brengt inderdaad het veeldeeltjesprobleem van wisselwerkende elektronen in een tijdsafhankelijk extern veld over op een hulpsysteem van deeltjes zonder wisselwerking in een effectief veld. De veeldeeltjeseffecten worden meegenomen in de zogenaamde uitwisseling-correlatiebijdragen aan de effectieve potentialen die dit veld beschrijven. Voor een gegeven begintoestand zijn deze effectieve potentialen uniek bepaald door de tijdsafhankelijke dichtheid. Essentieel in deze formulering is dat de tijdsafhankelijke dichtheid exact hetzelfde is in het echte systeem als in het hulpsysteem. De tijdsafhankelijke dichtheid kan aldus worden verkregen met behulp van dit hulpsysteem zodra we de effectieve potentialen kennen, die op hun beurt functionalen van de dichtheid zijn. Dit behoeft een zelfconsistente procedure waarin de benaderde dichtheden en potentialen op een iteratieve manier worden bijgewerkt. In dit proefschrift hebben we alleen systemen beschouwd, die zich aanvankelijk in de grondtoestand bevinden en die slechts zwak verstoord worden door een extern elektromagnetisch veld. In dit zogenaamde lineaire-reponsregime is de geïnduceerde dichtheid evenredig met het aangelegde veld. De uitwisseling-correlatiepotentialen hangen op een niet-triviale manier van de dichtheid af: de potentialen op tijd t en positie $\mathbf{r}$ hangen in het algemeen af van de dichtheid op eerdere tijden t' en van alle posities $\mathbf{r}'$. In het lineaire-responsregime wordt deze relatie uitgedrukt in een zogenaamde uitwisseling-correlatieresponskern. De meest gebruikelijke benadering voor de uitwisseling-correlatiepotentialen is de adiabatische lokale dichtheidsbenadering (ALDA), waarin deze potentialen instantane en lokale functionalen van de dichtheid zijn. Het scenario wordt ingewikkelder voor vaste stoffen, die behandelt kunnen worden als 'open' systemen, d.w.z. systemen zonder randen. Om deze systemen volledig te kunnen beschrijven wordt de dichtheid vervangen door de stroomdichtheid wat leidt tot tijdsafhankelijke stroomdichtheidsfunctionaaltheorie (TDCDFT). In dit proefschrift hebben we de lineaire respons van metallische kristallijne systemen op een elektrisch veld geformuleerd binnen dit theoretische raamwerk. Deze methode levert al redelijke resultaten op voor de diëlektrische functies en elektronenergieverliesfuncties binnen de ALDA. Hoewel deze methode het interbandgedeelte van de spectra goed beschrijft stelt zij minder tevreden voor het intrabandgedeelte waar relaxatieprocessen zoals elektron-elektron- en elektron-fononverstrooiing belangrijker worden. De Drude-achtige staart van het absorptiespectrum ontbreekt inderdaad in de ALDA-beschrijving. Benaderingen voor de uitwisseling-correlatiepotentialen die lokale functionalen zijn van de stroomdichtheid en daardoor niet-lokale functies van de dichtheid kunnen op een natuurlijke manier in onze formulering worden opgenomen. In deze benaderingen kunnen de uitwisseling-correlatiekernen geheugen hebben en aldus kan rekening gehouden worden met relaxatieprocessen ten gevolge van elektron-elektronverstrooiing. Andere soorten afwijkingen van experimentele resultaten kunnen optreden in systemen met zware elementen wanneer relativistische correcties worden verwaarloosd. Onze methode kan scalaire relativistische effecten en spin-baankoppeling behandelen zowel in de grondtoestands- als in de responsberekeningen door gebruik te maken van de nulde-orde reguliere benadering (ZORA). De spinafhankelijke formulering van deze methode, die toestaat om spin-baankoppeling te behandelen, vertegenwoordigt een eerste stap om de lineaire respons ten gevolge van een extern magnetisch veld te beschrijven.

In hoofdstuk 1 geven we een korte introductie over de optische eigenschappen van vaste stoffen, namelijk de diëlektrische functie en de elektronenergieverliesfunctie. Deze twee grootheden beschrijven de respons van het systeem op respectievelijk een macroscopisch en een extern elektrisch veld. Hoewel de experimenten die deze twee grootheden meten erg verschillend kunnen lijken, bevatten ze dezelfde informatie in de limiet van lange golflengte, d.w.z. voor externe velden die gekarakteriseerd worden door golflengten die lang zijn vergeleken met de interatomaire afstand. In hoofdstuk 2 hebben we een overzicht van het gebruikte theoretische raamwerk gepresenteerd. Tijdsafhankelijke stroomdichtheidsfunctionaaltheorie is een uitbreiding van de eerder geformuleerde dichtheidsfunctionaaltheorie. Wat een dichtheidsfunctionaalbenadering zo aantrekkelijke maakt voor theoretische analyse is het gebruik van de dichtheid als basisgrootheid. De dichtheid, eerder dan de veeldeeltjesgolffunctie, wordt gebruikt om een kwantummechanisch systeem te beschrijven, aangezien de grondtoestandseigenschappen van het systeem kunnen worden uitgedrukt als functionaal van deze grootheid. In de eerste plaats hebben we de fundamentele theorema's van Hohenberg en Kohn bediscussieert alsmede de praktische set van ééndeeltjesvergelijkingen die later door Kohn en Sham geïntroduceerd zijn. Deze vergelijkingen beschrijven een hulpsysteem van deeltjes zonder wisselwerking in een effectieve potentiaal die de dichtheid reproduceert van het echte systeem. We hebben vervolgens de formulering van een dichtheidsfunctionaalaanpak beschreven voor systemen die onderhevig zijn aan tijdsafhankelijke longitudinale velden door de uitdrukking en het bewijs van het Runge-Gross theorema te geven. Uiteindelijk hebben we dan tijdsafhankelijke stroomdichtheidsfunctionaaltheorie geïntroduceerd die ons toestaat om ook transversale velden te behandelen en om de lineaire respons in systemen met periodiciteit te behandelen. Deze theorie is als eerste geformuleerd door Ghosh en Dhara, maar we hebben de belangrijkste stappen in een recenter bewijs van Vignale gepresenteerd. De stroomdichtheid is de basisvariabele en bepaalt uniek de scalaire potentiaal en de vectorpotentiaal die op het systeem werken. Deze aanpak is gebruikt door Kootstra *et al.* om op een elegante manier de lineaire respons van niet-metallische systemen op een macroscopisch elektrisch veld te formuleren. De dynamische respons van het systeem wordt beschreven door het oplossen van de tijdsafhankelijke éénelektronvergelijkingen voor het Kohn-Sham hulpsysteem van deeltjes zonder wisselwerking in een effectieve geïnduceerde scalaire potentiaal en vectorpotentiaal die dezelfde dichtheid en stroomdichtheid geven als het echte systeem. De dichtheid en stroomdichtheid die geïnduceerd worden door de verstorende potentialen kunnen worden uitgedrukt in termen van de Kohn-Sham responsfuncties die alleen van de grondtoestandsorbitalen en hun energieën afhangen. Wanneer de set van vergelijkingen die de geïnduceerde dichtheid en stroomdichtheid beschrijven zelfconsistent opgelost is kan de diëlektrische functie uitgerekend worden met de macroscopische stroomdichtheid. We hebben deze formulering uitgebreid opdat we ook de lineaire respons van metallische kristallijne systemen kunnen behandelen. De afleiding van de methode wordt gegeven in hoofdstuk 3. In de behandeling van de respons van een metaal op een externe verstoring moeten de Kohn-Sham responsfuncties zowel de interband- als de intrabandbijdragen met nauwkeurige behandeling van het Fermi-oppervlak in de Brillouinzone-integraties bevatten. In het bijzonder moeten de intrabandbijdragen worden geëvalueerd gebruik makend van een beschrijving die afhangt van de golfvector. Om dit te bereiken hebben we een algemene verstoring met golfvector $\mathbf{q}$ en frequentie ω beschouwd en hebben we de lineaire respons van het systeem voor verdwijnende q, maar eindige ω afgeleid. Dit is het regime waarin optische eigenschappen worden beschreven.

We hebben gevonden dat binnen de ALDA en in de optische limiet $q \to 0$ we de zelfconsistentveld-vergelijkingen die de inter- en intrabandbijdragen aan de response beschrijven afzonderlijk kunnen oplossen. Wanneer deze vergelijkingen zijn opgelost, kan de diëlektrische functie $\epsilon(\omega) = [1 + 4\pi\chi_e^{inter}(\omega)] - 4\pi i/\omega\, \sigma^{intra}(\omega)$ worden berekend, waar $\chi_e^{inter}(\omega)$ de interbandbijdrage aan de elektrische susceptibiliteit is en $\sigma^{intra}(\omega)$ de intrabandbijdrage aan de macroscopische geleidingstensor is. We hebben ook laten zien dat we in onze aanpak de bekende relatie tussen de elektronenergieverliesfunctie en de diëlektrische functie terugvinden, d.w.z. $2\pi/(q^2V)\, S(\mathbf{q},\omega) = \Im\{-1/\epsilon_L(\mathbf{q},\omega)\}$, waarin $S(\mathbf{q},\omega)$ de dynamische structuurfactor is en $\epsilon_L(\mathbf{q},\omega)$ de longitudinale diëlektrische functie. We hebben de methode toegepast om de diëlektrische functies en de elektronenergieverliesfuncties van koper en zilver te berekenen en de overeenkomst met de experimentele resultaten is erg goed. Echter, sterke afwijkingen van de experimentele spectra kunnen verwacht worden voor zware metalen. Hier spelen relativistische effecten een belangrijke rol. In hoofdstuk 4 hebben we een introductie gegeven over een relativistische formulering van dichtheidsfunctionaaltheorie, die gebaseerd is op kwantumelektrodynamica. Analoog aan het niet-relativistische stationaire geval kan een één-op-één correspondentie tussen de externe vier-componentenpotentiaal en de vier-componentenstroomdichtheid van het systeem worden bewezen. We hebben beschreven op welke manier de Dirac-Kohn-Sham-vergelijkingen kunnen worden verkregen en op welke manier de vier-componenten-Hamiltoniaan naar een pseudorelativistische tweecomponenten-Hamiltoniaan kan worden gereduceerd door de nulde-orde reguliere benadering te gebruiken. Al in de nulde orde bevat de ZORA-Hamiltoniaan de dominante relativistische effecten. In hoofdstuk 5 hebben we deze aanpak gecombineerd met onze lineaire-responsformulering en hebben we de diëlektrische functie van goud berekend. We hebben laten zien dat in een niet-relativistische berekening het begin van de interbandabsorptie van goud bij ongeveer 3.5 eV ligt, terwijl het begin van deze absorptie bij ~1.9 eV ligt wanneer scalaire relativistische effecten worden meegenomen in de berekening. Dit verklaart aldus de gele kleur van goud. In hoofdstuk 6 hebben we in detail de bandstructuren, de Fermi-doorsneden en de optische eigenschappen van de groep VB bcc transitiemetalen V, Nb, Ta en de groep VIB bcc transitiemetalen (paramagnetisch) Cr, Mo, en W geanalyseerd. Hier wordt duidelijk hoe nauwkeurig en veelzijdig onze methode is. Enkele afwijkingen van de experimentele resultaten kunnen het gevolg zijn van het verwaarlozen van spin-baankoppeling. In hoofdstuk 8 hebben we een voorlopige spinafhankelijke formulering van de methode gepresenteerd, die ook als doel heeft om de lineaire respons ten gevolge van magnetische velden te behandelen. Als onmiddellijke toepassing hebben we de spin-baankoppeling in zowel de grondtoestand als de responsberekening meegenomen. We hebben de voornaamste veranderingen laten zien die gedaan moeten worden in de responsfuncties om ze uit te drukken in termen van twee-componentenspinoren. We hebben de methode getest op metallische en niet-metallische systemen. De ZORA-berekeningen van de diëlektrische functies van Au en W laten enkele spectrale kenmerken zien die ontbraken in de scalaire-ZORA-spectra, en zijn in overeenkomst met onze voorspellingen (hoofdstukken 5 en 6) en met de experimentele resultaten. We hebben het effect van de relativiteit op de grondtoestandseigenschappen en optische eigenschappen van ZnTe, CdTe, en HgTe geanalyseerd. Terwijl de eerste twee materialen van deze serie halfgeleiders zijn in zowel de niet-relativistische als de relativistische berekeningen, wordt HgTe een halfmetaal wanneer relativiteit wordt meegenomen. Het meenemen van spin-baankoppeling is onmiddellijk zichtbaar in de spectra, aangezien er een splitsing van de piek in het lage-frequentiegebied optreedt die erg goed de experimentele resultaten reproduceert, hoewel de spectra ~ 1 eV zijn opgeschoven naar lagere frequentie ten opzichte van de experimentele resultaten.

Hoewel de berekende spectra in het algemeen in goede overeenstemming zijn met de experimentele resultaten ontbreekt de Drude-achtige absorptie in het lage-frequentiegebied in onze berekeningen. Deze absorptie is het gevolg van relaxatieprocessen en kan dus niet beschreven worden binnen de adiabatische lokale dichtheidsbenadering waarin de responskern instantaan is. In hoofdstuk 7 hebben we een functionaal gebruikt die verder gaat dan de ALDA: de uitwisseling-correlatievectorpotentiaal wordt benaderd door een lokale functionaal van de stroomdichtheid gebruik makend van de uitdrukking die is afgeleid door Vignale en Kohn. De zelfconsistentveld-vergelijkingen die de inter- en intrabandbijdragen aan de respons beschrijven zijn nu gekoppeld. Binnen deze benadering heeft de responskern geheugen, om die reden kan deze kern relaxatieprocessen ten gevolge van elektron-elektronverstrooiing in beschouwing nemen. We hebben de diëlektrische functies en elektronenergieverliesfuncties van de edelmetalen Cu, Ag en Au berekend en onze resultaten reproduceren de experimentele resultaten redelijk goed.

Bibliography

[1] P. Nozières and D. Pines, *The Theory of Quantum Liquids* (Perseus Books, Cambridge, Massachusetts, 1999).

[2] S. L. Adler, Phys. Rev. **126**, 413 (1962).

[3] D. Pines, Rev. Mod. Phys. **28**, 184 (1956).

[4] W. Kohn, Phys. Rev. Lett. **51**, 1596 (1983).

[5] R. van Leeuwen, Adv. Quantum Chem. **43**, 26 (2003).

[6] P. Hohenberg and W. Kohn, Phys. Rev. **136**, B864 (1964).

[7] E. H. Lieb, Int. J. Quant. Chem. **51**, 1596 (1983).

[8] W. Kohn and L. J. Sham, Phys. Rev. A **140**, 1133 (1965).

[9] A. D. Becke, Phys. Rev. A **38**, 3098 (1988).

[10] J. P. Perdew, Phys. Rev. B **33**, 8822 (1986).

[11] C. Lee, W. Yang, and R. G. Parr, Phys. Rev. B **37**, 785 (1988).

[12] J. P. Perdew, K. Burke, and M. Ernzerhof, Phys. Rev. B **54**, 16533 (1996).

[13] E. Runge and E. K. U. Gross, Phys. Rev. Lett. **52**, 997 (1984).

[14] R. van Leeuwen, Phys. Rev. Lett. **82**, 3863 (1999).

[15] R. van Leeuwen, Int. J. Mod. Phys. B **15**, 1969 (2001).

[16] G. Vignale, Phys. Rev. Lett. **74**, 3233 (1995).

[17] L. V. Keldysh, Sov. Phys. JETP **20**, 1018 (1965).

[18] A. K. Dhara and S. K. Ghosh, Phys. Rev. A **35**, R442 (1987).

[19] S. K. Ghosh and A. K. Dhara, Phys. Rev. A **38**, 1149 (1988).

[20] G. Vignale, Phys. Rev. B **70**, 201102 (R) (2004).

[21] O. L. Brill and B. Goodman, Am. J. Phys. **35**, 832 (1967).

[22] A. Zangwill and P. Soven, Phys. Rev. Lett. **45**, 204 (1980); Phys. Rev. B **24**, 4121 (1981).

[23] G. Vignale, Phys. Lett. A **209**, 206 (1995).

[24] G. Vignale and W. Kohn, Phys. Rev. Lett. **77**, 2037 (1996).

[25] G. Vignale and W. Kohn, in *Electronic Density Functional Theory: Recent Progress and New Directions*, edited by J. Dobson, M. P. Das, and G. Vignale (Plenum Press, New York, 1998).

[26] E. K. U. Gross and W. Kohn, Adv. Quantum Chem. **21**, 255 (1990).

[27] E. K. U. Gross, J. F. Dobson, and M. Petersilka, Top. Curr. Chem. **181**, 81 (1996).

[28] R. van Leeuwen, in *Progress in Nonequilibrium Green's Functions II*, edited by M. Bonitz and D. Semkat, (World Scientific, New Jersey, 2003), p.427.

[29] O. -J. Wacker, R. Kümmel, and E. K. U. Gross, Phys. Rev. Lett. **73**, 2915 (1994).

[30] F. Kootstra, P. L. de Boeij, and J. G. Snijders, J. Chem. Phys. **112**, 6517 (2000).

[31] F. Kootstra, P. L. de Boeij, and J. G. Snijders, Phys. Rev. B **62**, 7071 (2000).

[32] R. Resta, Rev. Mod. Phys. **66**, 899 (1994).

[33] X. Gonze, P. Ghosez, and R. W. Godby, Phys. Rev. Lett. **74**, 4035 (1995), *ibid.* **78**, 294 (1997).

[34] G. F. Bertsch, J. I. Iwata, A. Rubio, and K. Yabana, Phys. Rev. B **62**, 7998 (2000).

[35] N. Wiser, Phys. Rev. **129**, 62 (1963).

[36] G. Onida, L. Reining, and A. Rubio, Rev. Mod. Phys. **74**, 601 (2002).

[37] R. O. Jones and O. Gunnarson, Rev. Mod. Phys. **61**, 689 (1989).

[38] Z. H. Levine and D. C. Allan, Phys. Rev. B **43**, 4187 (1991); **44**, 12781 (1991); Phys. Rev. Lett. **66**, 41 (1991).

[39] M. S. Hybertsen and S. G. Louie, Phys. Rev. B **34**, 5390 (1986).

[40] R. W. Godby, M. Schlüter, and L. J. Sham, Phys. Rev. Lett. **56**, 2415 (1986); Phys. Rev. B **37**, 10159 (1988).

[41] J. Chen, Z. H. Levine, and J. W. Wilkins, Phys. Rev. B **50**, 11514 (1994).

[42] V. I. Gavrilenko and F. Bechstedt, Phys. Rev. B **54**, 13416 (1996).

[43] L. Reining, V. Olevano, A. Rubio, and G. Onida Phys. Rev. Lett. **88**, 066404 (2002)

[44] Y. -H. Kim and A. Görling, Phys. Rev. B **66**, 035114 (2002); Phys. Rev. Lett. **89**, 096402 (2002).

[45] F. Sottile, V. Olevano, and L. Reining, Phys. Rev. Lett. **91**, 056402 (2003).

[46] R. Del Sole, G. Adragna, V. Olevano, and L. Reining, Phys. Rev. B **67**, 045207 (2003).

[47] A. Marini, R. Del Sole, and A. Rubio, Phys. Rev. Lett. **91**, 256402 (2003).

[48] I. V. Tokatly, R. Stubner, and O. Pankratov, Phys. Rev. B **65**, 113107 (2002).

[49] P. L. de Boeij, F. Kootstra, J. A. Berger, R. van Leeuwen, and J. G. Snijders, J. Chem. Phys. **115**, 1995 (2001).

[50] H. Ehrenreich and H. R. Philipp, Phys. Rev. **128**, 1622 (1962).

[51] P. B. Johnson and R. W. Christy, Phys. Rev. B **6**, 4370 (1972).

[52] K. Stahrenberg, Th. Herrmann, K. Wilmers, N. Esser, and W. Richter, Phys. Rev. B **64**, 115111 (2001).

[53] I. Campillo, A. Rubio, and J. M. Pitarke, Phys. Rev. B **59**, 12188 (1999).

[54] M. A. Cazalilla, J. S. Dolado, A. Rubio, and P. M. Eschenique, Phys. Rev. B **61**, 8033 (2000).

[55] G. Breit, Phys. Rev. **34**, 553 (1929); **39**, 616 (1932).

[56] T. Kjeldaas and W. Kohn, Phys. Rev. **105**, 806 (1957).

[57] M. Lax, *Symmetry Principles in Solid State and Molecular Physics* (Dover Publications, Inc. Mineola, New York, 2001).

[58] S. E. Schnatterly, in *Solid State Physics Vol.34*, edited by H. Ehrenreich, F. Seitz, and D. Turnbull (Academic Press, Inc., New York, 1979).

[59] G. Lehmann and M. Taut, Phys. Status. Solidi B **54**, 469 (1972).

[60] G. Wiesenekker and E. J. Baerends, J. Phys.: Condens. Matter **3**, 6721 (1991); G. Wiesenekker, G. te Velde, and E. J. Baerends, J. Phys. C **21**, 4263 (1988).

[61] G. te Velde and E. J. Baerends, Phys. Rev. B **44**, 7888 (1991); J. Comput. Phys. **99**, 84 (1992).

[62] C. Fonseca Guerra, O. Visser, J. G. Snijders, G. te Velde and E. J. Baerends, in *Methods and Techniques in Computational Chemistry*, edited by E. Clementi and G. Corongiu, (STEF, Cagliari, 1995), p. 305.

[63] G. te Velde, F. M. Bickelhaupt, E. J. Baerends, C. Fonseca Guerra, S. J. A. van Gisbergen, J. G. Snijders and T. Ziegler, J. Comput. Chem. **22**, 931 (2001).

[64] F. Herman and S. Skillman, *Atomic Structure Calculations*, (Prentice-Hall, Englewood Cliffs NJ, 1963).

[65] S. H. Vosko, L. Wilk and M. Nusair, Can. J. Phys. **58**, 1200 (1980).

[66] R. T. Beach and R. W. Christy, Phys. Rev. B **12**, 5277 (1977).

[67] G. R. Parkins, W. E. Lawrence, and R. W. Christy, Phys. Rev. B **23**, 6408 (1981).

[68] R. van Leeuwen, Phys. Rev. B **69**, 115110 (2004).

[69] J. A. Berger, P. L. de Boeij, and R. van Leeuwen, Phys. Rev. B **71**, 155104 (2005).

[70] E. D. Palik, *Handbook of Optical Constants of Solids* (Acaademic Press, New York, 1985).

[71] R. M. Morgan and D. W. Lynch, Phys. Rev. **172**, 628 (1968).

[72] G. B. Irani, T. Huen, and F. Wooten, Phys. Rev. B **3**, 2385 (1971).

[73] A. K. Rajagopal and J. Callaway, Phys. Rev. B **7**, 1912 (1973).

[74] E. Engel and M. R. Dreizler, in *Density Functional Theory II*, edited by R. F. Nalewajski, Topics in Current Chemistry Vol. 181 (Springer, Berlin, 1996), p. 1.

[75] E. Engel, in *Relativistic Electronic Structure Theory, Part 1. Fundamentals*, edited by P. Schwerdtfeger (Elsevier, Amsterdam, 2002), p. 523.

[76] A. K. Rajagopal, J. Phys. C **11**, L943 (1978).

[77] A. H. MacDonald and S. H. Vosko, J. Phys. C **12**, 2977 (1979).

[78] A. K. Rajagopal, Phys. Rev. B **50**, 3759 (1994).

[79] E. van Lenthe, E. J. Baerends, and J. G. Snijders, J. Chem. Phys. **101**, 9783 (1994).

[80] E. van Lenthe, R. van Leeuwen, E. J. Baerends, and J. G. Snijders, Int. J. Quant. Chem. **57**, 281 (1996).

[81] L. L. Foldy and S. A. Wouthuysen, Phys. Rev. **78**, 29 (1950).

[82] R. E. Moss, in *Advanced Molecular Quantum Mechanics*, (Chapman and Hall, London, 1973).

[83] E. J. Baerends, W. H. E. Schwarz, P. Schwerdtfeger, and J. G. Snijders, J. Phys. B **23**, 3225 (1990).

[84] P. Romaniello and P. L. de Boeij, Phys. Rev. B **71**, 155108 (2005).

[85] P. Pyykkö, Chem. Rev. **88**, 563 (1988).

[86] P. Pyykkö, Angew. Chem. Int. Ed. **43**, 4412 (2004).

[87] B. R. Cooper, H. Ehrenreich, and H. R. Philipp Phys. Rev. **138**, A494 (1965).

[88] N. E. Christensen and B. O. Seraphin, Phys. Rev. B **4**, 3321 (1971).

[89] S. Kupratakuln, J. Phys. C: Solid St. Phys. **3**, S109 (1970).

[90] M. Guerrisi, R. Rosei, and P. Winsemius, Phys. Rev. B **12**, 557 (1975); P. Winsemius, M. Guerrisi, and R. Rosei, Phys. Rev. B **12**, 4570 (1975).

[91] P. Winsemius, F. F. van Kampen, H. P. Lengkeek, and C. G. van Went, J. Phys. F: Metal Phys. **6**, 1583 (1976).

[92] G. B. Irani, T. Huen, and F. Wooten, Phys. Rev. B **6**, 2904 (1972).

[93] F. Kootstra, P. L. de Boeij, H. Aissa, and J. G. Snijders, J. Chem. Phys. **114**, 1860 (2001).

[94] The ellipsometry measurements were performed using a commercial ellipsometer Woollam operating in the spectral range 3000-6000 cm^{-1}. The angle of incidence was fixed at 70^o. The sample was a Au thin film of 500 nm thick deposited onto a silicon substrate by evaporation.

[95] P. L. de Boeij, F. Kootstra, and J. G. Snijders, Int. J. Quant. Chem. **85**, 449 (2001).

[96] G. te Velde, Ph.D. thesis, Free University, Amsterdam, 1990.

[97] E. J. Baerends, D. E. Ellis, and P. Ros, Chem. Phys. **2**, 41 (1973).

[98] R. N. Schmid, E. Engel, R. M. Dreizler, P. Blaha, and K. Schwartz, Adv. Quantum Chem. **33**, 209 (1999).

[99] A. Khein, D. J. Singh, and C. J. Umrigar, Phys. Rev. B **51**, 4105 (1995).

[100] O. D. Häberlen, S. Chung, M. Stener, and N. Rösch, J. Chem. Phys. **106**, 51889 (1997).

[101] J. P. Perdew, in *Electronic Structure of Solids 1991*, edited by P. Ziesche and H. Eschrig, (Akademie Verlag, Berlin, 1991), p. 11.

[102] D. E. Aspnes, E. Kinsbron, and D. D. Bacon, Phys. Rev. B **21**, 3290 (1980).

[103] G. P. Pells and M. Shiga, J. Phys. C **2**, 1835 (1969).

[104] J. H. Weaver, D. W. Lynch, and C. G. Olson, Phys. Rev. B **7**, 4311 (1973).

[105] J. H. Weaver, D. W. Lynch, and C. G. Olson, Phys. Rev. B **10**, 501 (1974).

[106] J. H. Weaver, C. G. Olson, and D. W. Lynch, Phys. Rev. B **12**, 1293 (1975).

[107] J. H. Weaver, C. G. Olson, M. Piacentini, and D. W. Lynch, Solid State Commoun. **16**, 163 (1975).

[108] D. W. Lynch, C. G. Olson, and J. H. Weaver, Phys. Rev. B **11**, 3617 (1975).

[109] J. H. Weaver, Phys. Rev. B **11**, 1416 (1975).

[110] P. Romaniello and P. L. de Boeij, J. Chem. Phys. **122**, 164303 (2005).

[111] J. E. Nestell, Jr. and R. W. Christy, Phys. Rev. B **21**, 3173 (1980).

[112] P. B. Johnson and R. W. Christy, Phys. Rev. B **9**, 5056 (1974).

[113] P. H. T. Philipsen, E. van Lenthe, J. G. Snijders, and E. J. Baerends, Phys. Rev. B **56**, 13556 (1997).

[114] P. Bagno, O. Jepsen, and O. Gunnarsson, Phys. Rev. B **40**, 1997 (1989).

[115] T. C. Leung, T. C. Chan, and B. N. Harmon, Phys. Rev. B **44**, 2923 (1991).

[116] A. Khein, D. J. Singh, and C. J. Umrigar, Phys. Rev. B **51**, 4105 (1995).

[117] D. J. Singh and J. Ashkenazi, Phys. Rev. B **46**, 11570 (1992).

[118] N. A. W. Holzwarth and Y. Zeng, Phys. Rev. B **49**, 2351 (1994).

[119] V. N. Antonov, A. I. Bagljuk, A. Ya. Perlov, V. V. Nemoshkalenko, Vl. N. Antonov, O. K. Andersen, and O. Jepsen Low Temp. Phys. **19**, 494 (1993).

[120] W. E. Pickett and P. B. Allen, Phys. Rev. B **13**, 1473 (1976).

[121] B. Chakraborty, W. E. Pickett, and P. B. Allen, Phys. Rev. B **14**, 3227 (1976).

[122] L. F. Mattheiss and L. R. Testardi, Phys. Rev. B **17**, 4640 (1978).

[123] E. S. Black, D. W. Lynch, and C. G. Olson, Phys. Rev. B **16**, 2337 (1977).

[124] A. R. Jani, N. E. Brener, and J. Callaway, Phys. Rev. B **38**, 9425 (1988).

[125] W. E. Pickett and P. B. Allen, Phys. Rev. B **11**, 3599 (1975).

[126] J. H. Weaver, D. W. Lynch, C. H. Culp, and R. Rosei, Phys. Rev. B **14**, 459 (1976).

[127] E. Colavita, A. Franciosi, C. Mariani, and R. Rosei, Phys. Rev. B **27**, 4684 (1983).

[128] D. L. Misell and A. J. Atkins, Phil. Mag. **27**, 95 (1973).

[129] D. M. Ceperley and B. J. Alder, Phys. Rev. Lett. **45**, 566 (1980).

[130] Z. Qian and G. Vignale, Phys. Rev. B **65**, 235121 (2002).

[131] S. Conti, R. Nifosì, and M. P. Tosi, J. Phys. Condens. Matter **9**, L475 (1997).

[132] J. A. Berger, P. L. de Boeij, and R. van Leeuwen, *in preparation.*

[133] H. J. Hagemann, W. Gudat, and C. Kunz, J. Opt. Soc. Am. **65**, 742 (1975).

[134] B. Dold and R. Mecke, Optik Am. **65**, 742 (1975).

[135] J. H. Weaver, C. Krafka, D. W. Lynch, and E. E. Koch, in *Optical properties of Metals*, (Physics Data, Fachinformationszentrum, Kalsruhe, 1981).

[136] G. Vignale, C. A. Ullrich, and S. Conti, Phys. Rev. Lett. **79**, 4878 (1997).

[137] S. Conti and G. Vignale, Phys. Rev. B **60**, 7966 (1999).

[138] C. A. Ullrich and G. Vignale, Phys. Rev. B **65**, 245102 (2002).

[139] H. M. Böhm, S. Conti, and M. P. Tosi, J. Phys. Condens. Matter **8**, 781 (1996).

[140] R. Nifosì, S. Conti, and M. P. Tosi, Phys. Rev. B **58**, 12758 (1998).

[141] A. J. Glick and W. F. Long, Phys. Rev. B **4**, 3455 (1971).

[142] J. B. Smith and H. Ehrenreich, Phys. Rev. B **25**, 923 (1982).

[143] G. R. Parkins, W. E. Lawrence, and R. W. Christy, Phys. Rev. B **23**, 6408 (1981).

[144] R. T. Beach and R. W. Christy, Phys. Rev. B **12**, 5277 (1977).

[145] S. R. Nagel and S. E. Schnatterly, Phys. Rev. B **9**, 1299 (1974).

[146] P. Romaniello and P. L. de Boeij, Phys. Rev. B **73**, 075115 (2006).

[147] S. H. Groves, R. N. Brown, and C. R. Pidgeon, Phys. Rev. **161**, 779 (1967).

[148] M. Cardona and D. L. Greenaway, Phys. Rev. **131**, 98 (1963).

[149] L. Vinã, C. Umbach, M. Cardona, and L. Vodopyanov, Phys. Rev. B **29**, 6752 (1984).

[150] D. J. Chadi, J. P. Walter, M. l. Cohen, Y. Petroff, and M. Balkanski, Phys. Rev. B **5**, 3058 (1972).

[151] D. J. Chadi and M. l. Cohen, Phys. Rev. B **7**, 692 (1973).

[152] A. Delin and T. Klüner, Phys. Rev. B **66**, 035117 (2002).

[153] A. I. Belogorokhov, A. A. Florentsev, I. A. Belogorokhov, N. V. Pashkova, and A. V. Elyutin, Semiconductors **40**, 276 (2006).

[154] A. Kisiel and P. M. Lee, J. Phys. F: Metal Phys. **2**, 395 (1972).

[155] M. Cardona, N. E. Christensen, and G. Fasol, Phys. Rev. B **38**, 1806 (1988).

[156] S. -H. Wei and A. Zunger, Phys. Rev. B **37**, 8958 (1988).

[157] R. Markowski and M. Podórny, J. Phys.: Condens. Matter **4**, 2505 (1992).

[158] N. J. Shevchikand, J. Tejeda, M. Cardona, and D. W. Langer, Phys. Status Solidi B **59**, 87 (1973).

[159] L. Ley, R. A. Pollak, F. F. Mcfeely, S. P. Kowalczyk, and D. A Shirley, Phys. Rev. B **9**, 600 (1974).

[160] E. P. Domashevskaya and V. A. Terekhov, Phys. Status Solidi B **105**, 121 (1981).

[161] See, for example, M. Cardona, K. L. Shaklee, and F. H. Pollak, Phys. Rev. **154**, 696 (1967).

[162] S. H. Groves and W. Paul, in *Proceedings of the Seventh International Conference on Semiconductors*, (Academic, New York, 1965).

[163] J. L. Freelouf, Phys. Rev. B **7**, 3810 (1973).

[164] W. A. Harrison, *Electronic Structure and the Properties of Solids*, (Dover Publications,Inc., New York, 1989).

List of Publications

1. P. Romaniello and P. L. de Boeij, *Relativistic effects in the linear response of solids within a time-dependent two-component formulation*, to be submitted (chapters 4 and 8)

2. J. A. Berger, P. Romaniello, R. van Leeuwen, and P. L. de Boeij, *Performance of the Vignale-Kohn functional in the linear response of metals*, Phys. Rev. B submitted (chapter 7)

3. P. Romaniello and P. L. de Boeij, F. Carbone and D. van der Marel, *Optical properties of bcc transition metals in the range 0-40 eV*, Phys. Rev. B **73**, 075115 (2006) (chapter 6)

4. P. Romaniello and P. L. de Boeij, *The role of relativity in the optical response of gold within the time-dependent current-density-functional theory*, J. Chem. Phys. **122**, 164303 (2005) (chapter 5)

5. P. Romaniello and P. L. de Boeij, *Time-dependent current-density-functional theory for the metallic response of solids*, Phys. Rev. B **71**, 155108 (2005) (chapter 3)

Acknowledgments

Heartfelt thanks to everyone who made this book possible and this experience here in Groningen unforgettable.

To Jaap, who believed in me and allowed me to start this research. Although for too short, I enjoyed to work with him and, above all, to be impressed by his knowledge.
To Ria goes my gratitude for accepting to become later on my promotor.
To Paul, who followed my research from the beginning to the end, I will be eternally grateful. Paul, thanks a lot for the time you have dedicated to teach me and to let me understand in a simple way also difficult concepts of any kind. Your brilliant solutions to intricate problems never failed to arrive and to amaze me.

I feel very grateful to prof. dr. Evert Jan Baerends, to prof. dr. Xavier Gonze, and to prof. dr. Rob de Groot for being members of my reading committee and for their useful suggestions.

Beyond their scientific value, these four years have also been an exceptional human experience. I have met many people and faced different customs, particular sensitivities, sometimes crazy phobias, and so special souls. I have always learnt something from them and received a lot. Many thanks!
Specially to you, Arjan, and to your family. Hartelijk bedankt voor het verlichten van mijn heimwee tijdens de donkere winters, de stormachtige herfst, de regenachtige lentes, en de niet-bestaande zomers. Arjan, thanks for your precious presence, specially in vulnerable moments, with your unconditional love, unlimited patience, and extraordinary humor!
And grazie! to all the nice people in my research group who have welcomed me and let me enjoy both the working and the free time.

Although so distant I have never lost contact with my Italy!

Special thanks to my friend of a thousand adventures. How would it have been without your calls, Ivan? Many thanks for listening to my Italian curses, for sharing our fears, our anger, our happiness!
I am very grateful to prof. Francesco Lelj. Our discussions about science and life also during these last years have been enlightening, inspiring, and sometimes decisive. I wish we will always find time for this.
And thanks to all my friends !!! Ogni volta che sono tornata in Italia è sempre stato come se mai fossi andata via. Le pizze, le discussioni sull'univeristà, sui professori, sulle emicranie, e sui vecchi tempi...indimenticabili!

Grazie all mia famiglia, fonte continua di amore, protezione e serenità. Sempre nei miei pensieri e nel mio cuore.

Pina Romaniello,
Groningen, October 2006